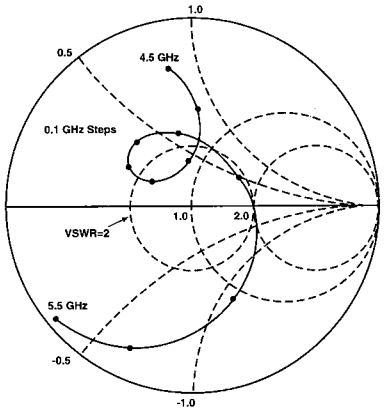

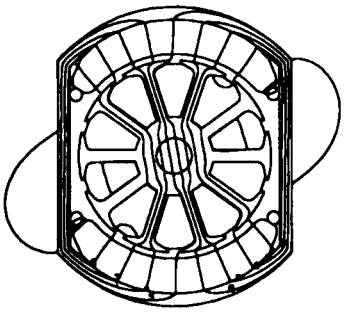

Applied Computational Electromagnetics Society Journal

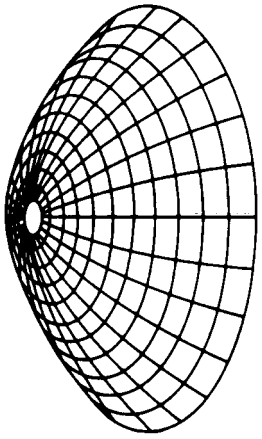

Editor-in-Chief
Atef Z. Elsherbeni

March 2005
Vol. 20 No. 1
ISSN 1054-4887

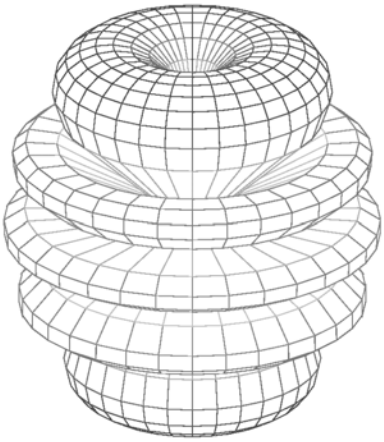

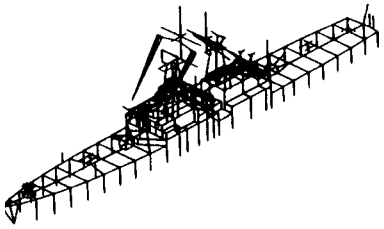

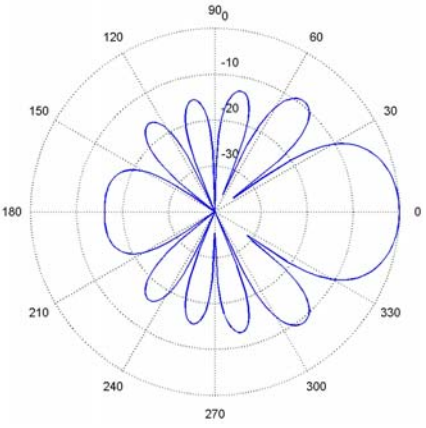

GENERAL PURPOSE AND SCOPE: The Applied Computational Electromagnetics Society ***(ACES)*** Journal hereinafter known as the ***ACES Journal*** is devoted to the exchange of information in computational electromagnetics, to the advancement of the state-of-the art, and the promotion of related technical activities. A primary objective of the information exchange is the elimination of the need to "re-invent the wheel" to solve a previously-solved computational problem in electrical engineering, physics, or related fields of study. The technical activities promoted by this publication include code validation, performance analysis, and input/output standardization; code or technique optimization and error minimization; innovations in solution technique or in data input/output; identification of new applications for electromagnetics modeling codes and techniques; integration of computational electromagnetics techniques with new computer architectures; and correlation of computational parameters with physical mechanisms.

SUBMISSIONS: The ***ACES Journal*** welcomes original, previously unpublished papers, relating to applied computational electromagnetics. Typical papers will represent the computational electromagnetics aspects of research in electrical engineering, physics, or related disciplines. However, papers which represent research in applied computational electromagnetics itself are equally acceptable.

Manuscripts are to be submitted through the upload system of ***ACES*** web site http://aces.ee.olemiss.edu See "Information for Authors" on inside of back cover and at ***ACES*** web site. For additional information contact the Editor-in-Chief:

Dr. Atef Elsherbeni
Department of Electrical Engineering
The University of Mississippi
University, MS 386377 USA
Phone: 662-915-5382 Fax: 662-915-7231
Email: atef@olemis.edu

SUBSCRIPTIONS: All members of the Applied Computational Electromagnetics Society who have paid their subscription fees are entitled to receive the ***ACES Journal*** with a minimum of three issues per calendar year and are entitled to download any published journal article available at http://aces.ee.olemiss.edu.

Back issues, when available, are $15 each. Subscriptions to ***ACES*** are through the web site. Orders for back issues of the ***ACES Journal*** and changes of addresses should be sent directly to ***ACES*** Executive Officer:

Dr. Richard W. Adler
ECE Department, Code ECAB
Naval Postgraduate School
833 Dyer Road, Room 437
Monterey, CA 93943-5121 USA
Fax: 831-649-0300
Email: *rwa@attglobal.net*

Allow four week's advance notice for change of address. Claims for missing issues will not be honored because of insufficient notice or address change or loss in mail unless the Executive Officer is notified within 60 days for USA and Canadian subscribers or 90 days for subscribers in other countries, from the last day of the month of publication. For information regarding reprints of individual papers or other materials, see "Information for Authors".

LIABILITY. Neither ***ACES***, nor the ***ACES Journal*** editors, are responsible for any consequence of misinformation or claims, express or implied, in any published material in an ***ACES Journal*** issue. This also applies to advertising, for which only camera-ready copies are accepted. Authors are responsible for information contained in their papers. If any material submitted for publication includes material that has already been published elsewhere, it is the author's responsibility to obtain written permission to reproduce such material.

APPLIED COMPUTATIONAL ELECTROMAGNETICS SOCIETY JOURNAL

Editor-in-Chief
Atef Z. Elsherbeni

March 2005
Vol. 20 No. 1

ISSN 1054-4887

The ACES Journal is abstracted in INSPEC, in Engineering Index, and in DTIC.

The first, fourth, and sixth illustrations on the front cover have been obtained from the Department of Electrical Engineering at the University of Mississippi.

The third and fifth illustrations on the front cover have been obtained from Lawrence Livermore National Laboratory.

The second illustration on the front cover has been obtained from FLUX2D software, CEDRAT S.S. France, MAGSOFT Corporation, New York.

THE APPLIED COMPUTATIONAL ELECTROMAGNETICS SOCIETY

JOURNAL

Vol. 20 No. 1 March 2005

TABLE OF CONTENTS

Generalization of Surface Junction Modeling for Composite Objects in an SIE/MoM Formulation Using a Systematic Approach

Joon Shin, Allen W. Glisson, and Ahmed A. Kishk
Department of Electrical Engineering
The University of Mississippi
University, MS 38677

Abstract— **This paper discusses the modeling of various kinds of surface junctions in an SIE/MoM formulation applied to complex objects consisting of arbitrarily shaped conducting and dielectric bodies. Methods of describing various types of junctions and systematically incorporating them in numerical solutions are presented. The procedures are of interest for the speci c application of arbitrarily shaped dielectric resonator antennas and their associated feed structures and packaging. An E-PMCHWT formulation in conjunction with a moment method procedure using multi-domain RWG basis functions is presented to deal with such general junctions. Some results are veri ed with the FDTD method.**

Index Terms— **surface junction modeling, composite object, SIE/MoM, E-PMCHWT, dielectric resonator antenna, multi-domain basis function, FDTD**

I. INTRODUCTION

THE modeling of general surface junctions in an SIE/MoM (Surface Integral Equation / Method of Moments) formulation is considered in this work. The speci c application leading to this study is that of Dielectric Resonator (DR) antennas. Since an experimental study of a cylindrical DR antenna was reported in 1983 [1], this antenna has drawn continued interest because of its small size, ef cienc y, and potential ability to perform multiple antenna tasks via simple mode coupling mechanisms. The con guration of a DR antenna may range from a very simple one that allows analytic solutions to a very complex one. A typical structure for a DR antenna is a DR element of high dielectric constant excited by a single feed such as a microstripline or coaxial cable. Various shapes and combinations of DR elements as well as various feed structures have been suggested, however, which may improve the antenna performance in the areas of bandwidth, power handling, and antenna ef cienc y. Rigorous SIE analysis methods for non-trivial DR antenna con gurations have been available mainly for Body of Revolution (BoR) objects [2,3]. DR antennas have also been treated with the constraint of a multi-layered environment [4,5]. where the dielectric layers are assumed to be of in nite extent. In this work we consider the modeling of general junctions encountered in such arbitrary con gurations of DR antennas, which may include general 3D (Three-Dimensional) composite objects, using an SIE/MoM method with RWG (Rao-Wilton-Glisson) basis functions. Arbitrary con gurations here refer to an arbitrary number of dielectric regions, arbitrary compositions of conductors and dielectrics, general excitations, etc., as well as arbitrary shapes.

The dif culty with an arbitrary 3D composite object comes mainly from the modeling of surface junctions. To model a surface junction, it has been considered necessary to properly enforce the electromagnetic boundary conditions and the continuity of the currents at the junction. For a given junction this may be accomplished easily, and the associated unknown currents and basis functions are assigned accordingly. However, for an arbitrary con guration consisting of different types of junctions, neither the formulation nor the implementation is trivial. A usual approach might be to implement the junction models only for some limited number of cases and to make modi cations when need arises for a speci c type of junction. A similar argument is true in general, but to a somewhat lesser extent, for the MoM technique regarding the number of dielectric regions and the geometry con guration. The objective of this study is to develop a rigorous yet ef cient numerical method for EM (Electromagnetic) modeling of arbitrary composite structures, which allows one, as a particular application, to ef ciently try various con gurations of DR antennas to optimize the performance.

The junction modeling problem has been considered in previous works for conducting surfaces [6], for dielectric surfaces [7], simple combinations of BoR objects [2,3,8,9], and general conducting, dielectric, resistive, and impedance boundary condition surfaces [10]. Finally, Kolundzija has also reported extensive junction modeling of composite objects [11]. A more detailed account for the junction modeling as well as various SIE/MoM formulations is found in his coauthored book [12]. Kolundzija employed a PMCHWT (Poggio-Miller-Chung-Harrington-Wu-Tsai) formulation [13-15] , which has been commonly been referred to as a PMCHW formulation, and entire domain basis functions de ned over bilinear surfaces, which required fewer unknowns, and thus electrically larger problem can be solved more ef ciently . The extent of his surface junction modeling is the same as ours. He describes the junction modeling in terms of *doublets*, while we do so using *multi-domain basis functions* and *multiplicity of basis function*. He treats an *open* metalic surface located at a dielectric interface as two *closed* metalic surfaces, while we treat it directly as another class of surfaces, which seems simpler to implement. While [11] presents general rules,

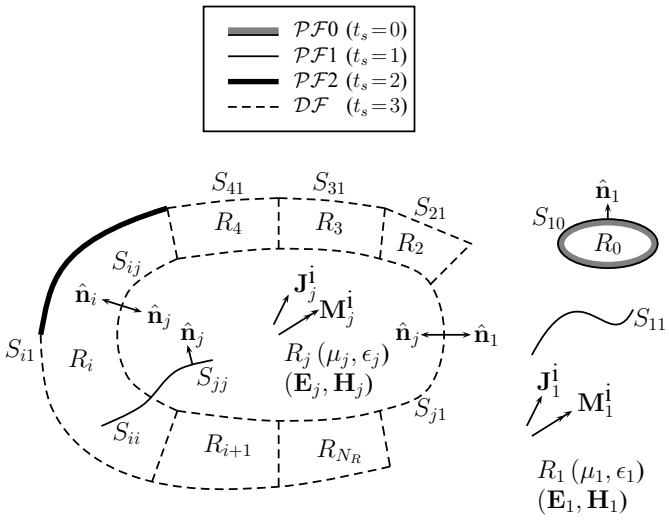

Fig. 1. General geometry under consideration.

we present speci c formulas for systematic and automatic construction of basis functions, and all kinds of junctions are classi ed into only a few cases, for which speci c formulas are given. In general we feel that our description of junction modeling is elegant and systematic. The advantage of such a systematic approach is that it enables a developer to set up a framework that can be easily extended to include new features more easily while maintaining code clarity. It should be noted that another procedure for junction treatment has also been recently described in [16].

II. FORMULATION

A. Problem Description

The geometry under consideration is a general inhomogeneous body with N_R dielectric regions, each of which may contain conducting bodies as well as impressed sources as shown in Fig. 1. The regions have permittivities ϵ_i and permeabilities μ_i, where $i = 1, \cdots, N_R$. Both ϵ_i and μ_i may be complex to represent lossy materials. Non-zero thickness conducting bodies denoted by R_0 may occupy any parts of the space. In nitely thin conducting bodies can reside in any region, at interfaces between regions, or they may penetrate from one region to another. All conductors are considered to be PEC (Perfect Electric Conductor) material. One of the regions, region R_1 in Fig. 1, may be of in nite extent. The total elds in each region are denoted by $\mathbf{E}_i$ and $\mathbf{H}_i$, where $i = 0, 1, 2, \cdots, N_R$, for electric and magnetic elds, respectively, and $i = 0$ denotes PEC regions with $\mathbf{E}_0 = \mathbf{H}_0 = \mathbf{0}$. The time variation, $e^{j\omega t}$, is assumed and suppressed throughout.

Any two adjacent regions, R_i and R_j, are separated by a surface denoted by $S_{ij}(t_s, t, f)$, where t_s is the type of the surface, and t and f are the 'to-region' and the 'from-region' of the surface, respectively, which de ne the region connectivity and the surface orientation. The interface between a non-zero thickness conducting body and a dielectric region also forms a surface denoted in the same way with the 'from-region' being region zero. An in nitely thin conducting body in a dielectric region forms yet another type of surface with the 'from-region' being the same as the 'to-region. Thus, there are four types of surfaces speci ed by t_s:

(i) $\mathcal{PF}0$ $(t_s = 0)$ — Interface between a conducting body and a dielectric region,
(ii) $\mathcal{PF}1$ $(t_s = 1)$ — In nitely thin conducting body within a dielectric region,
(iii) $\mathcal{PF}2$ $(t_s = 2)$ — In nitely thin conducting body between two dielectric regions, and
(iv) $\mathcal{DF}(t_s = 3)$ — Dielectric interface between two dielectric regions.

These surface types are graphically represented by thick shaded, solid, thick solid, and dashed lines, respectively, in Fig. 1. We refer to $\mathcal{PF}0$, $\mathcal{PF}1$, and $\mathcal{PF}2$ collectively by $\mathcal{PF}$ (PEC faces).

When more than two surfaces meet at a curved line segment, they form a junction. Depending on the numbers and types of the surfaces at a junction, there are a variety of possible junction types, all of which are considered in this study.

Each region R_i is surrounded by a closed surface S_i^C and is associated with an inward normal unit vector $\hat{\mathbf{n}}_i$. The surface interface between regions R_i and R_j, if one exists, is denoted as S_{ij}, for any i and j, $i = 1, \cdots, N_R$, $j = 0, 1, \cdots, N_R$. Thus, S_i^C is the set of all interface surfaces S_{ij}, where j represents all region numbers that interface with region R_i. Note that $S_{ij} = S_{ji}$ for $j \neq 0$; however, the normal unit vectors $\hat{\mathbf{n}}_i$ and $\hat{\mathbf{n}}_j$ are in opposite directions to each other on S_{ij}.

B. The Field Equivalences

According to the equivalence principle [17], the original problem can be decomposed into N_R auxiliary problems, one for each dielectric region. To obtain the auxiliary problem for region R_i, the impressed sources of the original problem are retained only in region R_i and the boundaries of the region are replaced by equivalent surface currents radiating in a homogeneous medium with the constitutive parameters of region R_i. Electric currents are used for the conducting surfaces, while electric and magnetic currents are used for the dielectric boundaries. The electric and magnetic currents appearing on opposite sides of a dielectric interface in different auxiliary problems are taken equal in magnitude and opposite in direction to assure the continuity of the tangential eld components on these boundaries as they are continuous in the original problem. In this procedure, the elds produced within the region boundaries by the equivalent currents and the impressed sources in region R_i must be the same as those in the original problem, while the zero eld is chosen to exist outside these boundaries. The electric and magnetic currents along S_i^C are then $\mathbf{J}_i = \hat{\mathbf{n}}_i \times \mathbf{H}_i$ and $\mathbf{M}_i = \mathbf{E}_i \times \hat{\mathbf{n}}_i$, respectively.

A system of surface integro-differential equations can be obtained by enforcing the boundary conditions of continuity of the tangential components of electric eld on the conducting surfaces and both electric and magnetic elds on the dielectric

surfaces. This results in the E-PMCHWT (Electric-PMCHWT) formulation [9] when there is no junction in the problem. For problems having general junctions, however, it is not easy to express the integral equation system explicitly apart from the testing procedure. Thus the system of integral equations is presented in the next section after describing the junction modeling and the basis functions.

C. Modeling of Junctions in the Moment Method Solution

Arbitrarily shaped surfaces are discretized in triangular patches and the equivalent surface currents are approximated by expansions in the RWG basis functions on the patches [18], which are expressed as

$$\mathbf{J}(\mathbf{r}) \cong \sum_{n=1}^{N_{T_j}} I_n \mathbf{B}_n^{T_j}(\mathbf{r}; S_{T_{n^+}}, S_{T_{n^-}}) \tag{1}$$

where

$$\mathbf{B}_n^{T_j}(\mathbf{r}) = \begin{cases} \pm\, \boldsymbol{\rho}_{n^\pm}/h_{n^\pm}, & \mathbf{r} \in S_{T_{n^\pm}} \\ \mathbf{0}, & \text{otherwise,} \end{cases} \tag{2}$$

N_{T_j} is the number of electric basis functions, and $S_{T_{n^\pm}}$ are the positive/negative domains or the from-/to- faces of the basis function, respectively. For magnetic currents, $\{\mathbf{B}_n^{T_m}\}_{n=1}^{N_{T_m}}$ can be de ned similarly. The testing functions $\mathbf{T}_n^{T_j}$ and $\mathbf{T}_n^{T_m}$ are also taken to be the same as (2). With the basis and testing functions de ned we have a matrix equation

$$\begin{bmatrix} \mathbf{Z}^{T_j\,T_j} & \mathbf{T}^{T_j\,T_m} \\ \mathbf{T}^{T_m\,T_j} & \mathbf{Y}^{T_m\,T_m} \end{bmatrix} \begin{bmatrix} |I^{T_j}\rangle \\ |I^{T_m}\rangle \end{bmatrix} = \begin{bmatrix} |V^{T_j}\rangle \\ |V^{T_m}\rangle \end{bmatrix}. \tag{3}$$

When there are general surface junctions, the current related to an unknown coef cient may exist on many different surfaces. In such cases, the expression (1) is not rigorous enough. For example, there is an electric current on a dielectric surface in the region R_i equivalent problem and another one o wing in the opposite direction in the region R_j problem, represented by '$-I_n$' as shown in Fig. 2(a). The expression in (1) for the electric currents has this sort of implication for the basis functions $\mathbf{B}_n^{T_j}$ when the domain of the unknown involves a dielectric interface, i.e., the single current coef cient I_n represents the current on both sides of the dielectric interface and one must identify which side of the interface carries the current coef cient with the negative sign.

When more than two dielectric surfaces meet at a junction, this scheme does not work. Thus for general junctions, we seek another way of expressing the generalized current more rigorously. We will use two different basis functions for the same unknown coef cient related to a dielectric surface as shown in Fig. 2(b). In other words, the unknown coef cient has a multiplicity of two when it represents the electric or magnetic current on the dielectric face. The current direction on each side of the interface in this case is accounted for by the direction of the basis function (Fig. 2(b)). This procedure is easily extended to account for a junction of multiple interfaces.

Extending this to the general case, the generalized current is de ned in terms of the generalized basis functions as

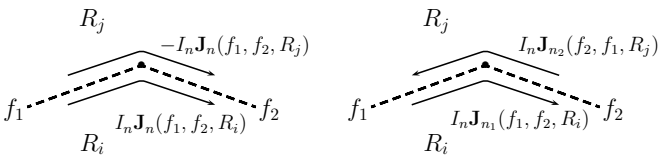

(a) Conventional representation (b) New representation

Fig. 2. Two methods of representing basis functions.

$$\mathbf{C}(\mathbf{r}) = \{\mathbf{J}(\mathbf{r}), \mathbf{M}(\mathbf{r})\} = \{\sum_{n=1}^{N_{T_j}} I_n \mathbf{B}_n(\mathbf{r}), \sum_{n=1+N_{T_j}}^{N} I_n \mathbf{B}_n(\mathbf{r})\} \tag{4}$$

where each $\mathbf{B}_n$ now represents τ_n simple basis functions as indicated below:

$$\mathbf{B}_n(\mathbf{r}) = \begin{cases} \mathbf{B}_k^{T_j}(\mathbf{r}), \text{ with } k = n, & n \le N_{T_j} \\ \mathbf{B}_k^{T_m}(\mathbf{r}), \text{ with } k = n - N_{T_j}, & n > N_{T_j} \end{cases} \tag{5}$$

where

$$\begin{aligned} N &= N_{T_j} + N_{T_m} \\ \mathbf{B}_k^{T_j}(\mathbf{r}) &= \sum_{v=1}^{\tau_k} \mathbf{B}_{k_v}^{T_j}(\mathbf{r}; ff_{k_v}, tf_{k_v}, R_{k_v}) \qquad (6) \\ \mathbf{B}_k^{T_m}(\mathbf{r}) &= \sum_{v=1}^{\tau_k} \mathbf{B}_{k_v}^{T_m}(\mathbf{r}; ff_{k_v}, tf_{k_v}, R_{k_v}) \qquad (7) \\ \mathbf{B}_{n_v} &= \text{the } v^{th} \text{ basis function of } I_n,\ v = 1, ..., \tau_n \\ \mathbf{B}_{k_v}^{T_j}, \mathbf{B}_{k_v}^{T_m} &= \text{RWG basis function de ned over the} \\ &\quad \text{corresponding patches as in (2)} \\ \tau_n &= \text{multiplicity of the unknown coef cient, } I_n \\ &= \begin{cases} n_{dfn}, & n_{dfn} = n_{tf} \\ n_{dfn} + 1, & \text{otherwise} \end{cases} \qquad (8) \end{aligned}$$

$$\begin{aligned} n_{tf} &= \text{total number of faces connected} \\ n_{dfn} &= \text{number of dielectric faces related to } I_n \\ ff_{n_v}, tf_{n_v} &= \text{from-face and to-face of } \mathbf{B}_{n_v}. \\ R_{n_v} &= \text{region of } \mathbf{B}_{n_v}. \end{aligned}$$

Notice that there is one-to-one correspondence between $\mathbf{B}_{n_v}^{T_j}$ or $\mathbf{B}_{n_v}^{T_m}$ and the parameter set $\{ff_{n_v}, tf_{n_v}, R_{n_v}\}$. The numbers of unknowns and basis functions for a given junction or edge are determined from the types and numbers of the faces connected to the junction by considering proper boundary conditions at the junction. The methods of determining them and systematically incorporating them in the MoM solutions have been developed and presented in Appendix, where $\mathbf{J}_n$ and $\mathbf{M}_n$ are used instead of $\mathbf{B}_n^{T_j}$ and $\mathbf{B}_n^{T_m}$, respectively. The generalized testing functions $\{\mathbf{T}_m^{T_j}\}_{m=1}^{N_{T_j}}$, $\{\mathbf{T}_m^{T_m}\}_{m=1}^{N_{T_m}}$, and $\{\mathbf{T}_m\}_{m=1}^{N}$ are also de ned in a similar manner. We also de ne $\mathbf{C}_i$, the generalized current for the region R_i equivalent problem, as

$$\mathbf{C}_i(\mathbf{r}) = \{\mathbf{J}_i(\mathbf{r}), \mathbf{M}_i(\mathbf{r})\} \tag{9}$$

where

$$\mathbf{J}_i(\mathbf{r}) = \sum_{n=1}^{N_{T_j}} I_n \sum_{v=1}^{\tau_n} \delta^S_{n_v i} \mathbf{B}_{n_v}(\mathbf{r}; ff_{n_v}, tf_{n_v}, R_{n_v}) \quad (10)$$

$$\mathbf{M}_i(\mathbf{r}) = \sum_{n=N_{T_j}+1}^{N} I_n \sum_{v=1}^{\tau_n} \delta^S_{n_v i} \mathbf{B}_{n_v}(\mathbf{r}; ff_{n_v}, tf_{n_v}, R_{n_v}) \quad (11)$$

$$\begin{aligned} \delta^S_{n_v i} &= \text{source contribution coefficient} \\ &= \begin{cases} 1, & R_{n_v} = R_i \\ 0, & \text{otherwise} \end{cases}. \end{aligned}$$

With the set of basis functions in (4)–(7), one may apply the boundary conditions of tangential field continuity at each subdomain of the basis functions. By merely applying the boundary conditions, however, the total number of equations may be greater than the number of the unknowns because of the multiplicity of some unknowns related to junctions. The usual methods of solving equations apply only when the number of equations equals to the number of unknowns, N. While the solution of an overdetermined system is certainly possible, it would increase the memory requirements to store the additional equations, and we prefer to generate equations that are equivalent to those we would obtain if modeling the junction in the usual manner.

Such a set of N equations can be obtained by taking the n^{th} integral equation as the set of simultaneous integral equations (or summation of them) which satisfy the proper boundary conditions on the subdomains of the basis functions ($\mathbf{B}_{n_v}, v = 1, ..., \tau_n$) related to the unknown coefficient, I_n. It is possible to obtain such a surface integral equation system by testing with the generalized testing functions as follows

$$\begin{aligned} \sum_{i=1}^{N_R} \langle\, \mathbf{E}_i^{scat}(\mathbf{C}_i), \sum_{u=1}^{\tau_m} \delta^F_{r_{m_u} i}\, \mathbf{T}_{m_u} \,\rangle = \\ -\sum_{i=1}^{N_R} \langle\, \mathbf{E}_i^{inc}, \sum_{u=1}^{\tau_m} \delta^F_{r_{m_u} i}\, \mathbf{T}_{m_u} \,\rangle, \\ m = 1, 2, \ldots, N_{T_j} \end{aligned} \quad (12)$$

$$\begin{aligned} \sum_{i=1}^{N_R} \langle\, \mathbf{H}_i^{scat}(\mathbf{C}_i), \sum_{u=1}^{\tau_m} \delta^F_{r_{m_u} i}\, \mathbf{T}_{m_u} \,\rangle = \\ -\sum_{i=1}^{N_R} \langle\, \mathbf{H}_i^{inc}, \sum_{u=1}^{\tau_m} \delta^F_{r_{m_u} i}\, \mathbf{T}_{m_u} \,\rangle, \\ m = N_{T_j}+1, \ldots, N_{T_j}+N_{T_m}, \end{aligned} \quad (13)$$

where

$$\begin{aligned} \langle\, \mathbf{f}, \mathbf{g} \,\rangle &= \int_S \mathbf{f} \cdot \mathbf{g}\, ds \\ r_{m_u} &= \text{region number of the testing function, } \mathbf{T}_{m_u}, \\ \delta^F_{r_{m_u} i} &= \text{field contribution coefficient} \\ &= \begin{cases} 1, & i = r_{m_u} \text{ (i.e., } R_i = R_{r_{m_u}}) \\ 0, & \text{otherwise} \end{cases} \end{aligned}$$

and ($\mathbf{E}_i^{scat}$, $\mathbf{H}_i^{scat}$) and ($\mathbf{E}_i^{inc}$, $\mathbf{H}_i^{inc}$) are the scattered fields due to $\mathbf{C}_i$ and incident fields, respectively. Equations (12) and (13) are the E-PMCHWT formulation [9] extended to general junctions.

The meaning of (12) is that the scattered and incident electric fields are tested by the electric testing functions. The testings are summed over the entire region ($i = 1, 2, \ldots, N_R$). However, the Kronecker delta function, $\delta^F_{r_{m_u} i}$, deselects the corresponding inner products if the region of the testing function, $\mathbf{T}_{m_u}$, is not R_i. The meaning of (13) is similar. The only difference is that the magnetic fields are tested with the magnetic testing functions as indicated by the range of the indices of the testing functions.

The electric and magnetic field operators, E_i^J, E_i^M, H_i^J, and H_i^M, are defined in terms of the magnetic vector, electric vector, electric scalar, and magnetic scalar potential functions $\mathbf{A}, \mathbf{F}, \Phi$, and Ψ, respectively, as [17]

$$\begin{aligned} \mathbf{E}_i(\mathbf{J}, \mathbf{M}) &= E_i^J \mathbf{J} + E_i^M \mathbf{M} \\ &= \{-j\omega \mathbf{A}_i - \nabla \Phi_i\} + \{-\frac{1}{\epsilon_i} \nabla \times \mathbf{F}_i\} \end{aligned} \quad (14)$$

$$\begin{aligned} \mathbf{H}_i(\mathbf{J}, \mathbf{M}) &= H_i^J \mathbf{J} + H_i^M \mathbf{M} \\ &= \{\frac{1}{\mu_i} \nabla \times \mathbf{A}_i\} + \{-j\omega \mathbf{F}_i - \nabla \Psi_i\}, \end{aligned} \quad (15)$$

where $\mathbf{E}_i$ and $\mathbf{H}_i$ are the electric and magnetic fields at the point $\mathbf{r} \in R_i$ due to the currents $\mathbf{J}$ and $\mathbf{M}$ on a specified surface, S_C. The surface S_C may be a subset of S_i^C, the closed surface of the region R_i, which supports equivalent currents, or it may be a source surface within the region R_i that supports impressed currents. However, there are situations in which no explicit impressed currents exist and the impressed fields are specified, for example, by incident plane wave. In (14) and (15), the subscript i represents the region number in which the fields or the potentials are evaluated. The potential functions are defined as

$$\mathbf{A}_i(\mathbf{r}) = \mu_i \int_{S_C} \mathbf{J}(\mathbf{r}')\, G_i(\mathbf{r}, \mathbf{r}')\, ds' \quad (16)$$

$$\mathbf{F}_i(\mathbf{r}) = \epsilon_i \int_{S_C} \mathbf{M}(r')\, G_i(\mathbf{r}, \mathbf{r}')\, ds' \quad (17)$$

$$\Phi_i(\mathbf{r}) = \frac{1}{\epsilon_i} \int_{S_C} \sigma_e(\mathbf{r}')\, G_i(\mathbf{r}, \mathbf{r}')\, ds' \quad (18)$$

$$\Psi_i(\mathbf{r}) = \frac{1}{\mu_i} \int_{S_C} \sigma_m(\mathbf{r}')\, G_i(\mathbf{r}, \mathbf{r}')\, ds', \quad (19)$$

where the electric and magnetic surface charge densities σ_e and σ_m are related to the surface currents through the equations of continuity,

$$\sigma_e(\mathbf{r}) = -\frac{\nabla_S \cdot \mathbf{J}(\mathbf{r})}{j\omega} \quad (20)$$

$$\sigma_m(\mathbf{r}) = -\frac{\nabla_S \cdot \mathbf{M}(\mathbf{r})}{j\omega}. \quad (21)$$

In (16)–(19), $G_i(\mathbf{r}, \mathbf{r}')$ is the scalar homogeneous region Green's function and is defined as

$$G_i(\mathbf{r}, \mathbf{r}') = \frac{e^{-jk_i R}}{4\pi R}, \quad (22)$$

where $R = \mid \mathbf{r} - \mathbf{r}' \mid$ is the distance between the field point $\mathbf{r} \in R_i$ and the source point $\mathbf{r}' \in S_C$, and $k_i = \omega\sqrt{\mu_i \epsilon_i}$ is the wave number of the region R_i.

Substituting $\mathbf{C}_i$ of (4) into (12) and (13), the impedance matrix and excitation vector elements in (3), $Z_{mn}^{T_j T_j}$ and $V_m^{T_j}$, for example, are expressed as

$$\begin{aligned} Z_{mn}^{T_j T_j} &= \sum_{i=1}^{N_R} \langle\, \mathbf{E}_i^{scat}(\sum_{v=1}^{\tau_n} \delta_{r_{n_v} i}^{S} \mathbf{B}_{n_v}(\mathbf{r}')),\ \sum_{u=1}^{\tau_m} \delta_{r_{m_u} i}^{F} \mathbf{B}_{m_u}(\mathbf{r}) \,\rangle \\ &= \sum_{i=1}^{N_R} \sum_{v=1}^{\tau_n} \sum_{u=1}^{\tau_m} \delta_{r_{n_v} i}^{S} \delta_{r_{m_u} i}^{F} \langle\, \mathbf{E}_i^{scat}(\mathbf{B}_{n_v}(\mathbf{r}')),\ \mathbf{B}_{m_u}(\mathbf{r}) \,\rangle \\ &= \sum_{i=1}^{N_R} \sum_{v=1}^{\tau_n} \sum_{u=1}^{\tau_m} \delta_{r_{m_u} r_{n_v} i}^{Z} \langle\, E_i^J \mathbf{J}_{n_v}(\mathbf{r}'),\ \mathbf{J}_{m_u}(\mathbf{r}) \,\rangle \\ &= \sum_{i=1}^{N_R} \sum_{v=1}^{\tau_n} \sum_{u=1}^{\tau_m} \delta_{r_{m_u} r_{n_v} i}^{Z} Z_{m_u n_v}^{T_j T_j} \\ &\qquad m = 1, \ldots, N_{T_j} \ \text{and} \ \ n = 1, \ldots, N_{T_j} \end{aligned} \tag{23}$$

$$V_m^{T_j} = -\sum_{i=1}^{N_R} \sum_{u=1}^{\tau_m} \delta_{r_{m_u} i}^{F} \,\langle\, \mathbf{E}_i^{inc},\ \mathbf{J}_{m_u}(\mathbf{r}) \rangle, \quad m = 1, \ldots, N_{T_j}, \tag{24}$$

respectively, where

$$\begin{aligned} Z_{m_u n_v}^{T_j T_j} &= \text{contribution from } \mathbf{J}_{n_v}(\mathbf{r}')/\mathbf{J}_{m_u}(\mathbf{r}) \text{ interaction} \\ &= \langle\, E_i^J \mathbf{J}_{n_v}(\mathbf{r}'),\ \mathbf{J}_{m_u}(\mathbf{r}) \,\rangle \\ \delta_{r_{m_u} r_{n_v} i}^{Z} &= \text{Z contribution coef cient} \\ &= \delta_{r_{n_v} i}^{S} \delta_{r_{m_u} i}^{F} = \begin{cases} 1, & r_{m_u} = r_{n_v} = i \\ 0, & \text{otherwise,} \end{cases} \end{aligned} \tag{25}$$

$\mathbf{B}_{n_v}$ is denoted by $\mathbf{J}_{n_v}$ to signify the electric currents, and E_i^J is the electric field operator defined in (14). Notice that the generalized testing functions are the same as the basis functions.

The meaning of (23) is that $Z_{m_u n_v}^{T_j T_j}$ is the interaction between $\mathbf{B}_n$ and $\mathbf{T}_m = \mathbf{B}_m$. The interaction is expressed by testing the scattered electric field due to the source currents $\mathbf{B}_n$ with the testing functions $\mathbf{T}_m$. Since $\mathbf{B}_n$ and $\mathbf{T}_m$ are multi-domain basis and testing functions, the testings are summed over the entire region ($i = 1, 2, \ldots, N_R$). Examples of the expressions for the testing equations and resultant matrix elements are provided for specific situations in Appendix B of [19].

It is worth noting that the triply indexed Kronecker delta functions select only terms whose related basis and testing functions have the same region as R_i, where i is the summation index. Although the expression for $Z_{mn}^{T_j T_m}$ in (23) contains the complicated-looking triple summation, typically only a few terms are left, e.g., only two terms for a dielectric surface, due to the Kronecker delta functions, and this notation automatically takes care of general multiple surface junctions.

The evaluation of the inner products of $\langle\, E_i^J \mathbf{J}_{n_v}(\mathbf{r}'),\ \mathbf{J}_{m_u}(\mathbf{r}) \,\rangle$ and $\langle\, \mathbf{E}_i^{inc},\ \mathbf{J}_{m_u}(\mathbf{r}) \,\rangle$ in (23) and (24), respectively, has been done using the approximate testing procedure explained in [18].

Other impedance matrix and excitation vector elements in (3) are obtained similarly from (12) and (13) as follows

$$\begin{aligned} T_{mn}^{T_j T_m} &= \sum_{i=1}^{N_R} \sum_{v=1}^{\tau_n} \sum_{u=1}^{\tau_m} \delta_{r_{m_u} r_{n_v} i}^{Z} \langle\, E_i^M \mathbf{M}_{n_v}(\mathbf{r}'),\ \mathbf{J}_{m_u}(\mathbf{r}) \,\rangle \\ &= \sum_{i=1}^{N_R} \sum_{v=1}^{\tau_n} \sum_{u=1}^{\tau_m} \delta_{r_{m_u} r_{n_v} i}^{Z} T_{m_u n_v}^{T_j T_m} \\ &= -\sum_{i=1}^{N_R} \sum_{v=1}^{\tau_{n'}} \sum_{u=1}^{\tau_m} \delta_{r_{m_u} r'_{n_v} i}^{Z} \langle\, H_i^J \mathbf{J}'_{n_v}(\mathbf{r}'),\ \mathbf{J}_{m_u}(\mathbf{r}) \,\rangle \\ &= -\sum_{i=1}^{N_R} \sum_{v=1}^{\tau_{n'}} \sum_{u=1}^{\tau_m} \delta_{r_{m_u} r'_{n_v} i}^{Z} T_{m_u n'_v}^{T_m T_j} = -T_{mn'}^{T_m T_j}, \\ &\qquad m = 1, \ldots, N_{T_j} \text{ and } n = N_{T_j}{+}1, \ldots, N_{T_j}{+}N_{T_m} \end{aligned} \tag{26}$$

$$\begin{aligned} T_{mn}^{T_m T_j} &= \sum_{i=1}^{N_R} \sum_{v=1}^{\tau_n} \sum_{u=1}^{\tau_m} \delta_{r_{m_u} r_{n_v} i}^{Z} \langle\, H_i^J \mathbf{J}_{n_v}(\mathbf{r}'),\ \mathbf{M}_{m_u}(\mathbf{r}) \,\rangle \\ &= \sum_{i=1}^{N_R} \sum_{v=1}^{\tau_n} \sum_{u=1}^{\tau_m} \delta_{r_{m_u} r_{n_v} i}^{Z} T_{m_u n_v}^{T_m T_j}, \\ &\qquad m = N_{T_j} + 1, \ldots, N_{T_j} + N_{T_m} \text{ and } n = 1, \ldots, N_{T_j} \end{aligned} \tag{27}$$

$$\begin{aligned} Y_{mn}^{T_m T_m} &= \sum_{i=1}^{N_R} \sum_{v=1}^{\tau_n} \sum_{u=1}^{\tau_m} \delta_{r_{m_u} r_{n_v} i}^{Z} \langle\, H_i^M \mathbf{M}_{n_v}(\mathbf{r}'),\ \mathbf{M}_{m_u}(\mathbf{r}) \,\rangle \\ &= \sum_{i=1}^{N_R} \sum_{v=1}^{\tau_n} \sum_{u=1}^{\tau_m} \sum_{i=1}^{N_R} \sum_{v=1}^{\tau_n} \sum_{u=1}^{\tau_m} \delta_{r_{m_u} r_{n_v} i}^{Z} Y_{m_u n_v}^{T_m T_m} \\ &= \sum_{i=1}^{N_R} \sum_{v=1}^{\tau_{n'}} \sum_{u=1}^{\tau_{m'}} \delta_{r'_{m_u} r'_{n_v} i}^{Z} \frac{1}{\eta_i^2} \,\langle\, E_i^J \mathbf{J}_{n'_v}(\mathbf{r}'),\ \mathbf{J}_{m'_u}(\mathbf{r}) \,\rangle \\ &= \sum_{i=1}^{N_R} \sum_{v=1}^{\tau_{n'}} \sum_{u=1}^{\tau_{m'}} \delta_{r'_{m_u} r'_{n_v} i}^{Z} \frac{1}{\eta_i^2} \, Z_{m'_u n'_v}^{T_j T_j}, \\ &m = N_{T_j}{+}1, \ldots, N_{T_j}{+}N_{T_m} \text{ and } n = N_{T_j}{+}1, \ldots, N_{T_j}{+}N_{T_m} \end{aligned} \tag{28}$$

$$\begin{aligned} V_m^{T_m} &= -\sum_{i=1}^{N_R} \sum_{u=1}^{\tau_m} \delta_{r_{m_u} i}^{F} \,\langle\, \mathbf{H}_i^{inc},\ \mathbf{M}_{m_u}(\mathbf{r}) \rangle, \\ &\qquad m = N_{T_j} + 1, \ldots, N_{T_j} + N_{T_m}, \end{aligned} \tag{29}$$

where

$$\begin{aligned} \eta_i &= \sqrt{\mu_i/\epsilon_i} \\ J_{n'_v} &= M_{n_v} \\ J_{m'_u} &= M_{m_u}, \end{aligned} \tag{30}$$

and E_i^J, E_i^M, H_i^J, and H_i^M are the field operators defined in (14) and (15), and $\mathbf{B}_{n_v}$ is denoted by $\mathbf{J}_{n_v}$ and $\mathbf{M}_{n_v}$ to signify the electric and magnetic currents, respectively. Notice that in (26) and (28) the duality property of the field operators is used and that there is one and only one $\mathbf{J}_{n'_u}$ which is the same as $\mathbf{M}_{n_u}$ for a dielectric interface. The prime in the subscript of $\mathbf{J}_{n'_u}$ is due to the fact that the indices n and n' are for the

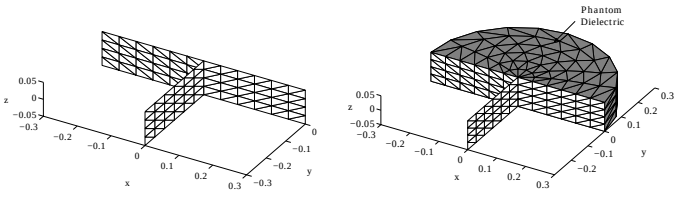

Fig. 3. Junction test case A — T-junctions with phantom dielectric.

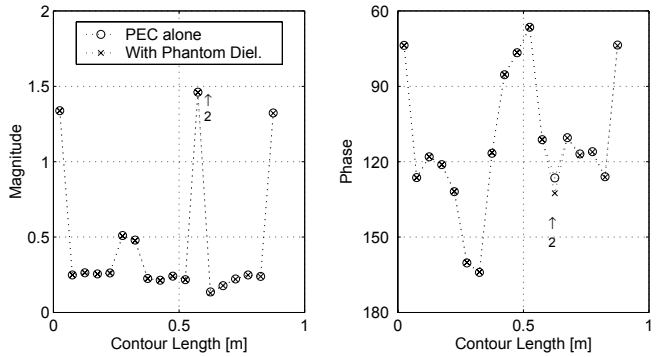

Fig. 4. z-directed current densities along the contours ($\circ$ - PEC alone, $\times$ - with phantom dielectric). The arrows denote the start of the second contour.

generalized basis functions (n, $n^{'} = 1, 2, \ldots, N$), and thus n and $n^{'}$ differ from each other for $\mathbf{J}_{n_u^{'}}$=$\mathbf{M}_{n_u}$.

Some subroutines of EMPACK [20] have been used for the integrations over the triangular domains which appear in (23) implicitly.

III. Numerical Results

A. Self Consistency Test — T-Junction

A T-shape junction of three 0.1-m wide and 0.3-m long PEC strips is taken as an example. For comparison, a semi-circular cylinder of phantom dielectric having 0.1-m height and 0.3-m radius is attached to the T-shape junction as shown in Fig. 3. The z-directed surface currents along the contour lines, $(-0.3, 0, 0) \rightarrow (0.3, 0, 0)$ and $(0, 0, 0) \rightarrow (0, -0.3, 0)$, located at the center of each strip are computed for a plane wave excitation. The plane wave is expressed as $\mathbf{E}^{inc} = E_o\, e^{k_o \hat{k}^i \cdot \mathbf{r}}$, where $\hat{k}^i = -\hat{x}\cos\phi^i \sin\theta^i - \hat{y}\sin\phi^i \sin\theta^i - \hat{z}\cos\theta^i$, $E_o = E_\theta^i(\hat{x}\cos\theta^i\cos\phi^i + \hat{y}\cos\theta^i\sin\phi^i - \hat{z}\sin\theta^i)$, $\theta^i = \phi^i = 45°$, $E_\theta^i = 1$, $k_o = 2\pi f\sqrt{\mu_o \epsilon_o}$, and $f = 300$ MHz. The results in Fig. 4 show very good agreement as well as the expected current peaks at the ends of the strips.

The $\phi-$directed magnetic currents along a circumferential contour ($\phi = 0° \rightarrow \phi = 180°$, $z = 0.0125$) are studied for three different grids. Grid-1 is shown in Fig. 3(b), and Grid-2 is a uniformly ne grid having 40 edges along the circumference. Grid-3 is similar to Grid-1, but it has locally ne grids near the conductor strips as shown in Fig. 5. As shown in Fig. 6, Grid-1 is not ne enough to result in the expected behavior of magnetic currents or electric elds near a conducting surface. At $\phi = 0°$ and $\phi = 180°$, where the conducting strips are located, the boundary conditions for the tangential electric eld dictates $E_z = 0$ or $M_\phi = 0$ at the conducting surface. The opposite trend of the numerical solution for M_ϕ near

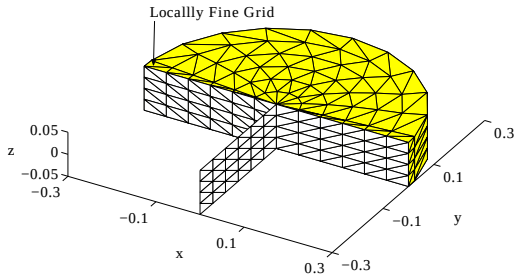

Fig. 5. Modeling with locally ne grids (Grid-3).

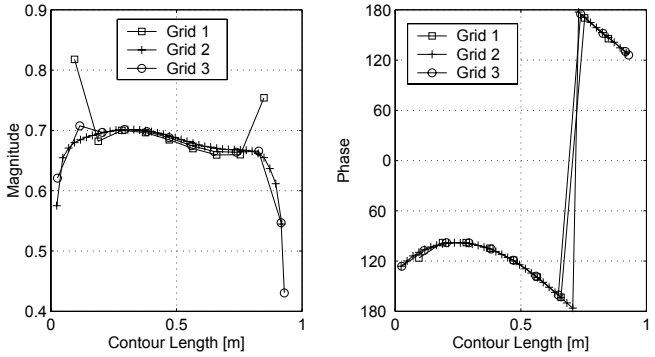

Fig. 6. ϕ-directed magnetic currents of T-junction with phantom dielectric along circumferential contour ($\phi = 0° \rightarrow \phi = 180°$, $z = 0.0125$ m). Grid-1 and Grid-3 refer to grids shown in Figs. 3(b) and 5, respectively. Grid-2 is uniformly ne grid using 40 edges along the circumfernce.

the conductor surface is due to the too coarse grid near the conductor, which cannot model the rapid eld variations properly. The locally ne grid, Grid-3, as well as the uniformly ne grid, Grid-2, result in the expected current distributions near the conducting surface. Similar behavior of the magnetic currents has been checked for a simple 0.1-m wide and 0.6-m long PEC strip without the center strip.

Fig. 7 shows the corresponding radar cross sections. It is worth noting that even Grid-1 results in very good agreement with the PEC-alone data in spite of the abnormal behavior of the magnetic currents described above.

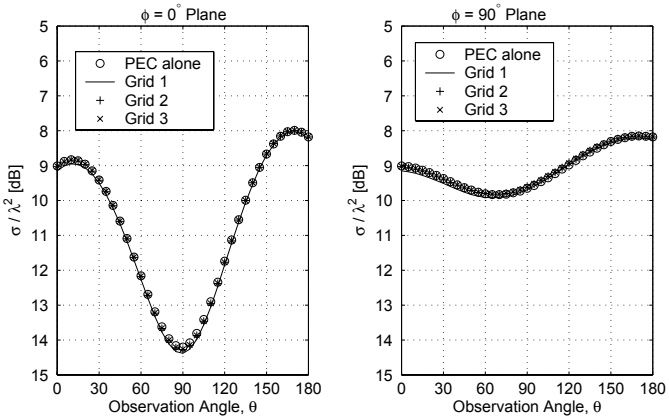

Fig. 7. RCS of T-junction with phantom dielectric.

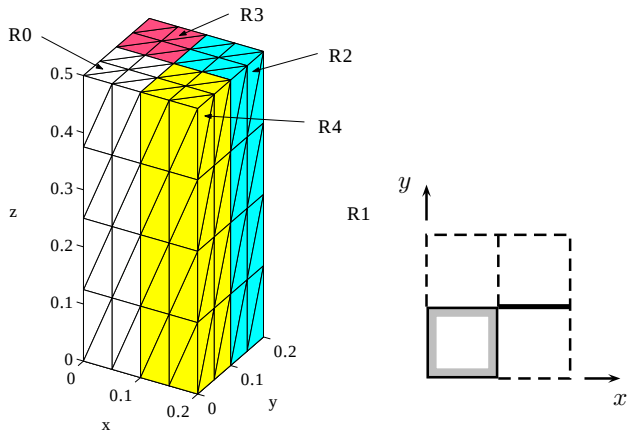

Fig. 8. Junction test case B — PEC block with three dielectric ones. Region R0 denotes conductor, and regions R2, R3, and R4 denote dielectric of ϵ_r=2, 3, and 4, respectively. The interface between R2 and R3 is dielectric, while that between R2 and R4 is PEC ($\mathcal{PF}2$). PF0-Model in Fig. 9 treats surface of PEC block as $\mathcal{PF}0$, while PF2-Model treats it as $\mathcal{PF}2$ with inside region being replaced by arbitrary dielectric. Units in m.

B. Self Consistency Test Using Two Different Models

In this section, a PEC square-bar with three dielectric ones attached to it as shown in Fig. 8 is considered. As shown in Fig. 9, the PEC bar can be modeled using either $\mathcal{PF}0$ or $\mathcal{PF}2$ surfaces. The surface of type $\mathcal{PF}0$ is modeled using one electric unknown, while $\mathcal{PF}2$ using two as discussed in section II. Moreover the process of assigning the basis functions and unknowns as described in the Appendix results in wildly different sets of unknowns as well as basis functions for the two models. The electric current distributions along twelve contours on the PEC bar and attached strip are plotted in Fig. 9 to show virtually the same results for the two different models. Each contour runs from $z = 0$ to $z = 0.5$, with (x, y) coordinates being (0.1, 0.0125), (0.1, 0.0375), (0.1, 0.0625), (0.1, 0.0875), (0.0875, 0.1), (0.0625, 0.1), (0.0375, 0.1), (0.0125, 0.1), (0.1125, 0.1), (0.1375, 0.1), (0.1625, 0.1), and (0.1875, 0.1) for contours 1 to 12, respectively. It should be noted that the results are obtained by using grid parameters for each block of `nex/ney/nez = 4/4/8` instead of `2/2/4` as suggested by the triangulation shown in Fig. 8 (`nex/ney/nez` are numbers of edges along x-, y-, and z-direction). The excitation parameters are $\theta^i = \phi^i = 45°$, $E^i_\theta = 1$, and $f = 300$ MHz.

C. Junction Tests Using FDTD

Extensive validation of the code for various types of junctions has been carried out. Here we present only sample results for the test case shown in Fig 10. It is a 0.1m $\times$ 0.1m $\times$ 0.5m dielectric bar of $\epsilon_r = 4$ with seven 0.1m $\times$ 0.1m PEC strips attached to it to result in $\mathcal{PF}1$-$\mathcal{DF}$-$\mathcal{PF}2$ and $\mathcal{PF}1$-$\mathcal{PF}2$-$\mathcal{PF}2$ junctions.

The top and bottom surfaces of the bar are dielectric. Fig. 11 shows good agreement between MoM and FDTD

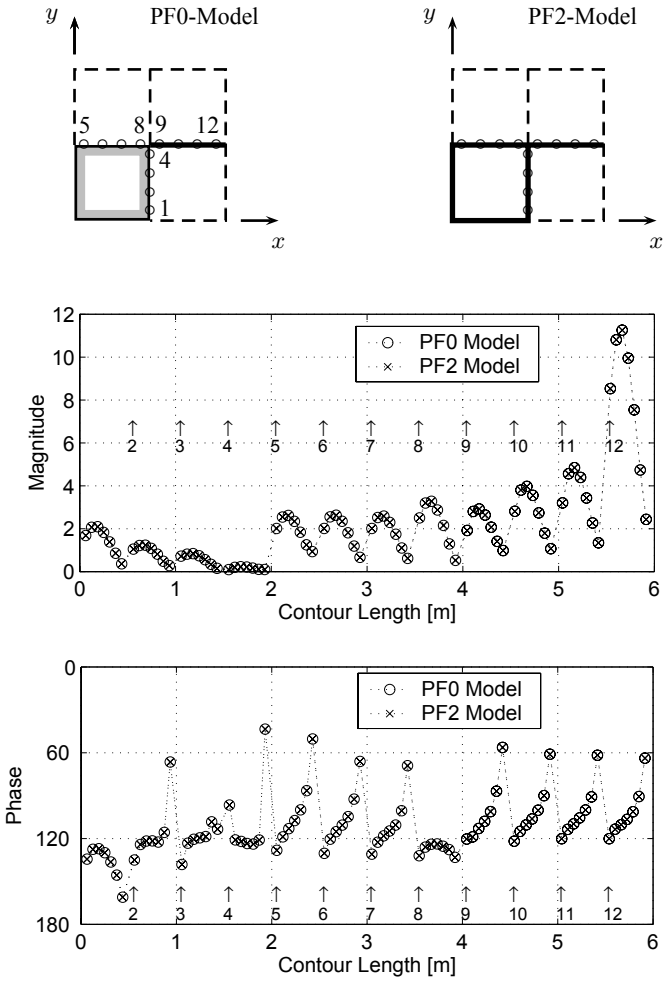

Fig. 9. Comparison of $z-$directed electric currents from two different models of PEC block shown in Fig. 8. Circles on geometry cross sections denote contour positions. Each contour runs from $z = 0$ to $z = 0.5$.

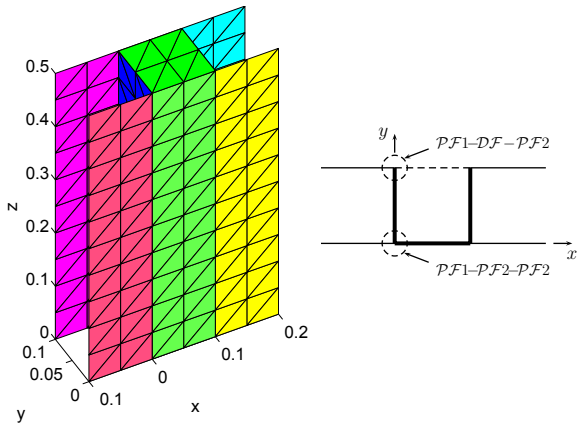

Fig. 10. Junction test case C — Dielectric bar with seven PEC strips. Units in m.

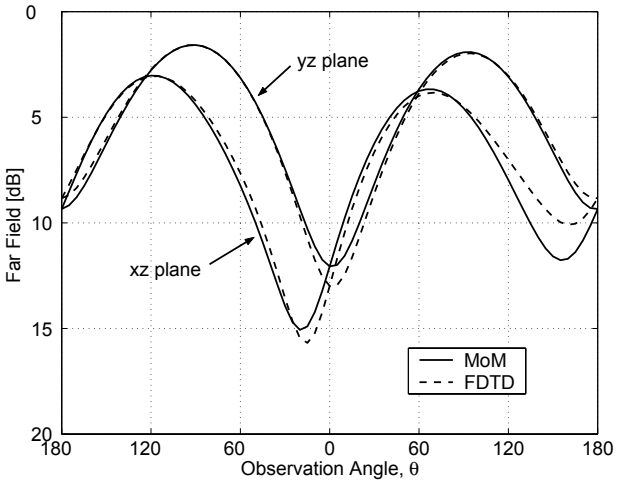

Fig. 11. Bistatic RCS for junction test case C shown in Fig. 10. $\theta^i = 45°$, $\phi^i = 30°$, $E^i_\theta = 1$, and $f = 300$ MHz.

(Finite Difference Time Domain) results except for around θ = 150° in xz-plane. The grid parameters are `nex/ney/nez = 3/3/10` for `ax/ay/az=0.1/0.1/0.5` (instead of `2/2/10` as suggested in Fig. 10), and the excitation parameters θ^i=45°, ϕ^i=30°, E^i_θ=1, and f=300 MHz. The FDTD parameters are: `dx = dy = dz` = 0.005 m, the second order Mur's RBC, 0.4-m distance from the scatterer boundary to the RBC, and a Gaussian pulse of with 0.4-ns width and 2-ns delay. The near- eld currents for the far- eld computation are sampled at surfaces ve cells away from the scatterer surfaces. The number of time steps used is 5000. However 2000 time steps should be enough.

D. Microstripline/Slot-Fed Rectangular DRA

A Rectangular DR Antenna (RDRA) fed by a microstripline through a narrow slot has been previously considered by Liu *et al.* [5]. The front and top views of such an RDRA are shown in Fig. 12. The geometry of the DR element and feed structure are taken from [5], where an in nite ground plane is assumed.

For the 3DIE code, the implementaion of the SIE/MoM formulation, a large nite ground plane is computationally expensive. It is even more expensive when the GP is backed by a substrate, in which case the GP PEC as well as the dielectric surface are modeled using two unknowns per edge. Thus, it is possible to reduce the number of unknowns signi cantly by truncating the substrate such that only a minimal portion of the substrate is used. The effect of the substrate truncation on the radiation patterns should be negligible as shown in Fig. 13. In Fig. 13, `x12y04f` and `x12y04` refer to the RDRAs with full and truncated substrates, respectively, while the numbers in them refer to the ground plane dimensions, $G_x = 12$ and $G_y = 4$, respectively, in cm.

We next verify that the 3DIE code computes the radiation patterns correctly and that the substrate truncation has no signi cant effects. Fig. 14 shows the MoM and FDTD computations of the radiation patterns of the smallest RDRA in the principal planes of $\phi = 0°/180°$ and $\phi = 90°/270°$. The

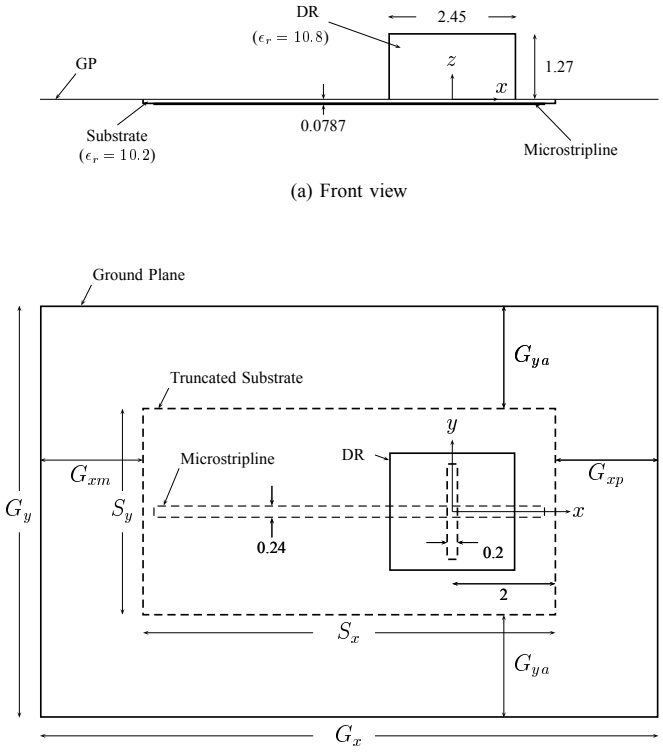

Fig. 12. RDRA with nite ground plane. DR dimensions are 2.45 × 2.5 × 1.27; slot length is 1.8; microstripline input and stub lengths are 5.8 and 1.8 from center of slot, respectively; S_x=8 and S_y=4, all in cm.

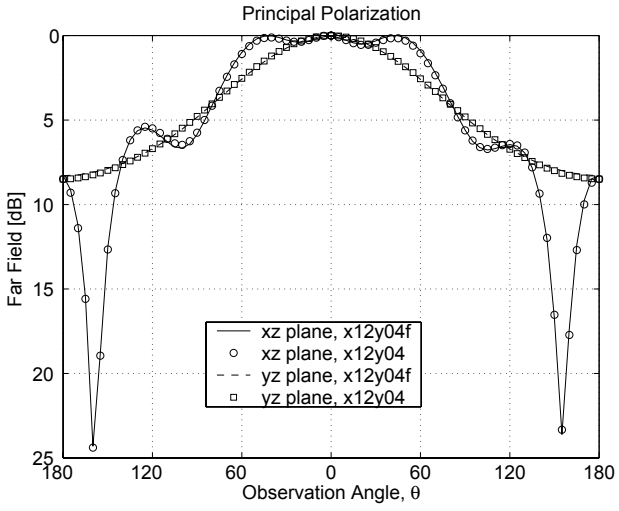

Fig. 13. Effect of substrate truncation of RDRA of Fig. 12 on radiation patterns with G_x=12, G_{xm}=0, G_{xp}=4, G_y=4, all in cm. RDRA `x12y04` has truncated substrate as shown in 12, while `x12y04f` has full substrate.

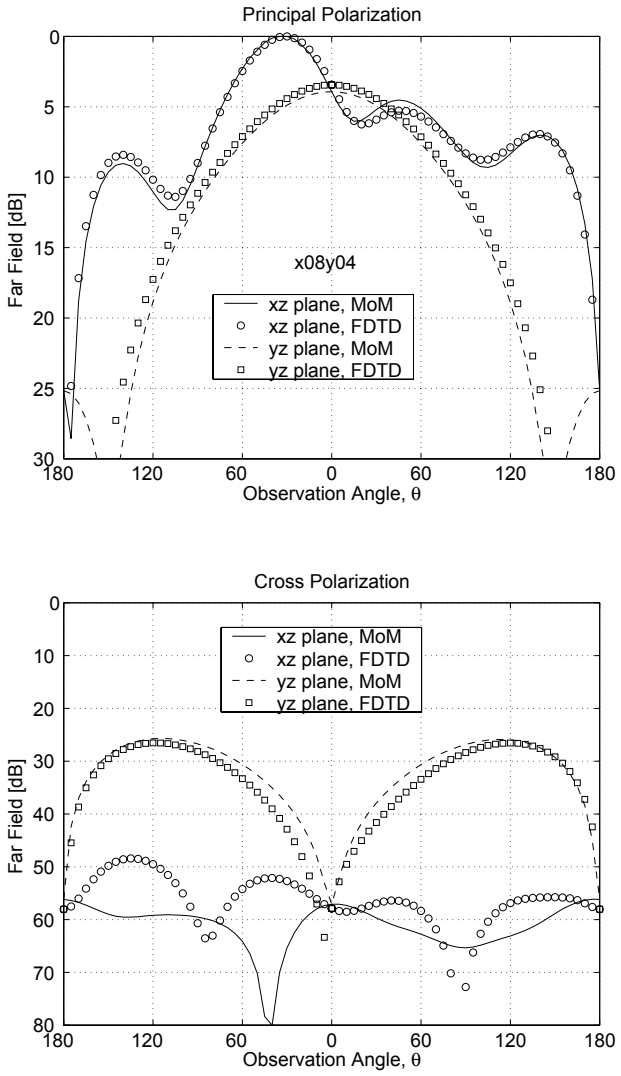

Fig. 14. Comparison of MoM and FDTD results for RDRA of Fig. 12 with $G_x = S_x = 8$ and $G_y = S_y = 4$, all in cm.

agreement between both methods is excellent for both the principal and cross polarization as shown in Fig. 14. It should be noted that the E-plane pattern (xz-plane principal polarization) shows high asymmetry. This is due to the asymmetry of the GP with respect to the DR element. The diffracted elds from the GP edges contribute differently to the elds radiated from the DR element due to the path differences in $\phi = 0^\circ$ and $\phi = 180^\circ$ planes. For RDRAs that have a symmetric GP, no such asymmetry has been observed in the radiation patterns. The cross polarization is shown to be low even for the minimal size of the GP. The effects of the nite ground plane size on the radiation patterns of the RDRA have been studied in [19].

IV. Conclusion

A systematic procedure for modeling of the general junctions of any combination of conducting and/or dielectric bodies in an SIE/MoM formulation has been presented. With the successful modeling of general junctions, it is possible to apply the E-PMCHWT formulation to a large class of problems including dielectric resonator antennas of complex con guration.

The procedure has been validated by modeling similar test structures in different manners and by comparison of results with FDTD solutions for a complex dielectric resonator antenna geometry.

V. Acknowledgment

This work was supported in part by The Army Research Of ce under grant No. DAAG55-98-0308.

References

[1] S. A. Long, M. W. McAllister, and L. C. Shen, "The resonant cylindrical dielectric cavity antenna," *IEEE Trans. Antennas Propagat.*, vol. AP-31, pp. 406–412, May 1983.

[2] T. E. Durham and C. G. Christodoulou, "Integral equation analysis of dielectric and conducting bodies of revolution in the presence of arbitrary surfaces," *IEEE Trans. Antennas Propagat.*, vol. AP-43, pp. 674–680, July 1995.

[3] G. P. Junker, A. A. Kishk, and A. W. Glisson, "Multiport network description and radiation characteristics of coupled dielectric resonator antennas," *IEEE Trans. Antennas Propagat.*, vol. AP-46, pp. 425–433, Mar. 1998.

[4] J. Y. Chen, A. A. Kishk, and A. W. Glisson, "Application of a new mpie formulation to the analysis of a dielectric resonator embedded in a multilayered medium coupled to a microstrip circuit," *IEEE Trans. Microwave Theory Tech.*, vol. MTT-49, pp. 263–279, Feb. 2001.

[5] Z. Liu, W. C. Chew, and E. Michielssen, "Numerical modeling of dielectric resonator antennas in a complex environment using the method of moments," *IEEE Trans. Antennas Propagat.*, vol. AP-50, pp. 79–82, Jan. 2002.

[6] S. U. Hwu and D. R. Wilton, "Electromagnetic scattering and radiation by arbitrary con gurations of conducting bodies and wires," Tech. Rep. TR 87-17, Applied Electromagnetics Laboratory, University of Houston, 1989.

[7] L. N. Medgyesi-Mitschang and J. M. Putnam, "Electromagnetic scattering from axially inhomogeneous bodies of revolution," *IEEE Trans. Antennas Propagat.*, vol. AP-32, pp. 797–806, Aug. 1984.

[8] J. M. Putnam and L. N. Medgyesi-Mitschang, "Combined eld integral equation formulation for inhomogeneous two- and three-dimensional bodies: The junction problem," *IEEE Trans. Antennas Propagat.*, vol. AP-39, pp. 667–672, May 1991.

[9] A. A. Kishk and L. Shafai, "Different formulations for numerical solution of single or multibodies of revolution with mixed boundary conditions," *IEEE Trans. Antennas Propagat.*, vol. AP-34, pp. 666–673, May 1986.

[10] J. M. Putnam and L. N. Medgyesi-Mitschang, "Generalized method of moments for three-dimensional penetrable scatterers," *J. Opt. Soc. Am. A.*, vol. 11, pp. 1384–1398, Apr. 1994.

[11] B. M. Kolundzija, "Electromagnetic modeling of composite metallic and dielectric structures," *IEEE Trans. Microwave Theory Tech.*, vol. MTT-47, pp. 1021–1032, July 1999.

[12] B. M. Kolundzija and R. D. Djordjevic, *Electromagnetic modeling of composite metallic and dielectric structures*. Artech House Inc., 2002.

[13] J. Poggio and E. K. Miller, *Integral equation solutions for three-dimensional scattering problems*. in *Computer Techniques for Electromagnetics*, R. Mitra, (ed.), Oxford, U.K.: Pergamon, 1973.

[14] Y. Chang and R. F. Harrington, "A surface formulation for characteric modes of material bodies," *IEEE Trans. Antennas Propagat.*, vol. AP-25, pp. 789–795, Nov. 1977.

[15] T. K. Wu and L. L. Tsai, "Scattering from arbitrarily-shaped lossy dielectric bodies of revolution," *IEEE Trans. Antennas Propagat.*, vol. AP-, pp. 406–412, May 1983.

[16] M. Carr, E. Topsakal, and J. L. Volakis, "A procedure for modeling material junctions in 3-D surface integral equation approaches," *IEEE Trans. Antennas Propagat.*, vol. AP-52, pp. 1374–1379, May 2004.

[17] R. F. Harrington, *Time Harmonic Electromagnetic Fields*. McGraw-Hill, 1963.

[18] S. M. Rao, D. R. Wilton, and A. Glisson, "Electromagnetic scattering by surfaces of arbitrary shape," *IEEE Trans. Antennas Propagat.*, vol. AP-30, pp. 409–418, May 1982.

[19] J. Shin, *Modeling of arbitrary composite objects with applications to dielectric resonator antennas*. PhD thesis, University of Mississippi, 2001.

[20] S. V. Yesantharao, "EMPACK — A software toolbox of potential integrals for computational electromagnetics," Master's thesis, University of Houston, 1989.

APPENDIX
MODELING OF GENERAL SURFACE JUNCTIONS

For surface junctions, there may be in nitely many possible con gurations regarding the number, order of connection, and types of the connected faces. Here, we develop a systematic procedure to model general junctions of arbitrary con guration.

A. Rules for Assigning Basis Functions and Unknowns

A single basis function is de ned over a pair of any two adjacent triangular faces. Each basis function is associated with the region into which it radiates and its type may be either electric or magnetic. When at least one face of type $\mathcal{DF}$ is involved in the junction, several different basis functions may be related to the same unknown number, so we refer to this as a multi-domain basis function.

The types and numbers of the unknowns and basis functions of a junction, as well as the fashion in which they are assigned, are mainly determined by the boundary conditions of the elds on the connected faces. The eld boundary condition on a PEC is that $E_{\tan} = 0$. Also the tangential magnetic eld is discontinuous. The boundary conditions for a dielectric face are that the tangential electric and magnetic elds are continuous across the interface. From the $E_{\tan}=0$ condition, it follows that there is no magnetic current for a junction which has at least one PEC face. The continuity of elds across a dielectric face leads to the multiplicity of an unknown coef cient given by (8). For a $\mathcal{PF}2$ face, the discontinuous magnetic eld results in two unknowns on each side of the face, while the total effect of the eld on the two sides is represented by a single unknown on the face for a $\mathcal{PF}1$ face.

When all the connected faces are $\mathcal{PF}$ in the same region, the KCL (Kirchhoff's Current Law), which states that the sum of currents o wing into the junction edge from connected face is zero, is applied. In such a case, The numbers of basis functions and unknowns are $N_{tf}-1$ where N_{tf} is the number of the connected faces.

In the following sections, the above rules are used to derive the numbers of basis functions and unknown coef cients and to set up a systematic procedure for assigning basis functions and unknown coef cients.

B. Numbers of Basis Functions and Unknowns

For each edge, we have certain numbers of basis functions and unknowns related to it, which are determined by applying the rules of the previous section at the junction. For the purpose of convenience, general surface junctions are classi ed into three cases —

(i) All faces are $\mathcal{PF}1$
(ii) All faces are $\mathcal{DF}$
(iii) General cases excluding cases 1 and 2.

Then the numbers of basis functions n_b and unknowns n_u related to a junction edge can be expressed as follows

$$n_b = \begin{cases} n_{tf}-1, & n_{tf}=n_{pf1} \\ 2\,n_{tf}, & n_{tf}=n_{df} \\ n_{tf}-n_{pf0}/2, & \text{otherwise} \end{cases} \quad \text{(A-1)}$$

$$n_u = \begin{cases} n_{uj}=n_{tf}-1, & n_{tf}=n_{pf1} \\ n_{uj}+n_{um}=1+1=2, & n_{tf}=n_{df} \\ n_{tf}-n_{pf0}/2-n_{df}, & \text{otherwise} \end{cases} \quad \text{(A-2)}$$

where

$$\begin{aligned} n_b &= \text{number of basis functions related to a junction} \\ n_u &= \text{number of unknowns related to a junction} \\ &= n_{uj}+n_{um} \\ n_{uj} &= \text{number of electric unknowns} \\ n_{um} &= \text{number of magnetic unknowns} \\ n_{tf} &= \text{total number of faces connected to a junction} \\ &= n_{pf}+n_{df} \\ n_{pf} &= \text{number of } \mathcal{PF} = n_{pf0}+n_{pf1}+n_{pf2} \\ n_{pf0} &= \text{number of } \mathcal{PF}0 \\ n_{pf1} &= \text{number of } \mathcal{PF}1 \\ n_{pf2} &= \text{number of } \mathcal{PF}2 \\ n_{df} &= \text{number of } \mathcal{DF} \end{aligned}$$

Having the numbers of the basis functions and the unknowns for each edge, the corresponding total numbers are given as

$$N_b = \sum_{N_{edg}} n_b \quad \text{(A-3)}$$

$$N_u = N_{uj}+N_{um} = \sum_{N_{edg}} n_{uj} + \sum_{N_{edg}} n_{um} = \sum_{N_{edg}} n_u = N, \quad \text{(A-4)}$$

respectively, where N_{edg} is the number of edges in the problem.

C. Setting up Basis Functions and Unknowns

There are a number of legitimate ways to assign the basis functions and unknowns for a surface junction consisting of n_{tf} faces. Here, we describe a speci c way which is chosen to facilitate convenient and systematic implementation of the code.

From the de nition of the multi-domain RWG basis functions of (5)–(7), it is necessary to specify its type (electric or magnetic), positive/negative domains (from-face and to-face, i.e. the assumed positive current direction), and region for a basis function. While the determination of the type and region

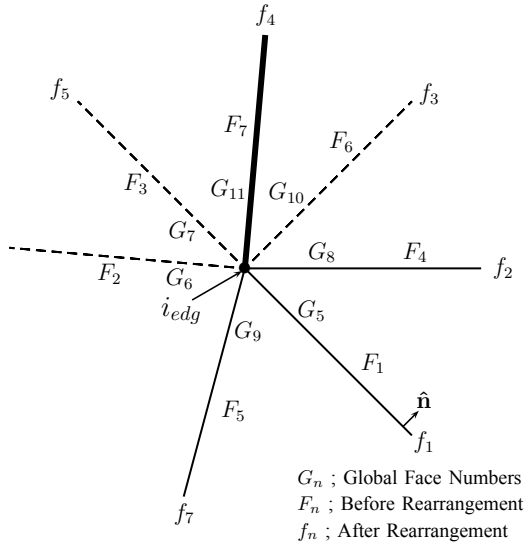

Fig. A-1. Rearrangement of local face numbers.

of the basis functions are relatively simple once their from-face and to-face are chosen, it is not a simple task to assign the from-face and to-face straightforwardly.

Initially the face numbers connected to a junction edge are listed in the order of increasing global face numbers. The resultant local face numbers may be spatially distributed without any order as shown in Fig. A-1. For a systematic junction modeling, it is necessary to rearrange them in an orderly manner. To this end, the rst face or the one with the lowest global number is chosen as the reference, from which the angles to others are measured. The direction of the increasing angle is determined by the surface normal of the reference face. Then consecutive local face numbers $(1, \ldots, n_{tf})$ are assigned to each face as shown in Fig. A-1. For the example shown the direction of increasing angle happened to be CCW (counter-clockwise) because of the surface normal $\hat{\mathbf{n}}$. When both PEC and dielectric faces are connected to an edge, the reference face must be a $\mathcal{PF}$. Thus if the lowest numbered face is a $\mathcal{DF}$, then the original local numbering is shifted until the reference becomes a $\mathcal{PF}$. Once the local face numbers are arranged in this way, we can determine the from-face, to-face, region number, type, and its unknown number straightforwardly. The from-face and to-face of the rst basis ($i_b = 1$) are assumed to be the rst and second faces, respectively. Considering the rules of the section A at the junction and the resultant numbers of basis functions and unknowns of (A-1) and (A-2), the from-face and to-face of other basis functions ($i_b = 2, 3, \ldots, n_b$) are determined as follows

(i) For $n_{tf} = n_{pf1}$ case (Fig. A-2(a)),

$$n_b = n_{tf} - 1 \quad \text{(A-5)}$$
$$ff = i_b \quad \text{(A-6)}$$
$$tf = i_b + 1 \quad \text{(A-7)}$$

(ii) For $n_{tf} = n_{df}$ case (Fig. A-2(b)),

$$n_b = 2\, n_{tf} \quad \text{(A-8)}$$
$$ff = \begin{cases} i_b, & i_b \le n_b/2 \quad (t_b = 1) \\ i_b + n_b/2, & i_b > n_b/2 \quad (t_b = 2) \end{cases} \quad \text{(A-9)}$$
$$tf = \begin{cases} i_b + 1, & i_b < n_b/2 \\ i_b + n_b/2 + 1, & n_b/2 < i_b < n_b \\ 1, & i_b = n_b/2 \quad \text{or} \quad i_b = n_b \end{cases} \quad \text{(A-10)}$$

(iii) For all other general cases (Fig. A-2(c)),

$$n_b = n_{tf} - n_{pf0}/2 \quad \text{(A-11)}$$
$$ff = \begin{cases} tf_p + 1, & tf_p \text{ is } \mathcal{PF}0 \\ tf_p, & \text{otherwise} \end{cases} \quad \text{(A-12)}$$
$$tf = \begin{cases} 1, & i_b = n_b \text{ and the last face is not } \mathcal{PF}0 \\ ff + 1, & \text{otherwise} \end{cases} \quad \text{(A-13)}$$

where

i_b = $2, 3, \ldots, n_b$ = consecutive indices for basis functions related to an edge
ff = local face number of the from-face of the i_b^{th} basis function $(1, \ldots, n_{tf})$
tf = local face number of the to-face of the i_b^{th} basis function $(1, \ldots, n_{tf})$
ff_p = ff of the $(i_b - 1)^{th}$ basis function
tf_p = tf of the $(i_b - 1)^{th}$ basis function
n_b = number of the basis functions related to an edge as given in (A-1)
t_b = type of basis function $= \begin{cases} 1, & \text{for electric} \\ 2, & \text{for magnetic.} \end{cases}$

The assignment of unknown numbers is self-explanatory in Fig. A-2(a) and (b) for cases (i) and (ii), respectively. For the general case of (iii), a new unknown number is assigned consecutively to each basis function unless the from-face is a dielectric face. When the from-face is a dielectric face, the previous unknown number is used again (see J_{3_2}, J_{3_3}, and J_{4_2} in Fig. A-2(c)). Thus, the multiplicity of an unknown is one if the related basis function does not have dielectric face for its domain. In general, τ_n, the multiplicity of an unknown number is given by

$$\tau_n = \begin{cases} n_{dfn}, & n_{dfn} = n_{tf} \\ n_{dfn} + 1, & \text{otherwise} \end{cases} \quad \text{(A-14)}$$

where

n_{tf} = total number of faces connected to the junction for I_n
n_{dfn} = number of dielectric faces related to I_n

Both J_1 and M_1 in Fig. A-2(b) have a multiplicity of four, while the unknowns J_5 and J_6 in Fig. A-2(c) have

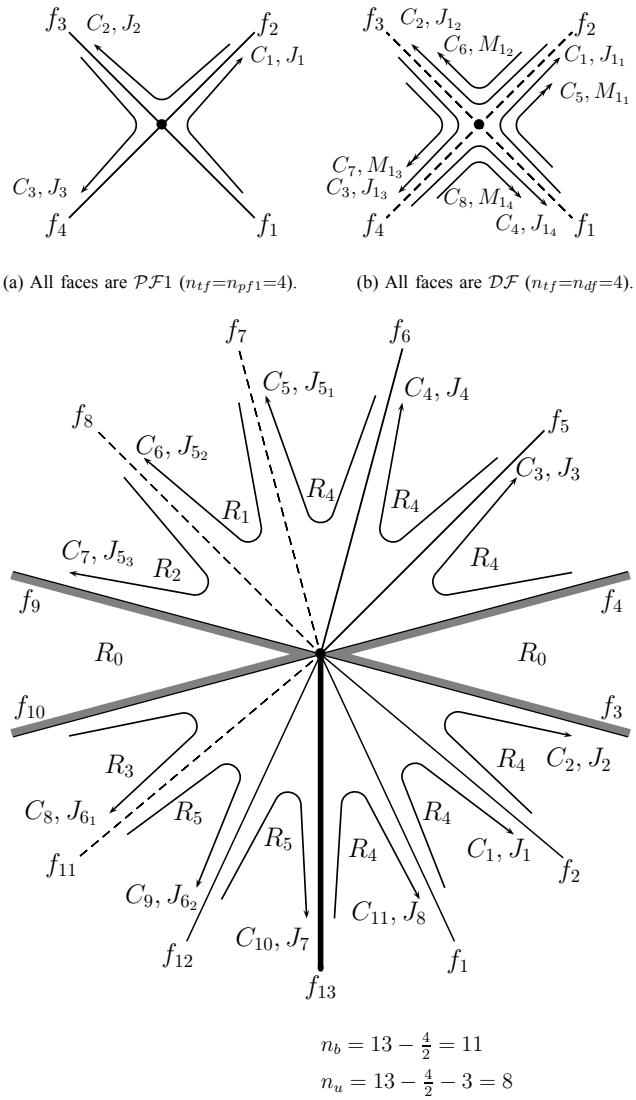

(a) All faces are $\mathcal{PF}1$ (n_{tf}=n_{pf1}=4). (b) All faces are $\mathcal{DF}$ (n_{tf}=n_{df}=4).

(c) A general case (n_{tf}=13, n_{pf0}=4, n_{pf1}=5, n_{pf2}=1, n_{df}=3).

Fig. A-2. Modeling of general surface junctions. (C_i, $i=1,2,3,\ldots$, is an entry-counting index.)

multiplicities of three and two, respectively. Notice that setting up the unknowns and basis functions of a given junction would be wildly different if the global edge or face numbers were set up differently.

After assigning the unknowns and the basis functions for all edges, it is possible to rearrange the order of the unknowns such that all electrical ones come before any magnetic ones so that the relationships in (5) hold.

Joon Shin received the B.E. and M.E. degrees in electrical engineering from the KyungPook National University, Korea, in 1981 and 1983, respectively. He earned the M.S. and Ph.D. degrees in electrical engineering from the University of Massachusetts at Amherst in 1996 and the University of Mississippi in 2001, respectively. He was employed at the Electromagnetics Laboratory of the Korea Research Institute of Standards and Science from 1982 to 1991 working on RF and microwave measurements. After working as a photonics design engineer at a private company, Anadigics Inc., NJ, for six months in 2001, he worked at the Electromagnetics Research Branch of the NASA Langley Research Center, Hampton, VA, as a National Research Council Research Associate in 2003. His current research interests are the development and application of numerical techniques (MoM, FDTD, and FEM) for treating electromagnetic problems.

Allen W. Glisson received the B.S., M.S., and Ph.D. degrees in electrical engineering from the University of Mississippi, in 1973, 1975, and 1978, respectively. In 1978, he joined the faculty of the University of Mississippi, where he is currently a Professor and Chair of the Department of Electrical Engineering. He was selected as the Outstanding Engineering Faculty Member in 1986, 1996, and 2004. His current research interests include the development and application of numerical techniques for treating electromagnetic radiation and scattering problems, and modeling of dielectric resonators and dielectric resonator antennas.

Dr. Glisson is a Fellow of the IEEE, a member of Commission B of the International Union of Radio Science, and a member of the Applied Computational Electromagnetics Society. Since 1984, he has served as the Associate Editor for Book Reviews and Abstracts for the IEEE Antennas and Propagation Society Magazine and he currently serves on the Board of Directors of the Applied Computational Electromagnetics Society. He has served as a member of the IEEE Antennas and Propagation Society Administrative Committee, as the secretary of Commission B of the U.S. National Committee of URSI, as an Associate Editor for Radio Science, as Co-Editor-in-Chief of the Applied Computational Electromagnetics Society Journal, and as Editor-in-Chief of the IEEE Transactions on Antennas and Propagation.

Ahmed A. Kishk received the BS degree in Electronic and Communication Engineering from Cairo University, Cairo, Egypt, in 1977, and in Applied Mathematics from Ain-Shams University, Cairo, Egypt, in 1980. In 1981 he joined the Department of Electrical Engineering, University of Manitoba, Winnipeg, Canada, where he obtained his M.Eng and PhD degrees in 1983 and 1986, respectively.

From 1977 to 1981, he was a research assistant and an instructor at the Faculty of Engineering, Cairo University. From 1981 to 1985, he was a research assistant at the Department of Electrical Engineering, University of Manitoba. From December 1985 to August 1986, he was a research associate fellow at the same department. In 1986, he joined the Department of Electrical Engineering, University of Mississippi, as an Assistant Professor. He was on sabbatical leave at Chalmers University of Technology during the 1994-1995 academic year. He is now a Professor at the University of Mississippi (since 1995). He was an Associate Editor of Antennas & Propagation Magazine from 1990 to 1993. He is now an Editor of Antennas & Propagation Magazine. He was a Co-editor of the special issue on Advances in the Application of the Method of Moments to Electromagnetic Scattering Problems in the ACES Journal. He was also an editor of the ACES Journal during 1997. He was an Editor-in-Chief of the ACES Journal from 1998 to 2001. He was the chair of Physics and Engineering division of the Mississippi Academy of Science (2001-2002).

His research interest includes the areas of design of millimeter frequency antennas, feeds for parabolic re ectors, dielectric resonator antennas, microstrip antennas, soft and hard surfaces, phased array antennas, and computer aided design for antennas. He has published over 120 refereed Journal articles and book chapters. He is a coauthor of the Microwave Horns and Feeds book (London, UK, IEE, 1994; New York: IEEE, 1994) and a coauthor of chapter 2 on Handbook of Microstrip Antennas (Peter Peregrinus Limited, United Kingdom, Ed. J. R. James and P. S. Hall, Ch. 2, 1989). Dr. Kishk received the 1995 outstanding paper award for a paper published in the Applied Computational Electromagnetic Society Journal. He received the 1997 Outstanding Engineering Educator Award from Memphis section of the IEEE. He received the Outstanding Engineering Faculty Member of the 1998. He received the Award of Distinguished Technical Communication for the entry of IEEE Antennas and Propagation Magazine, 2001. He received the 2001 Faculty research award for outstanding performance in research. He also received The Valued Contribution Award for outstanding Invited Presentation, "EM Modeling of Surfaces with STOP or GO Characteristics Arti cial Magnetic Conductors and Soft and Hard Surfaces" from the Applied Computational Electromagnetic Society. He received the Microwave Theory and Techniques Society Microwave Prize 2004. Dr. Kishk is a Fellow member of IEEE (Antennas and Propagation Society and Microwave Theory and Techniques), a member of Sigma Xi society, a member of the U.S. National Committee of International Union of Radio Science (URSI) Commission B, a member of the Applied Computational Electromagnetics Society, a member of the Electromagnetic Academy, and a member of Phi Kappa Phi Society.

Mode Expansion with Moment Method (ME-MM) to Analyze Dielectric Resonator Loaded Cavities

Zhongde Wang [(1)], Safieddin Safavi-Naeini [(2)] and John L. Volakis [(1, 3)]

Abstract—An efficient hybrid Mode Expansion-(ME) Moment Method (MM) or ME-MM is proposed to simulate the eigenvalue problem of multi-layer dielectric resonators (DRs) within cylindrical and rectangular cavities. Resonant frequencies and field distributions for several DRs are presented. The method's efficiency and accuracy are validated by comparison with commercial software, such as the HFSS, and other numerical methods. Finally, an air gap tunable DR analyzed via shows the ME-MM potential to design tunable DRs and filters.

Index Terms—Mode Expansion, Moment Method, Multi-layer Dielectric Resonators, Resonant Frequency, Field Distribution

I. INTRODUCTION

Resonators, filters and multiplexers play critical roles in many telecommunication systems, such as satellite and mobile communications [1], [2]. The size of these components is directly related to the wavelength and varies from less than one inch to more than a foot. Strip-line and micro-strip-line structures have been successfully adopted to avoid the bulkiness of waveguide structures. However, when high power-handling capability and/or low loss are needed, waveguide remain choice devices Since materials of high dielectric constant, high quality factor, and low coefficient of thermal expansion have been developed in the mid 70s [3], homogeneously and inhomogeneously-filled waveguide components have been studied and used in communications, navigation and various types of radar systems. With so much interest in dielectric structures, this paper presents a new methodology, referred to as a hybrid Mode Expansion Moment Method (ME-MM), to analyze dielectric resonator (DRs) loaded cavities. The efficiency and accuracy are compared with HFSS or other numerical methods.

Analysis and modeling of waveguide resonant and transmission structures have been research topics in the past decades, especially for DR loaded cavities. When a DR is placed in an open space, the analysis is usually performed under the assumption that the fields are completely restricted inside the dielectric materials due to its high dielectric constant. As such, the DR edges can be treated as perfect magnetic walls (PMW) and the modes and field distribution can be easily determined by calculating the field variations in each direction [4]-[6]. Obviously, this type of configuration is not practical and the PMW treatment is too approximate. A more accurate model was suggested by taking away the PMW on the two ends of a cylindrical DR, while keeping the PMW on the side of the DR and extending to infinity along the DR axial direction [7], [8]. In this case, the fields outside the DR decay exponentially along the axial direction. To represent these fields, an extra subscript δ is added to the normal TE_{01} and TM_{01} modes as $TE_{01\delta}$ and $TM_{01\delta}$. Further modifications assuming imperfect magnetic walls on all the surfaces were also suggested, but the analysis is still approximate with axial symmetric modes only [9-11].

Placing the DR between two parallel conducting plates provides a partial configuration. The resonator is formed by cutting a piece of cylindrical dielectric waveguide with a conducting plate at each end. This configuration is important for dielectric material measurement applications [12-14]. Rigorous modal analysis, including the axially symmetrical modes and the non-axial-symmetric modes for this geometry, was given in [13] In any practical applications, conducting enclosures for the DR are unavoidable. This is because fields the DR must be shielded and also for packaging because the DR array interact with circuits components outside.

A popular analytical method is the finite difference method [15], [16] which transforms the D.E. into a system of algebraic equations by simply replacing derivatives with finite differences. The finite element method is another popular approach and when making it more efficient and accurate for neural bars where Green's functions are used, an electromagnetic boundary value problem can be converted in a surface or volume integral equation in terms of the equivalent electric and/or magnetic currents. The integral equation itself is then transformed to a set of linear equations by expanding the unknown currents as a superposition of a set of basis functions and by

(1) The authors are with the Radiation Laboratory of Electrical Engineering and Computer Science Dept, University of Michigan, Ann Arbor, MI 48109. (2) The author is with the Electrical & Computer Engineering Dept., University of Waterloo, Ontario, Canada. (3) The author is with the Electrical and Computer Engineering Dept., ElectroScience Laboratory, The Ohio State University, Columbus, OH.

evaluating the inner products to get the equations with a set of testing functions (MM) [17-20].

The most popular configuration is the cylindrical, solid DR or ring DR coaxially loaded in a cylindrical enclosure. Recently, a configuration of cylindrical DRs loaded in a rectangular box was studied [21], [22]. In these cases, conductor loss was minimized by placing the enclosure conductor walls at some distance away from the DR. However, if the cylinder size is the major concern, those distances may be partially or completely eliminated.

The mode matching method is often employed to further characterize the guided modes in a waveguide and to find the scattering properties of a waveguide discontinuity. The configuration is typically divided into regions that the fields in each region can be typically expressed as a summation of its eigenmode functions. By matching the boundary conditions and using the orthogonal properties of the eigenmode functions, a set of linear equations then generated for the coefficients of the eigenmode functions. The resonant frequencies are then found by equating the determinant of the equation matrix to zero [23]. In this paper, a new method combining the Mode Matching and Moment Method (ME-MM) is proposed. The key advantage of the approach is that the matrix dimensions are determined by the number of basis functions used on the inter-surface rather than the number of modes in the expansion mode.

II. CONFIGURATION AND ANALYSIS

A typical configuration of the dielectric resonator is shown in Fig. 1. It depicts a dielectric cylinder of radius r_2 and height l_2, supported by a concentric circular dielectric ring of radius r_1 and height l_1. The entire configuration may be separated to two sections:

Region I Post Region P:

$$\begin{cases} \rho \le r_2 & \text{cylindrical case} \\ \rho \le a & \text{rectangular case}. \end{cases}$$

Region II Waveguide Region W:

$$\begin{cases} \rho \ge r_2 & \text{cylindrical case} \\ \rho \ge a,\ 0 \le z \le L,\ -a \le x \le a & \text{rectangular case} \end{cases}$$

The post region P (region II) is further subdivided into sub-regions as follows:

- cylindrical case

$$\begin{cases} \text{Region } P_1 : \rho \le r_1 \\ \text{Region } P_2 : r_1 \le \rho \le r_2 \end{cases}$$

- b) rectangular case

$$\begin{cases} \text{Region } P_1 : \rho \le r_1 \\ \text{Region } P_2 : r_1 \le \rho \le r_2 \\ \text{Region } P_3 : r_2 \le \rho \le a. \end{cases}$$

Here, $b \ge a$ for the rectangular case with $2b$ representing the long-side length (Fig.1b).

The linear system for the fields and eigenvalues in the resonator is constructed by introducing a modal function representation of the fields with linear multi-layer parallel plate waveguides.

At $z = L_k$ $(k = 1, 2 \ldots)$ and $\rho = r_i$ $(i = 1, 2 \ldots)$, the tangential field components are then enforced to be continuous along the axial and radial directions. After mode matching, this gives rise to the linear system of equation in the modal field coefficients in the outer region [22],

$$\begin{bmatrix} W_{11} & W_{12} & W_{13} & W_{14} \\ W_{21} & W_{22} & W_{23} & W_{24} \end{bmatrix} \begin{bmatrix} R_n^e \\ T_n^e \\ R_n^h \\ T_n^h \end{bmatrix} = 0 . \qquad (1)$$

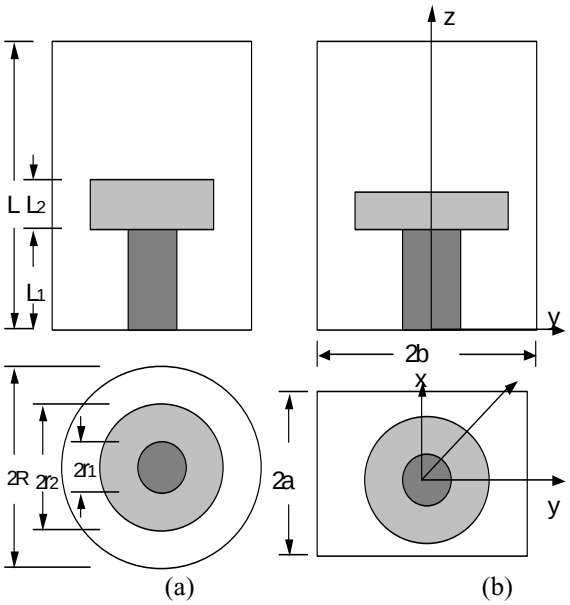

Fig.1. Configurations of Dielectric resonators: (a) Cylindrical enclosure, (b) Rectangular enclosure.

The submatrices W_{ij} and their element expressions are listed in [22]. Their dimensions are $J \times J$ with J representing the number of roots that the characteristic equation in the cylindrical post region. n is the index number along φ direction. And $R_n^e, T_n^e, R_n^h,$ and T_n^h are the field coefficients in the P_I region. The superscripts e and h represent *TM* and *TE* eigenmodes, respectively.

The fields in the P_I region (*I*=2 for the cylindrical configuration, and *I*=3 for rectangular configuration in Fig.1) can be expressed as:

$$\vec{E}_t^{P_I} = \sum_n \sum_j \left[R_{nj}^e B_n^{(1)}(\xi_j^{Ie} a) + T_{nj}^e B_n^{(2)}(\xi_j^{Ie} a) \right] \vec{e}_{tnj}^{Ie}$$
$$+ \sum_n \sum_j \left[R_{nj}^h B_n'^{(1)}(\xi_j^{Ih} a) + T_{nj}^h B_n'^{(2)}(\xi_j^{Ih} a) \right] \left| \xi_j^{Ih} \right| \vec{e}_{tnj}^{Ih} \qquad (2)$$

$$\vec{H}_t^{P_I} = \sum_n \sum_j \left[R_{nj}^h B_n^{(1)}(\xi_j^{Ih} a) + T_{nj}^h B_n^{(2)}(\xi_j^{Ih} a) \right] \vec{h}_{tnj}^{Ih}$$
$$+ \sum_n \sum_j \left[R_{nj}^e B_n'^{(1)}(\xi_j^{Ie} a) + T_{nj}^e B_n'^{(2)}(\xi_j^{Ie} a) \right] \left| \xi_j^{Ie} \right| \vec{h}_{tnj}^{Ie} \quad (3)$$

where,

$$\vec{e}_{tnj}^{Ie} = \hat{z} \begin{Bmatrix} \sin n\varphi \\ \cos n\varphi \end{Bmatrix} e_{zj}^{Ie}(\gamma_j^{Ie} z) + \hat{\varphi} \begin{Bmatrix} \cos n\varphi \\ -\sin n\varphi \end{Bmatrix} \frac{n}{r\left(\xi_j^{Ie}\right)^2} e_{zj}^{ie'}(\gamma_j^{Ie} z) \quad (4)$$

$$\vec{e}_{tnj}^{Ih} = \hat{\varphi} \begin{Bmatrix} \cos n\varphi \\ -\sin n\varphi \end{Bmatrix} \frac{1}{\left(\xi_j^{Ih}\right)^2} h_{zj}^{Ih}(\gamma_j^{Ih} z) \quad (5)$$

$$j\omega\mu \vec{h}_{tnj}^{Ie} = \hat{\varphi} \begin{Bmatrix} \sin n\varphi \\ \cos n\varphi \end{Bmatrix} \frac{k_i^2(z)}{\left(\xi_j^{Ie}\right)^2} e_{zj}^{Ie}(\gamma_j^{Ie} z) \quad (6)$$

$$j\omega\mu \vec{h}_{tnj}^{Ih} = \hat{z} \begin{Bmatrix} \cos n\varphi \\ -\sin n\varphi \end{Bmatrix} h_{zj}^{Ih}(\gamma_j^{Ih} z) + \hat{\varphi} \begin{Bmatrix} -\sin n\varphi \\ -\cos n\varphi \end{Bmatrix} \frac{n}{r\left(\xi_j^{Ih}\right)^2} h_{zj}^{Ih'}(\gamma_j^{Ih} z) . \quad (7)$$

As usual $e_{tnj}^{Ie}(\gamma_j^{Ie} z), e_{tnj}^{Ih}(\gamma_j^{Ie} z), h_{tnj}^{Ie}(\gamma_j^{Ih} z)$, and $h_{tnj}^{Ih}(\gamma_j^{Ih} z)$ are the eigen-functions in the parallel-plate waveguides [25]. The values for $\xi_j^{Ie}, \xi_j^{Ih}, \gamma_j^{Ie}$, and γ_j^{Ih} in each region can be easily obtained by solving its characteristic equation subject to $\xi^2 = \gamma^2 + k^2$. We also remark that $B_n^{(k)}$ is the k^{st} Bessel function or modified Bessel function given by:

$$B_n^{(1)}(x) = \begin{cases} J_n(x); x^2 \geq 0 \\ I_n(|x|); x^2 \leq 0 \end{cases} \quad (8)$$

$$B_n^{(2)}(x) = \begin{cases} Y_n(x); x^2 \geq 0 \\ K_n(|x|); x^2 \leq 0 \end{cases} . \quad (9)$$

The field expressions in the waveguide region can also be represented with a modal superposition. For the cylindrical configuration, the field expressions are the same as in (2) and (3) with different coefficients. For rectangular structure, the fields in the waveguide region are

$$E_t^{Wp} = \sum_m \sum_i \left[A_{mi}^{Wp} e^{-\gamma_{mj} y} + B_{mi}^{Wp} e^{\gamma_{mj} y} \right] \hat{e}_{tmi}^p \quad (10)$$

$$H_t^{Wp} = \sum_m \sum_i \left[A_{mi}^{Wp} e^{-\gamma_{mj} y} - B_{mi}^{Wp} e^{\gamma_{mj} y} \right] \hat{h}_{tmi}^p . \quad (11)$$

On the inter-surface between the post and the outer waveguide region, we expand the tangential electrical field $\vec{\varepsilon}_t(\varphi, z)$ as

$$\varepsilon_z^S(\varphi, z) = \sum_n \sum_i \left(U_{ni}^z \cos n\varphi + V_{ni}^z \sin n\varphi \right) e_z^s(k_{zi} z) \quad (12)$$

$$\varepsilon_\varphi^S(\varphi, z) = \sum_n \sum_i \left(U_{ni}^\varphi \cos n\varphi + U_{ni}^\varphi \sin n\varphi \right) e_\varphi^s(k_{zi} z) \quad (13)$$

where the basis functions $e_z^s(k_{zi} z)$ and $e_\varphi^s(k_{zi} z)$ can take different forms, including triangular, sinusoidal, or other sub-domain representations. Here we choose the sinusoidal full domain basis functions for $e_z^s(k_{zi} z)$ and $e_\varphi^s(k_{zi} z)$ since they closely represent the actual field distributions.

Applying the boundary condition of the tangential field components

$$\vec{E}_t\big|_{P_I} = \vec{E}_t\big|_W = \vec{E}_t^S \quad (14)$$

$$\vec{H}_t\big|_{P_I} = \vec{H}_t\big|_W = \vec{H}_t^S . \quad (15)$$

And getting the resulting equations via Galerkin's method coupled with Mode Matching yields

$$\begin{bmatrix} G_{11} & G_{12} & G_{13} & G_{14} \\ G_{21} & G_{22} & G_{23} & G_{24} \\ G_{31} & G_{32} & G_{33} & G_{34} \\ G_{41} & G_{42} & G_{43} & G_{44} \end{bmatrix} \begin{bmatrix} U^\varphi \\ V^\varphi \\ U^z \\ V^z \end{bmatrix} = 0 . \quad (16)$$

We should note that in (16), here $\bar{\bar{G}}_{ij}$'s are sub-matrices whose dimensions are determined by the number of basis functions (N_φ, N_z). Detailed element expressions for $\bar{\bar{G}}$ can be found in [25]. The resonant frequency of the DR loaded cavity is obtained by solving $\left|\bar{\bar{G}}\right| = 0$. Substituting the resonant frequency back into (2), (3), (10) and (11), the field distributions in different regions are readily obtained.

For the rectangular geometry (Fig.1b), similar procedures are applied and given in [25]. It is important to point out the analytical integration cannot be carried out from the mutual inner products, because of the different coordinate systems at the post region $P(\rho, \varphi, z)$ and the waveguide region $W(x, y, z)$. To reduce the CPU time spent on the numerical integrals, Bessel-Fourier series are used to translate the numerical integrations into simple summations as follows:

$$\sin\left[\frac{m\pi}{2a} (\rho \sin\varphi + a) \right] e^{\mp \gamma_{mi} \rho \cos\varphi} = \sum_{k=-\infty}^{\infty} \sin\left(\frac{m\pi}{2} + k\varphi \right) F(\mp k, \rho, \gamma_{mi}) \quad (17)$$

$$\cos\left[\frac{m\pi}{2a} (\rho \sin\varphi + a) \right] e^{\mp \gamma_{mi} \rho \cos\varphi} = \sum_{k=-\infty}^{\infty} \cos\left(\frac{m\pi}{2} + k\varphi \right) F(\mp k, \rho, \gamma_{mi}) \quad (18)$$

where

$$F = \begin{cases} J_k\left[T(\rho)\right] \exp\left[\mp jk \tan^{-1}\left(2a|\gamma_{mi}| / m\pi \right) \right], \\ \qquad \gamma_{mi}^2 \leq 0 \\ J_k\left[T(\rho)\right] \left[(m\pi + 2a\gamma_{mi}) / (m\pi - 2a\gamma_{mi}) \right]^{\mp k/2}, \\ \qquad \gamma_{mi}^2 \geq 0 \ \& \ m\pi \geq 2a|\gamma_{mi}| \\ (-1)^{k/2} I_k\left[|T(\rho)|\right] \left[(m\pi + 2a\gamma_{mi}) / (m\pi - 2a\gamma_{mi}) \right]^{\mp k/2}, \\ \qquad \gamma_{mi}^2 \geq 0 \ \& \ m\pi \leq 2a|\gamma_{mi}| \end{cases} \quad (19)$$

$$T(\rho) = \rho/2\pi \sqrt{(m\pi)^2 - 4a^2\gamma_{mi}^2} \tag{20}$$

$$\gamma_{mi}^2 + k^2 = \left(m\pi/2a\right)^2 + \left(i\pi/L\right)^2 \tag{21}$$

$$k^2 = \omega^2 \mu_0 \varepsilon \,. \tag{22}$$

Using the above transformation technique, rectangular-configuration is the same as that for the analysis for the circular-configuration. In the following section, several numerical examples for DRs inside a cylindrical or rectangular enclosure are presented.

III. NUMERICAL RESULTS

A FORTRAN program was developed to compute the resonant frequencies and field patterns of the cylindrical multi-layers DRs loaded inside a cylindrical or a rectangular waveguide junction.

Table 1 shows the convergence and accuracy of the ME-MM in comparison with HFSS for a two-layer DR (Fig.1 (a)). We can readily see that the ME-MM is convergent and very fast (only six basis functions needed).

Table 2 gives the calculation time and computer memory (the number of tetrahedrons in HFSS and basis functions number in ME-MM) in the HFSS and the new method for two different cases:

Table 1 Resonant Frequency Convergence Testing

$2a = 1.6cm; L = 3.0cm; 2r_1 = 1.6cm; 2r_2 = 1.6cm;$
$l_1 = 0.55cm; l_2 = 0.8cm; \varepsilon_{r1} = 10.; \varepsilon_{r2} = 35.7$
$N_\varphi = 0$ (TE case)

N_z	f_r (GHz)	HFSS result	Error (%)
4	3.3162	3.3258	0.29
6	3.3208		0.15
8	3.3210		0.14
12	3.3212		0.14

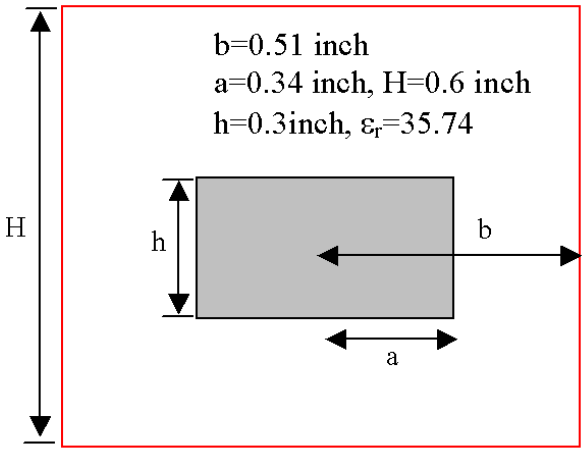

Fig. 2. Cross-sectional View of a DR loaded cavity.

Case A:

$2a = 1.6cm; L = 3.0cm; 2r_1 = 1.6cm; 2r_2 = 1.6cm$
$l_1 = 0.55cm; l_2 = 0.8cm; \varepsilon_{r1} = 10.; \varepsilon_{r2} = 35.7$

Case B: $2a = 1''; L = 1''; 2r_1 = 0''; 2r_2 = 0.689''$
$l_1 = 0.275''; l_2 = 0.23''; \varepsilon_{r1} = 1.; \varepsilon_{r2} = 38\,.$

From this table, it is seen that in order to reach the same accuracy, HFSS needs at least 100 times more memory and 50 times more CPU time as compared to the ME-MM.

Fig. 2 shows the dimensions and material parameters of another DR configuration in a cavity without substrate. The resonant frequencies for different modes using FEM [29], modal matching [30] and the new method are listed in Table 3. It is clear that ME-MM obtains results closer to the more accurate modal matching method. For the rectangular configurations, the resonant frequencies for two simple cases of dielectric rods within the cavities' are calculated and compared with HFSS in Table 4.

Table 2 Computer Resource Comparison

		Calculating Time/No. of Tetrahedrons or Basis Function)	Resonant Frequency (GHz)
Case A: *TE*	HFSS	896′16″ /(10492)	3.3258
	ME-MM	1′05″ /(6)	3.3208
Case A: *TM*	HFSS	896′16″ /(10492)	3.733
	ME-MM	1′27″ /(16)	3.763
Case B: *HE*	HFSS	149′46″ /(2894)	4.1264
	ME-MM	3′05″ /(12)	4.1545

Table 3 Resonant-Frequency Comparison

	Ref [29] (GHz)	Ref [30] (GHz)	ME-MM (GHz)
TE01	3.435	3.428	3.433
TE02	5.493	5.462	5.322
TM01	4.601	4.551	4.537
HE11	4.271	4.224	4.227
HE12	4.373	4.326	4.316

Table 4 Resonant Frequencies for Rectangular Configurations

(cm)	Calculating Result (GHz)	HFSS (GHz)	Δ =error (%)
Case (A) a=3; b=3; l=4; r0=1; $\varepsilon_r = 35$	1.320	1.301	1.54
Case(B) a=3; b=4; l=4;r0=1; $\varepsilon_r = 35$	1.210	1.220	0.82

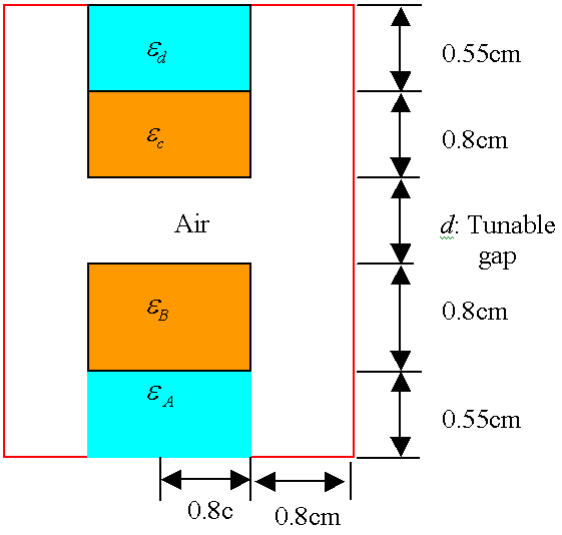

Fig. 3. Tunable DR with air gap, $\varepsilon_A = \varepsilon_D = 10, \varepsilon_B = \varepsilon_C = 35.7$.

Finally a tunable air-gap DR (resonant variable to the air gap *d*) model in Fig. 3 is investigated. As in Table 5, the resonant frequency increases 1.6% when the air gap changes from 0.3 cm to 0.45 cm. Also, we observe that the CPU time using ME-MM is at least 30 times faster and also with much less memory needs than HFSS.

The tangential field distributions of $E_\varphi \sim r$ and $H_z \sim z$ are shown in Fig. 4, and again it is obvious that the boundary conditions are matched perfectly by ME-MM with very few unknowns, and have much reasonable trend in comparison to HFSS curves. Accurate field distributions are essential for DR filters design. Typically they determine the excitation position, and coupling-windows choosing for multi-cavity DR filter [24].

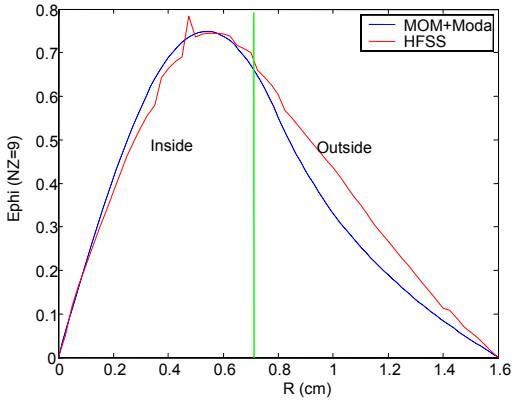

(a)

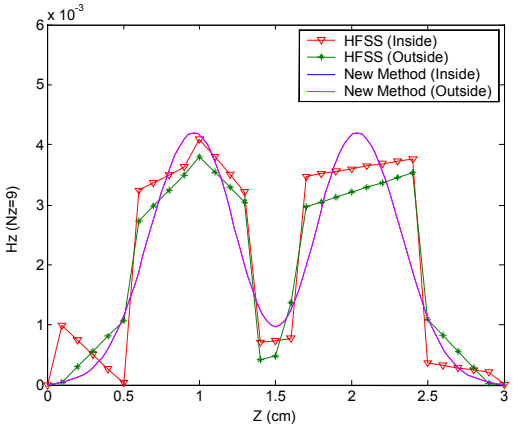

(b)

Fig. 4. Field distribution comparison (TE): (a) $E_\varphi \sim r$, (b) $H_z \sim z$.

Table 5 Tunable Resonance Frequency by Air Gap

TE	HFSS	d=0.3cm	3.14346
	ME-MM		3.1247
	HFSS	d=0.35cm	3.17595
	ME-MM		3.1440
	HFSS	d=0.45cm	3.21151
	ME-MM		3.1757

IV. CONCLUSION

A new analysis method (ME-MM) was proposed to analyze the multi-layer DR loaded cavities. Accurate resonant frequencies and field distributions for several different dielectric resonators were evaluated by ME-MM. As compared with HFSS and other numerical methods, our ME-MM saves substantial CPU time and memory, without loss of accuracy. Accurate field distributions can also be obtained by the proposed method essential to provide sufficient details for DR filter design. An air-substantial tunable DR was analyzed using the ME-MM, showing the capability of this methodology to design tunable cavity-loaded DR filters.

V. ACKNOWLEDGEMENT

The first author thanks Prof. R. Mansour and Prof. M. Taheri for their invaluable comments and inputs during the preparing process of his M.Sc. thesis.

VI. REFERENCES

[1] G. W. Anderson, D. C. Webb, A.E. Spezio, and J. N. Lee, "Advanced channelization technology for RF, microwave, and millimetre wave applications", *Proc. IEEE*, vol. 79, pp. 355-388, March 1991.

[2] K. Wakino, T. Nishikawa, and Y. Ishikawa, "Miniaturization technologies of dielectric filters for mobile communications", *IEEE Trans. Microwave Theory Tech*., vol.MTT-42, pp.1295-1300, July 1994.

[3] R. C. Kell, A.C. Greenharn, and G.C.E. Olds, "High-permittivity temperature-stable ceramic dielectric with low microwave loss", *J. Am. Ceramic Soc*., vol. 56, pp. 352-354, July 1973.

[4] H. M. Schliche, "Quasi-degenated modes in high-ε dielectric cavities*", Journal of Applied Physics*, vol. 24, pp. 187-191, Feb. 1953.

[5] H. Y. Yee, "Natural resonant frequencies of microwave dielectric resonators", *IEEE Trans. On Microwave Theory and Tech.,* vol. MTT-13, p.256, March 1965.

[6] J. C. Sehares and S. J. Naumann, "Design of microwave resonators", *IEEE Trans. on Microwave Theory and Tech.,* vol. MTT-14, pp. 2-7, Jan. 1966.

[7] S. B. Cohn, "Microwave band-pass filters containing high-Q dielectric resonators", *IEEE Trans. on Microwave Theory and Tech.,* vol. MTT-16, pp. 218-227, Oct. 1974.

[8] A. Okaya and L. F. Barash, "The dielectric microwave resonators". *Proceedings of IRE.* Vol. 50, pp. 2081-2092, Oct. 1962.

[9] J. V. Bladel, "On the resonance of a dielectric resonator of very high permittivity", *IEEE Trans. on Microwave Theory and Tech.,* vol. MTT-23, pp. 199-208, Feb. 1975.

[10] M. Verplanken and J. V. Bladel, "The electric dipole resonance of ring resonators of very high permittivity", *IEEE Trans. on Microwave Theory and Tech.,* vol. MTT- 24, pp. 108-112, Jan. 1976.

[11] M. Verplanken and J. V. Bladel, "The magnetic dipole resonance of ring resonators of very high permittivity", *IEEE Trans. on Microwave Theory and Tech.,* vol. MTT-27, pp. 328-333, Jan. 1979.

[12] M. W. Pospieszalski, "On the theory and application of the dielectric post resonator", *IEEE Trans. on Microwave Theory and Tech.,* vol. MTT- 25, pp. 228-231, Jan. 1977.

[13] Y. Kobayashi and S. Tanaka, "Resonant modes of a dielectric rod resonator short-circuited at both ends by parallel conducting plates", *IEEE Trans. on Microwave Theory and Tech.,* vol. MTT-28, pp. 1077-1085, Jan. 1980.

[14] B. W. Hakki and P. D. Coleman, "A dielectric resonator method of measuring inductive capacities in millimeter range", *IEEE Trans. on Microwave Theory and Tech.,* vol. MTT- 8, pp. 402-410, Jan. 1960.

[15] C. A. Muilwyk and J. B. Davis, "The numerical solution of rectangular waveguide junctions and discontinuities of arbitrary cross section", *IEEE Trans. on Microwave Theory and Tech.,* vol. MTT- 15, pp. 450-455, Jan. 1967.

[16] C. Wang, H. W. Yao, and K. A. Zaki, "An improved FDTD method for analysis of higher order modes high Q dielectric resonators", *IEEE AP-S Int. Symp. Digest, June 1994.*

[17] R. F. Harrington, *Time-Harmonic Electromagnetic Fields,* New York, McGraw-Hill, 1961.

[18] P. G. Li, A. T. Adams, Y. Leviatan, and J. Perini, "Multiple-post inductive obstacles in rectangular waveguide", *IEEE Trans. on Microwave Theory and Tech.,* vol. MTT-32, pp. 365-373, Jan. 1984.

[19] Y. Leviatan and G. S. Sheaffer, "Analysis of inductive dielectric posts in rectangular waveguide", *IEEE Trans. on Microwave Theory and Tech.,* vol. MTT-35, pp. 48-59, Jan. 1987.

[20] R. B. Keam and A. G. Williamson, "Analysis of a coaxial-line/radial-line region junction", *IEEE Trans. on Microwave Theory and Tech.,* vol. MTT-41, pp. 516-520, March 1993.

[21] X. P. Liang, K. A. Zaki, and A. E. Atia, "A rigorous three plane mode-matching technique for characterizing waveguide T-junctions and its application in multiplexer design", *IEEE Trans. on Microwave Theory and Tech.,* vol. MTT- 39, pp. 2138-2147, Jan. 1991.

[22] X. P. Liang and K. A. Zaki, "Modeling of cylindrical dielectric resonators in rectangular waveguides and cavities", *IEEE Trans. on Microwave Theory and Tech.,* vol. MTT-41, pp. 2174-2181, Jan. 1993.

[23] K. A. Zaki and A. E. Atia, "Modes in dielectric-loaded waveguides and resonators", *IEEE Trans. on Microwave Theory and Tech.,* vol. MTT-31, pp. 1039-1045, 1983.

[24] X. P. Liang, "Modeling of dual mode dielectric resonator filters and multiplexers", PhD thesis, 1993. University of Maryland.

[25] Z. D. Wang, "Modal Expansion with Moment method to analyze dielectric resonator loaded cavities", MASc thesis, 2001, University of Waterloo.

[26] G. R. Strachan, "An exact modal analysis of a dielectric resonator on a grounded substrate", M.A.Sc thesis, 1990. University of Waterloo.

[27] H. W. Yao, "EM simulation of resonant and transmission structures—applications to filters and multiplexers", PhD thesis, 1995. University of Maryland.

[28] R. E. Collin, *Field Theory of Guided Waves*, McGraw Hill Book Company, 1960.

[29] M. Taheri, D. Mirshekar-Syahkal, "Accurate determination of modes in dielectric-loaded cylindrical cavities using a one-dimensional finite element method," IEEE Trans. Microwave Theory and Techniques, vol.37, no.10, pp.1536-1541, Oct.1989.

[30] K. A. Zaki, and C. M. Chen, "New results in dielectric-loaded resonators," IEEE Trans. on Microwave Theory and Technologies, vol.34, no.7, pp.815-824, July 1986.

Zhongde Wang received BSc. in E.E., from Xidian University, Xi'an China in 1994, MSc in E.E. from University of Waterloo in 2001, Canada, and PhD in E.E. from University of Michigan, Ann Arbor, USA, in 2004.

His research interests include computational electromagnetics, RF MEMS structures modeling, and filter and antenna design. He has published over 20 papers in technical journals and conferences.

S. Safavi-Naeini received BSc. in E.E., from University of Tehran in 1974 and MSc. and PhD in E.E., both from U. of Illinois (Champaign-Urbana), USA, in 1975 and 1979 respectively. He is a professor in the Department of Electrical and Computer Engineering of University of Waterloo, where he also holds NSERC/RIM Industrial Research Chair in "Intelligent Integrated Radio/Antenna Systems and Novel Electromagnetic Media Technologies".

His research interests and activities include RF/microwave/millimeter wave and systems and circuits, antenna and propagation, wireless communication systems, very high speed digital circuits, photonics, and computational methods. He has published more than 120 papers in technical journals and conferences. He has been scientific and technical consultant to a number of national and international telecom industrial and research organizations over last 20 years.

John L. Volakis (S'77-M'82-SM'89-F96) was born on May 13, 1956 in Chios, Greece and immigrated to the U.S.A. in 1973. He obtained his B.E. Degree, summa cum laude, in 1978 from Youngstown State Univ., Youngstown, Ohio, the M.Sc. in 1979 from the Ohio State Univ., Columbus, Ohio and the Ph.D. degree in 1982, also from the Ohio State Univ.

From 1982-1984 he was with Rockwell International, Aircraft Division (now Boeing Phantom Works), Lakewood, CA and during 1978-1982 he was a Graduate Research Associate at the Ohio State University ElectroScience Laboratory. From January 2003 he is the Roy and Lois Chope Chair Professor of Engineering at the Ohio State University, Columbus, Ohio and also serves as the Director of the ElectroScience Laboratory. Prior to moving to the Ohio State Univ, he was a Professor in the Electrical Engineering and Computer Science Dept. at the University of Michigan, Ann Arbor, MI. since 1984

(19 years). He also served as the Director of the Radiation Laboratory from 1998 to 2000. His primary research deals with computational methods, electromagnetic compatibility and interference, design of new RF materials, multi-physics engineering and bioelectromagnetics. Dr. Volakis published about 220 articles in major refereed journal articles (9 of these have appeared in reprint volumes), more than 250 conference papers and 10 book chapters. In addition, he co-authored two books: *Approximate Boundary Conditions in Electromagnetics* (Institution of Electrical Engineers, London,1995) and *Finite Element Method for Electromagnetics* (IEEE Press, New York, 1998). He has also written two well-edited coursepacks on introductory and advanced numerical methods for electromagnetics, and has delivered short courses on numerical methods, antennas and frequency selective surfaces. In 1998 he received the University of Michigan (UM) College of Engineering Research Excellence award and in 2001 he received the UM, Dept. of Electrical Engineering and Computer Science Service Excellence Award. Dr. Volakis is listed by ISI among the top 250 most referenced authors (2004); He graduated/mentored nearly 40 Ph.D. students/post-docs, and co-authored with them 4 best paper awards at conferences.

Dr. Volakis served as an Associate Editor of the *IEEE Transactions on Antennas and Propagation* from 1988-1992, and as an Associate Editor of Radio Science from 1994-97. He chaired the 1993 IEEE Antennas and Propagation Society Symposium and Radio Science Meeting, and co-chaired the same Symposium in 2003. Dr. Volakis was a member of the AdCom for the IEEE Antennas and Propagation Society from 1995 to 1998 and serves as the 2004 President of the IEEE Antennas and Propagation Society. He also serves as an associate editor for the *J. Electromagnetic Waves and Applications,* the *IEEE Antennas and Propagation Society Magazine*, and the URSI Bulletin. He is a Fellow of the IEEE, and a member of Sigma Xi, Tau Beta Pi, Phi Kappa Phi, and Commission B of URSI. He is also listed in several Who's Who directories, including Who's Who in America.

On Second-Order Asymptotic Expansions at a Caustic

A.J. Booysen
Grintek Antennas
P.O. Box 8613, Centurion 0046, Republic of South Africa
Email: rbooysen@grintek.com

Abstract: **This paper presents a detailed analysis of second-order asymptotic expansions for the description of the geometrical optics field in the vicinity of a caustic. It is shown that the stationary phase solution commonly found in textbooks and papers is valid only at the caustic, but not away from the caustic, as is usually claimed. The exact stationary phase expansion is derived and is compared to steepest descent solutions presented elsewhere in the literature.**

I. INTRODUCTION

It is well known that the geometrical optics (GO) field reflected from a surface is equivalent to the first-order stationary phase (SP) asymptotic expansion of the corresponding radiation integral. When the reflector is concave, the reflected field forms a caustic surface as depicted in Figure 1. Near the caustic, where the first-order expansion begins to fail, two dominant stationary (saddle) points contribute to the asymptotic solution of the integral. These stationary points are each associated with a geometrical optics type ray, the rays merging into one another at the caustic. At the caustic the first-order expansions have a singularity and tend to infinity. Several second-order SP and steepest descent (SD) expansions describing the fields due to these stationary points are available in the literature ([1-19], listed in order of publication, including some related topics). The SP expansion originally introduced by Kay and Keller [1] involves only a single stationary point and does not decompose into two distinct GO expressions away from the caustic.Others employing the SP method derived similar expressions [2, 6 eq. (37), 9], all of which are not valid in the vicinity of or further away from the caustic, but only at the caustic itself. The incorrect application of this second-order SP solution away from the caustic has led to the introduction of heuristic caustic correction factors by Albertsen *et. al.* [8], which would not have been necessary if the exact expansion had been used. The limitations of these

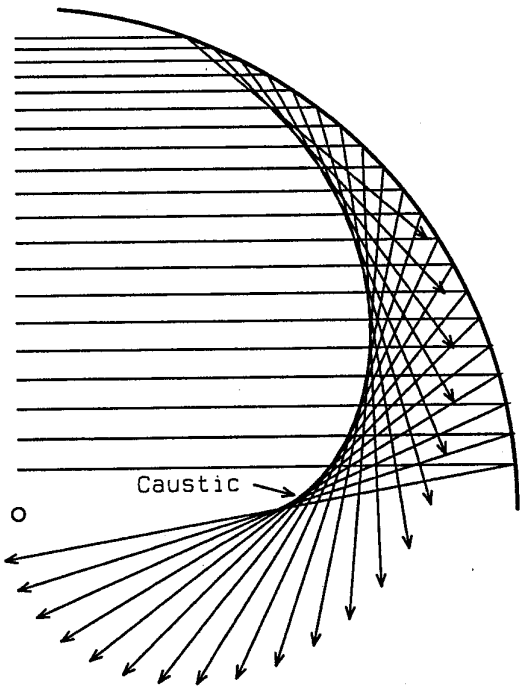

Figure 1. Reflected field of a concave reflector illuminated by a plane wave.

caustic correction factors have been pointed out by Meloling and Marhefka [19].

A Steepest Descent solution was introduced by Chester *et. al.* [3], which incorporated both stationary points and was valid at and away from the caustic. Their solution formed the basis of much of the work later published on the topic [4, 5, 7, 11, 14, 16, 19]. The new SP solution derived in this paper will be shown to yield results identical to these SD results. It is also possible to derive integral expressions for the fields in the vicinity of the caustic, as proposed by Ziolkowski and Deschamps [10], Hongo *et. al.* [12] and Hongo and Ji [13], but as a topic it falls beyond the scope of this paper. General reviews of high frequency techniques were presented by Arnold [11] and Bouche *et. al.* [17].

It will first be shown that the existing second-order SP solution is invalid away from the caustic. The exact second-order SP solution will then be derived and will be shown to be equivalent to the existing SD solutions. A detailed analysis of the scattering problem shown in Figure 1 will then be presented. This example will show clearly how the isolated rays contribute to the total solution. The paper is intended to present the new second-order SP solution, as well as to show those who are not well familiar with asymptotic theory how to interpret the various asymptotic solutions found in the literature.

II. EXISTING SP EXPANSIONS IN THE VICINITY OF A CAUSTIC

Returning to two-dimensional scattering problem depicted in Figure 1 of which the paramater definitions are shown in Figure 2, the scattered electric field for the Tm_z polarization can be expressed in integral form as [20]

$$E_z = \frac{-k\eta}{4}\int_S J(t)\, H_0^{(2)}(k\,r(t))\,dt$$

$$\sim \frac{-k\eta}{4}\sqrt{\frac{2j}{\pi k}}\int_S \frac{J(t)}{\sqrt{r(t)}}\, e^{-jkr(t)}\,dt \qquad (1)$$

$$= \frac{-k\eta}{4}\sqrt{\frac{2j}{\pi k}}\, R\int_S \frac{J(\theta)}{\sqrt{r(\theta)}}\, e^{-jkr(\theta)}\,d\theta,$$

where J is the induced current on the circular reflector of radius R, r the distance from the integration point $t=R\theta$ on the equivalent reflector surface to the field evaluation point, and $H_0^{(2)}$ is a Hankel function of the second type. In the second line of (1) the large argument form of the Hankel function [21] was employed. The incident field in Figure 1 is assumed to be a plane wave. For this particular problem and similar problems in general, the scattered field integral can be expressed as

$$I = \int_S F(t)e^{jkq(t)}\,dt \quad , \qquad (2)$$

where in this case

$$F(t) = \frac{J(t)}{\sqrt{r(t)}}$$

and $q(t) = -r(t)$.

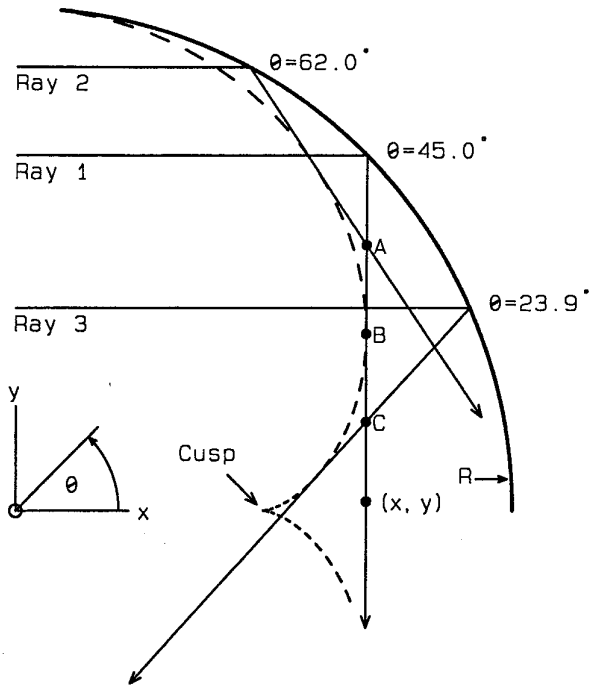

Figure 2. Problem geometry and parameter definition.

If the reflector is large enough in terms of wavelength, scattering from the reflector can be analysed by means of high frequency Geometrical Theory of Diffraction (GTD) [22] techniques, namely geometrical optics type reflected rays and diffraction from the edges of the reflector surface. This paper is not concerned with the diffracted fields, but only with the geometrical optics fields. For cases where the reflector is electrically large, also referred to as problems where k is large, the integral in (2) will have a stationary (or saddle) point for each geometrical optics ray. Such solutions are also referred to as the asymptotic solutions of the integral in (2). For any such stationary point, denoted by t_s and defined by $q'(t_s)=0$, the first-order stationary phase solution can be expressed as [7, p. 387]

$$I \sim F(t_s)\sqrt{\frac{2\pi}{kq''(t_s)}}\, e^{jkq(t_s)}\, e^{j\frac{\pi}{4}}, \qquad (3)$$

where $q''(t_s)$ is the second derivative of q with respect to t, evaluated at the stationary point, and it was assumed that $q''(t_s)>0$. When $q''(t_s)<0$, a phase jump of -90° occurs, since from (3) we have

$(-1)^{-1/2} = e^{-j\pi/2}$. The asymptotic solution of the integral in (2) can then be expressed as

$$I \sim F(t_s)\sqrt{\frac{-2\pi}{kq''(t_s)}}\, e^{jkq(t_s)}\, e^{-j\frac{\pi}{4}} \quad . \tag{4}$$

With some effort it can be shown that (3) is in fact identical to the associated geometrical optics ray reflected at point t_s [23].

For the problem shown in Figure 1, reflected rays will traverse the caustic surface as indicated. Figure 2 depicts isolated rays traversing the caustic. At every point near the caustic, but not near the cusp of the caustic ($\theta=0°$), the total field will be given by the sum of two distinct rays. In Figure 2 we keep Ray 1 fixed as the ray reflected at $\theta=45°$. Progressing from the reflector towards the caustic along the path of Ray 1, Ray 1 will be crossed by a Ray 2, which has already traversed the caustic surface (evaluation point A). At the caustic, Ray 2 will have merged into Ray 1(point B). As we continue to progress past the caustic along the path of Ray 1, Ray 1 will now be crossed by a Ray 3, which is yet to traverse the caustic (evaluation point C). At the indicated cross-over points, which are close to the caustic surface, both rays contribute to the total solution. At evaluation points far from the caustic, in both directions, the stationary points become well separated and the total field (excluding diffracted fields) is given by the sum of two GO rays, namely

$$I \sim F(t_{s1})\sqrt{\frac{-2\pi}{kq''(t_{s1})}}\, e^{jkq(t_{s1})}\, e^{-j\frac{\pi}{4}} + F(t_{s2})\sqrt{\frac{2\pi}{kq''(t_{s2})}}\, e^{jkq(t_{s2})}\, e^{j\frac{\pi}{4}} \quad , \tag{5}$$

where it was assumed that $q''(t_{s1}) < 0$ and $q''(t_{s2}) > 0$. Equation (5) is valid for those evaluation points in the region between the reflector and the caustic where the two stationary points are well separated. For evaluation points well beyond the caustic, such as the point (x,y) in Figure 2, the signs of the second derivatives will have changed and t_{s1} and t_{s2} in (5) must be interchanged.

As the caustic is approached, $t_{s1} \to t_{s2}$ where the derivatives $q''(t_{s1}), q''(t_{s2}) \to 0$ and equations (3) to (5) become invalid. To overcome this problem, a second-order SP solution must be derived. The general procedure as adopted by [1, 9] is as follows. It is assumed that $t_{s1} = t_{s2} = t_s$, which allows a Taylor expansion of q to be made about the stationary point t_s, yielding

$$q(t) \simeq q(t_s) + q'(t_s)(t-t_s) + \frac{q''(t_s)}{2}(t-t_s)^2 + \frac{q'''(t_s)}{6}(t-t_s)^3 \quad . \tag{6}$$

Only the first three derivatives were retained in (6) and by definition of a stationary point, $q'(t_s) = 0$. When (6) is substituted into (2), followed by the transformation of integration variable t to variable u (see [8] for details)

$$t - t_s = \left(\frac{2}{kq'''(t_s)}\right)^{\frac{1}{3}} u - \frac{q''(t_s)}{q'''(t_s)} \quad , \tag{7}$$

the asymptotic solution

$$I = 2\pi F(t_s)\left(\frac{2}{kq'''(t_s)}\right)^{\frac{1}{3}} e^{j\zeta} e^{jkq(t_s)} Ai(-\sigma) \tag{8}$$

is obtained, where Ai denotes the Airy function of the first kind [24],

$$\sigma = \left(\frac{k}{2}\right)^{\frac{2}{3}} \frac{[q''(t_s)]^2}{[q'''(t_s)]^{4/3}} \geq 0 \tag{9}$$

and

$$\zeta = \frac{2}{3}\sigma^{3/2} \quad . \tag{10}$$

At the caustic $q''(t_s) = 0$, yielding

$$I = 2\pi F(t_s)\left(\frac{2}{kq'''(t_s)}\right)^{\frac{1}{3}} e^{jkq(t_s)} Ai(0) \quad . \tag{11}$$

If (8) is supposed to represent the total field in the vicinity of the caustic, the contributions from the two distinct stationary points should become evident as one moves away from the caustic. This is clearly not the

case for (8), as it incorporates only one stationary point. If (8) is supposed to represent the contribution of a single stationary point only, and that a similar expression should be added for the contribution from the other stationary point, two problems arise. Firstly, at the caustic where $t_{s1} = t_{s2} = t_s$, the value of the field will be twice that given by (11), which is not correct. Secondly, when one moves away from the caustic, the two stationary points begin to separate and $\sigma > 0$. For widely separated stationary points, $\sigma \gg 0$ and one can employ the large argument form of the Airy function in (8). This is given by [8, 24]

$$Ai(-x) \sim \frac{1}{\sqrt{\pi}} \sigma^{-\frac{1}{4}} \sin\left(\frac{2}{3}x^{\frac{3}{2}} + \frac{\pi}{4}\right) \quad , \tag{12}$$

an oscillatory function which does not decrease monotonically away from the caustic as is characteristic of the GO field given by (3). Equation (8) thus represents neither the total field nor the contribution of a single stationary point away from the caustic. Keller and Kay however expressly state that (8) above, presented in a different form in their paper, is the transition function between the field at the caustic and the first-order solution given by (3) above [1, paragraph following eq. (50)].

In an attempt to overcome this problem, (12) was written as

$$Ai(-\sigma) \sim \frac{1}{2\sqrt{\pi}} \sigma^{-\frac{1}{4}} \left(e^{j\frac{2}{3}\sigma^{\frac{3}{2}} - \frac{\pi}{4}} + e^{-j\frac{2}{3}\sigma^{\frac{3}{2}} + \frac{\pi}{4}}\right) \tag{13}$$

by [8], which was then substituted back into (8). This substitution supposedly takes both rays into account, since (8) now "tends towards a sum of two terms, each of which is similar to" (3) above [8]. Since only one stationary point appears in (13), it was then suggested that each geometrical optics ray in (5) above be multiplied by a "caustic correction factor"

$$\frac{Ai(-\sigma)\sqrt{\pi}\,\sigma^{\frac{1}{4}}}{\sin\left(\frac{2}{3}\sigma^{\frac{3}{2}} + \frac{\pi}{4}\right)} \quad . \tag{14}$$

The very use of the term "correction factor" suggests that there is something wrong with the asymptotic expansion given in (8), which is not the case as long as (8) is evaluated at the caustic only. As will become clear, this confusion stems purely from the fact that (8) is not an exact asymptotic expansion for the field at *and away from* a caustic.

III. DERIVATION OF EXACT SP EXPANSION IN THE VICINITY OF A CAUSTIC

In order to derive an exact second-order SP solution for the field at a caustic, the general approach adopted by Felsen and Marcuvitz [7] will be followed. The general form of exponential integrals is

$$I = \int_P F(z) e^{kQ(z)} dz \quad , \tag{15}$$

where the integral is evaluated over a path P in the complex z-plane. As before, a Taylor expansion about the stationary point z_s and a substitution for z-z_s similar to (7) yields

$$I \sim F(z_s)\left(\frac{2}{kQ'''(z_s)}\right)^{\frac{1}{3}} e^{\xi} e^{kQ(z_s)} \int_P e^{\frac{u^3}{3} - \delta u} du \quad , \tag{16}$$

where

$$\delta = \left(\frac{k}{2}\right)^{\frac{2}{3}} \frac{[Q''(z_s)]^2}{[Q'''(z_s)]^{4/3}} \tag{17}$$

and

$$\xi = \frac{2}{3}\delta^{3/2} \quad . \tag{18}$$

For the sake of further analysis the sense of integration in (16) is reversed by performing the substitution u=-z. Furthermore, for the special case where $Q(z) = j\,q(z)$, (16) can be written as

$$I = I_p \sim F(z_s)\left(\frac{2}{kq'''(z_s)}\right)^{\frac{1}{3}} e^{\xi} e^{jkq(z_s)} e^{-j\frac{\pi}{6}} \times \int_{P'} e^{\delta z - \frac{z^3}{3}} dz \quad , \tag{19}$$

where the relevant parameters in the integral can now be expressed in terms of (9) and (10) as

$$\delta = \left(\frac{k}{2}\right)^{\frac{2}{3}} \frac{[q''(z_s)]^2}{[q'''(z_s)]^{4/3}} e^{j\frac{\pi}{3}} = \sigma e^{j\frac{\pi}{3}} \tag{20}$$

and

$$\xi = \frac{2}{3}\delta^{3/2} = j\frac{2}{3}\sigma^{\frac{3}{2}} = j\zeta \quad . \tag{21}$$

As we have assumed $q''(z_s) > 0$, the integral is designated $I = I_p$. Defining the integral in (19) as

$$C(\delta) = \int_P e^{\delta z - \frac{z^3}{3}} dz \quad , \tag{22}$$

and considering the possible integration paths for this integral as shown in Figure 3, the asymptotic solution of (22) is [7]

$$C(\delta) = \begin{cases} 2\pi j Ai(\delta) & \text{if } P = L_{32} \quad (23a) \\ \pi[Bi(\delta) - jAi(\delta)] & \text{if } P = L_{21} \quad (23b) \\ \pi[Bi(\delta) + jAi(\delta)] & \text{if } P = L_{31} \quad (23c) \end{cases}$$

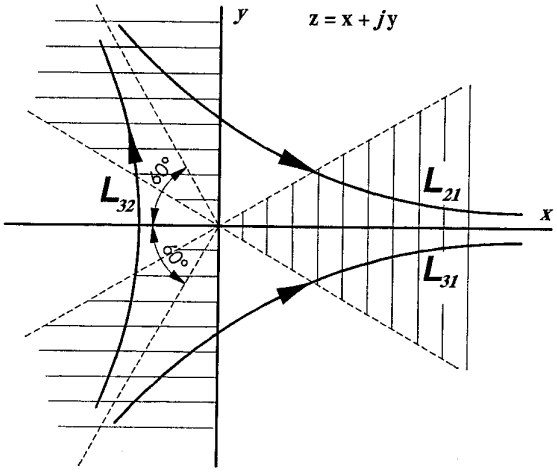

Figure 3. Integration paths for an Airy type integral of complex argument.

Since we need the integral to be in the form of (2) before we can derive a stationary phase path, following [7] we use the transformation $z = \Xi^{\frac{1}{3}} z'$ below to obtain

$$\int_{P'} e^{\delta z' - \frac{z'^3}{3}} dz' = \Xi^{\frac{1}{3}} \int_{P''} e^{\Xi(z - \frac{z^3}{3})} dz \quad , \tag{24}$$

where

$$\Xi = \delta^{\frac{3}{2}} = j\Omega \quad , \quad \Omega = \sigma^{\frac{3}{2}} \quad . \tag{25}$$

The transformation has now allowed us to express (22) as

$$\int_{P'} e^{\delta z - \frac{z^3}{3}} dz = \Xi^{\frac{1}{3}} \int_{P''} e^{\Omega g(z)} dz \quad , \tag{26}$$

where the function in the exponential term is

$$g(z) = j(z - \frac{z^3}{3}) \quad . \tag{27}$$

Equation (27) has stationary points where $g'(z_s) = 0$, which yields

$$z_s = \pm 1 \quad . \tag{28}$$

A stationary phase integration path requires that $\mathbb{R}e\{g(z)\} = \mathbb{R}e\{g(z_s)\}$, and with $z = x + jy$ we obtain the integration paths defined by

$$\begin{aligned} \mathbb{R}e\{g(z)\} &= -y + x^2 y - \frac{y^3}{3} \\ &= \mathbb{R}e\{g(z_s)\} = 0 \quad . \end{aligned} \tag{29}$$

These integration paths are shown in Figure 4 and it is clear that an integration path corresponding to L_{32} in Figure 3 can be selected. For this choice the stationary phase solution of the integral in (22) is given by (23a) and the stationary phase solution of (19) for an isolated stationary point z_s becomes

$$\begin{aligned} I_p \sim\ & 2\pi F(z_s) \left(\frac{2}{k q'''(z_s)} \right)^{\frac{1}{3}} e^{j\zeta} e^{jkq(z_s)} e^{j\frac{\pi}{3}} \\ & \times Ai(\sigma e^{j\frac{\pi}{3}}) \quad . \end{aligned} \tag{30}$$

When σ becomes large, we can use the large argument form of the Airy function of complex argument [24]

$$Ai(z) \sim \frac{1}{2\pi^{1/2} z^{1/4}} e^{-\frac{2}{3}z^{3/2}} \quad , \quad |\arg(z)| \le \pi \tag{31}$$

to show that (30) reduces (3).

When $q''(z_s) < 0$, we have from (25) and (20)

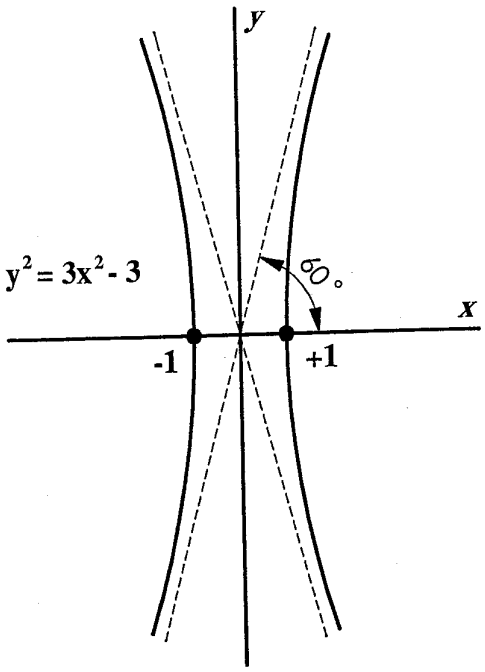

Figure 4. Stationary phase paths for an Airy type integral of complex argument.

$$\Xi_n = \delta^{\frac{1}{2}} = \frac{k}{2}\frac{[q''(z_s)]^3}{[q'''(z_s)]^2} e^{j\frac{\pi}{2}} = \frac{k}{2}\frac{[|q''(z_s)|]^3}{[q'''(z_s)]^2} e^{j\frac{\pi}{2}} e^{j\pi} = -\Xi \tag{32}$$

and

$$\Xi_n^{\frac{1}{3}} = \delta^{\frac{3}{2}\cdot\frac{1}{3}} = \left(\frac{k}{2}\right)^{\frac{1}{3}} \frac{|q''(z_s)|}{[q'''(z_s)]^{\frac{2}{3}}} e^{j\frac{\pi}{6}} e^{j\frac{\pi}{3}} = \Xi e^{j\frac{\pi}{3}} \quad . \tag{33}$$

The negative sign in (32) will not result in different integration paths as defined by (29), but the transformation $z = \Xi_n^{\frac{1}{3}} z' = \Xi e^{j\frac{\pi}{3}} z'$ implies that the integration path must be rotated by 60° with respect to the case where $q''(z_s) > 0$. If we rotate the path through $z_s = +1$ in Figure 4 by 60° anti-clockwise, we can select an integration path corresponding to L_{21}, resulting in (22) becoming

$$C(\delta) = \pi[Bi(\sigma e^{j\frac{\pi}{3}}) - jAi(\sigma e^{j\frac{\pi}{3}})] = 2\pi e^{-j\frac{\pi}{6}} Ai(\sigma e^{-j\frac{\pi}{3}}) \quad , \tag{34}$$

where we have used the relationship

$$2Ai(ze^{\pm j\frac{2\pi}{3}}) = e^{\pm j\frac{\pi}{3}}[Ai(z) \mp jBi(z)] \quad . \tag{35}$$

When (34) is substituted into (19) and recognising from (21) and (32) that ζ will also change in sign, we obtain

$$I_n \sim 2\pi F(z_s)\left(\frac{2}{kq'''(z_s)}\right)^{\frac{1}{3}} e^{-j\zeta} e^{jkq(z_s)} e^{-j\frac{\pi}{3}} \times Ai(\sigma e^{-j\frac{\pi}{3}}) \quad . \tag{36}$$

For σ becomes large, we can use (31) to show that (36) reduces to (4).

The asymptotic solution for the isolated stationary point $z_s = z_{s1}$ is thus given by (30) when $q''(z_{s1}) > 0$ and by (36) when $q''(z_{s1}) < 0$. For the second ray, defined by $z_s = z_{s2}$, we also apply either (30) or (36), depending on the sign of $q''(z_{s2})$. For evaluation points along the path of Ray 1, $q''(z_{s1}) < 0$ and $q''(z_{s2}) > 0$ before the caustic is traversed. Beyond the caustic $q''(z_{s1}) > 0$ and $q''(z_{s2}) < 0$. The total field is thus given by $I_{tot}(q_1'' < 0, q_2'' > 0) = I_n(z_{s1}) + I_p(z_{s2})$ for the case where the caustic is yet to be traversed, and by $I_{tot}(q_1'' > 0, q_2'' < 0) = I_p(z_{s1}) + I_n(z_{s2})$ beyond the caustic. At the caustic, having been approached from either side, $\sigma \to 0$ and the total field is given by $I = I_p + I_n$, namely

$$I_{tot} \sim 2\pi F(z_s)\left(\frac{2}{kq'''(z_s)}\right)^{\frac{1}{3}} e^{jkq(z_s)} e^{+j\frac{\pi}{3}} Ai(0) + 2\pi F(z_s)\left(\frac{2}{kq'''(z_s)}\right)^{\frac{1}{3}} e^{jkq(z_s)} e^{-j\frac{\pi}{3}} Ai(0) = 2\pi F(z_s)\left(\frac{2}{kq'''(z_s)}\right)^{\frac{1}{3}} e^{jkq(z_s)} Ai(0) \quad . \tag{37}$$

This is the same value as given by (11).

IV. SD ASYMPTOTIC EXPANSIONS FOR TWO NEARBY STATIONARY POINTS

A steepest descent asymptotic solution for the total field of (2) in the case of two nearby stationary (saddle) points is expressed by Felsen and Marcuvitz [7] as

$$\begin{aligned} I_{tot} \sim\ & \pi k^{-\frac{1}{3}}[h_1 F(t_{s1}) + h_2 F(t_{s2})] e^{ja_o k} \\ & \times Ai(-\sigma k^{\frac{2}{3}}) \\ & + j\pi \sigma^{-\frac{1}{2}} k^{-\frac{2}{3}} [h_1 F(t_{s1}) - h_2 F(t_{s2})] e^{ja_o k} \\ & \times Ai'(-\sigma k^{\frac{2}{3}}) \quad , \end{aligned} \tag{38}$$

where

$$h_1 = \sqrt{\frac{-2\sigma^{1/2}}{q''(t_{s1})}}, \quad h_2 = \sqrt{\frac{+2\sigma^{1/2}}{q''(t_{s2})}} \quad , \tag{39}$$

$$a_o = \frac{1}{2}[q(t_{s1}) + q(t_{s2})] \quad , \tag{40}$$

and

$$\frac{2}{3}\sigma^{\frac{3}{2}} = \frac{1}{2}[q(t_{s1}) - q(t_{s2})] \quad . \tag{41}$$

In (39) it is assumed that $q''(t_{s1}) < 0$ and $q''(t_{s2}) > 0$. The total field given by (38) is the sum of two rays, described respectively by

$$\begin{aligned} I_p \sim\ & \frac{\pi}{2} k^{-\frac{1}{3}} [h_1 F(t_{s1}) + h_2 F(t_{s2})] e^{ja_o k} \\ & \times [Ai(-\sigma k^{\frac{2}{3}}) + jBi(-\sigma k^{\frac{2}{3}})] \\ & + j\frac{\pi}{2} \sigma^{-\frac{1}{2}} k^{-\frac{2}{3}} [h_1 F(t_{s1}) - h_2 F(t_{s2})] e^{ja_o k} \\ & \times [Ai'(-\sigma k^{\frac{2}{3}}) + jBi'(-\sigma k^{\frac{2}{3}})] \quad , \end{aligned} \tag{42}$$

and

$$\begin{aligned} I_n \sim\ & \frac{\pi}{2} k^{-\frac{1}{3}} [h_1 F(t_{s1}) + h_2 F(t_{s2})] e^{ja_o k} \\ & \times [Ai(-\sigma k^{\frac{2}{3}}) - jBi(-\sigma k^{\frac{2}{3}})] \\ & + j\frac{\pi}{2} \sigma^{-\frac{1}{2}} k^{-\frac{2}{3}} [h_1 F(t_{s1}) - h_2 F(t_{s2})] e^{ja_o k} \\ & \times [Ai'(-\sigma k^{\frac{2}{3}}) - jBi'(-\sigma k^{\frac{2}{3}})] \quad . \end{aligned} \tag{43}$$

It is easily verified that the sum of (42) and (43) yields (38).

At the caustic $t_{s1} = t_{s2}$, $\sigma = 0$, and h_1 and h_2 assume the limiting value [7]

$$|h_1| = |h_2| = \left[\frac{2}{q'''(t_s)}\right]^{\frac{1}{3}} \quad . \tag{44}$$

Since the second term in (38) becomes zero, it is rudimentary to show that (38) reduces to (11). Equations (42) and (43) can likewise be shown to reduce to

$$I_p \sim 2\pi F(t_s) \left(\frac{2}{kq'''(t_s)}\right)^{\frac{1}{3}} e^{jkq(t_s)} e^{+j\frac{\pi}{3}} Ai(0) \tag{45}$$

and

$$I_n \sim 2\pi F(t_s) \left(\frac{2}{kq'''(t_s)}\right)^{\frac{1}{3}} e^{jkq(t_s)} e^{-j\frac{\pi}{3}} Ai(0) \tag{46}$$

respectively. To derive (45) and (46) the relationship

$$Ai(-\sigma) \pm jBi(-\sigma) = 2e^{\pm j\frac{\pi}{3}} Ai(\sigma e^{\pm j\frac{\pi}{3}}) \tag{47}$$

was used. When the two stationary points are widely separated, (38) reduces to (5), as is shown in Appendix A. It is also shown that (42) and (43) reduce to (3) and (4), respectively.

It should now be clear that at the caustic and far away from the caustic, the SD expressions for the total field and the two separate rays are identical to the corresponding SP expressions derived in the previous section. A numerical example presented later will show that the SD and SP expansions yield identical results in the intermediate region as well.

V. NUMERICAL EXAMPLE OF THE SCATTERED FIELD NEAR A CAUSTIC

In order to demonstrate how the field behaves in the vicinity of the caustic and how the isolated ray contributions should be interpreted, we return to the problem depicted in Figures 1 and 2. The scattered field will be calculated by means of geometrical optics, integration of the physical optics current induced on the reflector surface, the newly derived SP expansions

and the SD expansions discussed in the previous section.

The two-dimensional circular scatterer is assumed to have a radius R=200λ and is illuminated by a plane wave, which is TM_z polarised. The incident electric and magnetic fields at the reflector surface are given by

$$\boldsymbol{E}^i = E^i \hat{z} = e^{-jkR\cos\theta}\,\hat{z} \tag{48}$$

and

$$\boldsymbol{H}^i = H^i \hat{y} = -\frac{1}{\eta} e^{-jkR\cos\theta}\,\hat{y} \quad , \tag{49}$$

where η is the free space wave impedance. With $E^i=1$, the GO scattered electric field is given by

$$\boldsymbol{E}^s = E^s \hat{z} = -e^{-jkR\cos\theta}\sqrt{\frac{\rho}{\rho + l_2}}\, e^{-jkl_2}\,\hat{z} \tag{50}$$

where l_2 is the distance from the reflection point along the ray path and the radius of curvature ρ is given by

$$\frac{1}{\rho} = \frac{1}{l_1} - \frac{2}{R\cos\theta^i} = -\frac{2}{R\cos\theta^i} \quad . \tag{51}$$

In (51) it was furthermore assumed that $l_1 = \infty$ since the incident field is a plane wave. For a circular reflector, $\theta^i=\theta$.

The physical optics current $\boldsymbol{J}$ is given by

$$\begin{aligned} \boldsymbol{J} = J_z \hat{z} &= 2\hat{\boldsymbol{n}} \times \boldsymbol{H}^i = \frac{2}{\eta} e^{-jkR\cos\theta} n_x H_y \hat{z} \\ &= \frac{2}{\eta} e^{-jkR\cos\theta}\cos\theta\,\hat{z} \quad , \end{aligned} \tag{52}$$

where we have utilised the normal vector relationship $\hat{\boldsymbol{n}} = n_x\hat{x} + n_y\hat{y} = -\cos\theta\,\hat{x} - \sin\theta\,\hat{y}$. In subsequent integral calculations (1) was evaluated by means of Gaussian integration, with 5 integration points/ wavelength used for the 0°-90° circular integration sector (about 1570 integration points).

With (52) substituted into (1), we have from (2)

$$F(\theta) = -\frac{k}{2}\sqrt{\frac{2}{\pi k l_2}}\, e^{j\frac{\pi}{4}}\cos\theta \quad , \tag{53}$$

where for an observation point (x,y) shown in Figure 2,

$$l_2 = \sqrt{(x - R\cos\theta)^2 + (y - R\sin\theta)^2} \tag{54}$$

and

$$q(\theta) = -(l_2 + R\cos\theta) \quad . \tag{55}$$

The derivatives of $q(\theta)$ are given in Appendix B. The first- and second-order expansions discussed above give a phase jump of ±45° across the caustic. Since the GO field encounters a phase jump of +90° across the caustic, all SP and SD solutions were multiplied by a factor $e^{j\frac{\pi}{4}}$ to ensure that the GO and SP/SD phase terms are identical.

With the appropriate functions as defined above, the various field expressions were evaluated along the path of Ray 1 in Figure 2, which is vertically downward (θ_s=45°) . The evaluation points on this path progressed from the reflector surface to beyond the caustic surface. Ray 2 crosses Ray 1 at a distance of $\rho_o/2$ before the caustic, while Ray 3 crosses Ray 1 at a distance of $\rho_o/2$ past the caustic point of Ray 1, where $\rho_o = 0.5\,R\cos(\pi/4)$.

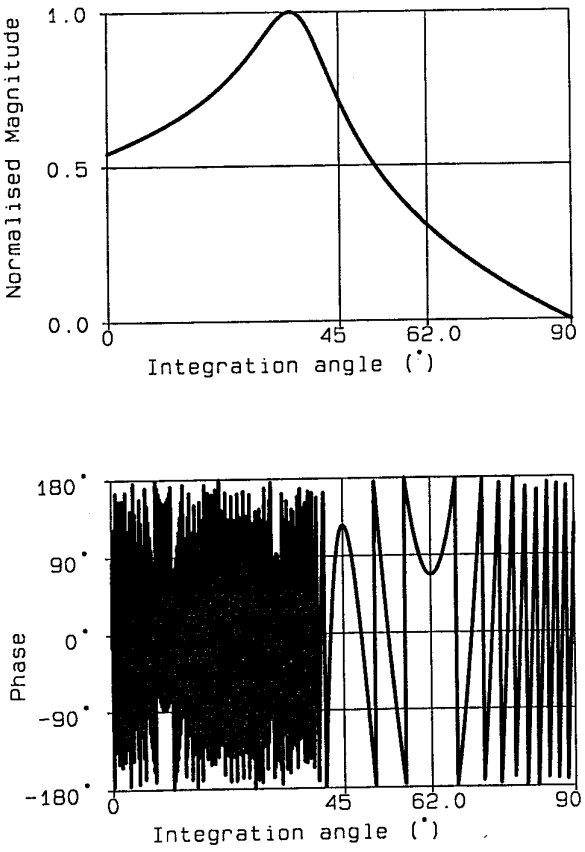

Figure 5. Integrand for Ray 2 crossing Ray 1.

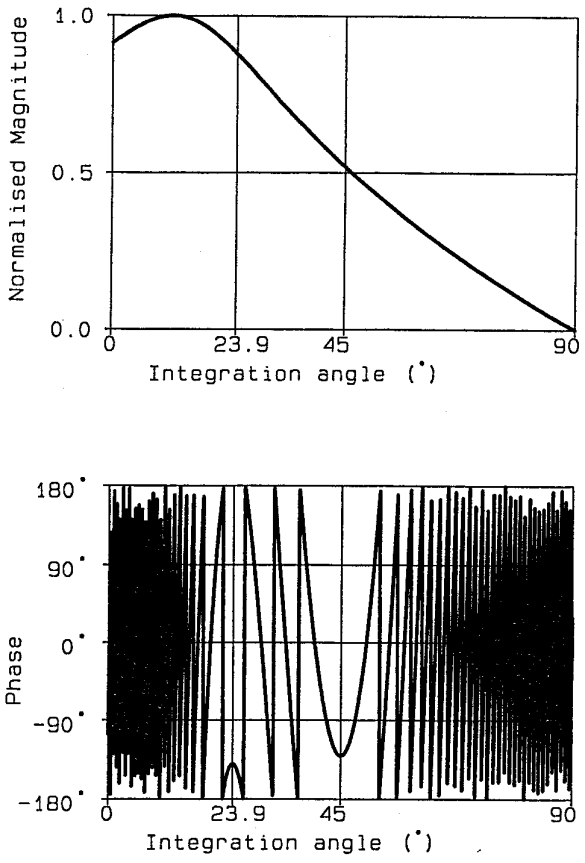

Figure 6. Integrand for Ray 3 crossing Ray 1.

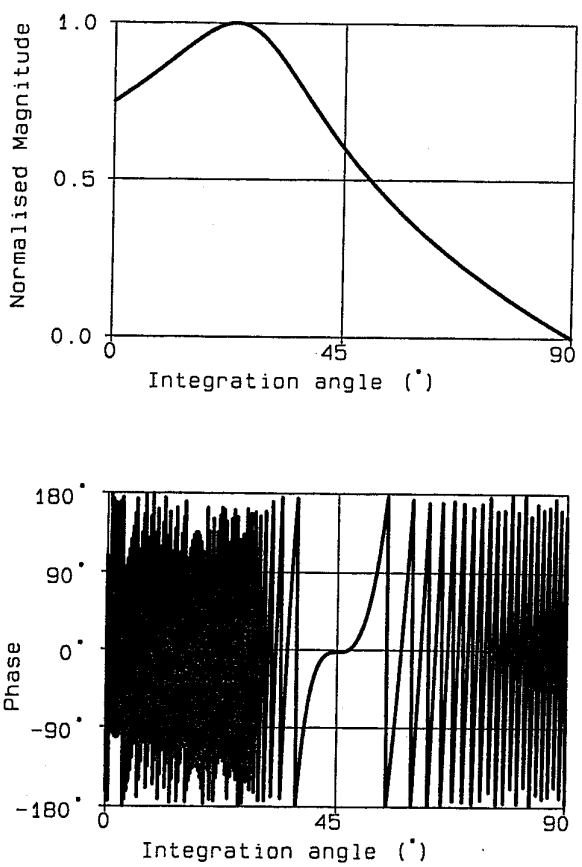

Figure 7. Integrand for Rays 1 and 2 having merged at the caustic.

Figures 5 to 7 show the magnitude (normalised) and phase (not normalised) of the integrand of (2) for the cases where the two stationary points are separated from each other and when the two rays have merged into each other at the caustic. In Figure 5, Ray 2 has a stationary point $\theta_s=62.0°$ and has already traversed the caustic surface (point A). The first derivative of q is clearly zero at the two stationary points (the definition of a stationary point), and it is also evident that $q''(\theta_{s1})<0$ and $q''(\theta_{s2})>0$. Figure 6 represents the case where Ray 1 is crossed by Ray 3 (point C). Ray 1 has already traversed the caustic, but Ray 3 ($\theta_s=23.9°$) is yet to do so. As expected, the signs of the second derivatives have reversed and we now have $q''(\theta_{s1})>0$ and $q''(\theta_{s3})<0$. Figure 7 shows the integrand magnitude and phase for the case where the two rays have merged into one, with the evaluation point at the caustic of Ray 1 in Figure 2 (point B). The phase of the integrand displays an inflection point at the caustic and one can by inspection see that $q''(\theta_{s1}) = q''(\theta_{s2}) = 0$.

The scattered electric field along the path of Ray 1 was next calculated by means of the techniques mentioned above. The ray path progressed from the surface of the reflector ($l_2=0$) to $l_2 = 1.5\rho_o$. Figure 8 shows the scattered field component of Ray 1 only, as calculated by means of geometrical optics (GO), the new stationary phase expansions derived above (SP) and the steepest descent expansions given by [7] (SD).

The phase of the scattered field (ϕ) was normalised with respect to the GO linear phase (excluding the phase jump which occurs when the caustic is traversed),and the normalised phase is thus given by the expression $\phi_{nor} = \phi + k(R\cos(\pi/4) + l_2) - \pi$, the phase term π accounting for the negative reflection coefficient in (50) above. The magnitude was normalised with respect to the value of the electric field at the caustic, designated by Ec.

Returning to Figure 8, Ray 1 seems to be discontin uous

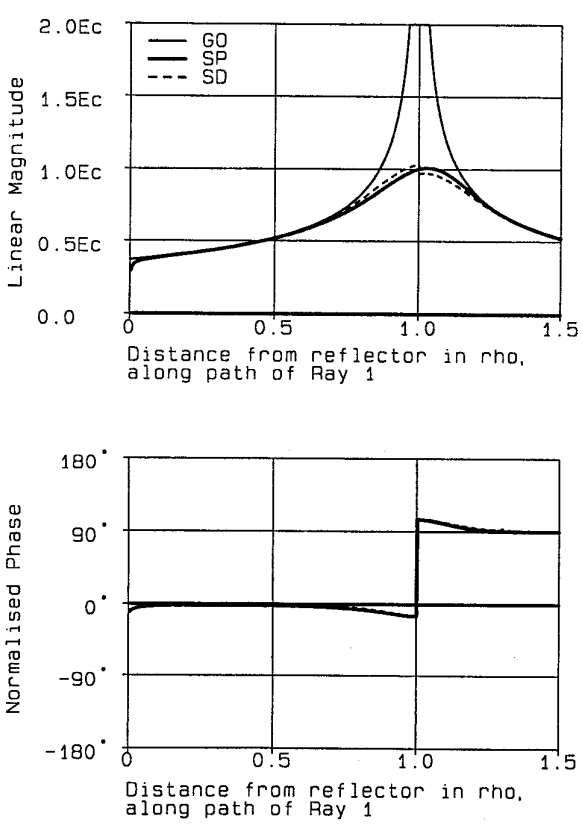

Figure 8. Partial field given by Ray 1.

across the caustic, as the phase jumps by more than 90°. It should be kept in mind that $q''(\theta_{s1}) < 0$ as long as Ray 1 has not traversed the caustic, and $q''(\theta_{s1}) > 0$ when it has already done so. One must then use (36) in the former case and (30) in the latter. At every evaluation point along the path of Ray 1, one should simply choose the appropriate asymptotic solution, which in turn depends on the si gn of $q''(\theta_s)$. The SP solution is not accurate right against the surface of the reflector, since we have used the large argument form of the Hankel function to derive (2), which is not correct when $l_2 \to 0$.

Calculation by means of the SD expansions is considerably more involved. It should be clear that (42) and (43) represent the case where Ray 1 is yet to traverse the caustic, with $q''(\theta_{s1}) = q_1'' < 0$ and $q''(\theta_{s2}) = q_2'' > 0$. When Ray 1 has traversed the caustic, the signs of these derivatives change and (42) and (43) are no longer valid. We can rewrite (42) and (43) in shorthand notation for the case where $q_1'' < 0$, $q_2'' > 0$, $l_2 < \rho_0$ as

$$\begin{aligned} I_{2p} = {} & C_1[h_1F_1 + h_2F_2][Ai + jBi] \\ & + C_2[h_1F_1 - h_2F_2][Ai' + jBi'] \\ & \sim F_2\sqrt{\frac{2\pi}{kq_2''}}\, e^{jkq_2}\, e^{+j\frac{\pi}{4}} \quad \text{for } \sigma \gg 0 \end{aligned} \tag{56}$$

and

$$\begin{aligned} I_{1n} = {} & C_1[h_1F_1 + h_2F_2][Ai - jBi] \\ & + C_2[h_1F_1 - h_2F_2][Ai' - jBi'] \\ & \sim F_1\sqrt{\frac{-2\pi}{kq_1''}}\, e^{jkq_1}\, e^{-j\frac{\pi}{4}} \quad \text{for } \sigma \gg 0 \quad . \end{aligned} \tag{57}$$

The corresponding expressions for the case where $q_1'' > 0$, $q_2'' < 0$, $l_2 > \rho_0$ are

$$\begin{aligned} I_{2n} = {} & C_1[h_1F_1 + h_2F_2][Ai - jBi] \\ & - C_2[h_1F_1 - h_2F_2][Ai' - jBi'] \\ & \sim F_2\sqrt{\frac{-2\pi}{kq_2''}}\, e^{jkq_2}\, e^{-j\frac{\pi}{4}} \quad \text{for } \sigma \gg 0 \end{aligned} \tag{58}$$

and

$$\begin{aligned} I_{1p} = {} & C_1[h_1F_1 + h_2F_2][Ai + jBi] \\ & - C_2[h_1F_1 - h_2F_2][Ai' + jBi'] \\ & \sim F_1\sqrt{\frac{2\pi}{kq_1''}}\, e^{jkq_1}\, e^{+j\frac{\pi}{4}} \quad \text{for } \sigma \gg 0 \quad . \end{aligned} \tag{59}$$

It should be noted that the SD expansions do not quite give the correct values as the caustic is approached. This is because of various terms (h_1, h_2, σ) in the SD expansions tend to either zero or infinity as the caustic is approached. These infinite/zero numbers are added and subtracted to give the total contribution of Ray 1, with an obvious numerical round-off error giving rise t o the discrepancy. The field value jumps from just more than to just less than the actual value as the caustic is traversed. We know from (45) and (46) that the SD

solutions for Ray 1 and Ray 2 give the correct value at the caustic. The phase curves are identical.

Figure 9 shows the GO, SP and SD results for the contribution of Ray 2 as the evaluation point p rogresses along the path of Ray 1. An algorithm was developed to find the appropriate stationary point of Ray 2 for each of these evaluation points. The phase of the Ray 2 results was normalised by the same factor as used in Figure 8. Near the caustic Ray 2 tends to Ray 1 and experiences a similar phase variation, except that the phase jump is now -90°. When the results of Figures 8 and 9 are overlaid, one can see that the total field will be continuous in magnitude and phase.

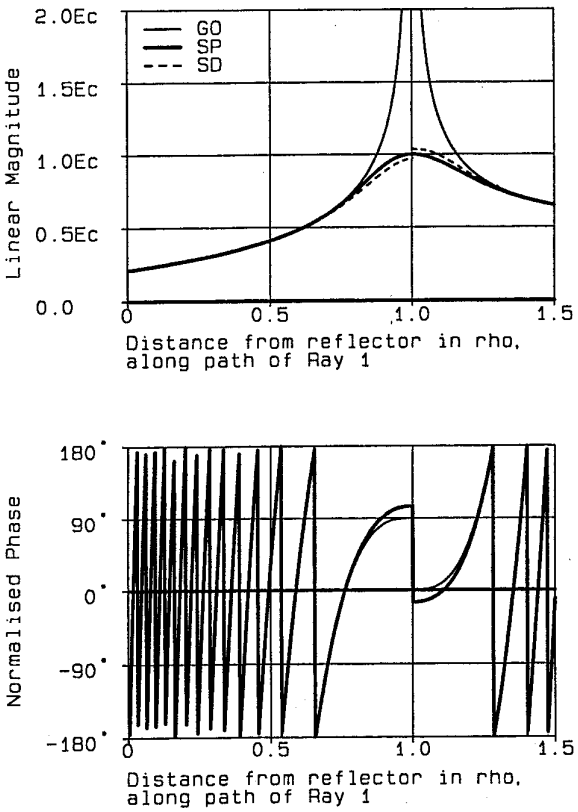

Figure 9. Partial field given by Ray 2.

It should be stressed that the expansions for isolated stationary points given by (30), (36) and (56) to (58) can yield an absolute phase va riation of maximum 15°, as is evident from Figures 8 and 9.

The total field as calculated by geometrical optics, the SP and SD expansions and integration of the physical optics (PO) current is shown in Fi gure 10. There is no discernable difference between the results of any of the latter three methods. The physical optics integral solution should actually be regarded as the bench -mark, as it is based on the least number of approximations.

Of particular interest is the phase of the total field in th e vicinity of the caustic. The phase of the total field was normalised by the same fac tor used in Figures 8 and 9. Had there been no caustic effect present, the normalised phase at $1.0\,\rho_o$ would have been zero (the field would

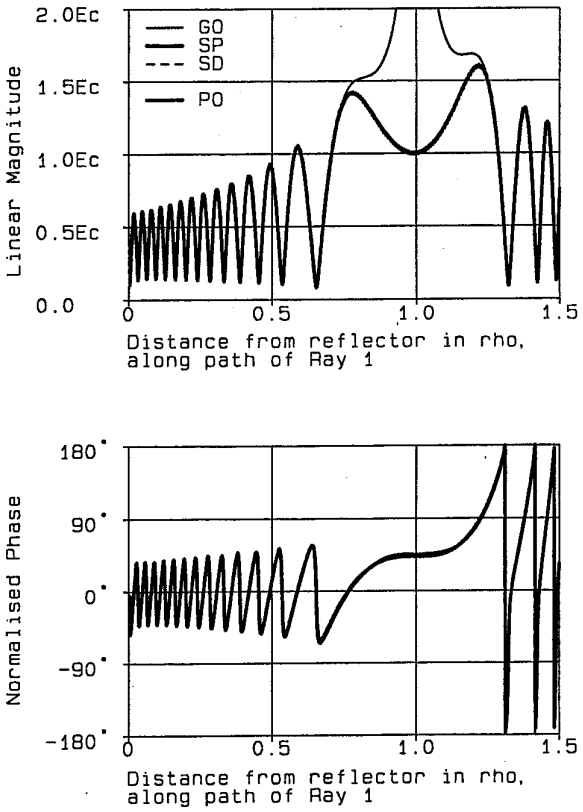

Figure 10. Total field taking both stationary points into account.

have been purely GO in nature). However, with the caustic present, the phase at the caustic is +45° with respect to the linear phase of Ray 1. In fact, if one considers the normalised phase in the region where the GO and SP magnitude curves begin to separate (the caustic region), it is clear that there is a gradual phase jump from 0° to +90° across the caustic region. This is in perfect agreement with the phase jump predicted by the first-order SP (and thus the GO) solutions of the

scattered field integral.

VI. CONCLUSION

Of the various published forms of asymptotic expansions for the field in the vicinity of a causti c, only the steepest descent expansions were found to be correct. The corresponding second-order stationary phase expansion which is commonly found in the literature and textbooks was found to be valid only at the caustic itself, but incorrect away from the caustic. In this paper the exact second-order stationary phase expansions were derived. These expansions yield identical results to the steepest descent expansions, but are considerably less complex to evaluate than the latter. This is due mainly because the new stationary phase expansions were derived in terms of the contribution of a single stationary point only, whilst the steepest descent expansions were derived in terms of two nearby saddle points. It is instructive to see that two seemingly different sets of expansions yield the same results. This is of course to be expected if both are correct.

The purpose of the paper was not only to present the exact stationary phase expansions, but also to serve as a tutorial for those who are not experienced in the fie ld. The importance of the numerical example presented here lies in the clear exposition of how the various expansions should be used, and in that it shows how th e phase of the total field experiences a gradual phase jump of 90° as the caustic is trav ersed. The expansions for the isolated stationary points do not yield a continuous phase jump across the caustic by themselves, only when they are added to obtain the total field. The second-order solutions discussed in this paper are not valid in the region of a caustic cusp, where higher order derivatives for the various functions are required [1].

It is hoped that this paper will contribute to a better understanding of asymptotic solutions at a caustic.

REFERENCES

[1] I. Kay and J. B. Keller, "Asymptotic Evaluation of the Field at a Caustic", *J. Appl. Phys.*, Vol. 25, No. 7, pp. 876-883, July 1954.

[2] I. Kay, "Fields in the neighborhood of a caustic", *IRE Trans. Antennas and Propagat.*, pp. 255-260, 1959.

[3] C. Chester, B. Friedman and F. Ursell, "An Extension of the Method of Steepest Descents", *Proc. Cambridge Phil. Soc.*, Cambridge, London, U.K., Vol. 53,. Pp599-611, 1957.

[4] D. Ludwig, "Uniform Asympt otic Expansions at a Caustic", *Comm. Pure Appl. Math.*, vol. XIX, pp. 215-220, 1966.

[5] N. Bleistein, "Uniform asymptotic expansions of integrals with many nearby stationary point s and algebraic singularities", *J. Math. Mech.*, vol. 17, no. 6, pp. 533-559, 1967.

[6] G. Hyde, "Studies of the focal region of a spherical reflector: stationary phase evaluation", *IEEE Trans. Antennas and Propagat.*, vol. AP-16, pp. 646-656, 1968.

[7] L.B. Felsen and N. Marcuvitz, *Radiation and Scattering of Waves*, Englewood Cliffs, N.J.: Prentice-Hall, 1973, pp. 370-416.

[8] N.C. Albertsen, P. Balling and N.E. Jensen, "Caustics and Caustic Corrections to the Field Diffracted by a Curved Edge", *IEEE Trans. Antennas Propagat.*, vol. AP-25, pp. 297-303, 1977.

[9] G.L. James, *Geometrical theory of diffraction for electromagnetic waves*, London: IEE (Peter Peregrinus), 1976, 1980, p.30.

[10] R.W. Ziolkowski and G.A Deschamps, "Asymptotic evaluation of high frequency fields near a caustic, an introduction to Maslov's method," *Radio Sci.*, vol. 19, no. 4,. pp. 1001-1025, Jul.-Aug., 1984.

[11] J.M. Arnold, "Geometrical theories of wave propagation: a contemporary review", *IEE Proc.*, vol. 133, Pt. J, pp. 165-188, 1986.

[12] K. Hongo, Y. Ji and E. Nakajima, "High-frequency expression for the field in the caustic region of a reflector using Maslov's method", *Radio Sci.*, vol. 6, pp. 911-919, Dec. 1986.

[13] K. Hongo and Y. Ji, "Study of the field around the focal region of a sphe rical reflector antenna", *IEEE Trans. Antenna and Propagat.*, vol. AP-36, pp. 592-598, 1988.

[14] P.H. Pathak and M-C. Liang, "On a uniform asymptotic solution valid across smooth caustics of rays reflected by smoothly ind ented boundaries", *IEEE Trans. Antennas and Propagat.*, vol. AP-38, pp. 1192-1203, 19 90.

[15] E. D. Constantinides and R.J. Marhefka, "Efficient and accurate computation of the incomplete Airy functions", *Radio Sci.*, vol. 28, no. 4, pp. 441-457, July-August 1993.

[16] E. D. Constantinides and R.J. Marhefka, "A UGO/EUTD solution for the scattering and diffrcation from cubic polynomial strips", *IEEE Trans. Antennas and Propagat.*, vol. AP-41, pp. 1088-1098, 1993.

[17] D.P. Bouche, F.A. Molinet and R. Mittra, "Asymptotic and hybrid techniques for electromagnetic scattering," *Proc. IEEE*, vol. 81, no. 12, pp. 1658-1684, 1993.

[18] E. D. Constantinides and R.J. Marhefka, "An extended UTD analysis for RCS computations involving higher order curved surfaces", *Annales Des Telecommunications*, vol. 50, no. 5-6, pp. 474-486, May-June 1995.

[19] J. H. Meloling and R.J. Marh efka, "A caustic corrected UTD solution for the fields radiated by a source on a flat plate with a curved edge", *IEEE Trans. Antennas and Propagat.*, vol. AP-45, pp. 1839-1849, 1997.

[20] R.F. Harrington, *Field Computation by Moment Methods*, Kriegler Publishing Company, pp. 41-61, 1982.

[21] R.F. Harrington, *Time-Harmonic Electromagnetic Fields*, McGraw-Hill, p. 463, 1961.

[22] J.B. Keller, "Geometrical Theory of Diffraction", *J. Opt. Soc. Amer.*, vol. 52, pp. 116-130, 1962.

[23] A.J. Booysen, "On the equivalence of geometrical-optics reflected fields and the stationary-phase solution of the associated radiation integrals", *IEEE Antennas and Propagation Magazine*, Vol. 44, Issue 5, pp. 120-123, Oct. 2002.

[24] M. Abramovitz and I. A. Stegun, *Handbook of Mathematical Functions*, Dover Publications, 1965.

APPENDIX A

Equation (38) can be shown to reduce to (5) as follows. For widely separated stationary points, σ becomes large and we can use the large argument form of the Airy functions in (38). With (12) and [24]

$$Ai'(-x) \sim -\frac{1}{\sqrt{\pi}}\sigma^{\frac{1}{4}}\cos\left(\frac{2}{3}x^{\frac{3}{2}}+\frac{\pi}{4}\right) \tag{60}$$

substituted into (38), we obtain

$$\begin{aligned} I \sim & \sqrt{\frac{\pi}{k}}\left[F_1\sqrt{\frac{-2}{q_1}}+F_2\sqrt{\frac{2}{q_2}}\right]e^{ja_o k}\sin\alpha \\ & - j\sqrt{\frac{\pi}{k}}\left[F_1\sqrt{\frac{-2}{q_1}}-F_2\sqrt{\frac{2}{q_2}}\right]e^{ja_o k}\cos\alpha \ , \end{aligned} \tag{61}$$

where the shorthand notation $F_1 = F(t_{s1})$ and $q_1 = q''(t_{s1})$ was introduced for the sake of simplicity and

$$\alpha = \frac{2}{3}\sigma^{\frac{3}{2}}+\frac{\pi}{4} \ . \tag{62}$$

Rearranging (61), we obtain

$$\begin{aligned} I \sim & \ F_1\sqrt{\frac{-2\pi}{kq_1}}(\sin\alpha - j\cos\alpha)\, e^{ja_o k} \\ & + F_2\sqrt{\frac{+2\pi}{kq_2}}(\sin\alpha + j\cos\alpha)\, e^{ja_o k} \ . \end{aligned} \tag{63}$$

Equation (63) can be written as

$$\begin{aligned} I \sim & \ F_1\sqrt{\frac{-2\pi}{kq_1}}e^{-j\frac{\pi}{2}}e^{j\alpha}\, e^{ja_o k} \\ & + F_2\sqrt{\frac{+2\pi}{kq_2}}e^{j\frac{\pi}{2}}e^{-j\alpha}\, e^{ja_o k} \end{aligned} \tag{64}$$

which with the aid of (40) and (41) reduces to

$$I \sim F_1\sqrt{\frac{-2\pi}{kq_1}}e^{-j\frac{\pi}{4}}e^{jkq_1} + F_2\sqrt{\frac{2\pi}{kq_2}}e^{j\frac{\pi}{4}}e^{jkq_2} \ . \tag{65}$$

Equation (65) is identical to (5).

The isolated rays given by (42) and (43) can in similar fashion be shown to reduce to the first and second term s in (5), respectively. Only (42) will be discussed. The large argument forms of the Airy functions of the second type are [24]

$$Bi(-x) \sim \frac{1}{\sqrt{\pi}} x^{-\frac{1}{4}} \cos\left(\frac{2}{3}x^{\frac{3}{2}} + \frac{\pi}{4}\right) \tag{66}$$

and

$$Bi'(-x) \sim \frac{1}{\sqrt{\pi}} \sigma^{\frac{1}{4}} \sin\left(\frac{2}{3}x^{\frac{3}{2}} + \frac{\pi}{4}\right) \quad . \tag{67}$$

With (12), (60), (66) and (67) substituted into (42), we obtain

$$\begin{aligned} I \sim & \sqrt{\frac{\pi}{k}} \left[F_1 \sqrt{\frac{-2}{q_1}} + F_2 \sqrt{\frac{2}{q_2}}\right] e^{ja_o k} \\ & \times [+\sin\alpha + j\cos\alpha] \\ & + j\sqrt{\frac{\pi}{k}} \left[F_1 \sqrt{\frac{-2}{q_1}} - F_2 \sqrt{\frac{2}{q_2}}\right] e^{ja_o k} \\ & \times [-\cos\alpha + j\sin\alpha] \ , \end{aligned} \tag{68}$$

which upon further simplification yields (3).

APPENDIX B

Differentiation of

$$q(\theta) = -\sqrt{(R\cos\theta - x)^2 + (R\sin\theta - y)^2} - R\cos\theta \tag{69}$$

with respect to θ yields

$$\begin{aligned} q'(\theta) = & -[(R\cos\theta - x)^2 + (R\sin\theta - y)^2]^{-\frac{1}{2}} \\ & \times (xR\sin\theta - yR\cos\theta) + R\sin\theta . \end{aligned} \tag{70}$$

Further differentiation yields

$$\begin{aligned} q''(\theta) = & [(R\cos\theta - x)^2 + (R\sin\theta - y)^2]^{-\frac{3}{2}} \\ & \times (xR\sin\theta - yR\cos\theta)^2 \\ & - [(R\cos\theta - x)^2 + (R\sin\theta - y)^2]^{-\frac{1}{2}} \\ & \times (xR\cos\theta + yR\sin\theta) + R\cos\theta \end{aligned} \tag{71}$$

and differentiation once more

$$q'''(\theta) = -\frac{\partial A}{\partial \theta} - \frac{\partial B}{\partial \theta} - R\sin\theta \tag{72}$$

where

$$\begin{aligned} \frac{\partial A}{\partial \theta} = & 3[(R\cos\theta - x)^2 + (R\sin\theta - y)^2]^{-\frac{5}{2}} \\ & \times (xR\sin\theta - yR\cos\theta)^3 \\ & - 2[(R\cos\theta - x)^2 + (R\sin\theta - y)^2]^{-\frac{3}{2}} \\ & \times (xR\sin\theta - yR\cos\theta)(xR\cos\theta + yR\sin\theta) \end{aligned} \tag{73}$$

and

$$\begin{aligned} \frac{\partial B}{\partial \theta} = & -[(R\cos\theta - x)^2 + (R\sin\theta - y)^2]^{-\frac{3}{2}} \\ & \times (xR\sin\theta - yR\cos\theta) \\ & \times (xR\cos\theta + yR\sin\theta) \\ & + [(R\cos\theta - x)^2 + (R\sin\theta - y)^2]^{-\frac{1}{2}} \\ & \times (-xR\sin\theta + yR\cos\theta) \quad . \end{aligned} \tag{74}$$

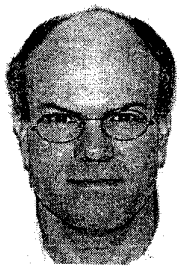

Adriaan (Riaan) J. Booysen was born in Pretoria, South Africa, on September 17, 1961. He received the BEng, MEng and PhD degrees in Electronic Engineering from the University of Pretoria in 1983, 1987 and 1991, respectively. He has been with the Antenna Division of Grintek TCI since August 1990, where he is responsible for the design and development of antennas for defence and commercial applications.

Dr. Booysen has a keen interest in the theoretical aspects of antenna engineering and has published a couple of technical papers in local and international antenna magazines.

NF–FF Transformation with Bi-Polar Scanning From Nonuniformly Spaced Data

F.Ferrara, C.Gennarelli, M.Iacone, G.Riccio
Dipartimento di Ingegneria dell'Informazione ed Ingegneria Elettrica
University of Salerno
via Ponte Don Melillo, I-84084 Fisciano (Salerno), Italy.
email: gennar@diiie.unisa.it

C.Savarese
Istituto di Teoria e Tecnica delle Onde Elettromagnetiche
University of Naples "Parthenope"
via Acton, 80133 Naples, Italy.
email: catello.savarese@uninav.it

ABSTRACT

An efficient probe compensated near-field–far-field transformation technique from irregularly spaced bi-polar samples is developed in this paper. The singular value decomposition method is applied to recover the uniformly distributed data, whose position is fixed by a nonredundant sampling representation of the electromagnetic field. Then an optimal sampling interpolation algorithm is used for reconstructing the plane-rectangular samples required to carry out the standard near-field–far-field transformation. This last step is required to benefit by the use of FFT algorithm. Numerical examples are reported to assess the effectiveness of the proposed technique.

1. INTRODUCTION

The method of constructing antenna radiation patterns from near-field (NF) measurements has been widely investigated in the last two decades and used for applications ranging from cellular phone antennas to large phased arrays and complex multi-beam communication satellite antennas. It has been proved to be an efficient and attractive alternative to conventional far-field (FF) range and compact range measurements. There are diverse methods for the FF evaluation depending on the ways data are acquired. Among them, that employing the bi-polar scanning [1-3] is particularly attractive for its mechanical characteristics. The antenna under test (AUT) rotates axially, whereas the probe is attached to the end of an arm which rotates around an axis parallel to the AUT one. This allows one to collect the NF data on a grid of concentric rings and radial arcs (see Fig. 1). The bi-polar scanning maintains all the advantages of the plane-polar one [4, 5] while providing a compact, simple and cost-effective measurement system. In fact, only rotational motions are required and this is convenient since rotating tables are more accurate than linear positioners. Moreover, since the arm is fixed at one point and the probe is attached at its end, the bending is constant and this allows one to hold the planarity.

An efficient probe compensated NF–FF transformation technique with bi-polar scanning has been developed in [3] by taking advantage of the nonredundant sampling representations of electromagnetic (EM) fields [6], properly extended to the probe voltage (the voltage measured by a nondirective probe has the same effective bandwidth of the field [7]). An optimal sampling interpolation (OSI) algorithm has been applied to recover the plane-rectangular data from the bi-polar ones, thus enabling the FFT use in the NF–FF transformation. Such a technique allows one to lower the number of needed NF data in a significant way with respect to the approach in [1, 2], without losing the efficiency.

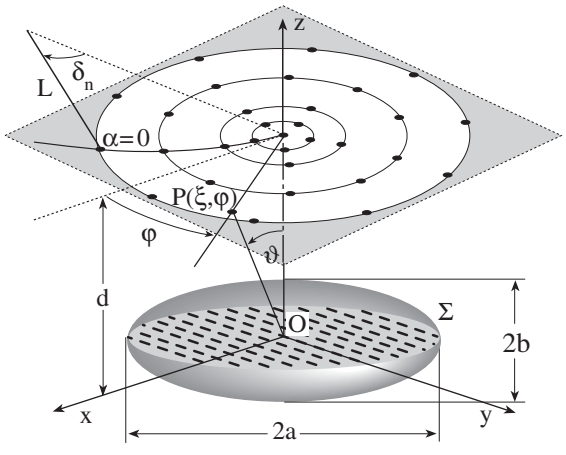

Fig. 1 - Geometry of the problem.

Unfortunately, due to an inaccurate control of the positioning systems, it may be practically impossible to get regularly spaced NF measurements. On the other hand, their position can be accurately read by optical devices. Moreover, the finite resolution of the positioning devices prevents the possibility to locate exactly the receiving probe at the points fixed by the sampling representation. According to these considerations, the development of an accurate and stable reconstruction process from the knowledge of nonuniformly distributed data becomes relevant. It must be stressed that, in this context, the formulas available in literature for the direct reconstruction from nonuniform samples are not user friendly, unstable and valid only for particular sampling points arrangements. A convenient strategy is to recover the uniform samples from those irregularly spaced and then determine the value at any point of the scanning surface by an accurate and stable OSI formula. In this framework, the approach proposed in [8, 9] is based on an iterative technique which has been found convergent only if it is possible to build a biunique correspondence, which associates at each uniform sampling point the nearest nonuniform one. With reference to the field reconstruction on a plane, this restriction has been overcome in [10] by developing an approach based on the use of the singular value decomposition (SVD) method [11] for reconstructing the uniform plane-polar data. This latter approach is preferable to that based on the iterative technique, since it is more flexible and allows one to take advantage of data redundancy for increasing the algorithm stability [10].

The aim of this paper is just the extension of the NF–FF transformation technique with bi-polar scanning developed in [3] to the case of irregularly spaced NF data.

2. THEORETICAL BACKGROUND

A point on the scanning plane can be specified by the bi-polar coordinate system using the AUT angle α, the angle δ and the arm length L (see Fig. 1). The polar coordinates ρ, φ are related to them by the following relations:

$$\rho = 2L\sin(\delta/2)\ ; \qquad \varphi = \alpha - \delta/2\ . \tag{1}$$

To cover the circular scanning region with a bi-polar scanner, the probe passes from one acquisition ring to another by travelling along the arc described by the end of the arm. During this movement, the AUT stays fixed. Once the probe is located on the ring to be considered, the AUT rotation allows one to perform the data acquisition at the sampling points. The choice of the distance from one ring to another and the angular sampling rate on them can be fixed according to a nonredundant sampling representation, which uses radial lines instead of radial arcs, thus remarkably reducing the number of rings and sampling points on them as shown in [3]. Moreover, if the AUT is quasi-planar, an effective source modelling [6] is obtained by choosing the surface Σ enclosing it coincident with the smallest oblate ellipsoid having major and minor semi-axes equal to a and b (see Fig. 1). Note that, because of the rotational movement of the scanner arm, the positions of the samples on the n-th ring are shifted by $\varphi_0(\xi_n) = -\delta_n/2$ with respect to the corresponding ones in the plane-polar grid.

According to [6], when considering an observation curve C described by an analytical parameterization $\underline{r} = \underline{r}(\xi)$, the "reduced electric field"

$$\underline{F}(\xi) = \underline{E}(\xi)\ e^{j\gamma(\xi)}\ , \tag{2}$$

$\gamma(\xi)$ being a phase function to be determined, can be closely approximated by a spatially bandlimited function. For electrically large antennas, the bandlimitation error becomes negligible as the bandwidth exceeds a critical value W_ξ and can be effectively controlled by choosing a bandwidth equal to $\chi' W_\xi$, $\chi' > 1$ being an excess bandwidth factor. When considering a radial line, by adopting $W_\xi = \beta\ell'/2\pi$ (β being the wavenumber and ℓ' the length of the ellipse C', intersection curve between Σ and the meridian plane), we get:

$$\gamma = \beta a\left[v\sqrt{\frac{v^2-1}{v^2-\varepsilon^2}} - E\left(\cos^{-1}\sqrt{\frac{1-\varepsilon^2}{v^2-\varepsilon^2}}\,\middle|\,\varepsilon^2\right)\right] \tag{3}$$

$$\xi = (\pi/2)\left[E\left(\sin^{-1}u\,\middle|\,\varepsilon^2\right)\Big/E\left(\pi/2\,\middle|\,\varepsilon^2\right)\right] \tag{4}$$

where $E(\cdot\,|\,\cdot)$ denotes the elliptic integral of the second kind [12], $\varepsilon = f/a$ is the eccentricity of C', f is its focal distance, $u = (r_1 - r_2)/2f$, $v = (r_1 + r_2)/2a$ are the elliptic coordinates, $r_{1,2}$ being the distances from the observation point P to the foci of C'. Moreover, $\sin^{-1}u = \vartheta_\infty$, ϑ_∞ being the polar angle of the asymptote to the hyperbola through P.

When the observation curve is a ring, it is convenient to utilize the azimuthal angle φ as parameter and the corresponding bandwidth

$$W_\varphi(\xi) = \beta\, a \sin\vartheta_\infty(\xi). \tag{5}$$

By taking into account that the voltage measured by a nondirective probe has the same effective bandwidth of the field, the above theoretical results hold also for the probe voltage and then the "reduced voltage" $\tilde{V}$ at the point (ξ,φ) on the radial line fixed by φ can be evaluated via the OSI expansion:

$$\tilde{V}(\xi,\varphi) = \sum_{n=n_0-p+1}^{n_0+p} \tilde{V}(\xi_n,\varphi)\, \Omega_N(\xi-\xi_n)\, D_{N''}(\xi-\xi_n) \tag{6}$$

where $n_0 = \mathrm{Int}(\xi/\Delta\xi)$, $2p$ is the number of retained samples and

$$\xi_n = n\Delta\xi = \frac{2n\pi}{2N''+1}\ ; \qquad N'' = \mathrm{Int}(\chi\, N') + 1 \tag{7}$$

$$N' = \mathrm{Int}(\chi' W_\xi) + 1\ ; \qquad N = N'' - N' \tag{8}$$

$\chi > 1$ being an oversampling factor needed to control the truncation error. Moreover,

$$D_{N''}(\xi) = \frac{\sin\left[(2N''+1)\,\xi/2\right]}{(2N''+1)\sin(\xi/2)} \tag{9}$$

$$\Omega_N(\xi) = \frac{T_N\left[2\left(\cos(\xi/2)/\cos(\xi_0/2)\right)^2 - 1\right]}{T_N\left[2/\cos^2(\xi_0/2) - 1\right]} \tag{10}$$

are the Dirichlet and Tschebyscheff Sampling (TS) functions, respectively, $T_N(\cdot)$ is the Tschebyscheff polynomial of degree N, and $\xi_0 = p\Delta\xi$.
The intermediate samples $\tilde{V}(\xi_n,\varphi)$ are given by:

$$\tilde{V}(\xi_n,\varphi) = \sum_{m=m_0-q+1}^{m_0+q} \tilde{V}(\xi_n,\varphi_{m,n})\, \Omega_{M_n}(\varphi-\varphi_{m,n})\, D_{M_n''}(\varphi-\varphi_{m,n}) \tag{11}$$

where $\tilde{V}(\xi_n,\varphi_{m,n})$ are the uniformly spaced samples on the ring specified by ξ_n, $2q$ is the number of retained samples along φ, $m_0 = \mathrm{Int}((\varphi-\varphi_0(\xi_n))/\Delta\varphi_n)$ and

$$\varphi_{m,n} = \varphi_0(\xi_n) + m\Delta\varphi_n = \varphi_0(\xi_n) + \frac{2m\pi}{2M_n''+1} \tag{12}$$

$$M_n'' = \mathrm{Int}(\chi M_n')+1\,; \qquad M_n' = \mathrm{Int}(\chi^* W_{\varphi_n})+1 \tag{13}$$

$$M_n = M_n'' - M_n'\,; \quad \chi^* = 1 + (\chi'-1)\left[\sin\vartheta_\infty(\xi)\right]^{-2/3}. \tag{14}$$

The basic theory of the classical probe compensated NF measurements on a plane as proposed in [13] is based on the application of the Lorentz reciprocity theorem. According to such a theory, the AUT far-field components are related to: i) the two-dimensional Fourier transforms of the output voltages V_V and V_H of the probe for two independent sets of measurements (the probe is rotated by 90° in the second set); ii) the far-field components radiated by the probe and the rotated probe, when used as transmitting antennas. The key relations in the reference system used in the present work are explicitly reported in [3, 10]. However, these equations are valid whenever the probe maintains its orientation with respect to the AUT and this requires its co-rotation with the AUT. Obviously, the scanning equipment is remarkably simplified when this is avoided. Probes exhibiting only a first-order azimuthal dependence in their radiated far-field (f.i., an open-ended cylindrical waveguide excited by a TE_{11} mode) can be used without co-rotation, since V_V and V_H can be evaluated from the measured voltages V_φ and V_ρ, through simple trigonometric relations [3].
According to the above considerations, an efficient probe compensated NF–FF transformation from a nonredundant number of bi-polar data is achieved by recovering the values of V_V and V_H in the plane-rectangular grid needed to perform the described NF–FF transformation.

3. NF DATA RECONSTRUCTION FROM NONUNIFORM SAMPLES

Let us now assume that, apart from the sample at the origin of the coordinate system on the scan plane, the irregularly distributed samples lie on $K \geq N_{us}$ nonuniformly spaced rings (see Fig. 2), where N_{us} is the number of the rings uniformly spaced according to the nonredundant sampling representation considered in the previous section. This hypothesis can represent the spatial distribution of the NF measurements. In fact, since the scanning procedure fixes each ring by means of a rotational movement of the arm and collects the data on it by rotating the AUT, errors can occur on the ring location and on the position of the samples on it. As a consequence, the starting two-dimensional problem is reduced to find the solution of two independent one-dimensional problems. In this frame-work, let us assume to know the probe voltage at

$J \geq 2M_k'' + 1$ nonuniform sampling points $(\bar{\xi}_k, \bar{\varphi}_j)$ on the nonuniform ring having radius $\rho(\xi_k)$. The corresponding reduced voltage at each nonuniform sampling point can be expressed via the OSI expansion (11), so obtaining the linear system

$$\tilde{V}\left(\bar{\xi}_k, \bar{\varphi}_j\right) = \sum_{m=m_0-q+1}^{m_0+q} \tilde{V}\left(\bar{\xi}_k, \varphi_{m,k}\right) \Omega_{M_k}\left(\bar{\varphi}_j - \varphi_{m,k}\right) D_{M_k''}\left(\bar{\varphi}_j - \varphi_{m,k}\right) \qquad j = 1,...,J \tag{15}$$

It can be rewritten in matrix form as

$$\underline{\underline{A}}\ \underline{x} = \underline{b}, \tag{16}$$

where $\underline{b}$ is the sequence of the known nonuniform samples, $\underline{x}$ is the sequence of the unknown uniformly distributed samples, and $\underline{\underline{A}}$ is the $J \times (2M_k'' + 1)$ matrix, whose elements are given by the weight functions in the considered OSI expansion:

$$a_{jm} = \Omega_{M_k}\left(\bar{\varphi}_j - \varphi_{m,k}\right) D_{M_k''}\left(\bar{\varphi}_j - \varphi_{m,k}\right) . \tag{17}$$

It is useful to note that, for a fixed row j, these elements are equal to zero if the index m is out of the range $[m_0(\bar{\xi}_k, \bar{\varphi}_j) - q + 1,\ m_0(\bar{\xi}_k, \bar{\varphi}_j) + q]$. The best approximated solution (in the least squares sense) of the overdetermined linear system (16) is obtained by using the SVD algorithm.

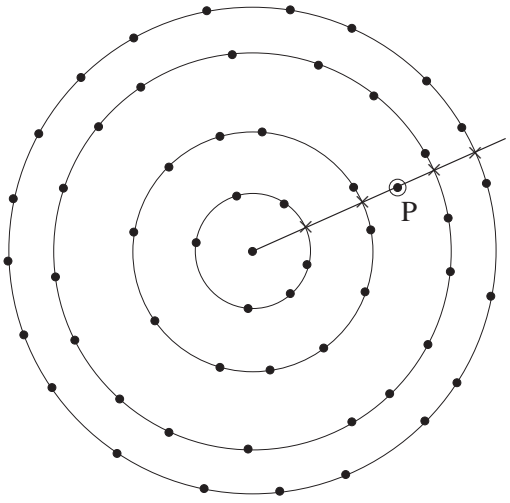

Fig. 2 - Distribution of nonuniform samples.

Let us now tackle the problem of evaluating the probe voltage at a generic point $P(\xi, \varphi)$ on the plane from the knowledge of the recovered uniform samples on the irregularly spaced rings. To this end, the OSI expansion (11) can be employed to determine the intermediate samples $\tilde{V}\left(\bar{\xi}_k, \varphi\right)$ (crosses in Fig. 2) on the radial line through P. Since the intermediate samples are nonuniformly distributed on the considered radial line, the voltage at P can be found in analogous way by recovering the regularly spaced intermediate samples again via SVD and then interpolating them via the OSI expansion (6). The overdetermined linear system to be considered is now:

$$\tilde{V}\left(\bar{\xi}_k, \varphi\right) = \sum_{n=n_0-p+1}^{n_0+p} \tilde{V}\left(\xi_n, \varphi\right) \Omega_N\left(\bar{\xi}_k - \xi_n\right) D_{N''}\left(\bar{\xi}_k - \xi_n\right) \qquad k = 1,...,K \tag{18}$$

which can be expressed in matrix form as (15).

It must be stressed that, in order to minimize the computational effort for computing the plane-rectangular data needed to perform the probe compensated NF–FF transformation described in the previous paragraph, it is convenient to determine on each ring the same number N_φ of uniform samples with plane-polar distribution. This number is fixed according to the sampling rate on the outer ring. In such a way, although the so recovered NF data are redundant in φ, the number of SVD on the radial lines is minimized since these samples are radially aligned. It is worthy to note that the overall number of SVD required to recover these samples is $K + N_\varphi$. Once these latter have been determined, the plane-rectangular data can be evaluated by using the corresponding OSI expansion in [5].

4. NUMERICAL RESULTS

The validity of the developed technique has been assessed by many numerical tests. The following simulations refer to the field radiated by a uniform planar circular array having diameter equal to 33.6 λ, λ being the wavelength. Its elements, symmetrically placed with respect to the plane $y = 0$, are elementary Huygens sources linearly polarized along the y axis and are radially and azimuthally spaced at 0.7λ. Accordingly, this antenna can be modelled as enclosed in an oblate ellipsoid having a = 17 λ and b = 2.2 λ. An open-ended cylindrical waveguide with radius equal

to 0.338 λ is considered as measurement probe. The scanning plane is 20 λ away from the AUT center and the bi-polar measurement system is characterized by L = 80 λ and $\delta_{max} \approx 53°$, so that the NF data lie in a circular zone of radius $\approx 72\,\lambda$. The nonuniform samples have been generated by imposing that the distances along ξ and φ between the position of each nonuniform sample and the associate uniform one are random variables uniformly distributed in $[-\Delta\xi/4, \Delta\xi/4]$ and $[-\Delta\varphi_n/2, \Delta\varphi_n/2]$. It must be stressed that this is a very pessimistic occurrence in a real scanning system.

The process for recovering V_V and V_H from the nonuniformly distributed bi-polar samples of V_φ and V_ρ has yielded fast and accurate results. Figure 3 shows a representative reconstruction example of V_V on the radial line at φ = 90°. As can be seen, there is an excellent agreement between the exact and the reconstructed probe voltage save for the peripheral region, where an unavoidable truncation error occurs due to the lack of needed guard samples. The algorithm performances have been assessed in a more quantitative way by evaluating the maximum and mean-square errors occurring in the reconstruction of the uniform plane-polar samples of V_V. These errors (see Figs. 4 and 5) are normalized to the voltage maximum value on the plane and have been obtained by comparing the aforementioned reconstructed uniform samples and the exact ones. Note that this comparison has been made in the central zone of the scanning plane, so that the existence of the required guard samples is assured. Obviously, even better results are to be expected when the nonuniform samples are closer to the uniform ones.

The stability of the algorithm has been investigated by adding random errors to the exact data. Both a background noise (bounded to Δa in amplitude and with arbitrary phase) and uncertainties on the data of $\pm\Delta a_r$ in amplitude and ±Δφ in phase have been simulated. As shown in Fig. 6, the algorithm is stable. In any case, it is possible to take advantage of the data redundancy for improving the stability (see Fig. 7).

The developed algorithm has been employed to determine in a fast and accurate way the plane-rectangular data required for the probe compensated NF–FF transformation [13]. The E-plane pattern, reconstructed from the recovered plane-rectangular data lying in a 100λ×100λ square grid, is shown (crosses) in Fig. 8. The pattern reconstructed (via the uncompensated NF–FF transformation) from the exact plane-rectangular field samples lying in the same grid is also reported as reference (solid line). As can be seen the FF reconstruction is very accurate, thus assessing the effectiveness of the proposed technique.

A further example of simulated NF–FF transformation from nonuniformly distributed bi-polar data is shown in Fig. 9. It refers to an AUT obtained from the previously considered array by changing the excitations of its elements in order to obtain a Tschebyscheff-like behaviour with sidelobe ratio (SLR) = 40 dB in the FF region. Also in this case the FF reconstruction is resulted to be very accurate.

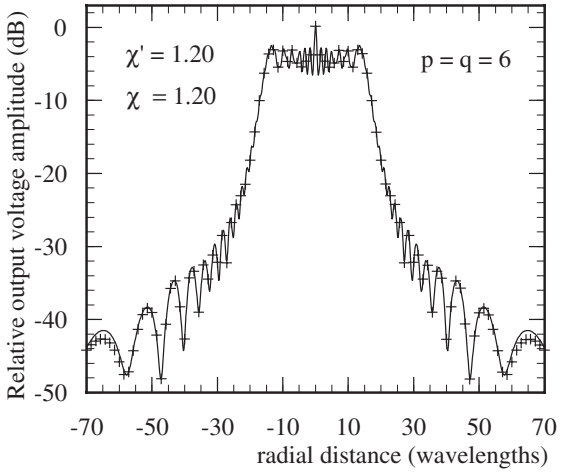

Fig. 3 - Amplitude of the probe output voltage V_V on the radial line at φ = 90°. Solid line: exact. Crosses: reconstructed from nonuniform samples.

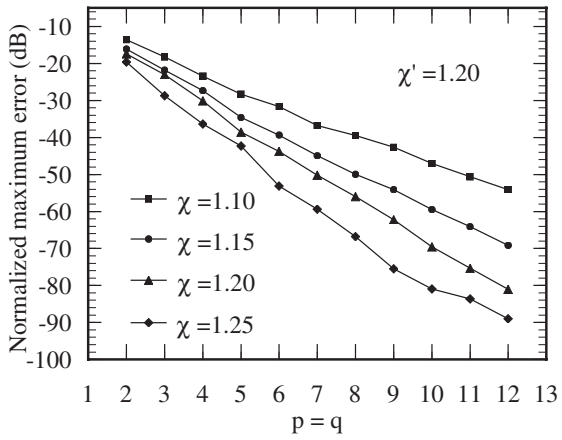

Fig. 4 - Normalized maximum error in the reconstruction of the uniform plane-polar samples relevant to the probe output voltage V_V.

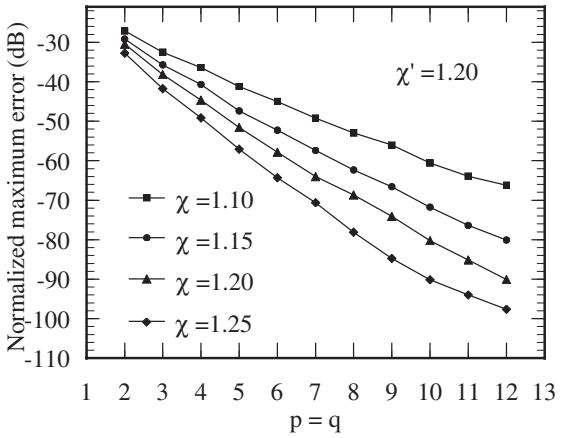

Fig. 5 - Normalized mean-square error in the reconstruction of the uniform plane-polar samples relevant to the probe output voltage V_V.

5. CONCLUSIONS

The problem of an efficient AUT pattern reconstruction from the knowledge of irregularly spaced bi-polar data has been tackled and solved in this work. The developed method takes advantage of a nonredundant sampling representation of the probe voltage and of the use of the corresponding OSI expansion for interpolating the samples. This has allowed the building of linear systems whose best solution in least squares sense has been obtained by applying the SVD technique. The reconstruction process has yielded accurate and stable results even in presence of very large position errors.

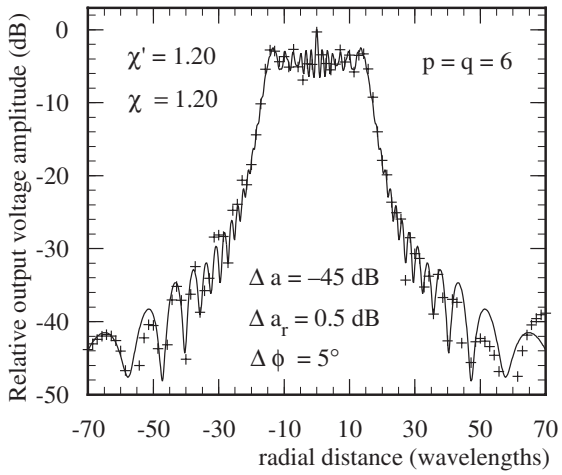

Fig. 6 - Amplitude of the probe output voltage V_V on the radial line at $\varphi = 90°$. Solid line: exact. Crosses: reconstructed from error affected nonuniform samples.

REFERENCES

[1] L. I. Williams, Y. Rahmat-Samii, and R. G. Yaccarino, "The bi-polar planar near-field measurement technique, Part I: implementation and measurement comparisons," *IEEE Trans. Antennas Propagat.,* vol. 42, pp.184-195, February 1994.

[2] R. G. Yaccarino, Y. Rahmat-Samii, and L. I. Williams, "The bi-polar near-field measurement technique, Part II: NF to FF transformation and holographic methods," *IEEE Trans. Antennas Propagat.*, vol. 42, pp.196-204, February 1994.

[3] F. D'Agostino, C. Gennarelli, G. Riccio, and C. Savarese, "Data reduction in the NF-FF transformation with bi-polar scanning," *Microwave Optical Tech. Lett.,* vol. 36 pp. 32-36, January 2003.

[4] M.Gatti and Y.Rahmat-Samii, "FFT applications to plane-polar near-field antenna measurements," *IEEE Trans. Antennas Propagat.,* vol. AP-36, pp. 781-791, June 1988.

[5] O. M. Bucci, F. D'Agostino, C. Gennarelli, G. Riccio, and C. Savarese, "NF–FF transformation with plane-polar scanning: ellipsoidal modelling of the antenna," *Automatika,* vol. 41, pp. 159-164, 2000.

[6] O. M. Bucci, C. Gennarelli, and C. Savarese, "Representation of electromagnetic fields over arbitrary surfaces by a finite and nonredundant number of samples," *IEEE Trans. Antennas Propagat.*, vol. 46, pp. 351-359, March 1998.

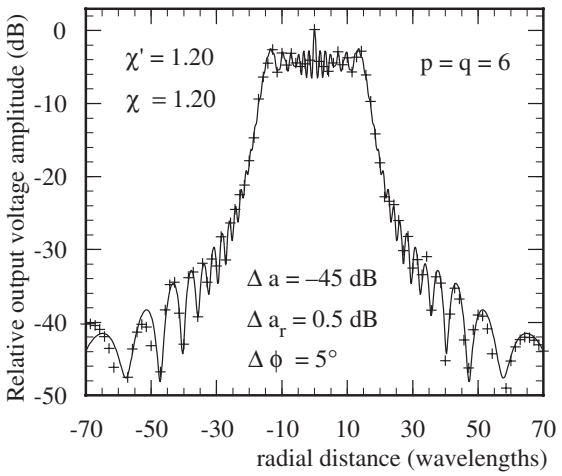

Fig. 7 - Amplitude of the probe output voltage V_V on the radial line at $\varphi = 90°$. Solid line: exact. Crosses: reconstructed from error affected nonuniform samples (increased by 20%).

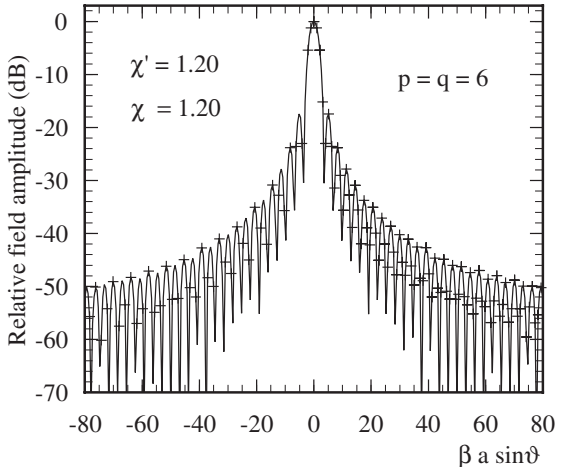

Fig. 8 - FF pattern in the E-plane. Solid line: reference. Crosses: reconstructed from probe compensated nonuniform NF measurements.

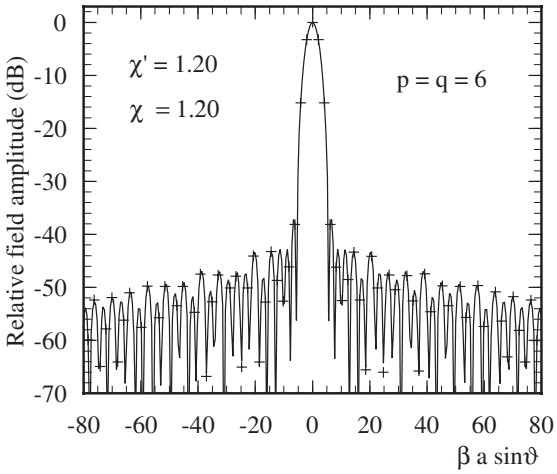

Fig. 9 - FF pattern in the E-plane of a Tschebyscheff-like planar circular array. Solid line: reference. Crosses: reconstructed from probe compensated nonuniform NF measurements.

[7] O. M. Bucci, G. D'Elia, and M. D. Migliore, "Advanced field interpolation from plane-polar samples: experimental verification," *IEEE Trans. Antennas Propagat.,* vol. 46, pp. 204-210, February 1998.

[8] O. M. Bucci, C. Gennarelli, and C. Savarese, "Interpolation of electromagnetic radiated fields over a plane from nonuniform samples," *IEEE Trans. Antennas Propagat.,* vol. AP-41, pp. 1501-1508, November 1993.

[9] O. M. Bucci, C. Gennarelli, G. Riccio, and C. Savarese, "Electromagnetic fields interpolation from nonuniform samples over spherical and cylindrical surfaces," *IEE Proc. Microw. Antennas Propagat.,* vol. 141, pp. 77-84, April 1994.

[10] F. Ferrara, C. Gennarelli, G. Riccio, and C. Savarese, "Far field reconstruction from nonuniform plane-polar data: a SVD based approach," *Electromagnetics,* vol. 23, pp. 417-429, July 2003.

[11] G. H. Golub and C. F. Van Loan, *Matrix computation.* Baltimore: J.Hopkins University Press, 1996.

[12] M. Abramowitz and I. Stegun. *Handbook of mathematical functions*. New York: Dover, 1965.

[13] D. T. Paris, W. M. Leach, Jr., and E. B. Joy, "Basic theory of probe-compensated near-field measurements," *IEEE Trans. Antennas Propagat.,* vol. AP-26, pp. 373-379, May 1978.

Flaminio Ferrara was born near Salerno, Italy, in 1972. He received the Laurea degree in electronic engineering from the University of Salerno in 1999. Since the same year he has been with the Research Group in Applied Electromagnetics at the University of Salerno. He received the Ph.D. degree in Information Engineering at the same University, where he is actually an Assistant Professor of Electromagnetics Fields. His interests include: application of sampling techniques to the efficient reconstruction of electromagnetic fields; monostatic radar cross section evaluations of corner reflectors.

Claudio Gennarelli was born in Avellino, Italy, in 1953. He received the Laurea degree (summa cum laude) in electronic engineering from the University of Naples, Italy, in 1978. From 1978 to 1983 he worked with the Research Group in Electromagnetics at the Electronic Engineering Department of the University "Federico II" of Naples. In 1983 he

became a Research Engineer at IUN, Naples. In 1987 he was appointed Associate Professor of Antennas, formerly at the Engineering Faculty of Ancona University and subsequently at the Engineering Faculty of Salerno University. In 1999 he has been appointed Full Professor at the same University. The main topics of his scientific activity are: reflector antennas analysis, diffraction problems, radar cross section evaluations, scattering from surface impedances, application of sampling techniques to electromagnetics and to near-field far-field transformations. Dr. Gennarelli is co-author of about 200 scientific papers, mainly in international journals and conference proceedings. He is a Senior Member of the IEEE.

Marcello Iacone was born near Naples, Italy, in 1975. He received the Laurea degree in computer science engineering from the University of Naples in 2000. From 2001 he worked with the Research Group in Electromagnetics at the Department of Electrical and Information Engineering of the University of Salerno. Currently he is a Ph.D. student at the same University. His current research interests are in the areas of electromagnetic fields, near-field far-field measurement techniques, and computer algorithms.

Giovanni Riccio received the Laurea degree in electronic engineering from the University of Salerno, in 1992. Since the same year he has been with the Research Group in Applied Electromagnetics at the University of Salerno. In 1995 he became Assistant Professor at the same University, where he is presently Associate Professor of Electromagnetics Fields. His interests include: application of sampling techniques to the efficient recovery of electromagnetic fields and to near-field far-field transformation techniques, radar cross section evaluations of corner reflectors, scattering from penetrable and nonpenetrable structures. Dr. Riccio is co-author of about 150 scientific papers, mainly in international journals and conference proceedings. He is a Member of the IEEE Society, the Applied Computational Electromagnetics Society, and the Electromagnetics Academy.

Catello Savarese was born in Naples, Italy, in 1941. He received the Laurea degree (summa cum laude) in electronic engineering from the University of Naples in 1967. Since 1970 he worked with the research group in electromagnetics at the Naples University and at IUN, Naples. In 1976 he was appointed an Assistant Professor of Theory and Techniques of Electromagnetic Waves at IUN and in the same year became Associate Professor of Electromagnetics Fields at the University of Naples. Since 1986 he has been appointed Full Professor of Antennas and Radiowaves Propagation at IUN. His scientific activity deals with electromagnetic properties of material media; antennas in dispersive media; surface impedance loaded reflector antennas; microwave antennas analysis; representation of radiated electromagnetic fields and near-field far-field measurement techniques. Dr. Savarese is Member of the Electromagnetics Academy and a Senior Member of the IEEE.

Electromagnetic Modeling of an Adaptable Multimode Microwave Applicator for Polymer Processing

Rensheng Sun[1], Leo C. Kempel[1], Liming Zong[2], Shuangjie Zhou[2], Martin C. Hawley[2]
[1] Department of Electrical and Computer Engineering, Michigan State University
[2] Department of Chemical Engineering and Materials Science, Michigan State University
East Lansing, MI 48824, USA
E-mail: sunrensh@egr.msu.edu

***Abstract*—This paper presents the electromagnetic modeling of a novel adaptable multi-feed multimode cylindrical cavity applicator where the spatial distribution of the electric field can be specified *a priori* to accomplish a desired processing task. The electric field intensity inside the cavity can be tailored by just varying the power delivered to each port, and the mode-switching can be realized without mechanically adjusting the cavity dimensions. An orthogonal feeding mechanism is developed to reduce the cross coupling between the ports. Numerical simulations are performed for the cavity applicator to verify the theoretical analysis.**

***Index Terms*—Electromagnetic modeling, adaptable multimode applicator, orthogonal feeding.**

I. INTRODUCTION

MICROWAVES have been investigated as an attractive and efficient alternative energy source compared to inefficient pressurized ovens for material processing, including polymers and composites. The observed advantages are volumetric heating, direct and fast heating, high selectivity, and high controllability. Results have been reported on enhanced polymerization rates [1-2], increased glass transition temperatures of cured epoxy [1], improved interfacial bonding between graphite fibers and the polymer matrix [3], and increased mechanical properties of the composites [4]. However, industrial use of microwave processing has been impeded by the lack of proper applicator design, modeling, and control/monitoring methods. Most existing applicators are for specific applications only and the applicator design has to be performed over and over again for new processes, mostly by trial and error without the assistance of a model. The development of adaptable applicators, which can be configured to accomplish a variety of processing tasks, is therefore very important.

Commonly used applicators for materials processing can be classified into three basic types: waveguide, multimode and single-mode applicators. A waveguide applicator is a hollow conducting pipe with either a rectangular or a circular cross-section. The wave inside a waveguide applicator is fundamentally different from that inside multimode and single-mode applicator. The former is a traveling wave and the latter is a standing wave. Energy from the microwave generator travels through the waveguide and is partially absorbed by the material being processed. The remainder of the energy is directed to a terminating load. Traveling wave applicators are primarily used for continuous processing of high-loss materials; low-loss materials require an excessively long waveguide or a long processing period to absorb the necessary energy.

The most popular applicator type is the overmoded or multimode cavity where the electric field distribution is given by the sum of all the modes excited at a particular frequency. The frequent use of multimode cavity applicators is a result of their low cost, simplicity of construction, and adaptability to many different heating loads. This kind of applicator is very versatile in that it can accept a wide range of material loads of different dielectric losses, size and shape [5]. However, that may limit product quality, particularly with regard to the uniformity of temperature distribution in processed materials. Difficulties for multimode cavity analysis of electric field distributions result essentially from coexistence of many resonant modes. By rotating the sample and/or using metal stirrers, it is possible to improve the E-field uniformity and, thus, the heating uniformity inside the multimode applicator [6]. The mode-stirrer is a fan within a multimode cavity designed to change the resonance of multiple modes within a 4 MHz band near 2.45 GHz. As the mode-stirrer rotates, the resonant conditions of the cavity change, focusing the energy into different field patterns. The rotation of the fan cycles the cavity through the different resonant modes with a pattern that accepts whatever random heating occurs across the sample. This may improve the heating uniformity to a certain degree, but makes it more difficult to predict the electric field distribution and not suitable for precision material processing.

The single-mode resonant applicator is designed to support only one resonant mode, therefore resulting in highly localized heating. These applicators can efficiently provide high field strength at mode-specific locations within the cavity since single frequency systems can be tuned for maximum throughput. Although single-mode applicators have a high efficiency relative to multimode and traveling wave applicators, sometimes it is very difficult for them to provide desired uniform heating across a large sample. To obtain uniform heating under these conditions, a technique called mode-switching was developed, in which several modes with complementary heating patterns are alternatively excited [7].

With a fixed frequency microwave power source, mode-switching can be achieved by mechanically adjusting the length of the cavity. This mechanical process slows the response of the system to temperature changes. With a variable frequency power source, modes can be changed by changing frequency. As a result of the instantaneous variable frequency mode switching, not only the speed of the process but also the controllability of the process is much improved [8]. However, variable frequency sources are inherently less efficient than the single frequency versions; the equipment is also very expensive. In our research effort, mode-switching can be obtained by varying the power delivered to multiple ports, hence eliminating the need for mechanical applicator adjustments.

In this case, we can tailor the field intensity to achieve high field strength in the regions of the applicator requiring high fields (and hence regions where heating is desirable) and low field intensities in regions where heating is not desired. We will explore multi-port multi-feed applicators where the field spatial distribution can be specified *a priori* to accomplish a desired processing task. Single frequency operation is preferred since the over-all system efficiency is generally higher for such "tuned" systems.

Specifically, in our modeling, we are exciting a cylindrical cavity via two ports to get a TM mode and a TE mode simultaneously. With these separately controllable TM and TE modes, we not only get desired field strength distribution at specific locations inside the cavity, but also have the ability to heat along a preferred direction; this is particularly useful when anisotropic materials are processed. Taking advantages of TM and TE modes, it is easy for us to get low port-to-port coupling, especially when a lossy load is present. This will be shown later in both theoretical analysis and numerical results.

II. Adaptable Multimode Applicator

Inside a circular cylindrical cavity, the resonant frequencies for TE and TM modes as functions of cavity height h and radius a can be expressed as [9]:

$$(f)_{npq}^{TE} = \frac{1}{2\pi a\sqrt{\mu\varepsilon}}\sqrt{x'_{np}{}^{2} + \left(\frac{q\pi a}{h}\right)^{2}} \tag{1}$$

$$(f)_{npq}^{TM} = \frac{1}{2\pi a\sqrt{\mu\varepsilon}}\sqrt{x_{np}{}^{2} + \left(\frac{q\pi a}{h}\right)^{2}} \tag{2}$$

where x_{np} and x'_{np} are tabulated zeros of the Bessel's function and the derivative of the Bessel's function, respectively. Resonant frequency f can be plotted as a function of cavity length in a mode diagram for a fixed radius, as shown in Fig. 1.

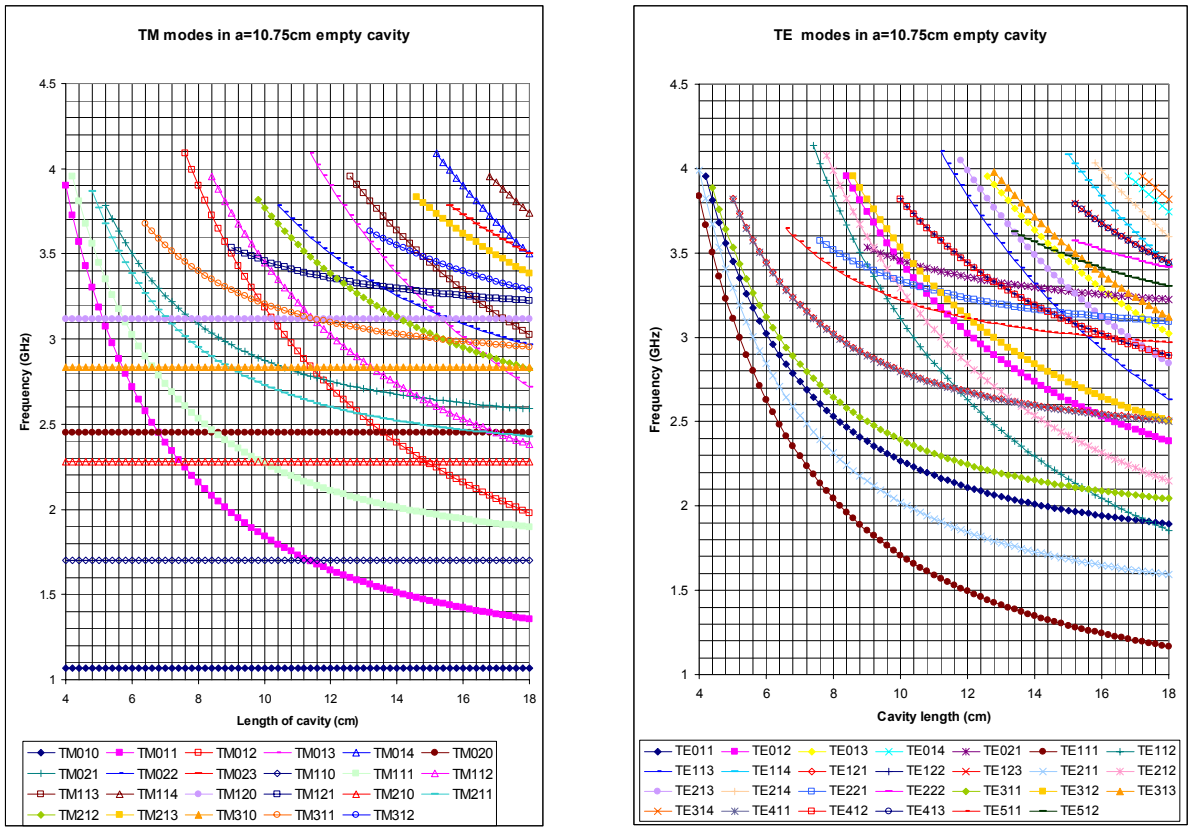

Figure 1. Mode diagrams for a circular cylinder (TM: left, TE: right).

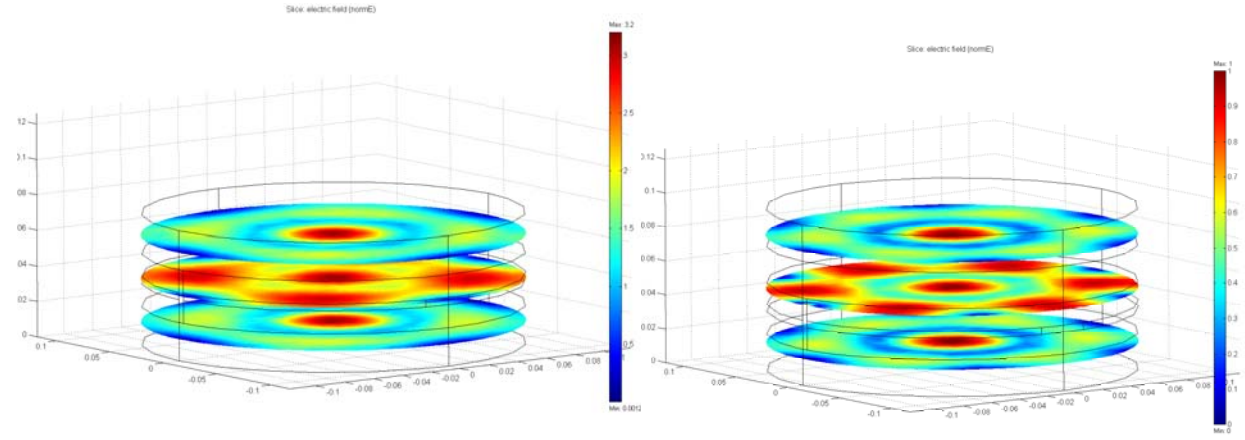

(a) $TM_{020} + TE_{211}$ (b) $TM_{020} + TE_{311}$

Figure 2. Electric field distributions for different combination of TM and TE modes.

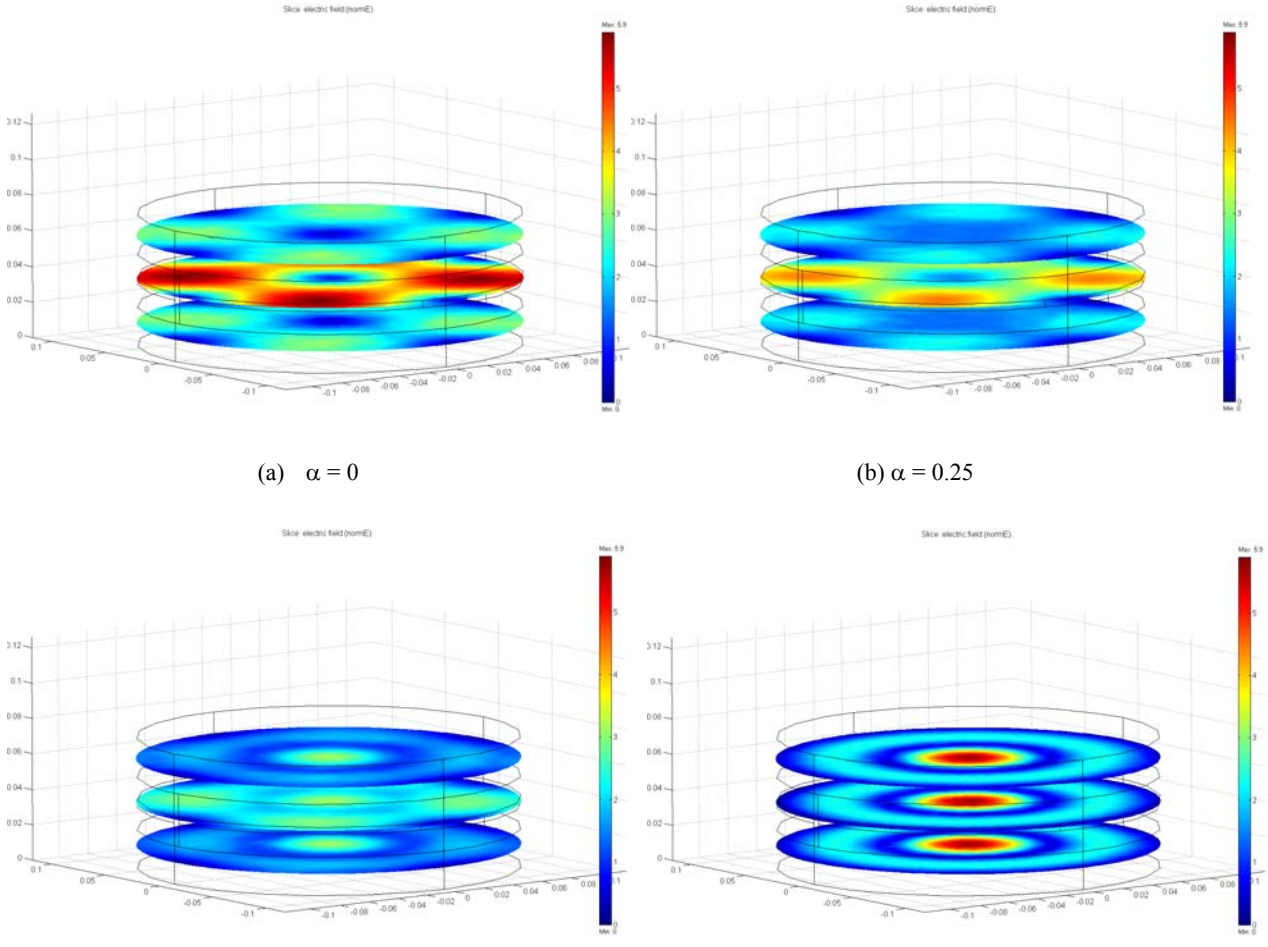

(a) $\alpha = 0$ (b) $\alpha = 0.25$

(c) $\alpha = 0.55$ (d) $\alpha = 1$

Figure 3. Parametric study on the weighting factor α for the combination of the two modes.

Typically, inside the cavity, TM modes are excited with a coaxial probe while TE modes are excited with sidewall-mounted loops. Although these are useful methods for feeding, they may not lead to sufficient decoupling of the two ports. If the feeds are ideally orthogonal, the mutual coupling between ports is zero (e.g. $S_{21} = 0 = S_{12}$). This is a desirable condition since a non-zero transmission term indicates that

power from one port will exit the cavity through the other port doing no significant heating of the polymer. Our cavity design has two feed ports. The feed mechanism chosen, to minimize mode cross-coupling, are an axial slot (to excite a TE mode) and an azimuthal slot (to excite a TM mode). These slots are electrically very narrow to avoid mode cross-coupling.

By observing the mode diagrams, it is seen that when the cavity height is adjusted, we can have different combinations of TM and TE modes resonant at 2.45 GHz, and thus get different electric field distribution inside the cavity. When the radius a = 10.75 cm and height h = 7.34 cm, we can get the combination of TM_{020} and TE_{211}, which is shown in Fig. 2(a); while a = 10.75 cm and h = 9.50 cm, the combination of TM_{020} and TE_{311} is shown in Fig. 2(b). For both cases, we have an axisymmetric electric field pattern (TM_{020}) at the center as well as some distributed spots (TE_{211} or TE_{311}) around it. TM mode has the electric fields along the central axis of the cylinder, which is best suited for heating rods and cylinders located along the axis of the cylinder; TE mode has the electric fields parallel to the bottom plate of the applicator, which is best suited for heating flat panels or disks.

For each combination of TM and TE mode with fixed cavity height, by varying the power delivered to each port, mode-switching can be obtained at a single frequency without mechanically adjustment of the cavity dimensions. This transition can be shown in Fig. 3 for the combination of TM_{020} and TE_{211} case. To investigate the curing field for simultaneous mode excitation, a parameter α is introduced. A pure TE mode excitation has $\alpha = 0$ while a pure TM mode excitation is given by $\alpha = 1$. The cavity model was verified for these two cases using the appropriate slot excitation methods. The numerical simulations using COMSOL's FEMLAB code [10] were performed for different α, which means different relative power delivered to each port. Fig. 3 illustrates the field distribution for each α, where (c) is the same as that in Fig. 2(a) but with different scale. It was determined that $\alpha = 0.55$ yielded the most uniform curing field in the center plane of the applicator. A uniform field is desirable since that will allow the curing of the largest diameter part.

III. Port-to-Port Coupling Analysis

As mentioned above, the mutual coupling between the two ports is a very important factor that influences the performance of the applicator. To get better performance, we wish to get lowest possible coupling in order to avoid the energy leakage through the ports. In a homogeneous, source-free cylindrical cavity with perfectly conducting walls, the electromagnetic fields inside the cavity can be derived from Maxwell's equations and boundary conditions [9]. For TM_{020} mode, we can get:

$$\begin{aligned} &E_\rho = E_\phi = 0 \\ &E_z = \frac{k^2}{j\omega\varepsilon} J_0\left(\frac{5.52\rho}{a}\right) = -j\omega\mu J_0\left(\frac{5.52\rho}{a}\right) \\ &H_\rho = H_z = 0 \\ &H_\phi = -\frac{\partial \psi_{020}^{TM}}{\partial \rho} = \frac{5.52}{a} J_1\left(\frac{5.52\rho}{a}\right). \end{aligned} \tag{3}$$

For TE_{211} mode, we have:

$$\begin{aligned} &E_\rho = -\frac{1}{\rho}\frac{\partial \psi_{211}}{\partial \phi} = \frac{2}{\rho} J_2\left(\frac{3.054}{a}\rho\right)\sin(2\phi)\sin\left(\frac{\pi z}{h}\right) \\ &E_\phi = \frac{\partial \psi_{211}}{\partial \rho} = \cos(2\phi)\sin\left(\frac{\pi z}{h}\right)\left[J_1\left(\frac{3.054}{a}\rho\right) - \frac{2a}{3.054\rho} J_2\left(\frac{3.054}{a}\rho\right)\right] \\ &E_z = 0 \\ &H_\rho = \frac{1}{j\omega\mu}\frac{\partial^2 \psi_{211}}{\partial \rho \partial z} = \frac{\pi/h}{j\omega\mu}\cos(2\phi)\cos\left(\frac{\pi z}{h}\right)\left[J_1\left(\frac{3.054}{a}\rho\right) - \frac{2a}{3.054\rho} J_2\left(\frac{3.054}{a}\rho\right)\right] \\ &H_\phi = \frac{1}{j\omega\mu}\frac{1}{\rho}\frac{\partial^2 \psi_{211}}{\partial \phi \partial z} = -\frac{2\pi/h}{j\omega\mu\rho}\sin(2\phi)\cos\left(\frac{\pi z}{h}\right) J_2\left(\frac{3.054}{a}\rho\right) \\ &H_z = \frac{1}{j\omega\mu}\left(\frac{\partial^2 \psi_{211}}{\partial z^2} + k^2 \psi_{211}\right) = \frac{1}{j\omega\mu}\left(\omega^2\mu\varepsilon - \left(\frac{\pi}{h}\right)^2\right) J_2\left(\frac{3.054}{h}\rho\right)\cos(2\phi)\sin\left(\frac{\pi z}{h}\right). \end{aligned} \tag{4}$$

Considering the field generated by azimuthal slot for TM_{020} mode, E_ρ and E_ϕ are zero, and E_z is very difficult to be coupled out through the axial slot; similarly, for the field generated by axial slot for TE_{211} mode, E_z is zero and it is very difficult for E_ρ and E_ϕ to be coupled out through the azimuthal slot. So it is seen that with these two specific modes, we can have very low port-to-port coupling, which is essential for achieving improved efficiency.

In practice, the microwave power is delivered into the cylindrical cavity by rectangular waveguides (for this work, WR-284) via iris-coupling (shown in Fig. 4 as meshed geometry in FEMLAB). The dominant mode inside the

waveguide is TE_{10} mode. The dimensions of the irises need to be determined so that the S_{11}, S_{21}, S_{22}, and S_{12} are minimized. Under these conditions, the maximum power is delivered to the load for processing. Fig. 5 and Fig. 6 show the simulated S-parameters for this empty two-port-feed cavity, where we call the TE-port as port 1 and TM-port as port 2. The resonant frequency shifted down a little bit from 2.45 GHz due to the existence of the irises. After the lossy epoxy samples are loaded inside the cavity, the S_{21} and S_{12} are expected to be even smaller. This multimode applicator is primarily designed for the processing of epoxy resins DGEBA/DDS mixture. The ε_r' and ε_r" as a function of temperature and extent-of-cure are measured at MSU using perturbation technique with single-mode cavity, and are shown in Fig. 7. More information about DGEBA/DDS to be processed with this cavity applicator can be found in [11]. Since the complex permittivity of DGEBA/DDS varies as a function of temperature and extent-of-cure during microwave heating, the S_{11} and S_{22} are expected to vary significantly due to the loaded epoxy sample. In practice, in order to adjust the reflection coefficients at the two ports, a brass plunger can be introduced lying very close to each coupling iris [12], so that the S_{11} and S_{22} can be retuned in real-time.

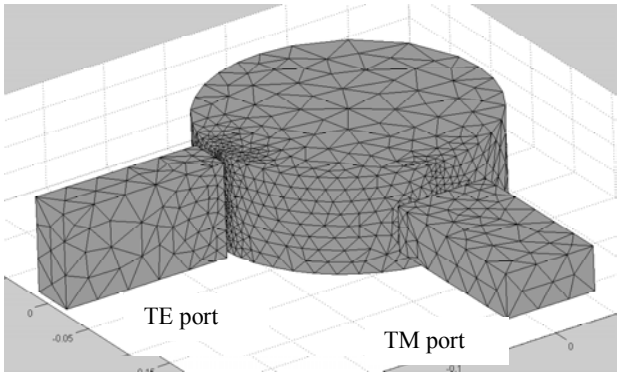

Figure 4. Cavity fed with waveguides via irises.

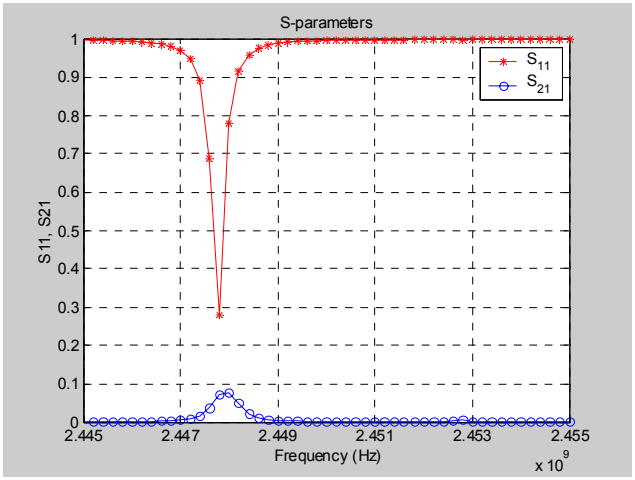

Figure 5. TE mode (S_{11} and S_{21}) for the two-port cavity.

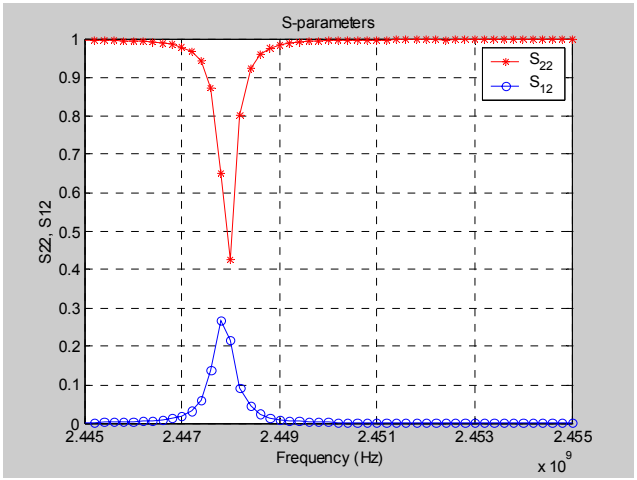

Figure 6. TM mode (S_{22} and S_{12}) for the two-port cavity.

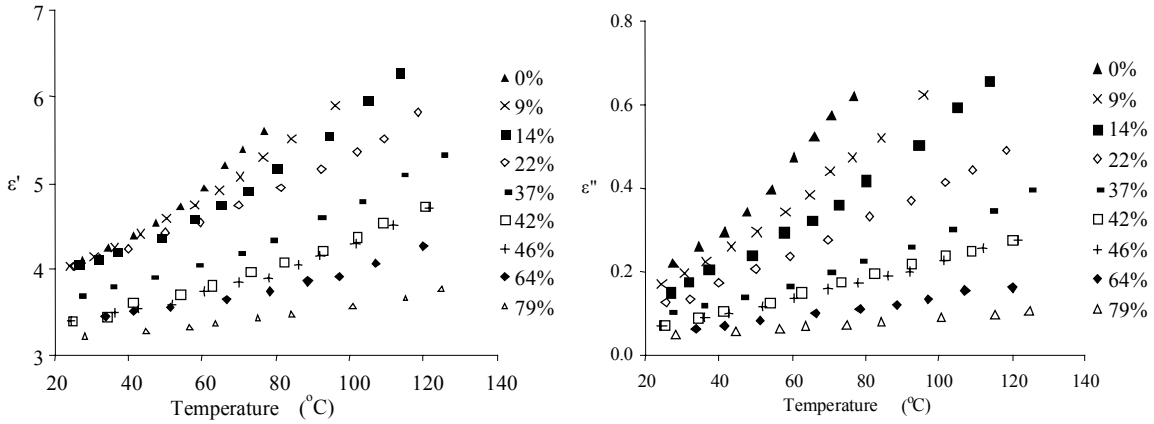

Figure 7. Dielectric properties of DGEBA/DDS as a function of temperature and extent-of-cure measured at MSU.

IV. Conclusion

In this paper, we have presented the electromagnetic modeling of an adaptable multimode microwave cavity applicator for polymer processing. It is shown that the mode-switching can be realized by just varying the power delivered to each port, without mechanically adjustment of the cavity dimensions. An orthogonal feeding mechanism is developed to reduce the cross coupling between the ports. The feed network that consists of coax-to-waveguide transition followed by iris-coupled cavity is being implemented. Experiments will be carried out to verify the model and develop control strategies.

Acknowledgment

This work was supported by the National Science Foundation (DMI-0200346).

References

[1] J. Wei, M. C. Hawley, and J. D. Delong, "Comparison of Microwave and Thermal Cure of Epoxy Resins," *Polymer Engineering and Science,* vol. 33, no. 17, pp. 1132-1140, 1993.

[2] D. A. Lewis, J. C. Hedrick, T. C. Ward, and J. E. McGrath, "The Accelerated Curing of Epoxy Resins Using Microwave Radiation," *Polymer Preprints*, vol. 28, no. 2, pp. 330-331, 1987.

[3] R. Agrawal and L.T. Drzal, "Effects of Microwave Processing on Fiber-Matrix Adhesion in Composites," *Journal of Adhesion*, vol. 29, pp. 63-79, 1989.

[4] J. Wei, J. Jow, J. D. DeLong, and M. C. Hawley, "Microwave Processing of Crossply Continuous Graphite Fiber/Epoxy Composites", *SAMPE Journal*, vol. 27, no. 1, pp. 33-39, 1991.

[5] J. E. Gerling, "Microwave Oven Power: a Technical Review," *Journal of Microwave Power and Electromagnetic Energy*, vol. 22, no. 4, pp. 199-207, 1987.

[6] A. C. Metaxas and R. J. Meredith, *Industrial Microwave Heating*, pp. 137-138, IEE Power Engineering Series, Peter Peregrinus Ltd., London, 1983.

[7] L. A. Fellows and M. C. Hawley, "Microwave Heating of Composites with Complex Geometries in Cylindrical Single-Mode Resonant Microwave Cavities," *Proceedings of the 29th Microwave Power Symposium*, pp. 91-94, Chicago, IL, July 1994.

[8] Y. Qiu and M. C. Hawley, "Computer Controlled Variable Frequency Microwave Processing of Complex-Shaped Graphite/Epoxy Composite," *Proceedings of the 14th American Society for Composites Annual Technical Conference*, pp. 52-61, Dayton, OH, September 1999.

[9] R. F. Harrington, *Time-Harmonic Electromagnetic Fields*, McGraw-Hill, New York, 1987.

[10] COMSOL, Inc., *FEMLAB User's Manual*, version 3.0a, 2004.

[11] L. Zong, S. Zhou, R. Sun, L. C. Kempel, and M. C. Hawley, "Dielectric Analysis of a Crosslinking Epoxy Resin at a High Microwave Frequency," *Journal of Polymer Science Part B: Polymer Physics*, vol. 42, no. 15, pp. 2871-2877, August 2004.

[12] L. Chen, C. K. Ong, and B. T. G. Tan, "A Resonant Cavity for High-Accuracy Measurement of Microwave Dielectric Properties," *Measurement Science and Technology*, vol. 7, no. 9, pp. 1255-1259, September 1996.

Rensheng Sun was born in Heilongjiang, China, in 1975. He received the B.E. degree from Tsinghua University, Beijing, China, and the M.S. degree from Villanova University, Villanova, PA, both in electrical engineering, in 1999 and 2002, respectively. He is currently working toward the Ph.D. degree in electrical engineering at Michigan State University, East Lansing. His current research interests include computational electromagnetics, numerical modeling on microwave processing of materials, and multimode cavity design. He is a student member of IEEE and a member of Eta Kappa Nu and Tau Beta Pi.

Leo C. Kempel was born in Akron, OH, in October 1965. He earned his B.S.E.E. at the University of Cincinnati in 1989 having been a co-op student with General Dynamics Corporation in Fort Worth Texas. He earned the M.S.E.E. and Ph.D. degrees at the University of Michigan in 1990 and 1994, respectively.

After a brief Post-Doctoral appointment at the University of Michigan, Dr. Kempel joined Mission Research Corporation in 1994 as a Senior Research Engineer. He led several projects involving the design of conformal antennas, computational electromagnetics, scattering analysis, and high power/ultrawideband microwaves. He joined Michigan State University in 1998 as an Assistant Professor and was promoted to Associate Professor in 2002. Prof. Kempel's current research interests include computational electromagnetics, large-scale computing, conformal antennas, microwave/millimeter wave materials, mixed-signal electromagnetic interference, and measurement techniques. Prof. Kempel has been awarded a CAREER award by the National Science Foundation and the Teacher-Scholar award by Michigan State University in 2002. He also received the MSU College of Engineering's Withrow Distinguished Scholar (Junior Faculty) Award in 2001. He is affiliated with the National Science Foundation's Wireless Integrated Microsystems Engineering Research Center. He is serving with the Air Force Research Laboratory Sensors Directorate as an IPA during 2004-2005. Prof. Kempel has published over 27 peer-reviewed journal papers, 65 conference papers, one book, and a book chapter.

Dr. Kempel is serving as an Associate Editor for the *IEEE Transactions on Antennas and Propagation*. He was the technical chairperson for the 2001 Applied Computational Electromagnetics Society (ACES) Conference and technical co-chair for the Finite Element Workshop held in Chios, GREECE in 2002. He is a Member of the ACES Board of Directors and is serving as Secretary for the Board of Directors. He has organized several sessions at recent URSI, ACES, and Antenna Measurements Techniques Association (AMTA) meetings as well as serving on the technical committees for APS/URSI (in Columbus, OH), AMTA, and ACES. He is an active reviewer for several IEEE publications as well as JEWA, ACES Journal, and Radio Science. He co-authored *The Finite Element Method for Electromagnetics* published by IEEE Press. Dr. Kempel is a member of Tau Beta Pi, Eta Kappa Nu, Commission B of URSI, ACES, AMTA as well as the IEEE Antennas and Propagation and Microwave Theory and Techniques Societies.

Liming Zong was born in Heilongjiang, China, in 1971. He received a B.E. degree in chemical engineering from Dalian University of Technology, Liaoning, China, in 1992, a M.S. degree in chemical engineering from Tsinghua University, Beijing, China, in 1995, and an MBA degree from Michigan State University, East Lansing, MI, in 2004. He joined China National Offshore Oil Corp. in 1995 as a Chemical Engineer. He led and involved planning, evaluation, and management of several chemical plant projects. Since 2000 he has been working toward the Ph.D. degree in chemical engineering at Michigan Sate University, East Lansing, MI. His current research interests include microwave processing of polymers and composites.

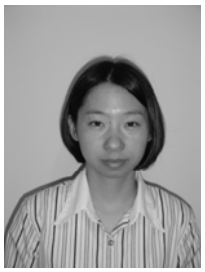

Shuangjie Zhou was born in Nei Mongol, China. She received a M.S. in electrical engineering and a Ph.D. in chemical engineering in 2002, from Michigan State University. She worked as a Research Associate at Michigan State University from Aug. 2002 to Aug. 2004. Her research included modeling of microwave processing and synthesis of carbon nanotubes. Currently she works as an Integration Engineer at Freescale Semiconductor, Inc.

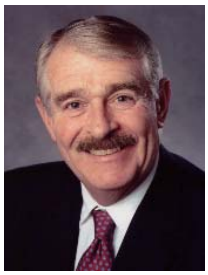

Martin C. Hawley is currently professor and chairperson of the department of Chemical Engineering and Materials Science at Michigan State University. He teaches and has developed graduate and undergraduate courses in chemical kinetics and chemical reactor design; applied mathematics; process design, economics and optimization. Present research is concerned with chemicals from biomass; free radical production in microwave plasmas; electromagnetic coupling and measurements for materials processing; and basic reaction and transport studies in thick-section composites. Dr. Hawley consults for industry and government in areas of computer simulation, chemical reactor design, process design, and materials processing.

He has developed text materials and taught courses to students in international education programs on project engineering and management. Professor Hawley holds six patents and has published over 200 articles and books.

The Mid-Michigan Section of AIChE named Dr. Hawley “Chemical Engineer of the Year” for 1975 and 1976 for his overall contributions to the Chemical Engineering profession. In 1982 he was honored by Michigan State University with a Distinguished Faculty Award.

Comparative Evaluation of Some Empirical Design Techniques for CAD Optimization of Wideband U-Slot Microstrip Antennas

V. Natarajan and **D. Chatterjee**

Abstract— **In this paper three different empirical techniques, for design of wideband U-slot microstrip patch antennas on infinite, grounded substrates (ϵ_r = 1.0, 4.0, and 6.15), has been studied extensively. Methods I and III, developed by the present authors, commonly utilize the property of** *dimensional invariance* **in designing the radiating patch of the U-Slot microstrip antenna. These two methods use empirical (quadratic) curve-fit equations, and formulas for design of probe-fed rectangular patches, respectively, to initiate the corresponding probe-fed U-Slot patch designs. The second (method II) approach, published earlier by different authors, principally utilizes the distinction between four resonant frequencies and calculates the various dimensions associated with the U-Slot patch radiator. The initial U-slot designs from the three empirical techniques have been further optimized for enhanced bandwidths via: (a) parametric simulation, and (b) built-in global optimizers such as Powell and Genetic algorithms in the commercially available microstrip CAD software, IE3D. Extensive analysis, based on: (a) comparison of the three empirical design algorithms (methods I, II and III) , and, (b) impedance behavior (and VSWR characteristics) of U-slot antennas on low, medium and high permittivity substrates, show that method III is generally superior to methods I and II. Additionally, since the overall U-Slot patch dimensions follow the relation $\frac{\mathrm{W}}{\mathrm{L}} \approx 1.385$ (methods I and III), and, $\frac{\mathrm{W}}{\mathrm{L}} \approx 2.0$ (method II), U-Slot designs via methods I and III have** *lower* **cross-polar levels in the principal ($\phi = 0°, 90°$) planes compared to those obtained via method II.**

I. Introduction

Microstrip antennas are an extremely popular choice for wireless applications due to their low-profile, ease of fabrication and integration with RF circuitry [1], [2]. However, conventional probe-fed, microstrip patch configuration antennas suffer from low bandwidth characteristics. Recently, wideband impedance characteristics were achieved by properly etching a U-shaped slot on the metallic surface of the rectangular radiating patches, as in Fig. 1, on both foam [3] and microwave substrates [4]. (In this paper bandwidth of an antenna is dictated by the range of frequencies for which the return loss is $\leq$ -10 dB).

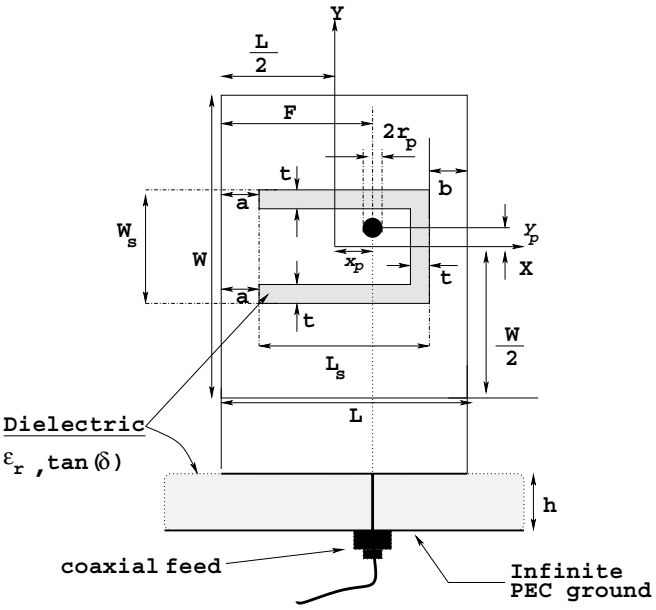

Fig. 1. Physical topology of probe-fed, wideband, U-slot microstrip antenna on microwave substrate. The dimensions shown here are independent of the coordinate system; the probe location however, is defined w.r.t the coordinate system which is located at the center of the rectangular patch. Note that the U-Slot is also located symmetrically with respect to the origin. In this paper the probe has a radius $\mathrm{r_p}$ and is located on the x-axis *i.e.*, $\mathrm{y_p} = 0$, and, $\mathrm{F} = \frac{\mathrm{L}}{2} + \mathrm{x_p}$ as shown here.

While no analytical models are available to describe the working of this novel U-slot microstrip antenna configuration, two different empirical methods to initiate the design of wideband U-slot antennas were presented in [5] and [6]. The subject of this investigation is to present a comparative analysis of these empirical techniques to design wideband U-slot

Department of Computer Science and Electrical Engineering, 570-F Flarsheim Hall, University of Missouri Kansas City (UMKC), 5100 Rockhill Road, KC, MO 64110, USA; e-mail:**chatd@umkc.edu**

microstrip antennas.

The empirical technique in [5] is based on dimensional invariance relationships observed in the U-slot geometry, and some empirical design equations. The design equations in [5, Section VI] were developed for specific substrate permittivities and thicknesses. The method in [6], which has been described here in subsection V. B for the sake of completeness, assumes the existence of four distinct resonant frequencies to determine the dimensions of the U-Slot. However, the applications of these equations were carried out on U-slot antenna on low permittivity (ϵ_r = 2.2) dielectrics only.

For most cases, the U-slot antenna geometries designed via the empirical techniques documented in [5] and [6] need to be further optimized, through the use of CAD tools like IE3D [7], for achieving the desired wideband impedance bandwidth behavior. The ability of these empirical techniques to generate initial U-slot antenna geometries, which can be rapidly optimized using the global optimizer sub-routines in IE3D is presented in [8]. The results indicate that the empirical technique in [5] generates initial U-slot antenna designs, which are more suitable for rapid optimization via IE3D. Extensive parametric modeling results are also presented in [5], [9] and [10] to aid designers in the selection of parameters for rapid optimization of initial U-slot antenna geometries. While the use of parametric modeling results is advocated in [6, Section V] for further optimization of the U-slot antennas, no methodology/procedure is available.

Apart from these results, the capabilities of built-in optimizers in IE3D, namely Genetic, Powell and Random algorithms, for rapid optimization and generation of wideband U-slot topologies are documented in [11]. The results reported in [11] are restricted to optimization of initial U-slot antennas designed via empirical method in [5]. A systematic approach to setting up the optimization simulations on IE3D is also described therein. The effects of dielectric permittivity and thicknesses on the performance characteristics like impedance bandwidth, gain etc., of the U-slot antennas on low, medium and high substrate permittivities are examined in [12]. These results enable a designer to select an optimal combination of substrate permittivity (ϵ_r) and thickness (h) - given a center frequency of operation (f_r) of the U-slot antenna. Such optimal selection would lead to reduced optimization cycle time.

One of the main purposes of this investigation, in addition to comparative analysis, is to present a third empirical technique for the design of wideband U-slot antennas, that is distinct from [5], [6]. A comparative analysis of the capabilities of the three empirical methods to generate initial U-slot antenna geometries, which can be rapidly optimized with minimum number of optimization cycles, is also investigated in this paper, including some appropriate case studies. To that end, parametric ([5], [9], [10]), and global optimization techniques, with the commercially available CAD software IE3D [7], are used for a comparative assesment of the three empirical design techniques.

The scope of the results presented here are restricted to probe-fed, single-layer U-slot antenna geometries on infinite grounded substrates, modeled and simulated using CAD tool IE3D. The capabilities of the global optimizers namely Genetic, and Powell optimizers are restricted to their implementations in IE3D [7]. Since optimization is an open-ended process, the procedure is stopped after achieving the desired wideband impedance characteritics. Therefore, in some cases, these designs could be modified for further enhancement of bandwidth characteristics.

The empirical equations for the resonant frequencies in [6] and [13] have been validated for low permittivity substrates in [14]. The third empirical technique (method III), described in Section III of this paper, employs the algorithm developed in [15] based on the information in [2]. The outline of the remainder of the paper is described next.

The basic problem of wideband U-slot antenna design is presented in Section II. The detailed algorithm of the proposed technique (i.e. the third empirical technique), to initiate the design of wideband U-slot antennas, is presented in Section III. The methodology followed to initiate the design of wideband U-slot antenna geometries via the different empirical techniques is outlined in Section IV. Three design examples are presented in Section V, to illustrate the abilities of the three empirical methods to initiate the design of wideband U-slot antennas. The results of simulation performance of the these initial U-slot antennas are discussed in Section VI. The step-by-step procedure used to optimize the initial U-slot antennas to achieve wideband impedance charcteristics is also described in this section. Finally, the results of the paper are summarized in Section VII, followed by the list of relevant references.

II. Problem Description

The problem associated with wideband microstrip designs as discussed in [5, Section III], concerns forming a loop in the input (Z_{in}) impedance on the

Smith chart. The loop should lie within the VSWR $\leq$ 2 circle, and most of the frequencies should be contained by the loop. All empirical techniques, followed by appropriate optimization schemes, are solely concerned in generating a U-slot design that closely satisfies this criterion.

The technique in [5, Section VII] relies on empirical design equations derived with specific substrate permittivity (ϵ_r) and thickness (h). However, it is quite impractical to derive similar equations for all possible ϵ_r and h combinations. Therefore, the applicability of these relations over all practical values of ϵ_r and design center frequency (f_r) remains very tedious.

The information gleaned from the review of [5] suggests seeking an alternate method to the design of U-slots that is much more straightforward; thus a possible alternate approach has been described in Section III.

The method in [6] is based on resonant frequency equations obtained via parametric simulations on U-slot antenna geometries on low permittivity (ϵ_r = 2.2) dielectrics. The applicability of these equations to design wideband U-slot antennas on medium and high permittivity dielectrics has not been documented. Also, the algorithm presented in [6, Section III] may generate non-physical and ambigous values for certain values of input specifications. (This aspect of the algorithm is further explored in Section V).

An empirical technique which generates the desired wideband impedance results with the least number of optimization cycles may be considered superior to others. This observation forms the basis of the comparative analysis. In this investigation, the number of optimization cycles may be characterized/identified on the basis of the following features:

- Number of optimization variables required.
- Range of optimization required in the variable.
- Optimization time.

III. An Empirical Procedure for Wideband U-Slot Antenna Design (Method III)

The empirical method in [5] relies on derived empirical formulations to obtain $\frac{W}{h}$ ratio, and the subsequent use of dimensional invariance relationships to design the U-slot antennas. As mentioned earlier, derivation of these empirical equations for every practical substrate permittivity and thickness combinations becomes quite cumbersome. The proposed empirical technique employs semi-analytical techniques [1, ch. 4], [2] to design a rectangular patch geometry, and subsequently uses the dimensional invariance relationships to design a U-shaped slot on the radiating rectangular patch.

To that end, cavity model based, custom built Fast Iterative Code (FIC) [15] is utilized to obtain the dimensions of the rectangular patch following the appropriate information in [2]. The algorithm of FIC [15] is briefly described below.

(i) Select the substrate permittivity (ϵ_r), thickness (h) and operating frequency (f_r) for the design of rectangular patch. The information presented in [14] may be used in the optimal selection of ϵ_r, h. In addition, the total number of iterations `ITMAX` is also required as input.

(ii) To account for the fringing effects, a slightly higher frequency $f_r^o \approx 1.25 f_r$ is chosen and the resonant length (L) of the radiating patch is calculated via the formula:

$$L = \frac{c}{2 f_r^o \sqrt{\epsilon_r}}. \tag{1}$$

A nominal patch width W$\approx$ 1.5$\times$L is also selected in order to facilitate the working of the FIC algorithm.

(iii) The effect of fringing fields on the resonant length of the rectangular microstrip antenna are calculated as

$$\Delta L = \frac{0.412h[\epsilon_{\mathtt{eff}}(W) + 0.3](\frac{W}{h} + 0.264)}{[\epsilon_{\mathtt{eff}}(W) - 0.258](\frac{W}{h} + 0.8)}, \tag{2}$$

where the effective relative permittivity

$$\epsilon_{\mathtt{eff}}(X) = \frac{\epsilon_r + 1}{2} + \frac{\epsilon_r - 1}{2\sqrt{1 + \frac{10h}{X}}}, \tag{3}$$

and the symbol $X \Rightarrow$ L or W, in (3).

(iv) The resonant frequency of the rectangular patch is now computed via (Hammerstad's)[1, p. 267, Eq. (4.28)]

$$f_H = \frac{c}{2(L + \Delta L)\sqrt{\epsilon_r}}, \tag{4}$$

and (James's)[1, p. 267, Eq. (4.31)]

$$f_J = \frac{f_r^o \epsilon_r}{(1 + \mathcal{X})\sqrt{\epsilon_{\mathtt{eff}}(L)\epsilon_{\mathtt{eff}}(W)}} \tag{5}$$

empirical formulas, where,

$$\begin{aligned} \mathcal{X} &= \left(\frac{h}{L}\right)\Big[0.882 + \Big(\frac{0.164(\epsilon_r - 1)}{\epsilon_r^2}\Big) \\ &+ \frac{\epsilon_r + 1}{\pi\epsilon_r}\Big(0.758 + \ln[1.88 + \frac{L}{h}]\Big)\Big]. \end{aligned} \tag{6}$$

(v) Having computed f_H and f_J the algorithm checks for the condition

$$\mathtt{min}(f_H, f_J) \leq f_r \leq \mathtt{max}(f_H, f_J). \quad (7)$$

In [2] it has been shown that the measured resonant frequency, defined by $\Im\mathrm{m}(\mathrm{Z_{in}}) = 0$, remains bounded by these two limits for low and moderate permittivity substrates. (For high permittivity substrates, resonances may not occur if the substrate thickness is too large. In that case the frequency at which the VSWR is the lowest may be considered to satisfy (7)).

(a) if the condition (7) is satisfied, the procedure stops, and resonant length L of the rectangular patch is thus found.

(b) if however, $\mathrm{f}_r < \mathtt{min}(f_H, f_J)$, then a new frequency $\mathrm{f}_r^o \Rightarrow \mathrm{f}_r^o - 0.05 \times \mathrm{f}_r$, with f_r^o given in step (ii), is selected and the procedure is repeated till the condition in (7) is satisfied.

(c) if $\mathrm{f}_r > \mathtt{max}(f_H, f_J)$, then a new frequency with $\mathrm{f}_r^o \Rightarrow \mathrm{f}_r^o + 0.05 \times \mathrm{f}_r$, with f_r^o given in step (ii), is selected and the procedure is repeated till the condition in (7) is satisfied. In the steps (a) to (c) f_r is the original operating frequency as in step (i). If the conditions (v) (a), (b) or (c) are not satisfied in the total number of iteration steps, ITMAX, then the algorithm stops.

(vi) The patch resonant length L and width W $\approx 1.5 \times$ L are obtained whenever (7) is satisfied.

The U-slot design now proceeds with the knowledge of the broader dimension W as in Fig. 1. Note that the patch resonant length, L, is redundant in the design of the U-slot. With the knowledge of W, the dimensional invariance properties [5, Section IV, Table I] are employed to obtain initial design of the U-slot.

In the process of obtaining the complete U-slot dimensions via the dimensional invariance relations, it was observed that $\frac{W}{L} \approx 1.385$, where L is the overall length of the U-slot as shown in Fig. 1, and is distinct from the length L obtained earlier for the rectangular patch from the Fast Iterative Code [15]. An alternate approach would be to apply W = 1.385 L, in step (vi) in the preceding algorithm and then obtain the complete U-slot antenna geometry via the dimensional invariance relations. However, this alternative approach is not pursued in this paper.

Having obtained the complete set of dimensions, this antenna is then modeled and simulated via commercial CAD tool IE3D (or equivalent). Based on the location and size of the impedance locus obtained on the Smith chart, the antenna geometry is further optimized for wideband performance. Note that, with the exception of the procedure used to obtain the dimensions of the width of the radiating patch, all the steps (to generate the location and dimensions of a U-shaped slot) are common to methods I and III. However, it must be emphasized that both these empirical methods produce different set of dimensions of the U-slot antennas.

The criteria $\frac{h\sqrt{\epsilon_r}}{\lambda} \approx 0.1$, 0.12, 0.14 and 0.18 [12] are used to obtain initial values of substrate permittivity (ϵ_r) and thickness (h), to design wideband U-slot antennas on air (ϵ_r = 1.0), low ($\epsilon_r \approx 2.94$), medium ($\epsilon_r \approx 4.5$) and high ($\epsilon_r \approx 9.8$) permittivity dielectrics, respectively. These choices of inputs, satisying the above criteria were observed to have small overall optimization cycles [12].

IV. Methodology

A brief description of the empirical techniques used to initiate the design of wideband U-slot antennas are presented in this section. Methods I and III essentially are based on [5] and Section III, respectively, hence are omitted here for brevity.

In [6], the effect of variation of : (a) the length of the vertical arms of the slot (L_s - t), lengths of (b) the horizontal arms of the slot (W_s), and (c) the rectangular radiating patch (L), on the resonant frequencies (assuming four distinct resonant frequencies occur) are documented for U-slot antenna on low (ϵ_r = 2.2) permittivity substrate. Based on the observation of these specific parametric modeling results, empirical equations are dervied for each of the last three resonant frequencies of the U-slot geometry. These formulas, coupled with equations in [1, ch. 4, pp. 266 - 268] to design probe-fed, rectangular microstrip antennas, are used to obtain a complete set of dimensions of U-slot antenna geometry. However, as the empirical formulas for resonant frequencies are based on parametric studies of U-slot antenna on low permittivity (ϵ_r = 2.2) dielectrics, their applicability to initiate the design of wideband U-slot antennas on other (medium or high) permittivity dielectrics remain unknown. The details of implementing the empirical design algorithm [6, Section III], and its validation, are included in Section V. B of this paper.

The wideband U-slot microstrip antenna may be considered as a structural perturbation to the classical probe-fed, rectangular microstrip patch. Therefore, once a rectangular patch antenna is designed via any

of the analytical methods in [1, ch. 4], a U-shaped slot may be etched on the surface of the radiating patch. This is the basis of a third (method III) empirical method to initiate the design of wideband U-slot antennas as presented in Section III. The location and size of the slot on the radiating patch are obtained from the dimensional invariance relations presented in [5, Section IV]. The salient features of the three empirical techniques are summarized in Table I.

TABLE I
SUMMARY OF EMPIRICAL TECHNIQUES TO INITIATE DESIGN OF WIDEBAND U-SLOT MICROSTRIP ANTENNAS

Method	Basic Concepts & Features	Reference	Inputs Required
I	Empirical design equations to calculate $\frac{W}{h}$ ratio and dimensional invariance relations.	[5]	ϵ_r, h, f_r
II	Empirically derived resonant frequency formula of the U-slot geometry and rectangular microstrip antenna design equations in [1, ch. 4, pp. 266 to 268]	[6]	ϵ_r, h, f_r, % bandwidth, $\frac{(L_s-t)}{W}$ ratio
III	Design rectangular patch microstrip antenna via analytical models in [1, ch. 4]. A U-shaped slot is cut on the surface of the radiating patch using dimensional invariance relations [5]	Section III, this paper	ϵ_r, h, f_r

The initial U-slot antenna geometries obtained from the three empirical techniques may require further optimization to yield wideband impedance behavior. These initial U-slot antennas are modeled and simulated assuming infinite, grounded dielectrics via IE3D [7]. Based on the impedance behavior of each of these initial U-slot topologies, they were optimized for further bandwidth enhancement. The optimization of these initial U-slot antennas designed via the three empirical techniques were carried out by the following two approaches.

(a) Use of parametric simulation results in [5, Section V], [9] and [10] in the selection of optimization parameters, and subsequent variation of these parameters to generate wideband impedance behavior.
(b) Selection of optimization variables based on the parametric modeling results in [5, Section V], [9] and [10] and use of global optimizers in commercial CAD tool IE3D, namely Genetic, Random and Powell optimizers [7] to generate wideband radiators.

The immediately preceding steps (a) and (b) together form the central part of this investigation as presented in this paper. Results corresponding to steps (a) and (b) are included in Sections VI A and B, respectively.

The ability of the three empirical methods to generate initial U-slot antenna geometries, which can be rapidly optimized via these two approaches is illustrated with some design examples in the ensuing section.

V. CASE STUDIES AND DESIGN ISSUES

This section documents the capabilities and limitations of the three empirical methods to initiate the design of wideband U-slot antennas, via the following design examples.

- Design Example (a): ϵ_r = 1.0 and f_r = 0.9 GHz
- Design Example (b): ϵ_r = 4.0 and f_r = 3.26 GHz
- Design Example (c): ϵ_r = 6.15 and f_r = 2.4 GHz

In all the three examples U-slot antennas exhibiting 2:1 VSWR bandwidths $\geq$ 20% are considered wideband radiators.

A. Design Using Methods I and III

Applying the criteria $\frac{h\sqrt{\epsilon_r}}{\lambda} \approx 0.10$, 0.14 and 0.16 [12], substrate thicknesses (h) of 33.31 mm, 6.45 mm and 7.56 mm were chosen to initiate the design of U-slot antennas, for design examples (a), (b) and (c), via empirical method in [5] (or method I). Here λ corresponds to the respective design frequencies (f_r) of the design examples. Since no formulations exist to initiate the design of U-slot antennas for design example (a) via method I at h = 33.31 mm, the empirical equations derived for ϵ_r = 1.0 and h = 18.0 mm [5, Table II] were used to obtain the $\frac{W}{h}$ ratio. As indicated earlier, this is one of the difficulties of method in [5]. Similarly, empirical equations derived for ϵ_r = 4.5 and h = 6.35 mm and ϵ_r = 4.5 and h = 10.0 mm were used to calculate the $\frac{W}{h}$ ratios for design examples (b) and (c), respectively. The remaining dimensions of the U-slot antenna geometries for the three design examples were calculated following the procedure documented in [5, Section VII].

For U-slot antennas designed via method III, criteria similar to those used for method I were used to select the values of substrate thicknesses (h). The cavity model based FIC and dimensional invariance relations were then used to obtain the dimensions of a rectangular patch and U-shaped slot, respectively.

B. Design Using Method II

The algorithm for the empirical design method in [6, Section III] (or method II), is described here including its implementation and validation. The description is necessary for a comparative analysis of the three methods, later in this paper.

The algorithm assumes existence of four distinct resonant frequencies for the U-Slot patch antenna, f_{res1}, f_{res2}, f_{res3} and f_{res4}. Before presenting the algorithm, the various physical distinctions associated with the resonant frequencies are identified following their original description in [6].

- f_{res1} is associated with the resonance of the slot embedded in the microwave substrate
- f_{res2} is related to the resonance of the TM_{01} mode of the patch
- f_{res3} is dependent in a complex manner with the x- and y-directed patch resonant modes
- f_{res4} can be related to the resonance of the slot in air including the effects of the "pseudopatch" that is formed inside the U-Slot

Since no analytical theory is presented in [6], one simply cannot be assured of the validity of these distinctions. In addition, for electrically "thick" substrates the existence of distinct resonant frequencies is not always possible. However, it is also known from the basic theory of microstrip antennas that an increase in the electrical thickness ($\frac{h\sqrt{\epsilon_r}}{\lambda}$) of the substrate increases the impedance bandwidth [1, p. 288, Fig. 4.16]. This observation suggests that the design technique in [6] may work well only for electrically thin substrates. Consequently, one may expect that the initial design of the U-Slot via [6] would exhibit lower impedance bandwiths and hence would need to undergo significant optimization cycles using the CAD tool IE3D [7]. One of the major purposes of this study is to investigate, via several case studies, if the initial U-Slot design via [6] (or method II) is indeed relatively difficult to optimize as compared to the initial designs via methods I [5], and III. The sequence of steps of the design algorithm from [6, Section III] are summarized next. (The dimensions are as shown in Fig. 1.)

Step 1: The algorithm requires the following inputs: (a) f_{res3}, (b) 10 dB return loss bandwidth ($\frac{\Delta f}{\mathrm{f}_{res3}}$) in %, (c) the ratio $\frac{\mathrm{L}_s-\mathrm{t}}{\mathrm{W}}$. One then calculates

$$\mathrm{f}_{res2} = \mathrm{f}_{res3} - \frac{\Delta f}{2} \times 100, \tag{8}$$

and,

$$\mathrm{f}_{res4} = \mathrm{f}_{res3} + \frac{\Delta f}{2} \times 100, \tag{9}$$

respectively.

Step 2: The substrate thickness (h) and permittivity (ϵ_r) are chosen to satisfy

$$\mathrm{h} \geq 0.06 \frac{\lambda_{res3}(\mathrm{air})}{\sqrt{\epsilon_r}}. \tag{10}$$

In (10) $\lambda_{res3}(\mathrm{air}) = \frac{v_\circ}{\mathrm{f}_{res3}}$ is the free-space wavelength corresponding to the frequency f_{res3}, and $v_\circ = 2.997925 \times 10^{+10}$ cms/sec is the velocity of electromagnetic waves in free-space.

Step 3: The overall resonant length (Fig. 1) of the patch plus the extensions due to fringe effects, is given by

$$\mathrm{L} + 2\Delta\mathrm{L} \approx \frac{v_\circ}{2\sqrt{\epsilon_r}\mathrm{f}_{res3}}. \tag{11}$$

Step 4: The overall width of the patch is given by $\mathrm{W} = 1.5 \times (\mathrm{L} + 2\Delta\mathrm{L})$.

Step 5: The overall effective permittivity and the patch resonant length extension are calculated separately as,

$$\epsilon_{\mathtt{eff}} = \frac{\epsilon_r + 1}{2} + \frac{\epsilon_r - 1}{2}\left(1 + \frac{12\mathrm{h}}{W}\right)^{-\frac{1}{2}}, \tag{12}$$

and,

$$2\Delta\mathrm{L} = 0.824\mathrm{h}\frac{(\epsilon_{\mathtt{eff}} + 0.3)(\frac{\mathrm{W}}{h} + 0.262)}{(\epsilon_{\mathtt{eff}} - 0.258)(\frac{\mathrm{W}}{h} + 0.813)}. \tag{13}$$

Interestingly, (12) and (13) are closely similar and identital to equations (3) and (2), respectively.

Step 6: The overall patch resonant length is now re-calculated as

$$\mathrm{L} = \frac{v_\circ}{2\sqrt{\epsilon_{\mathtt{eff}}}\mathrm{f}_{res3}} - 2\Delta\mathrm{L}. \tag{14}$$

Step 7: The slot thickness, t, is calculated via the relationship

$$\mathrm{t} = \frac{\lambda_{res3}(\mathrm{air})}{60}. \tag{15}$$

Step 8: Calculate the slot width

$$\mathrm{W_s} = \frac{v_\circ}{\sqrt{\epsilon_{\mathtt{eff}}}\mathrm{f}_{res2}} - 2(\mathrm{L} + 2\Delta\mathrm{L} - t). \tag{16}$$

Step 9: Select L_s such that

$$\frac{\mathrm{L}_s - t}{\mathrm{W}} \geq 0.3 \text{ and } \frac{\mathrm{L}_s - t}{\mathrm{W_s}} \geq 0.75. \tag{17}$$

Step 10: Calculate the effective permittivity and the length extension of the "pseudopatch" as

$$\epsilon_{\mathtt{eff}(\mathrm{pp})} = \frac{\epsilon_r + 1}{2} + \frac{\epsilon_r - 1}{2}\left(1 + \frac{12\mathrm{h}}{\mathrm{W}_s - 2t}\right)^{-\frac{1}{2}}, \tag{18}$$

and,

$$2\overline{\Delta}_{\rm pp} = 0.824{\rm h}\frac{(\epsilon_{\tt eff(pp)}+0.3)(\frac{{\rm W}_s-2t}{h}+0.262)}{(\epsilon_{\tt eff(pp)}-0.258)(\frac{{\rm W}_s-2t}{h}+0.813)}. \quad (19)$$

Step 11: The quantity

$$\begin{aligned} {\rm b} &\approx {\rm L}-t+2\overline{\Delta}_{\rm pp}-\frac{1}{\sqrt{\epsilon_{\tt eff(pp)}}} \\ &\times \left(\frac{v_\circ}{{\rm f}_{res4}}-\{2({\rm L}_s-t)+{\rm W}_s\}\right). \quad (20) \end{aligned}$$

Step 12: The algorithm checks the condition

$$({\rm L}_s+{\rm b}) \leq {\rm L}.$$

If this condition is not satisfied, one adjusts the quantity $({\rm L}_s-t)$ step # 9 and keeps recalculating b in step # 11, till the condition in step # 12 is satisfied and a physically realizable design for the U-Slot microstrip patch antenna is feasible.

The implementation of the above algorithm was validated for the design of the U-Slot dimensions of $\epsilon_r = 2.2$ and ${\rm h} = 0.635$ cms at ${\rm f}_{res3} = 2.15$ GHz, as available in [6, Table IV]. However, when the algorithm of method II was subsequentlly applied to the calculation of the initial U-Slot dimensions for $\epsilon_r = 4.0$ and 6.15, one of the dimensions turned out non-physical. The details are included in Table II, below.

TABLE II
NON-PHYSICAL OUTPUTS OBTAINED VIA METHOD II ([6]), REFERRING TO FIG. 1. (ALL DIMENSIONS IN MM)

Parameter; (Type: Input/Output)	Example (b)	Example (c)
ϵ_r (input)	4.0	6.15
h (input)	6.45	7
$\frac{\Delta {\rm f}}{{\rm f}_{res3}}$(% bandwidth); (input)	25	30
${\rm f}_{res3}$ in GHz;(input)	3.26	2.4
$\frac{({\rm L}_s-t)}{\rm W}$; (input)	0.4	0.4
W; (output)	34.49	37.78
L; (output)	17.15	19.18
${\rm L}_s$; (output)	15.33	15.11
${\rm W}_s$; (output)	14.66	19.46
t; (output)	1.53	2.08
b; (output)	-2.0018	-5.1102
Comment	b $<$ 0.0 (*non-physical*)	b $<$ 0.0 (*non-physical*)

At this stage, in view of the results in Table II, it appears appropriate that a comparative analysis of the three methods be presented. This, expectedly, would help in understanding the salient features of method II and its standing with respect to methods I and III.

Following [5], application of methods I and III is initiated by the combination of substrate parameters, satisfying the criterion $\frac{{\rm h}\sqrt{\epsilon_r}}{\lambda} \approx 0.14$ for low and medium permittivities. (For substrates with $\epsilon_r \geq 6.0$ a value of 0.18 was found to yield acceptable results [5]). Beyond this point, methods I and III differ noticeably and their intrinsic differences are briefly summarized below.

For method I, assuming the substrate geometry is known uniquely, empirical equations [5, Table II] are used. (For situations where there exists no empirical equations corresponding exactly to the particular substrate type, an 'average' design procedure is adopted as explained in detail in [5, Section VII]). The main purpose of method I, however, is to obtain the appropriate $\frac{\rm W}{\rm h}$ ratio from the empirical equations. Knowing the substrate thickness, h, one readily calculates the overall U-Slot patch width W for a typical ϵ_r and design/operating frequency, ${\rm f}_r$. Once W is known, the other dimensions of the U-Slot can be calculated very quickly by using the dimensional invariance relationships as in [5, Table I]. The rapid calculation of the dimensions essentially resembles the back-of-the-envelope process. The main disadvantage of method I, however, is that the starting empirical equations are available for a few select substrate cases, and hence the accuracy of the average design procedures are questionable. For greater accuracy, one needs to derive empirical equations for a given combination of ϵ_r and h, which in itself can be very tedious.

The preceding limitation of method I is circumvented by the algorithm of method III, described in Section III. With the knowledge of the substrate geometry and the design frequency, one can determine the larger patch width, W, via eqs. (1) to (7). Once W is known, regardless of the $\frac{\rm W}{\rm h}$ ratio, the dimensional invariance relationships from [5, Table I] can be used to complete the U-Slot radiating patch design, just as in method I. The primary advantage of this approach, over method I, is that equations (1) to (7) apply to an arbitrary class of substrate topologies, as long as the assumptions of the cavity-model remains valid in that particular case. (In [2] it has been shown that these cavity-model formulas are applicable to $\epsilon_r \approx 12.0$.) Thus even for substrates where the empirical equations (method I) are not directly available, one can still proceed to design a U-Slot by first obtaining the overall rectangular patch dimensions (method III). Since the theoretical validity of these cavity-model formulas is well-known [1], [2], method III is far more

versatile and expected to be accurate than method I.

Method II in [6], as discussed here, has some inherent limitations in its applications. The two initial U-Slot patch designs for $\epsilon_r = 4.0$ and 6.15, as shown in Table II, could yield non-physical dimensions, b, (Fig. 1). Incidentally, one notes that from a numerical standpoint the condition in step 12 is still satisfied even with the negative value of the b dimension in Fig. 1. In absence of a comprehensive analytical theory for the U-Slot, this apparent limitation for method II was investigated as explained below.

Since the initial design [6] for the U-Slot relies on the existence of distinct resonant frequencies, it maybe hypothesized that the design algorithm would be physically viable if the parameter $\frac{\mathrm{h}\sqrt{\epsilon_r}}{\lambda_{\mathrm{res3}}(\mathrm{air})}$ is small. For the two cases listed in Table II, one finds $\frac{\mathrm{h}\sqrt{\epsilon_r}}{\lambda_{\mathrm{res3}}(\mathrm{air})} \approx 0.09$ and 0.125 for $\epsilon_r = 4.0$ and 6.15, respectively. The exact nature of dependence of b on the substrate permittivity ϵ_r and thickness h is complicated, because of the nature of the algebraic forms of the various intermediate quantities as appearing in equations (12) to (20). Preliminary examination of (20) indicates that for $\mathrm{b} > 0$, (physically realizable geometry), the additional condition

$$\mathrm{L} - \mathrm{t} + 2\overline{\Delta}_{\mathrm{pp}} \gg \frac{1}{\sqrt{\epsilon_{\mathtt{eff}}(\mathrm{pp})}}\left[\frac{\mathrm{v}_\circ}{\mathrm{f}_{res4}} - 3.5\mathrm{W_s}\right] \quad (21)$$

needs to be satisfied. (Condition (21) easily follows from the second condition in (17), and (20)). From the present investigations, it appears that (21) is generally satisfied when $\frac{\mathrm{h}\sqrt{\epsilon_r}}{\lambda_{\mathrm{res3}}(\mathrm{air})} \leq 0.075$. Consequently, in light of the current analysis, it appears that the condition (10) in step 2 could be modified to read:

$$0.06 \leq \frac{\mathrm{h}\sqrt{\epsilon_r}}{\lambda_{\mathrm{res3}}(\mathrm{air})} \leq 0.075. \quad (22)$$

This implies that physically valid initial U-Slot patch designs following the algorithm in [6] are feasible for low permittivity substrates. This observation has the further impact that these initial designs via [6] could exhibit low, 10 dB return loss bandwidths. Hence, these initial designs obtained from method II (or [6]), when subjected to parametric or global optimization schemes via commercial CAD softwares such as IE3D [7], would require increased optimization cycles (as defined in Section II).

However, it is emphasized that this aspect of implementing the algorithm in [6] needs to be investigated in more detail, before the condition (22) could be considered acceptable.

The dimensions of the U-slot antennas obtained via the three methods for design examples (a), (b) and (c) are tabulated in Tables III, IV and V, respectively. The U-slot antenna geometries obtained via methods I, II and III, for the three design examples, were modeled and simulated assuming infinite grounded dielectrics via commercial CAD tool IE3D [7]. Based on the location and size of the impedance locus on the Smith chart, optimization parameters were chosen for subsequent optimization of the initial U-slot antenna geometries. The analysis of the results are discussed in the following section.

VI. Results and Discussion

The results of the performed simulations, and the subsequent optimization of the initial U-slot antennas designed via the three empirical methods, are discussed in details in this section. To that end, the results obtained via the use of parametric simulation results in [5], [9] and [10] are discussed next in part A, followed by results obtained via `IE3D` global optimizers in part B. In addition, boresight gain vs. frequency, and principal plane ($\phi = 0^\circ$ and 90°) co- and cross-polar radiation patterns, for initial and optimized U-Slot patch geometries (for $\epsilon_r = 4.0$ in Table IV), are also included in part C for a complete understanding of the antenna performance. A comparative performance analysis of the three empirical design techniques, based on bandwidth, gain and radiation characteristics, is presented in part D.

A. Optimization via Parametric Modeling Results in [5], [9] and [10]

The results of U-slot antennas, designed via the three empirical techniques and further optimization via parametric modeling results are shown in Figs. 2 to 14. The impedance loci of the U-slot antennas obtained from the three empirical methods for design example (a) are shown in Fig. 2. From the Smith chart results, U-slot antennas designed via methods I and III form impedance loops close to the center of the Smith chart. In contrast, the U-slot antenna from method II appears to be highly capacitive, with its impedance loop on the lower half and farthest from the center of the Smith Chart.

The impedance loci of the (final) optimized U-slot antenna geometries obtained from methods I, II and III, for design example (a), are shown in Fig. 3. All three optimized U-slot antennas appear to exhibit wideband impedance behavior.

The results of the initial and optimized U-slot antennas designed via the three empirical techniques, for examples (b) and (c), are in Figs. 4 to 8. The

TABLE III
DIMENSIONS OF INITIAL AND OPTIMIZED, (VIA PARAMETRIC MODELING RESULTS IN [5], [9], [10]) U-SLOT ANTENNAS OBTAINED VIA THE THREE EMPIRICAL METHODS FOR DESIGN EXAMPLE (A), REFERRING TO FIG. 1. (ALL DIMENSIONS IN MM)

Parameter	Method I		Method II		Method III	
	Initial	Optimized	Initial	Optimized	Initial	Optimized
ϵ_r	1.0	1.0	1.0	1.0	1.0	1.0
$\tan(\delta)$	0.0	0.0	0.0	0.0	0.0	0.0
h	33.31	33.31	25.0	25.0	33.31	33.31
L	159.24	159.24	131.56	131.56	129.42	129.42
W	220.38	220.38	249.83	249.83	178.85	178.85
L_s	110.24	110.24	80.45	80.45	89.46	89.46
W_s	85.65	85.65	48.12	55.0	69.51	69.51
t	12.33	12.33	5.55	5.55	10.01	10.01
a	24.5	24.5	2.99	2.99	19.98	19.98
b	24.5	24.5	48.12	48.12	19.98	19.98
F	79.62	83.62	65.78	65.78	64.71	66.71
R_{probe}	3.0	4.0	2.0	2.0	3.0	3.5

TABLE IV
DIMENSIONS OF INITIAL AND OPTIMIZED, (VIA PARAMETRIC MODELING RESULTS IN [5], [9], [10]) U-SLOT ANTENNAS OBTAINED VIA THE THREE EMPIRICAL METHODS FOR DESIGN EXAMPLE (B), REFERRING TO FIG. 1. (ALL DIMENSIONS IN MM)

Parameter	Method I		Method II		Method III	
	Initial	Optimized	Initial	Optimized	Initial	Optimized
ϵ_r	4.0	4.0	4.0	4.0	4.0	4.0
$\tan(\delta)$	0.002	0.002	0.002	0.002	0.002	0.002
h	6.45	6.45	5.5	5.5	6.45	6.45
L	21.18	21.18	17.96	17.96	18.44	18.44
W	29.32	29.32	34.49	34.49	25.54	25.54
L_s	14.66	14.66	16.01	13.53	12.76	12.76
W_s	11.39	11.39	15.94	12.0	9.93	9.93
t	1.64	1.64	1.53	1.53	1.43	1.43
a	3.76	3.76	0.95	2.43	2.84	2.84
b	3.76	3.76	1.0	2.0	2.84	2.84
F	10.59	9.59	8.96	8.96	9.22	7.72
R_{probe}	0.635	0.635	0.635	0.635	0.635	0.635

TABLE V
DIMENSIONS OF INITIAL AND OPTIMIZED, (VIA PARAMETRIC MODELING RESULTS IN [5], [9], [10]) U-SLOT ANTENNAS OBTAINED VIA THE THREE EMPIRICAL METHODS FOR DESIGN EXAMPLE (C), REFERRING TO FIG. 1. (ALL DIMENSIONS IN MM)

Parameter	Method I		Method II		Method III	
	Initial	Optimized	Initial	Optimized	Initial	Optimized
ϵ_r	6.15	6.15	6.15	6.15	6.15	6.15
$\tan(\delta)$	0.002	0.002	0.002	0.002	0.002	0.002
h	7.56	7.56	3.1	7.0	7.56	7.56
L	21.06	21.06	22.42	22.42	20.22	20.22
W	29.14	29.14	37.78	37.78	27.98	27.98
L_s	14.58	14.58	21.35	17.35	14.0	14.0
W_s	11.53	11.53	18.89	14.89	10.87	10.87
t	1.63	1.63	2.08	2.08	1.57	1.57
a	3.24	3.24	0.16	2.16	3.11	3.11
b	3.24	3.24	0.95	2.95	3.11	3.11
F	10.53	8.03	11.21	11.23	10.11	7.61
R_{probe}	0.635	0.635	0.635	0.635	0.635	0.635

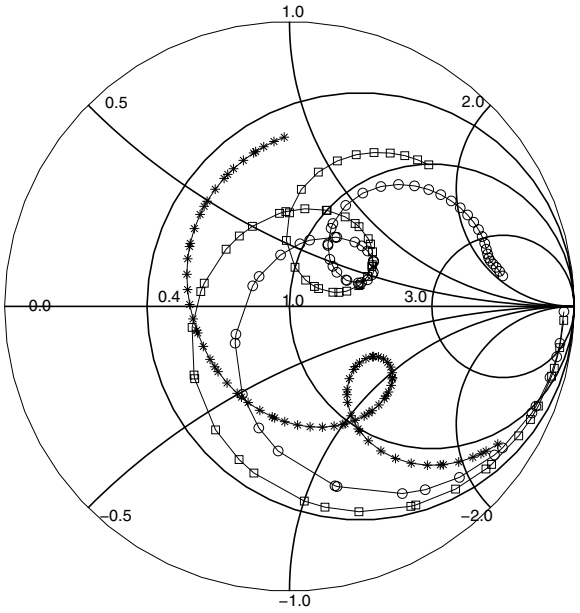

Fig. 2. Comparison of impedance loci of initial U-slot antennas from the three empirical methods for design on dielectric substrates with $\epsilon_r = 1.0$ via IE3D [7]; $\square - \square - \square$- method I; $* - * - *$- method II; $\circ - \circ - \circ$-method III.

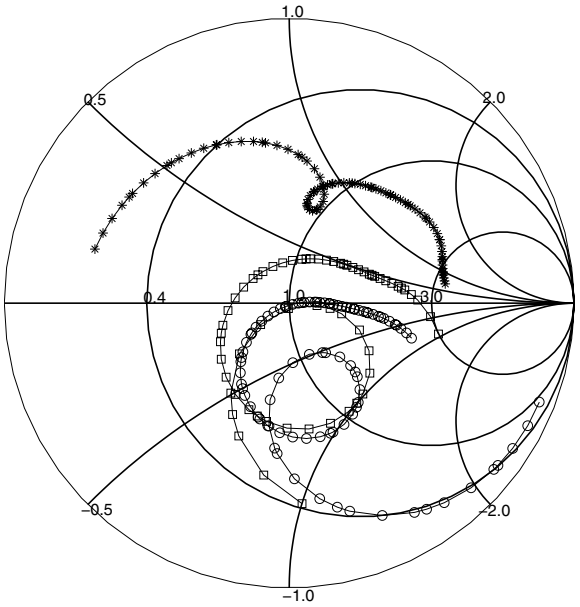

Fig. 4. Comparison of Smith Chart results of initial U-slot antennas from the three empirical methods on dielectric substrates with $\epsilon_r = 4.0$ via IE3D [7]; $\square - \square - \square$- method I; $* - * - *$- method II; $\circ - \circ - \circ$- method III.

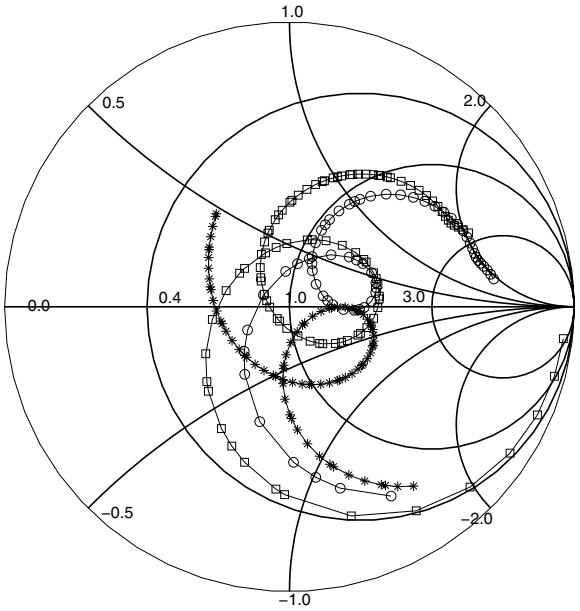

Fig. 3. Comparison of impedance loci of final, optimized U-slot antennas from the three empirical methods on dielectric substrates with $\epsilon_r = 1.0$ via IE3D [7]; $\square - \square - \square$- method I; $* - * - *$- method II; $\circ - \circ - \circ$- method III.

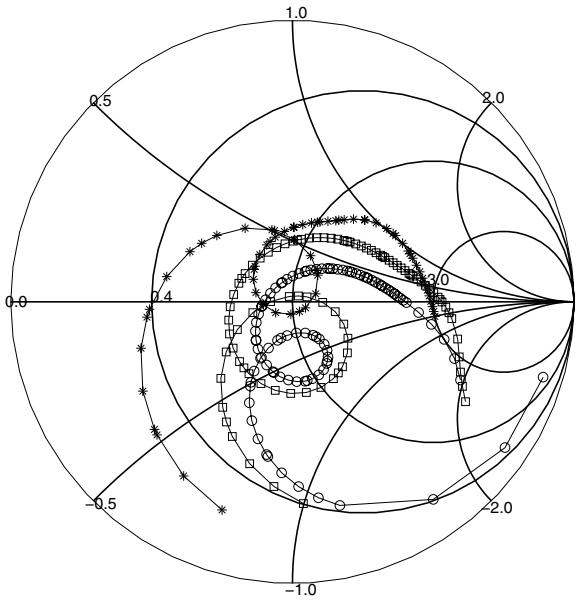

Fig. 5. Comparison of Smith Chart results of final, optimized U-slot antennas from the three empirical methods on dielectric substrates with $\epsilon_r = 4.0$ via IE3D [7]; $\square - \square - \square$-method I; $* - * - *$- method II; $\circ - \circ - \circ$- method III.

impedance behavior of the initial U-slot antenna designs on ϵ_r = 4.0 (Fig. 4) and ϵ_r = 6.15 (Fig. 7) show that the design via method II, for examples (b) and (c), do not form loops close to the center of the Smith Chart, in contrast with methods I and III. Following parametric modeling results in [5], [9] and [10], these U-slot antennas were optimized for wideband impedance characteristics, as shown in Figs. 5 to 6 for example (b), and Fig. 8 for example (c), respectively. In both cases, the final optimized impedances loci form loops in the VSWR ≤ 2 region of the Smith chart.

The choice of the optimization parameters (such as

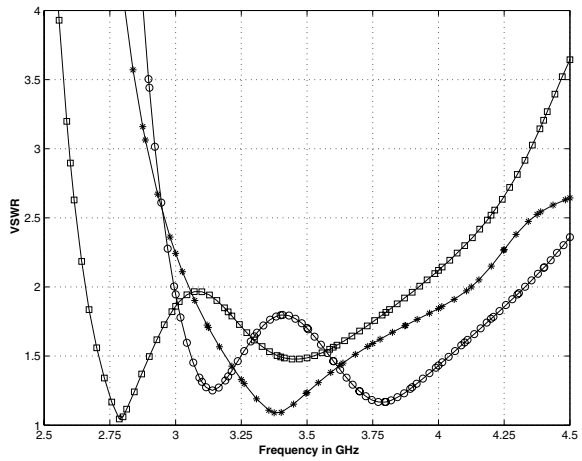

Fig. 6. Comparison of VSWR results of final, optimized U-slot antennas from the three empirical methods on dielectric substrates with $\epsilon_r = 4.0$ via IE3D [7]; $\square - \square - \square$- method I; $* - * - *$- method II; $\circ - \circ - \circ$- method III.

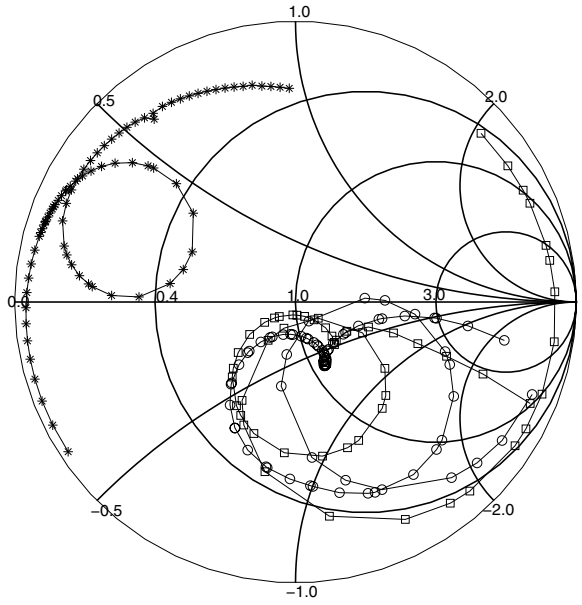

Fig. 7. Comparison of Smith Chart results of initial U-slot antennas from the three empirical methods on dielectric substrates with $\epsilon_r = 6.15$ via IE3D [7]; $\square - \square - \square$- method I; $* - * - *$- method II; $\circ - \circ - \circ$- method III.

width of slot, length of slot, probe location etc.), is based on the size and location of the impedace loci of the initial U-slot antennas on the Smith chart, and the knowledge of the parametric simulations results documented in [5], [9] and [10].

To that end, probe location and radii were chosen as optimization variables for U-slot antennas for example (a), designed via methods I and III. In contrast, for the U-slot antenna designed via method II, the length of the horizontal arm (W_s) was chosen as the optimization variables.

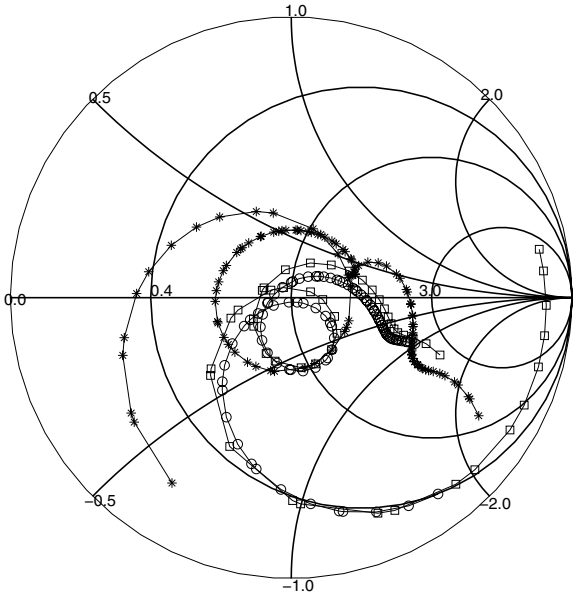

Fig. 8. Comparison of Smith Chart results of final, optimized U-slot antennas from the three empirical methods on dielectric substrates with $\epsilon_r = 6.15$ via IE3D [7]; $\square - \square - \square$-method I; $* - * - *$-method II; $\circ - \circ - \circ$- method III.

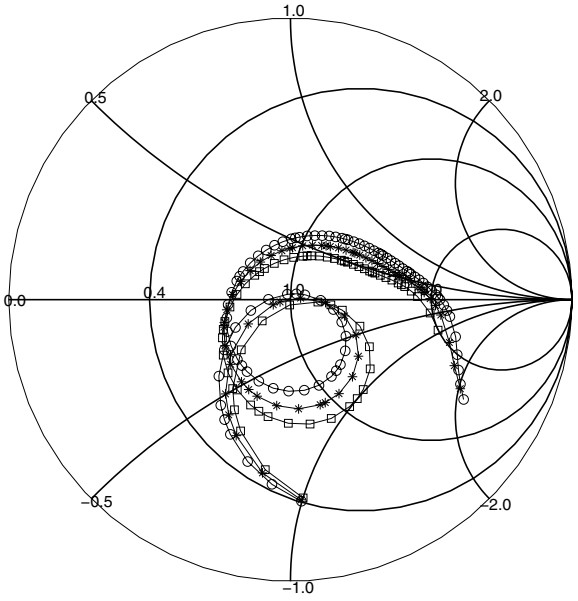

Fig. 9. Optimization Process for U-slot antenna designed via method I on dielectric substrates with $\epsilon_r = 4.0$ using parametric modeling results in [5], [9] and [10]; $\square - \square - \square$- Initial, unoptimized; X_p = 0.0, Y_p = 0.0; $* - * - *$- X_p = 0.0, Y_p = 0.5; $\circ - \circ - \circ -$ X_p = 0.0, Y_p = 1.0; all other dimensions of the U-slot antenna are kept constant - all dimensions in mm.

It is interesting to note (from Table III) that, while, methods I and III require two optimization variables to produce wideband bandwidth characteristics, the range of variation of each of these optimization variable is quite small. In comparison, method II requires

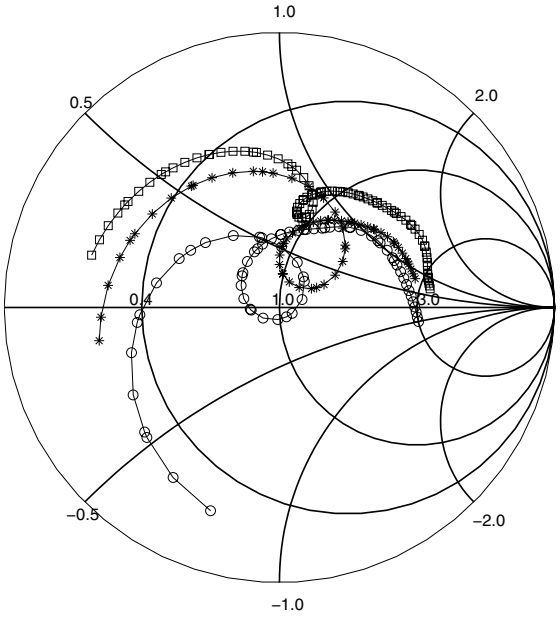

Fig. 10. Optimization Process for U-slot antenna designed via method II on dielectric substrates with ϵ_r = 4.0 using parametric modeling results in [5], [9] and [10]; □ − □ − □- Initial, unoptimized; L_s = 16.01, W_s = 15.94, a = 0.95 and b = 1.0; ∗ − ∗ − ∗- Step1 -L_s = 12.0, W_s = 15.94, a = 2.43 and b = 2.0; ○ − ○ − ○− Step2 - L_s = 12.0, W_s = 13.0, a = 2.43 and b = 2.0; all other dimensions of the U-slot antenna are kept constant - all dimensions in mm.

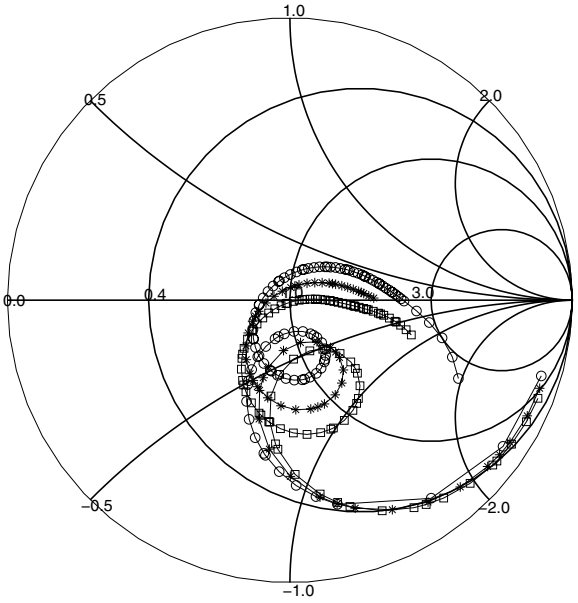

Fig. 11. Optimization Process for U-slot antenna designed via method III on dielectric substrates with ϵ_r = 4.0 using parametric modeling results in [5], [9] and [10]; □ − □ − □- Initial, unoptimized; X_p = 0.0, Y_p = 0.0; ∗ − ∗ − ∗- X_p = 0.0, Y_p = 0.75; ○ − ○ − ○− X_p = 0.0, Y_p = 1.5; all other dimensions of the U-slot antenna are kept constant - all dimensions in mm.

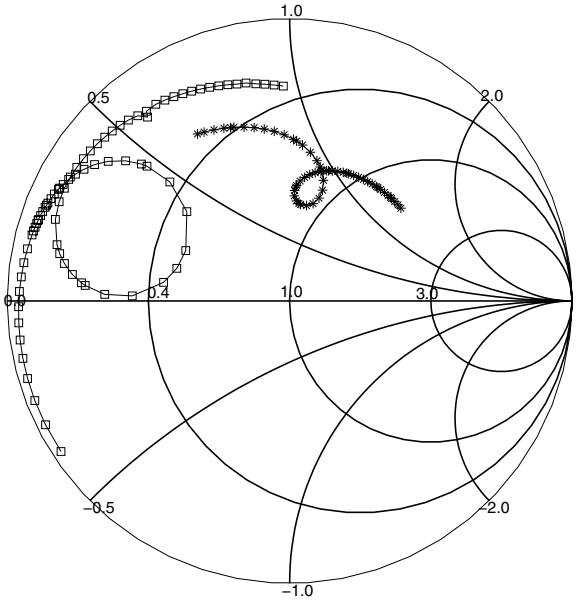

Fig. 12. Optimization Process for U-slot antenna designed on dielectric substrates with ϵ_r = 6.15 via method II; □ − □ − □- Initial; h = 3.1; ∗ − ∗ − ∗- h = 7.0; all other dimensions of the U-slot antenna are kept constant - all dimensions in mm.

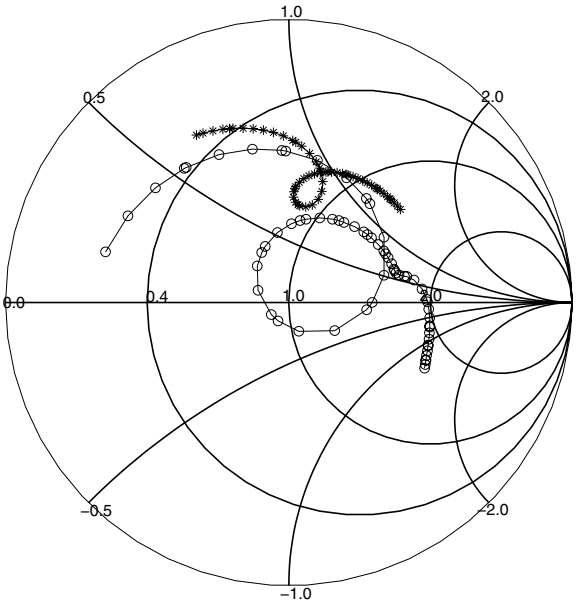

Fig. 13. Optimization Process for U-slot antenna designed on dielectric substrates with ϵ_r = 6.15 via method II; ∗ − ∗ − ∗- h = 7.0, L_s = 21.35, a = 0.6 and b = 0.95; ○ − ○ − ○- h = 7.0, L_s = 17.35, a = 2.16 and b = 2.95; all other dimensions of the U-slot antenna are kept constant - all dimensions in mm.

only one optimization variable. However, the range of variation required to achieve wideband impedance characteristics is quite large (W_s - from 48.12 mm to 55.0 mm). This may increase the optimization time and hence the optimization cycle for method II in comparison with methods I and III.

For design example (b), the initial U-slot antennas obtained from both methods I and III, form impedance

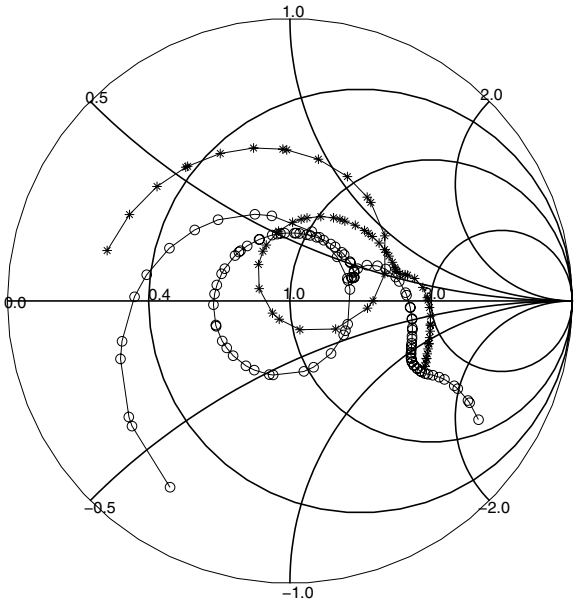

Fig. 14. Optimization Process for U-slot antenna designed on dielectric substrates with ϵ_r = 6.15 via method II; $*-*-*$- h = 7.0, L_s = 17.35, a = 2.16, b = 2.95 and $W_s = 18.89$; $\circ-\circ-\circ$- Optimized- h = 7.0, L_s = 17.35, a = 2.16, b = 2.95 and W_s = 14.89; all other dimensions of the U-slot antenna are kept constant - all dimensions in cms.

loops very close to the center of the Smith chart (Fig. 4). Therefore, only their probe locations were varied to obtain wideband impedance characteristics as evident from Figs. 9 and 11, respectively. In contrast, the U-slot antenna designed via method II does not form an impedance loop close to the center of the Smith chart. (Fig. 4). Hence, multi-step (multi-parameter) optimizations must be pursued to achieve wideband impedance characteristics. The multi-parameter/multi-step optimization procedure is shown in Fig. 10.

As seen in Fig. 10, in step 1, the length of the vertical arms of the U-slot are varied from 16.01 mm to 11.53 mm. This optimization moves the impedance loop closer to the center of the Smith chart. Then, the width of the horizontal arm (W_s) is chosen as the optimization variable in step 2 to shift the impedance locus within the 2:1 VSWR circle.

A similar feature is observed in the optimization procedure for U-slot antennas for example (c) via the three empirical methods. For U-slot antennas designed via methods I and III, the location of the probe feed is chosen as optimization variable. The optimization procedure of U-slot antennas designed via methods I and III are similar to those shown in Figs. 9 and 11, and are omitted here for brevity. In contrast, substrate thickness (h), width of the horizontal arm (W_s) of the U-slot and lengths of the arms (L_s) were chosen as optimization variables for U-slot antennas designed via method II. The step-by-step optimization procedure is documented in Figs. 12 to 14.

In the first step of the optimization process, (in Fig. 12), the substrate thickness of the U-slot antenna is increased from h = 3.1m to 7.0 mm, shifting the impedance locus closer to the center of the Smith Chart. Then, in the second step, the length of the arms of the slot (L_s) are reduced, as shown in Fig. 13, to further move the impedance closer to the center. Finally, the width of the slot (W_s) is adjusted to obtain wideband U-slot antenna geometry as evident from Fig. 14.

The 2:1 VSWR bandwidths of all the final, optimized U-slot antennas for the three design examples are tabulated in Table VI. The details of the optimization procedure followed to obtain wideband impedance results are discussed next.

TABLE VI
2:1 VSWR BANDWIDTHS OF PARAMETRICALLY OPTIMIZED U-SLOT ANTENNA GEOMETRIES DESIGNED VIA THE THREE EMPIRICAL TECHNIQUES FOR THE DESIGN EXAMPLES (A), (B) AND (C)

ϵ_r	method I (%)	method II (%)	method III (%)
1.0	34.21	34.29	29.47
4.0	37.58	30.56	36.81
6.15	30.20	40.39	31.54

B. Optimization via Global Optimizing Sub-Routines in `IE3D [7]`

The results of global optimization of the initial U-slot antennas designed via the three empirical techniques, are presented in Figs. 15 to 18. While, all three algorithms were used in the optimization studies, only results from Genetic and Powell optimizers are presented here.

The ability of the built-in optimizing sub-routines in IE3D, namely Genetic, Powell and Random optimizers, to rapidly optimize initial U-slot antennas, designed via method I, is discussed in [11] and is omitted here for brevity. The results presented therein indicate that the initial U-slot antennas designed via method I can be rapidly optimized via global optimizers in IE3D. The sensitivity of these optimizers to the selection of range of optimization is also documented.

In this section, the ability of the global optimizers to rapidly optimize the initial U-slot antennas, designed by methods II and III, is discussed. It must be emphasized at this point that, since IE3D is a general purpose electromagnetic simulator, the designer must

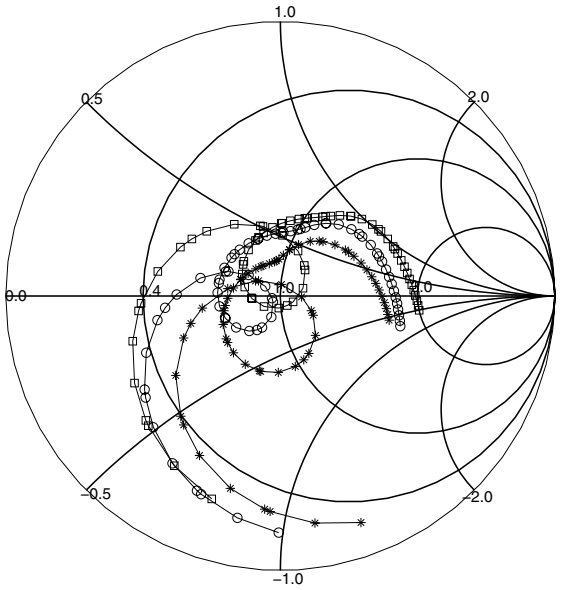

Fig. 15. Comparison of Smith Chart results of final, optimized U-slot antennas designed via method II on dielectric substrates with $\epsilon_r = 4.0$. Optimization variables - L_s and W_s; $\square - \square - \square$- parametric modeling results based optimization, $* - * - *$- after 800 generations of Genetic optimizer and $\circ - \circ - \circ -$ after 100 iterations on Powell optimizer.

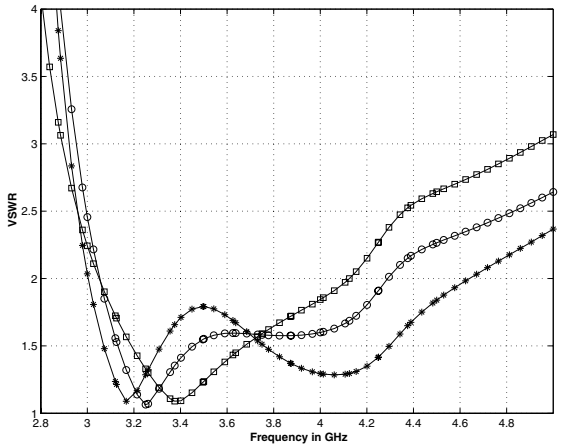

Fig. 16. Comparison of VSWR results of final, optimized U-slot antennas designed via method II on dielectric substrates with $\epsilon_r = 4.0$. Optimization variables - L_s and W_s; $\square - \square - \square$- parametric modeling results based optimization, $* - * - *$- after 800 generations of Genetic optimizer and $\circ - \circ - \circ -$ after 100 iterations on Powell optimizer.

essentially choose the optimization variables, criteria and the range over which the antenna geometry must be optimized. Here, parametric simulation results presented in [5], [9] and [10] play a vital role in selection of optimization variables for IE3D (or CAD) based optimizations.

For U-slot antenna designed via method II, both length (L_s) and width (W_s) of the slot were chosen as an optimization variable. Similarly probe location was chosen as optimization variable for U-slot antenna designed via method III. The dimensions of the final, optimized U-slot antennas, designed via methods II and III, obtained from IE3D are presented in Tables VII and VIII, respectively. The various details of the input used to set up these optimization simulations on IE3D for these optimization studies are also presented therein. The performance of the corresponding U-slot antennas, optimized via parametric modeling results, are also shown for comparison.

As seen from the figures, both Genetic and Powell optimizers on IE3D generate wideband impedance behavior in U-slot antenna geometries designed via method II. In contrast, in Figs. 17 and 18, only Powell optimizer appears to generate wideband U-slot antenna topologies for U-slot designed via method III. Overall, the results from the global optimizers in IE3D are in good agreement with the information obtained from optimization studies based on parametric modeling results in [5], [9] and [10].

TABLE VII
DIMENSIONS OF FINAL, OPTIMIZED (VIA GLOBAL OPTIMIZERS ON IE3D) U-SLOT ANTENNAS OBTAINED FOR U-SLOT ANTENNA GEOMETRY DESIGNED BY METHOD II [6], FOR DESIGN EXAMPLE (B), REFERRING TO FIG. 1. (ALL DIMENSIONS IN MM)

Parameter	Initial	Genetic Optimizer	Powell Optimizer
ϵ_r	4.0	4.0	4.0
$\tan(\delta)$	0.002	0.002	0.002
h	5.5	5.5	5.5
L	17.96	17.96	17.96
W	34.49	34.49	34.49
L_s	16.01	12.85	14.1
W_s	15.94	12.0	11.65
t	1.53	1.53	1.53
a	0.95	2.55	1.9
b	1.0	2.56	1.96
F	8.96	8.96	8.96
R_{probe}	0.635	0.635	0.635
lower freq. (f_l) in GHz	-	3.1	3.1
upper freq.(f_u) in GHz	-	4.1	4.1
Optimization variable(s)	-	L_s,W_s	L_s,W_s
Optimization criterion	-	$\lvert S_{11}\rvert \leq$ -10 dB	$\lvert S_{11}\rvert \leq$ -10 dB
Number of generations / iterations	-	800	100

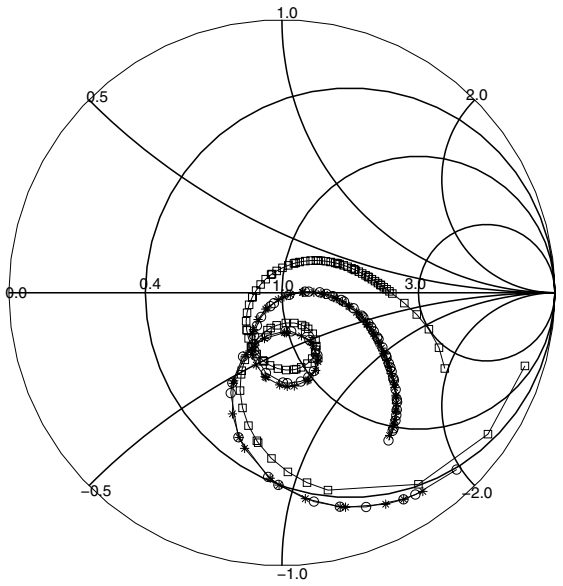

Fig. 17. Comparison of Smith Chart results of final, optimized U-slot antennas designed via method III on dielectric substrates with $\epsilon_r = 4.0$. Optimization variables - probe location; $\square - \square - \square$- parametric modeling results based optimization, $* - * - *$- after 400 generations of Genetic optimizer and $\circ - \circ - \circ -$ after 100 iterations on Powell optimizer.

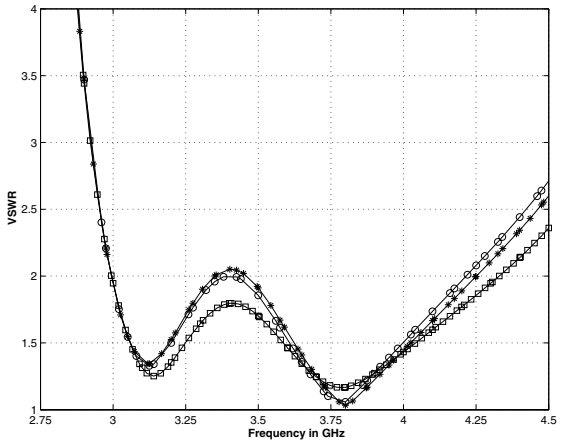

Fig. 18. Comparison of VSWR results of final, optimized U-slot antennas designed via method III on dielectric substrates with $\epsilon_r = 4.0$. Optimization variables - probe location; $\square - \square - \square$- parametric modeling results based optimization, $* - * - *$- after 400 generations of Genetic optimizer and $\circ - \circ - \circ -$ after 100 iterations on Powell optimizer.

C. Comparison of Gain and Radiation Characteristics

In the previous sections of this paper, focus had been directed towards broadband characteristics of U-Slot geometries generated from the three empirical techniques, *viz.*, methods I, II and III. Return-loss and impedance data for both initial (unoptimized) and final (optimized) U-Slot designs have shown that method III, introduced in Section III of this paper, is a better choice for wideband applications of all the three empirical techniques. However for a complete performance appraisal of the three methods, it is necessary to examine other aspects of antenna performance, namely, the gain and radiation characteristics. To avoid tedium, results for gain vs. frequency and co and cross-polar radiation patterns in the $\phi = 0^\circ$ and 90° cardinal planes are included in this subsection for substrate permittivity $\epsilon_r = 4.0$ and for both initial and optimized U-Slot designs from each of the three techniques. The dimensions of the U-Slot antenna from the three techniques are available in Table IV (for both initial and optimized cases). Figs. 19 to 24 shows the relevant results, and are briefly discussed below.

In Figs. 19 and 20 the peak boresight ($\phi = 0^\circ, \theta = 0^\circ$) gain is seen to be slightly higher for designs via methods I and II, compared to method III. Interestingly, the peak gain occurs at 3.2 GHz for designs via methods II and III, while for method I the gain is at the peak around 2.8 GHz in both initial and optimized

TABLE VIII
DIMENSIONS OF FINAL, OPTIMIZED (VIA GLOBAL OPTIMIZERS ON IE3D) U-SLOT ANTENNAS OBTAINED FOR U-SLOT ANTENNA GEOMETRY DESIGNED BY METHOD III [SECTION III], FOR DESIGN EXAMPLE (B), REFERRING TO FIG. 1. (ALL DIMENSIONS IN MM)

Parameter	Initial	Genetic Optimizer	Powell Optimizer
ϵ_r	4.0	4.0	4.0
$\tan(\delta)$	0.002	0.002	0.002
h	6.45	6.45	6.45
L	18.44	18.44	18.44
W	25.54	25.54	25.54
L_s	12.76	12.76	12.76
W_s	9.93	9.93	9.93
t	1.43	1.43	1.43
a	2.84	2.84	2.84
b	2.84	2.84	2.84
F	9.22	6.57	6.445
R_{probe}	0.635	0.635	0.635
lower freq. (f_l) in GHz	-	3.0	3.0
upper freq.(f_u) in GHz	-	4.2	4.2
Optimization variable(s)	-	probe location	probe location
Optimization criterion	-	$\lvert S_{11}\rvert \leq$ -10 dB	$\lvert S_{11}\rvert \leq$ -10 dB
Number of generations / iterations	-	400	100

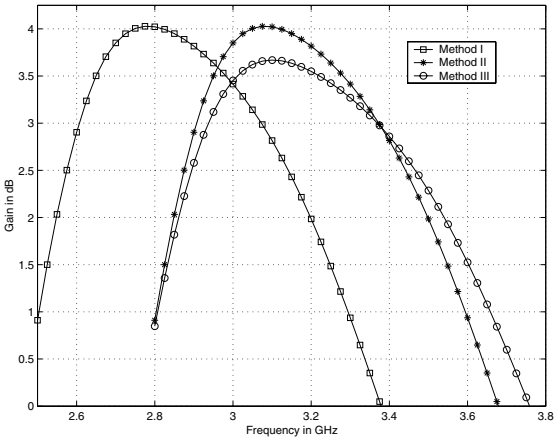

Fig. 19. Boresight gain vs. frequency for *initial* U-Slot patch designs for data in Table IV and dielectric substrates with $\epsilon_r = 4.0$

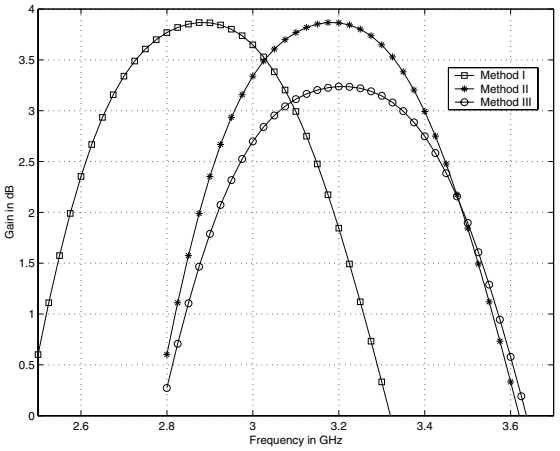

Fig. 20. Boresight gain vs. frequency for *optimized* U-Slot patch designs for data in Table IV and dielectric substrates with $\epsilon_r = 4.0$

designs.

Following the design example in [5, Section VII], empirical equations from [5, Table II] for substrate $\epsilon_r = 4.5$ were used to calculate the $\frac{\mathrm{W}}{\mathrm{h}}$ ratio for $\epsilon_r = 4.0$ at a resonant frequency of $\mathrm{f_r} = 3.2$ GHz. Subsequently the dimensional invariance relationships [5, Table I] were used to obtain the other dimensions of the U-Slot for $\epsilon_r = 4.0$. Thus, when the method I design was simulated via IE3D [7], the peak gain occured at 2.8 GHz as seen in Figs. 19 and 20. This can be realized since U-Slot dimensions obtained via method I (using empirical equations for $\epsilon_r = 4.5$) were not appropriate for $\epsilon_r = 4.0$.

One also notices in Figs. 19 and 20 the peak boresight gain differences between U-Slot designs from methods I and III are roughly 1 dB but occur at frequencies of 2.8 GHz and 3.2 GHz, respectively. The same figures also show that U-Slots designs via methods II and III have different peak boresight gains, but at the same frequency of 3.2 GHz. These features are briefly explained, below.

For U-Slots designs via methods I and III, we note from Table IV that $\frac{\mathrm{W}}{\mathrm{L}} = 1.385$ for both cases. The overall radiating (patch) area for U-slot design via method I is *larger* than that via method III. In addition, $\frac{\mathrm{h}\sqrt{\epsilon_r}}{\lambda} \approx 0.12048$ (method I at 2.8 GHz), and ≈ 0.14028 (method III at 3.2 GHz), respectively. Since the radiation efficiency, $\mathrm{e_r}$, decreases with increase in $\frac{\mathrm{h}\sqrt{\epsilon_r}}{\lambda}$ values [1, p. 288, Fig. 4.16], [2, p. 247, Fig. 5.8], it follows that the overall boresight ($\phi = 0^\circ, \theta = 0^\circ$) gain from [1, p. 277, Eq. (4.54)]

$$\mathrm{G}(\theta, \phi) = \mathrm{e_r D}(\theta, \phi). \tag{23}$$

will be larger for method I compared to method II. The same line of arugment can be extended to show that peak boresight gains for designs via methods I and II at 2.8 GHz and 3.2 GHz, respectively, will be the same as seen in Figs. 19 and 20. (We note from Table IV that the overall U-Slot patch areas via methods I and II are almost the same.)

The radiation patterns of the initial and optimzied U-Slot geometries obtained from each of the individual methods I, II and III in Figs. 21 to 24 are discussed, briefly, next.

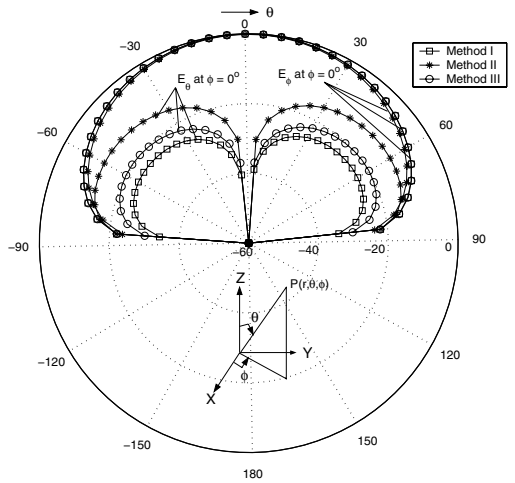

Fig. 21. Co-polar (E_ϕ) and cross-polar (E_θ) patterns for the *initial* U-Slot patch designs or data in Table IV and dielectric substrates with $\epsilon_r = 4.0$, in the cardinal plane $\Phi = 0^\circ$, at $\mathrm{f} = 3.26\mathrm{GHz}$.

The co- (E_ϕ) and cross-polar (E_θ) radiation patterns in the $\phi = 0^\circ$ principal planes are shown in Figs. 21 and 22 for the initial and optimized cases, respectively. One notices that the design via method II has the highest level of cross-polar component in comparison with the other two designs. Also, method III design has the lowest crosspolar level.

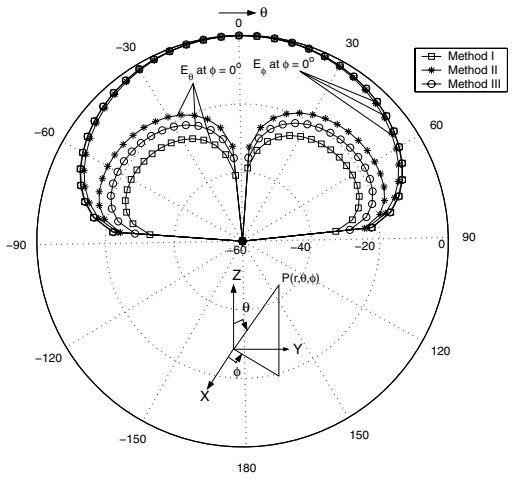

Fig. 22. Co-polar (E_ϕ) and cross-polar (E_θ) patterns for the *optimized* U-Slot patch designs or data in Table IV and dielectric substrates with $\epsilon_r = 4.0$, in the cardinal plane $\Phi = 0^\circ$ at f = 3.26GHz.

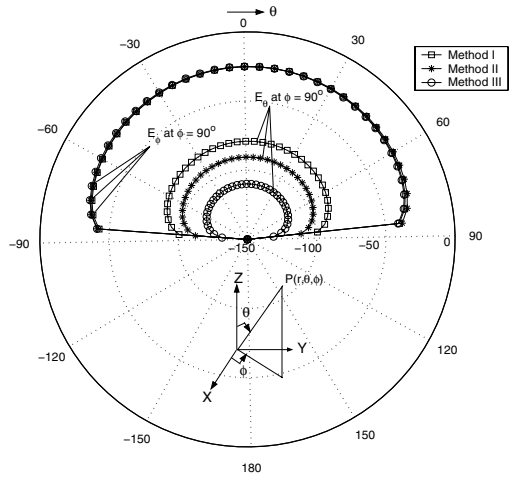

Fig. 23. Co-polar (E_ϕ) and cross-polar (E_θ) patterns for the *initial* U-Slot patch designs or data in Table IV and dielectric substrates with $\epsilon_r = 4.0$, in the cardinal plane $\Phi = 90^\circ$, at f = 3.26GHz.

One notices identical characteristics in the radiation behavior in the $\phi = 90^\circ$ principal plane as shown in Figs. 23 and 24. The crosspolar (E_θ) levels are much higher for the design via method II when compared to methods I and III.

The reasons can be traced back to the designs in Table IV. From this table, one notices that the $\frac{W}{L} \approx 1.385$ for the U-Slot designs via methods I and III. Quite interestingly $\frac{W}{L} \approx 1.98$ for the U-Slot design from method II. Since $\frac{W}{L} \approx 1.5$ yields a patch with lowest crosspolar power [1, p. 290, Fig. 4.17], one can conclude that the overall dimensions of a rectangular U-Slot patch via method II would yield the highest crosspolar levels as shown. In contrast for

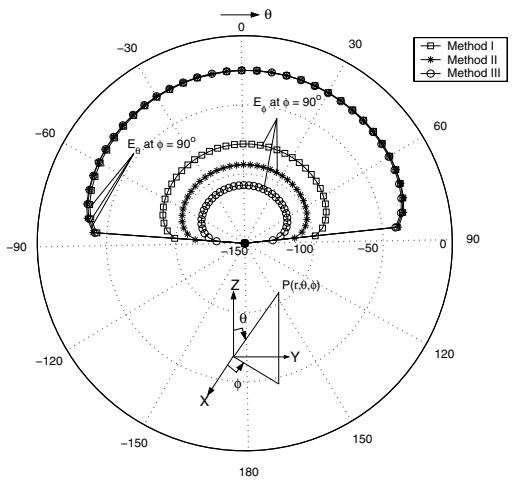

Fig. 24. Co-polar (E_ϕ) and cross-polar (E_θ) patterns for the *optimized* U-Slot patch designs or data in Table IV and dielectric substrates with $\epsilon_r = 4.0$, in the cardinal plane $\Phi = 90^\circ$ at f = 3.26GHz.

U-Slot designs via methods I and III, the crosspolar levels are comparatively smaller by roughly 10 dB.

This phenomenon was also observed for U-Slot designs on $\epsilon_r = 1.0$ and 6.15 substrate geometries. It is interesting to note that both the boresight gain and crosspolar levels could be explained fairly accurately from the corresponding characteristics of a probe-fed rectangular patch having the same overall W and L dimensions. This phenomenon suggests that the effect of the slot in the U-Slot patch is primarily to cancel the probe-inductance and produce a second resonance and contribute to the wideband characteristics.

D. Summary of Comparative Performance Analysis of Three Empirical Design Methods

In this section the main features of the three methods are summarized in Table IX.

In [5, Table II] (method I) the empirical (quadratic) curve-fit equations were developed from IE3D code [7] (method of moments) simulation results to obtain relationships of the generic form

$$\frac{W}{h} = C_2 f_r^2 + C_1 f_r + C_0, \tag{24}$$

where f_r is the design (or operating) frequency in GHz. In the above, the constants, $C_{2,1,0}$ need to be determined for specific substrate ϵ_r and h. Note that f_r is not necessarily the resonant frequency. In fact, as observed in [5], for U-Slot designs on higher ϵ_r substrates a proper resonant frequency on the Smith Chart may not strictly be found, but a minimum VSWR for a given f_r may still be viable. This approach, though very tedious, is in principle applicable to all classes

TABLE IX

Performance Evaluation of the Three Empirical Design Techniques

Empirical Techniques	**General Features of Initial Designs**	**Performance and Features of Optimization Approach**	
		Parametric Modeling Results [5], [9], [10]	**Global optimizers in IE3D (Genetic and Powell) [7]**
Method I [5]	(1) Initial designs, for most cases, exhibit wideband characteristics and have an overall $\frac{W}{L} \approx 1.385$. (2) Use of the empirical equations in [5, Section VI, Table II] may not always work well for all substrates, but is unique for substrates with $\frac{h\sqrt{\epsilon_r}}{\lambda} \geq 0.1$ (3) Acceptable boresight gain and cross-polar performance observed for low to high permittivity substrates	(a) Most significant control on wideband performance is exercised by a proper choice of the substrate thickness, or equivalently, the $\frac{h\sqrt{\epsilon_r}}{\lambda} \geq 0.1$ parameter. (b) Peak values of boresight gains and pattern shape remains relatively unaffected in the final optimized design (c) Readily optimized for enhanced bandwidth performance with smaller computational resources	(i) Results from parametric optmization studies agree with the global optimizers, *viz.,* Genetic and Powell algorithms in the commercial software, IE3D (ii) Other features are the same as that of parametric optimization scheme(s) for method I
Method II [6]	(4) The empirical design algorithm assumes *four distinct* resonant frequencies, although the first one is never used in the design of the U-Slot. (5) The design approach could yield negative or non-physical values for the dimension b shown in Fig. 1 for select substrate permittivities and yet the algorithm would still predict successful completion of design (6) Physically realizable designs appear viable on smaller substrate thicknesses and may not demonstrate wideband performance, compared to methods I and III (7) The initial designs have an overall $\frac{W}{L} \approx 2.0$ and have high cross-polar levels compared to methods I and III; the boresight gain is however higher than the designs via method III	(d) Parametric simulation approaches applied to the initial design from method II does indeed yield 10 dB return loss bandwidths $\geq 20\%$. (See Table VI for select performance data.) (e) Since initial designs from method II often exhibit poor bandwidths, their optimization for enhanced bandwidth performance generally requires several optimization variables over wide ranges resulting in increased demands on available computational resources. This is the *major disadvantage* of using method II. (f) Other antenna parameters such as boresight gain, radiation patterns remain largely unaffected in the final optimized design	(iii) The dimensions of the optimized U-Slot designs via global optimizers (Genetic and Powell algorithms) in the IE3D are different for the identical set of constraints. (See Table VII.) (iv) Parametric and global optimization results show acceptable agreement in performance behavior. ((See Figs. 15 and 16 for impedance and VSWR performances, respectively.) (v) Optimizing the design for bandwidth does not appear to affect the gain and radiation pattern behavior
Method III, Section III, this paper	(8) This empirical design algorithm is more verstatile and straightforward than method I, because it starts with the design of a rectangular patch that is extensively documented and well understood [1], [2]. (9) The initial design has the lowest cross-polar components of all three methods studied here. It also has the smallest boresight gain. The overall patch $\frac{W}{L} \approx 1.385$.	(g) Of all the three empirical design techniques, method III requires the least number of optimization cycles for designs exhibiting enhanced bandwidths (h) Other features were observed to be identical to (b) and (c) for method I, above	(vi) The dimensions of the optimized U-Slot designs via global optimizers (Genetic and Powell algorithms) in the IE3D are nearly identical for the identical set of constraints. (See Table VIII.) (vii) Parameric and Global optimizer results are agree very closely. (See Figs. 17 and 18 for impedance and VSWR performances, respectively.) (viii) Gain and radiation patterns remain almost unaffected in the final optimized design for enhanced bandwidths.

of substrates, and hence will work for those values of $\frac{\mathrm{h}\sqrt{\epsilon_r}}{\lambda}$ where the cavity model may not be accurate. This feature is unique only to method I and thus merits its application.

Method II is additionally constrained by the design algorithm [6] that proceeds by assuming a-priori existence of four distinct resonant frequencies of the U-Slot. As shown here, this additional assumption could sometimes result in non-physical dimensions for the U-Slot geometry. However, this apparent drawback of method II needs to be investigated in the future in more details for larger values of $\frac{\mathrm{h}\sqrt{\epsilon_r}}{\lambda}$. The present investigations found that it generated physically realizable U-Slot designs on low ϵ_r substrates with smaller h values.

Method III is versatile but is strictly restricted to substrate geometries satisfying the criterion $\frac{\mathrm{h}\sqrt{\epsilon_r}}{\lambda} \leq 0.1$ dictated by the applicability of the cavity model formulas [1], [2]. (However, for the U-Slot designs presented and studied here, method III did not show any limitations when applied to high ϵ_r substrates.) The design of the rectangular patch and its modification by the dimensional invariance technique to realize the U-Slot, appears to be the most straightforward of all the three approaches, and is free from the limitations that are intrinsic to methods I and II.

VII. Conclusion

In this investigation three empirical methods for the design of a probe-fed, U-Slot microstrip patch antennas on substrate permittivities $\epsilon_r = 1.0, 4.0,$ and 6.15 has been extensively studied for a comparative assessment of their performances. The analysis of the results from the three algorithms suggest that two of the methods (I and III), generate initial designs that exhibit superior wideband behavior. In contrast, method II was found to be limited to electrically thin and low ϵ_r substrates. Consequently, initial designs via method II have smaller bandwidths compared to other two techniques. Interestingly, the initial designs via methods I and III had lower peak cross-polar levels, when compared to method II by a factor of 10 dB. This was attributed to the fact that overall U-Slot patch dimension $\frac{\mathrm{W}}{\mathrm{L}} \approx 2.0$ (via method II). In comparison, $\frac{\mathrm{W}}{\mathrm{L}} \approx 1.385$ for U-Slot designs via I and III, which is close to the optimum value of $\frac{\mathrm{W}}{\mathrm{L}} \approx 1.5$ for a retangular patch. Therefore, methods I and III generate initial U-Slot patch designs that have good return loss bandwidths, and cross-polar performances when compared to method II.

Parametric, and global (Genetic and Powell) optimization methods were employed for further bandwidth enhancements of the three designs. The results showed that intital designs via methods I and III were rapidly optimized when compared to method II. Since method II design worked well when restricted to substrates with low $\frac{\mathrm{h}\sqrt{\epsilon_r}}{\lambda}$, its optimization for bandwidth enhancement was feasible with more (input) variables and allowing wide range parametric variations, resulting in increased computational resource requirements. The optimization process(es) did not affect the far-field (gain, radiation) behavior for all the cases studied here.

Acknowledgement

The authors thank Edwin Chettiar for generating results and careful reading of the manuscript. Thanks are due to Richard D. Swanson, Senior Staff Engineer, Honeywell FM &T, KC, MO, for his continued active interest and support. The authors gratefully acknowledge the financial support of Honeywell and the University of Missouri Research Board (UMRB) grant. It is a pleasure to acknowledge the help of Ms. Julie Burchett, Rogers Corp, Chandler, AZ for the TMM and Ultralam substrate samples. The authors also thank one of the anonymous reviewers for the suggestions that helped to improve the quality of this paper.

References

[1] R. Garg, P. Bhartia, I. Bahl and A. Ittipiboon, *Microstrip Antenna Design Handbook*. Norwood, MA, USA: Artech House, Inc., 2001.

[2] D. R. Jackson *et. al.*, "Computer-Aided Design of Rectangular Microstrip Antennas," chapter 5 in *Advances in Microstrip and Printed Antennas*, Kai-Fong Lee and Wei Chen (eds.), John-Wiley & Sons, Inc., NY, USA, 1997.

[3] K.-F. Lee, K.-M. Luk, K.-F. Tong, S.-M. Shum, T. Huynh, and R. Q. Lee, "Experimental and Simulation Studies of the Coaxially Fed U-Slot Rectangular Patch Antenna,"*IEE Proc. Microw. Antennas Propag.*, part H, vol. 144, no. 5, pp. 354-358, October 1997.

[4] K.-F. Tong, K.-M. Luk, K.-F. Lee and R. Q. Lee, "A Broad-Band *U*-Slot Rectangular Patch Antenna on a Microwave Substrate,"*IEEE Trans. Antennas Propagat.*, vol. 48, no. 6, pp. 954-960, June 2000.

[5] V. Natarajan and D. Chatterjee, "An Empirical Approach for Design of Wideband, Probe-Fed, U-Slot Microstrip Patch Antennas on Single-Layer, Infinite, Grounded Substrates,"*Applied Computational Electromagnetics Society* (ACES) *Journal*, vol. 18, no. 3, pp. 191-201, November 2003.

[6] S. Weigand, G. H. Huff, K. H. Pan and J. T. Bernhard, "Analysis and Design of Broad-Band Single-Layer Rectangular U-Slot Microstrip Patch Antennas,"*IEEE Trans. Antennas Propagat.*, vol. 51, no. 3, pp. 457-468, March 2003.

[7] Zeland Software, Inc., *IE3D User's Manual*, Release(s) 9.0. Fremont, CA, USA.

[8] V. Natarajan, E. Chettiar, and D. Chatterjee, "Performance of Two Empirical Techniques for Design of Optimized, Wideband, U-Slot Antennas," *IEEE Antennas and Propagation and* URSI/USNC *Symposium Digest*, vol. 3, pp. 2424-2427, Monterey, CA, June, 2004.

[9] E. Chettiar, V. Natarajan, and D. Chatterjee, "Effect of Slot Width Variation on Performance of Wideband, Probe-Fed, U-slot Patch Antennas,"*IEEE Antennas and Propagation and* URSI/USNC *Symposium Digest*, vol. 2, pp. 1792-1795, Monterey, CA, June, 2004.

[10] V. Natarajan and D. Chatterjee, "An Empirical Design Technique for U-slot Microstrip Antennas on Microwave Substrates; Part-I: Infinite Ground Plane Analysis," technical report ECE-UMKC02-HNYWL-TR01, prepared under contract for Honeywell Federal Manufactoring and Technologies, KC, MO, ECE Division, SICE, UMKC, September 2002.

[11] V. Natarajan and D. Chatterjee, "Optimization Studies for Single-Layer, Wideband, U-Slot Antennas on Microwave Substrates Using the IE3D Code," *Proceedings of* 20^{th} *Annual Review of Progress in Applied Computational Electromagnetics* at Syracuse, NY, April 19-23, 2004.

[12] V. Natarajan and D. Chatterjee, "Effect of Substrate Permittivity and Thickness on Performance of Single-Layer, Wideband, U-Slot Antennas on Microwave Substrates," *Proceedings of* 20^{th} *Annual Review of Progress in Applied Computational Electromagnetics* at Syracuse, NY, April 19-23, 2004.

[13] R. Bhalla and L. Shafai, "Resonance Behavior of Single U-Slot Microstrip Patch Antennas," *Microwave and Optical Technology Letters*, vol. 32, no. 5, pp. 333-335, March 5 2002.

[14] E. Chettiar, V. Natarajan, and D. Chatterjee, "Comparison of Resonant Frequency Calculations for Wideband U-Slot Antennas on Microwave Substrates," *IEEE Antennas and Propagation and* URSI/USNC *Symposium Digest*, vol. 4, pp. 3713-3716, Monterey, CA, June 21-27, 2004.

[15] D. Chatterjee, "Development of a Fast, Iterative Computer Code for Simulations of Probe-Fed, Rectangular Patch Microstrip Antennas," part II of report ECE-UMKC00-HNYWL-TR01, June 2000, prepared under contract for Honeywell International Inc., FM&T, KC, MO.

Venkataraman Natarajan was born in Chennai, India on July 2, 1978. He received his M.S. and B.S. degrees in Electrical Engineering from the University of Missouri-Columbia, USA, and University of Madras, Chennai, India, in 2002 and 2000, respectively. Since August 2000 he has been working as a Graduate Research Assistant at the Computational Electromagnetics Laboratory at the University of Missouri Kansas City. He was awarded the Outstanding Graduate Student award in April 2001. He has been an IEEE Student Member since August 1998. Mr. Natarajan is currently working as a technical consultant at Seattle, WA.

Deb Chatterjee received B.E.Tel.E (Bachelor's) degree in Electronics and Telecommunication Engineering from Jadavpur University, Kolkata (Calcutta), India, in 1981, M.Tech (Master's) degree in Electronics and Electrical Communication Engineering from IIT Kharagpur, India, in 1983, M.A.Sc (Master of Applied Science) degree in Electrical and Computer Engineering from Concordia University, Montreál, Canada, in 1992, and, the Ph.D. degree in Electrical Engineering from the Department of Electrical Engineering and Computer Science, University of Kansas, Lawrence, USA in 1998. From 1983-1986 he worked with the Antenna Group at Hindustan Aeronautics Limited (HAL), Hyderabad, India, on monopulse feeds for applications to the Fire Control Radar. Since August 1999 he is an Assistant Professor with the Electrical and Computer Engineering, University of Missouri Kansas City (UMKC). His current research interests are, analytical and numerical techniques in electromagnetics - with an emphasis on (asymptotic) high-frequency applications, modeling of planar and conformal phased and smart antenna arrays, analysis and design of wideband microstrip antenna elements, and, electromagnetic effects in biological systems. Dr. Chatterjee is a member of the IEEE Antennas and Propagation and Applied Computational Electromagnetics Societies, and has served as a technical reviewer for the *IEEE Transactions on Antennas and Propagation*, *IEEE Antennas and Wireless Propagation Letters*, *IEEE Transactions on Vehicular Technology*, *Applied Computational Electromagnetics Society Journal*, and *Radio Science*. He has also served as a summer technical consultant to Honeywell Federal Manafacturing and Technologies, KC, MO.

BROADBAND ANTENNA RESPONSE USING HYBRID TECHNIQUE COMBINING FREQUENCY DOMAIN MoM AND FDTD

R.A. Abd-Alhameed[1], P.S. Excell[1], and M.A. Mangoud[2]

[1]Telecommunications Research Centre, Bradford University, Bradford, West Yorkshire, BD7 1DP, UK, [2]Electronics and Communications Engineering Department, Arab Academy for Science and Technology and Maritime Transport (AAST), Alexandria, Egypt

***Abstract*—** A hybrid technique is proposed for computation of broadband characteristics of an antenna in the presence of a dielectric scatterer. The technique links the frequency domain Method of Moments (MoM) and the Finite Difference Time Domain (FDTD) method. The coupling of these methods is achieved by using the Equivalence Principle, applied over the intervening surface. A great reduction in computation time is achieved in the MoM domain by using an impedance interpolation technique. The Gaussian pulse (GP) and Derivative Gaussian pulse (DGP) are investigated as the excitation sources for the MoM. Examples are given and the results found to be in good agreement with alternative methods.

***Index Terms*—**Method of Moments (MoM, Finite Difference Time domain (FDTD, Hybrid computational, Equivalence surface.

I. INTRODUCTION

Hybrid techniques linking the frequency-domain Method of Moments (MoM, i.e. as applied to an integral equation formulation) and the Finite Difference Time Domain (FDTD) method provide a powerful and flexible approach to the numerical solution of a complex antenna structure in the presence of a relatively large lossy dielectric volume [1-4]. If broadband analysis is required, such as the transient response for sub-surface radar, this can be accurately investigated by computing the field propagation over the two different domains and on the equivalence-principle surface (the surface that couples the two domains), over the entire bandwidth.

Previous work in the literature includes Bretones et al's [5] use of a time-domain integral equation (TDIE) method in a hybrid approach for studying the transient excitation of a thin wire antenna located in the proximity of an inhomogeneous dielectric scatterer and above a PEC ground plane. Cerri et al. [6] also used a TDIE method in developing a hybrid technique. This method has the advantage of generating information over a wide frequency band: it does not require an iterative procedure to couple with FDTD, but it requires very large run-times when treating a junction with more than two wires [7], unlike the frequency-domain version, in which the complex metallic structures may be modelled accurately in shorter run-times and with more flexibility for modelling complex geometries. Huang et al. [8] employed a hybrid technique for modelling the interaction of ground-penetrating radar (GPR) with complex ground using a combination of frequency domain MoM, Fourier transformation and iterations; however, the reaction of the back-scattered field and the source is not discussed in detail and the run time for the MoM part is time-consuming for large source regions. Another hybrid MoM/FDTD method [9] was applied for the specific case of numerical simulations of SAR and the magnetic field of shielded RF coils loaded with a human head for a biomedical application. In another case [10] the source antenna is modelled as a stack of Hertzian dipoles. However, in both [9] and [10] the authors neglect the effect of the back-scattered field on the source. The same approximation is used in [11], which is oriented towards two-dimensional UHF/VHF propagation problems: the FDTD domain is excited just by a vertical slice near the problem area.

Research is still proceeding and more groups have become interested in the hybrid method. Bretones et al have recently published a method to combine the NEC with FDTD [12]. Unfortunately, the back-scattered field on the wire is calculated in a non-optimal way, as the algorithm entails running the FDTD code N_s times (where N_s is the number of the basis functions on the wire antenna). This requires extensive computational time, which could be prohibitive in the case of complex mobile phone handsets with (for example) helical antennas using hundreds of basis functions. Some interesting comparisons between the MoM and FDTD numerical methods are published in [13] for modelling electrically small antennas and in [14] for radiation and scattering involving dielectric objects. The advantages of each technique are discussed: this shows how a hybrid method combining the advantages of the two is a powerful and effective technique.

In this paper, the fields are computed over a wide bandwidth using the method of interpolation of impedance/admittance matrices on the antenna side, applied to frequency-domain MoM [15-17]. This saves execution time and memory requirements for the MoM, while retaining the power and maturity of FDMoM (or

FDIE). Basically, the Inverse Discrete Fourier Transform (IDFT) is performed on the equivalence-principle surface within the FDTD domain and, on the other hand, the Discrete Fourier Transform (DFT) is used to account for the back-scattered fields for the MoM domain. The number of frequency samples required to predict the coupling fields between the two domains over the entire bandwidth was investigated. The positions of these samples over the selected bandwidth were also studied in relation to their effect on recovery of the time-domain fields for different resonant structures. If the conducting structure is of a modest electrical size, such that it obviously cannot support more than one resonant mode, at a frequency that can be approximately estimated, as few as three interpolation points can be sufficient to cover the required mode bandwidth.

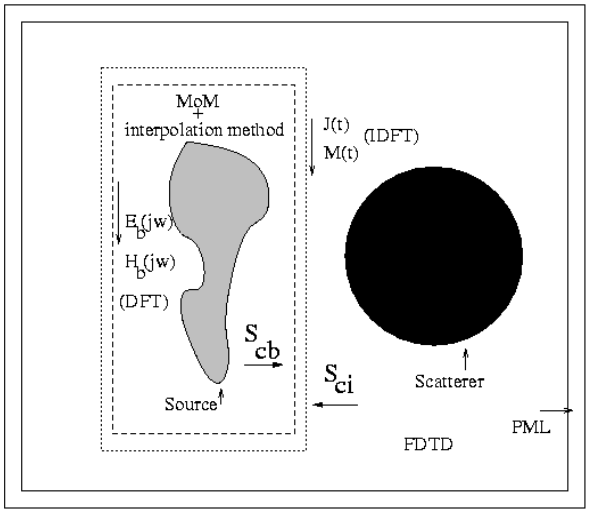

Fig. 1. Basic geometry of the hybrid combination of frequency domain MoM and FDTD.

II. SUMMARY OF THE METHOD

Consider Fig. 1, which shows two different regions. One contains a source and the other a scatterer. The coupling domains between the two regions have been addressed fully in refs. [1-3]. Usually, the coupling is implemented using a single excitation frequency with iteration across the equivalence-principle surface. The forward fields from the source to the scatterer (E(jω), H(jω)) are computed using the frequency domain MoM. The induced surface currents $J_{si}(j\omega)$ and $M_{si}(j\omega)$ that represent the FDTD excitation over the closed surface S_{ci} can be given by:

$$M_{si}(j\omega) = E(j\omega) \times \hat{n} \tag{1}$$

$$J_{si}(j\omega) = \hat{n} \times H(j\omega) \tag{2}$$

where $\hat{n}$ is the normal vector directed outward from the closed surface S_{ci}.

The back-scattered fields ($E_b(t)$, $H_b(t)$) on the enclosing surface are derived from the FDTD computation. Then the reaction of these fields on the source region can be stated as:

$$\begin{aligned} R_B &= < E_{ts}, J_{ib} > - < H_{ts}, M_{ib} > \\ &= \int_{S_{cb}} (E_{ts} \bullet J_{ib} - H_{ts} \bullet M_{ib}) ds_{cb} \end{aligned} \tag{3}$$

where E_{ts} and H_{ts} are the test electric and magnetic fields from the source. M_{ib} and J_{sb} are the induced magnetic and electric surface currents on the closed surface S_{cb}. "<>" and "•" represent the inner product and the vector dot product respectively.

The procedure is repeated until a steady state solution for this single frequency is reached. In general, if broadband antenna analysis is required, many frequency samples are required to cover the entire bandwidth on the FDMoM side to predict the required time variations of the induced surface current on the enclosed equivalent surface (for use by the FDTD side). Using IDFT, these samples can be combined as the excitation of the FDTD domain. The main problem is the computational time required to evaluate these samples on the MoM side of the problem because the MoM has to be executed once for each sample.

Thus, an impedance/admittance interpolation method on the MoM side was developed to predict these fields on the equivalence-principle surface. The method requires storage of impedance matrices for a few different frequencies over the specified bandwidth. Then, using the quadratic interpolation method (requiring three selected points), the impedance can be found at any frequency between these points, as follows.

The interaction [Z] matrices for the three selected frequencies are directly computed by FDMoM [1-3]. The elements of [Z] for the intermediate frequencies are approximated by a quadratic function:

$$Z_{mn}(f) = A_{mn} f^2 + B_{mn} f + C_{mn} \tag{4}$$

where f denotes frequency and A_{mn}, B_{mn}, *and* C_{mn} are the *mn*th elements of the complex coefficient matrices [A], [B], and [C]. Equation (4) can be cast into a system of three equations and three unknowns. These equations, together with the elements of the directly computed [Z] matrices that are calculated at three selected frequencies, are used to determine the coefficient matrices. If the frequency band of interest is especially wide, it may be necessary to divide the band into several interpolation frequency ranges and implement a process of stepping through them.

The frequency characteristics of the [Z] matrix elements can be determined by the Electric Field Integral Equation (EFIE) and the form of the basis and test functions used [15]. These equations reveal that the term e^{-jkR} dominates the frequency behaviour of the [Z]

elements. For matrix element Z_{mn}, R equals $r_{mn} = |\mathbf{r_m}-\mathbf{r_n}|$, where $\mathbf{r_m}$ is the observation location and $\mathbf{r_n}$ is the source location. When the observation and source points are close to each other, r_{mn} is small and $e^{-jkr_{mn}}$ varies slowly with frequency. When they are far from each other, r_{mn} is large and $e^{-jkr_{mn}}$ fluctuates rapidly with frequency and thus dominates the frequency variations of the [Z] matrix elements. An improved method for computation of [Z] elements in this case can be implemented by direct interpolation of the [Z] elements divided by the factor $e^{-jkr_{mn}}$ and then the resultant interpolation value is multiplied by the same factor [15,16].

The interpolation function can also be cast in a form that accurately models the behaviour of the large-amplitude terms in [Z], i.e. the self-terms and those quantifying the coupling between very close segments. This has been implemented for thin wire antennas [16]. However, this was done to increase the accuracy in evaluating the terms of [Z] at the intermediate frequencies or to allow larger interpolation frequency ranges.

Thus, the currents for a particular frequency, resulting from a wideband excitation (e.g. a Gaussian Pulse) can be found once the impedance matrix at that frequency can be predicted. Therefore, the scattered fields on the equivalence-principle surface due to the predicted currents can be computed. Once these fields are computed, the finite difference equations at the equivalent surface can be stated as follows:

$$\mathbf{E} = \mathbf{E}_{FDTD} + IDFT(\hat{\mathbf{n}} \times \mathbf{H}(j\omega))/(\varepsilon/\Delta t + \sigma/2) \quad (5)$$

$$\mathbf{H} = \mathbf{H}_{FDTD} - IDFT(\mathbf{E}(j\omega) \times \hat{\mathbf{n}})/(\Delta t/\mu) \quad (6)$$

where E_{FDTD} and H_{FDTD} are the normal electric and magnetic field finite-difference updating equations. Δt is the time step, ε, μ and σ are the absolute permittivity, permeability and conductivity of the surrounding medium, respectively. The above equations are executed for each FDTD iteration and hence simultaneously cover all of the frequency samples, taking into the account the frequency spectrum of the pulse applied, obtained from MoM and interpolation by performing the IFDT on the transferred excitation data. Using the above technique and the theory presented in [2] it can be deduced that the computation time required for the hybrid method depends predominantly on the execution time of FDTD method.

III. RESPONSES AND NUMBER OF SAMPLES

Consider Fig. 2, which shows the frequency responses of two different forms of the real part of the antenna input impedance. Usually the selected points shown in both of them can be used for interpolation, to predict the entire response. This response will be used to obtain the time-domain performance of the antenna using the inverse Fourier transform. For the case shown in Figure 2a, uniform frequency sampling can be used since the rate of change of the curve at resonance is slow. However, for the case shown in Figure 2b, a very large number of frequency samples would be required to resolve the detail in the resonance peaks. Since the location of the resonances cannot normally be known beforehand, there is no convenient way to quickly determine the order of the samples required for interpolation. For a limited known bandwidth the resonances can usually be predicted with sufficient accuracy for some extended set of interpolation points by applying approximated analytical approaches: confidence in the choices can be strengthened by repeating the simulation two or three times with differing choices to test for stability.

To save time, and use the same number of frequency samples to predict the frequency response, the non-uniform inverse Fourier transform was used:

$$x(t) = 2\sum_{i=1}^{n} \Delta\omega_i \,\mathrm{Re}(X(j\omega_i)e^{j\omega_i t}) \quad (7)$$

where ω_i (for i=1,2,…,n) is the i^{th} frequency sample.

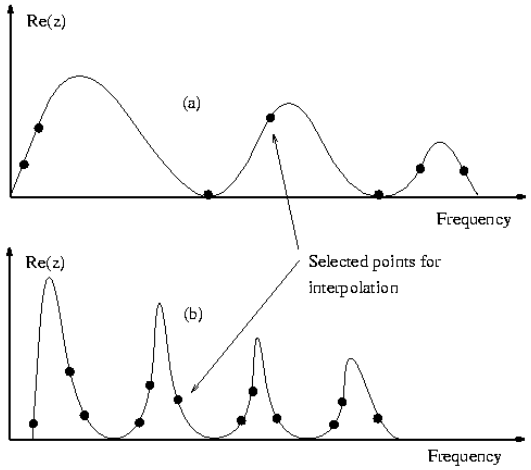

Fig. 2. Frequency response of the real part of input impedance. (a) wide resonance, (b) sharp resonance.

$\Delta\omega_i$ is the frequency width from the preceding sample to the frequency sample ω_i. A substantially higher density of frequencies ω_i (for i=1,2,…,n) is chosen around the sharp resonance regions of the frequency response. This method must be used when a strong resonance is present, either inherently in one part of the system (e.g. a helical antenna) or as a result of strong coupling between the source and a scattering element. Since the time-domain behaviour of the antenna can be found, the scattered fields in the time domain can be found easily, subject to the proper selection of frequency samples that adequately predict the approximated antenna response. Therefore, these fields can be used to replace the actual source (the antenna) by a chosen equivalent surface. This surface can then be coupled to any time-domain method, such as FDTD, in a hybrid technique.

IV. EXCITATION SOURCE

The input voltage source considered was either a Gaussian pulse (GP) or a derivative Gaussian pulse (DGP). The temporal behaviour of this impressed voltage source can be given as follows. For GP excitation:

$$v(t) = Ae^{-g^2(t-t_d)^2} \tag{8}$$

where A is the amplitude of the pulse, g is the inverse of the rise time, and t_d is the time delay.

The frequency domain version of this source can be found using Fourier transformation, thus:

$$v(j\omega) = \frac{\sqrt{\pi}}{g} e^{-jt_d\omega} e^{-(\omega/(2g))^2} . \tag{9}$$

A pulse with parameters A=1V, g=1.5×10^9 s^{-1} and t_d = 2.5ns was chosen as an example having a 3dB bandwidth somewhat less than 1 GHz. This provides excitation across the operating band for antennas with a bandwidth of 1 GHz. The time-recovered GP, reconstituted from the frequency domain using 128 selected frequency samples uniformly distributed over the frequency spectrum, was found to be close to the shape of the original pulse. The working bandwidth of this pulse was taken to be 1.5 GHz.

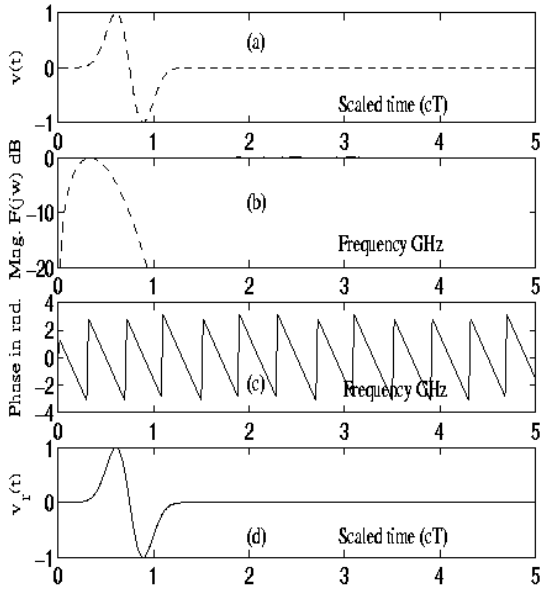

Fig. 3. Example of a differential Gaussian pulse for g=1.5×10^{9}s^{-1} and t_d=2.5ns. (a) vs. scaled time. (b) Spectrum magnitude vs. frequency. (c) Phase vs. frequency. (d) Recovered pulse for 128 frequency samples, vs. scaled time.

The second excitation source was represented by a DGP. Originally, this pulse was used because there is no DC component in its frequency spectrum. It is given by:

$$v(t) = -Ag^2(t-t_d)e^{-g^2(t-t_d)^2} \tag{10}$$

where A is the amplitude. The frequency domain version of the above pulse can be found, using a Fourier transform, as:

$$v(j\omega) = -j\frac{A\omega}{g}\sqrt{\pi}e^{-jt_d\omega}e^{-(\omega^2/4g^2)} . \tag{11}$$

The time-domain version of the DGP, its spectrum and phase are shown in Fig. 3. The time reconstruction of this pulse over 128 frequency samples, uniformly distributed over 1.5 GHz, is presented in Fig. 3d. This was obtained using the inverse discrete Fourier transform.

V. SIMULATION AND RESULTS

Several examples are given to highlight the features of the method. The results are compared with those from some homogeneous time-domain methods such as pure FDTD and TDIE [18]. In all cases, the dielectric volume was considered to be free space. This is adequate to test the stability of the method and its agreement with the results of other methods (which may not be able to handle dielectrics).

Example 1. A straight wire antenna of length 0.5m and radius 1mm was analysed when driven by a DGP with g=1.5×109 s^{-1} and t_d=2.5 ns. The number of frequency samples for the Z-matrix interpolation used here was 9. The proposed method was executed over the entire bandwidth of 1.5 GHz. The numbers of frequency samples over the bandwidth were chosen to be 64 and 128, in order to match the inverse discrete Fourier transforms: a uniform discretisation technique was used in this case. The source current versus time is shown in Fig. 4 and the results are compared with those from standard packages implementing the FDTD and TDIE methods. The results of the proposed method are in good overall agreement with those obtained from FDTD and TDIE.

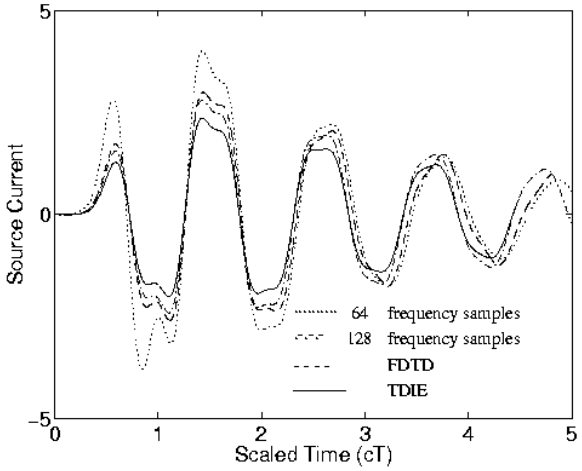

Fig. 4. The input source current versus scaled time for a dipole excited by a DGP.

Example 2. The same wire antenna geometry of example 1 was used, but excited by a GP having $g=1.5\times109\ s^{-1}$ and $t_d=2.5$ ns. The number of frequency samples used for Z-matrix interpolation was 14. The lowest frequency sample was chosen at 25Hz to exclude DC effects, which would require a different treatment. The proposed method was run over the rest of the entire bandwidth of 1.5 GHz. The number of frequency samples used to cover the bandwidth was chosen to be 128, uniform discretisation again being used. The source current versus time is shown in Fig. 5. The results are in good agreement with those obtained from FDTD alone and TDIE.

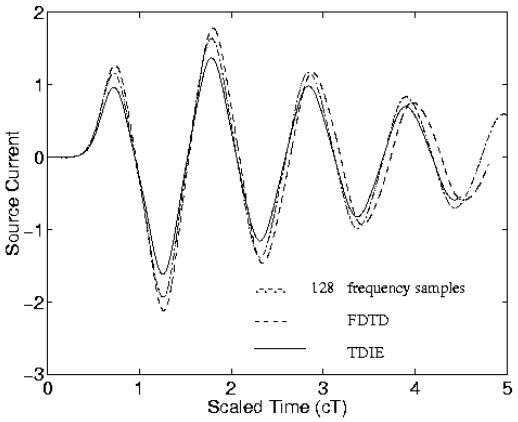

Fig. 5. The input source current versus scaled time for a dipole excited by a GP.

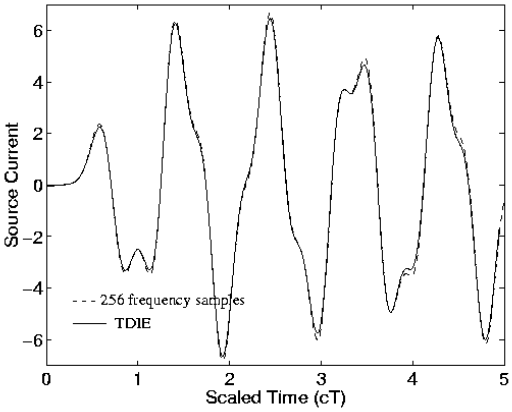

Fig. 6. The input source current versus the scaled time for a helix excited by a DGP.

Example 3. A source consisting of a helical wire antenna was analysed, using the same excitation voltage as in Example 1. The helix had the following geometry: pitch distance 0.01m; helix radius 0.015m; wire radius 0.5mm; no. of turns 6. The excitation was located at the centre of the helix. Fifteen points were used for Z-matrix interpolation to cover the entire 1.5 GHz bandwidth. 256 frequency samples were predicted, applying the non-uniform discretisation technique. The source current is presented in Fig. 6: compared to the results obtained from TDIE, the proposed method is quite acceptably accurate for such a complex geometry as the helix. The FDTD results are not presented in Figure 6 since no real model for the exact geometry of the antenna can be developed using this method, due to its curved wire nature.

Example 4. A near field due to a dipole, having similar configuration and voltage excitation as in Example 1, was investigated using the proposed technique. The dipole was replaced by the closed equivalence-principle surface inside the FDTD region that represents the scattered fields, as shown in Fig. 7. The size of the closed surface was 4×4×61 cells (cell size = 1cm). A suitable number of frequency samples used inside the FDTD zone, as predicted from the selected frequency points, was 256. The memory required for field transformation was around 4Mbyte. The interval time considered in this example was double the time taken by the previous examples, to illustrate the stability of the method. The near fields at 0.05m from the antenna are shown in Fig. 8. The results show a good agreement of the present method with that computed from the pure FDTD and the TDIE methods, both in the decay of the amplitude and the periods of the following pulses, for interval times of most interest. A maximum of less than 5% difference was detected between these field amplitudes. The computation time was two hours on a Sun Sparc 10 workstation.

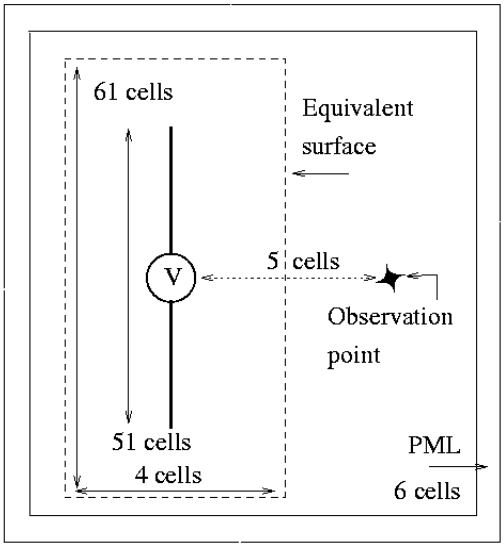

Fig. 7. The antenna geometry of example 4 inside the hybrid method domains.

Example 5. A two-arm square-spiral wire antenna with a scatterer formed of two crossed wire dipoles (Fig. 8) were investigated. The square spiral was selected here simply to compare the results with FDTD, as its shape is conformal to the rectangular grid. The radius of all of

the wires was chosen to be 1mm. The spiral was located 3cm above the cross point (origin point) of the crossed dipoles. The source excitation was placed at the centre of the spiral using the same DGP as in Example 1. The spiral antenna was then replaced by the closed equivalence-principle surface inside the FDTD region that represents the scattered fields, as shown in Fig. 8. The size of the closed surface was 16×18×4 cells (cell size = 1cm). The number of frequency samples predicted from the selected frequency points was 256 and the memory required to store the fields on the equivalent surface was 2Mbyte. The near electric field was recorded at x = 0.0m, y = 0.08m, z = 0.03m, as shown in Fig. 9. There is good agreement between the two methods although the peak values differ by approximately 3%. The total simulation time was two hours on a Sun Sparc 10 workstation.

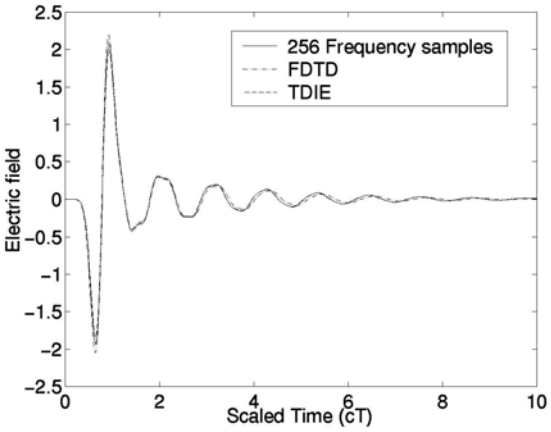

Fig. 8. The electric field component E_z versus the scaled time at 0.05m from a source dipole excited by a DGP.

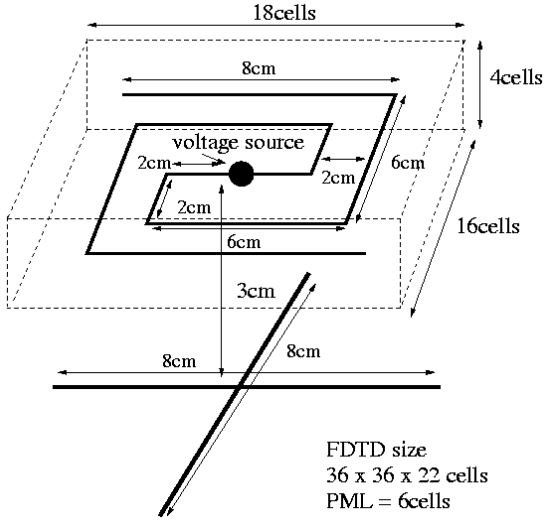

Fig. 9. The antenna geometry of example 5 inside the hybrid method domains.

VI. CONCLUSIONS

A method to obtain broadband antenna responses from the hybrid technique using the frequency-domain Method of Moments (IE Method) and the Finite Difference Time Domain method has been presented. This has the advantages that complex arbitrarily-shaped metallic antenna structures can be simulated with the mature FDMoM method, in combination with large complex penetrable dielectric bodies that can be efficiently modelled with the FDTD method. A [Z]-matrix interpolation methodology on the MoM side was used in order to significantly reduce the computational time required for wide-band performance evaluation of antennas. Quadratic interpolation was found sufficient to predict the time-limited responses. The use of non-uniform frequency samples on sharp resonances has been shown to be a viable technique for minimisation of computational and memory requirements. The results were in reasonable agreement with available data from relevant (but less flexible) single-algorithm methods: it is likely that the disagreement in amplitude (of less than 5%) with the FDTD method could be due to deficiencies in the representation of wires in the latter: this does not invalidate the fundamental merits of the hybrid method. Particularly, the computation time for the present method depends mostly on the running time of the FDTD method.

An enhancement to the technique can be achieved by implementation of the method in Ref. [2]. In a single-frequency example, this showed how current crossing the boundary between the two domains can be represented: this has great advantages for the present work because it can reduce the memory requirements and the computation time since only the most complex part of the antenna need to be modeled.

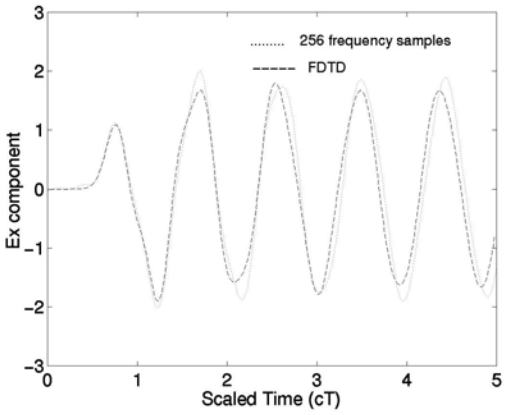

(a)

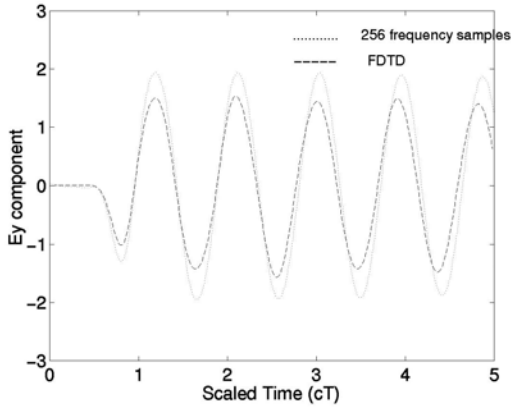

(b)

Fig. 10. The electric field component versus the scaled time at position x = 0.0m, y = 0.08m, z = 0.03m of Fig. 8; (a) E_x component, (b) E_y component.

REFERENCES

[1] R.A. Abd-Alhameed, P.S. Excell, J.A. Vaul and M.A. Mangoud, "A Hybrid Treatment for Electromagnetic Field Computation in Multiple Regions", Electronics Letters, Vol. 34, No. 20, pp 1925-1926, Oct. 1998.

[2] M.A. Mangoud, R.A. Abd-Alhameed, P.S. Excell and J.A. Vaul, "Conduction current crossing domain boundaries in heterogeneous hybrid computational electromagnetics formulation", Electronics Letters, Vol. 35, No. 21, pp. 1786-1788, Oct. 1999.

[3] M.A. Mangoud, R.A. Abd-Alhameed and P.S. Excell, "Simulation of human interaction with mobile telephones using hybrid techniques over coupled domains", IEEE Trans. Microwave Theory and Techniques, Vol. 48, No. 11, pp. 2014-2021, Nov. 2000.

[4] G. Cerri, S. Chiarandini, P. Russo and A. Schiavoni, "Electromagnetic coupling between arbitrarily bent wires and scatterers analysed by a hybrid MoMTD/FDTD approach", IEE Proc., Vol. 2, No.1, pp. 261-267, 2000.

[5] A. R. Bretones, R. Mittra, and G. Martin, "A hybrid technique combining the MoM in the Time domain and FDTD", IEEE Microwave and Guided Wave Lett., Vol. 8, no. 8, pp. 281-283, 1998.

[6] G. Cerri, P. Russo, A. Schiavoni, G. Tribellini, and P. Bielli, "MoM-FDTD hybrid technique for analysing scattering problems," Electronics Letters, vol. 34, no. 5, pp. 433-440, 1998.

[7] A. D. Tinniswood, "Time Domain Integral Equations," Ph.D Dissertation, University of York, 1996.

[8] Z. Huang, K. Demarest and R. Plumb, "An FDTD/MoM hybrid technique for modeling complex antenna in the presence of heterogeneous grounds", IEEE Trans. Geoscience and Remote Sensing, vol. 37, no. 6, pp. 2692-2698, 1999.

[9] J. Chen, Z. Feng and J. Jin, "Numerical Simulation of SAR and B1-field inhomogenity of shielded RF coils loaded with human head", IEEE Trans. Biomed. Eng., vol. 45, no. 5, 1998.

[10] E. A. Forgy, W. C. Chew and J. M. Jin, "A Hybrid MoM/FDTD Technique for studying Human Head/Antenna Interactions", IEEE Antennas and Propagation Soc. Conference, Boston, pp. 81-84, 1998.

[11] K. A. Lysiak, J. K. Breakall, and J. Zmyslo, "A Hybrid MoM/FDTD Approach to UHF/VHF Propagation Problems", IEEE Antennas and Propagation Soc. Int. Symp., Baltimore, MD, pp. 358-361, 1996.

[12] A. Rubio Bretones, R. Mittra and R. Gomez Martin, "Hybrid NEC/FDTD approach for analysing electrically short thin-wire antennas located in proximity of inhomogeneous scatterers", Electronics Letters, vol. 35 no. 19, pp. 1594-1596, 1999.

[13] A. D. Monk, M. Rayner and A. D. Olver, "A Comparison of FDTD and Method of Moments to Model Electrically Small Antennas", IEEE Antennas and Propagation Soc. Int. Symp., vol. 1 pp. 565-68, 1994.

[14] J. S. Colburn, M. A. Jensen and Y. Rahmat-Samii, "Comparison of MoM and FDTD for Radiation and Scattering involving Dielectric objects", IEEE Antennas and Propagation Soc. Int. Symp., vol. 1 pp. 644-47, 1995.

[15] K.L. Virga and Y. Rahmat-Samii, "Efficient wide-band evaluation of mobile communications antennas using [Z] or [Y] matrix interpolation with the Method of Moments", IEEE Trans. Antennas and Prop., Vol. 47, No. 1, pp. 65-76, 1999.

[16] E.H. Newman, "Generation of wide-band data from the method of moments by interpolating the impedance matrix", IEEE Trans. Antennas & Prop., Vol. 36, pp. 1820-1824, Dec. 1988.

[17] E.K. Miller, "Model-based parameter estimation in electromagnetics: Part III. Applications to EM integral equations", IEEE Antennas & Prop. Magazine, Vol. 40, No. 3, pp. 49-66, June 1998.

[18] E.K. Miller, A.J. Poggio and G.J. Burke, "An integro-differential equation technique for the time-domain analysis of thin wire structures", J. Computational Physics, Vol. 12, pp. 24-48, 1973.

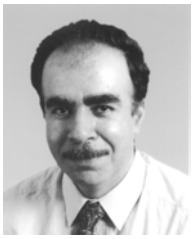

Raed A. Abd-Alhameed was born in Basrah, Iraq in 1959. He received the B.Sc. and M.Sc. degrees from Basrah university, Iraq, in 1982 and 1985 respectively, and the Ph.D. degree from the university of Bradford, UK, in 1997, all in electrical engineering. From 1997 to 1999 he was a Postdoctoral Research Fellow at the university of Bradford, specialisation in computational modelling of electromagnetic field problems, microwave nonlinear circuit simulation, signal processing of preadaption filters in adaptive antenna arrays and simulation of active inductance. From 2000 to 2003 he has been a lecturer in the University of Bradford. Since August 2003 he was appointed as a senior lecturer in applied Electromagnetics in the same University. His current research interests include hybrid electromagnetic computational techniques, antenna design, low SAR antennas for mobile handset, RF mixers and active antennas. Dr Abd-Alhameed is a member of the Institution of Electrical Engineers and Institution of Learning and Teaching for Higher Education.

Peter S. Excell is Professor of Applied Electromagnetics and Director of Research in the School of Informatics at the University of Bradford, UK, where he has worked since 1971. He obtained his BSc in Engineering Science from the University of Reading in 1970 and his PhD from the University of Bradford in 1980 for research in electromagnetic hazards. His research interests cover computational electromagnetics, EMC, antenna design and bioelectromagnetics and he has published about 200 papers; he also holds two patents. He is a UK national representative on the management committee of the EU consortium COST 261 (electromagnetic compatibility in large and distributed systems). He is a Senior Member of the Institute of Electronics and Electrical Engineers, a Fellow of the Institution of Electrical Engineers and a Chartered Engineer.

Mohab A. Mangoud was born in Alexandria, Egypt, in 1971. He received the B.Sc. and M.Sc. degrees, both in electrical engineering, from Alexandria University, Egypt, in 1993 and 1996 respectively, and the Ph.D. degree in electrical and Electrical Engineering, University of Bradford, UK in 2001. He is currently an Assistant Professor in the Electronics and Communications Engineering Department, Arab Academy for Science and Technology and Maritime Transport (AAST), Alexandria, Egypt, where he worked since 1993. He is responsible for teaching Antennas and wireless communications courses. His research interests include modeling of electromagnetic systems, Antenna Design and smart antennas. Dr. Mangoud is a member of Institute of Electrical and Electronics Engineering.

An Optimized High-Order Implicit FDTD Solver with One-Sided TF/SF for Simulation of Photonic Devices

Hossam A Abdallah
The George Washington University, Washington DC-USA

Abstract: In this paper an optimized high-order implicit finite difference time domain (FDTD) solver with one-sided total-field/scattered-field (TF/SF) excitation is developed for numerical simulation of integrated optical components. The optimized FDTD algorithm reduces the number of operations and the storage requirements to perform the matrix inversion using LU decomposition. It is shown that the one-sided TF/SF formulation is more accurate in launching the exact power into the simulation domain as well as decreasing the load on the PML-ABCs. The implementation of this tool was done in the Prometheus program, a software package of Kymata Netherlands.

Keywords: FDTD, TF/SF, Photonic devices

1. Introduction

There are different wave modeling techniques that are successfully used in modeling integrated optical structures. Finite difference time domain (FDTD), Fourier transform-beam propagation method (FT-BPM), finite difference-beam propagation method (FD-BPM), and finite element beam propagation method (FE-BPM) are the most popular and useful techniques for the simulation of integrated optics structures. FT-BPM, FD-BPM, and FE-BPM were developed for the case of weakly guiding structures where the use of the paraxial approximation and the neglection of any back reflections offer solutions in the frequency-domain. These characteristics limited the use of these methods when these assumptions are no longer valid.

The FDTD method overcomes the disadvantages of the previous methods. In simulating guided-wave optics the method became increasingly popular due to its attractive features such as ease of implementation and full-wave simulation including multiple reflections and radiation. The first FDTD algorithm proposed by Yee [1] provides a simple and a direct solution to the Maxwell's equations. However, the Yee FDTD scheme that is second order in both space and time, we refer to it as Yee(2,2), is dispersive, less accurate, and computational expensive. Higher-order FDTD schemes [2] overcome these problems but come at a higher computational cost. In this paper we implemented an implicit fourth order scheme in space and second order in time [3], we refer to it as Implicit(2,4). The Implicit(2,4) scheme introduces substantial accuracy and improvement over Yee(2,2) and because it is unconditional stable arbitrary time steps can be chosen. Detail analysis of the dispersion and accuracy of the Yee(2,2) and Implicit(2,4) schemes were performed in 1D and the results in [4]. The Implicit(2,4) algorithm requires the inversion of a tridiagonal matrix, which can be replaced by decomposing the matrix using the LU decomposition. We derive a simple algorithm to perform the LU decomposition. The new algorithm reduces the number of operations and the storage requirements to perform the LU decomposition.

It is known that implementation of sources in FDTD simulations requires more complicated procedures. The complications come from the requirements to terminate waveguides that are extended beyond the grid boundaries. All excitation techniques intend to couple the exact incident power to the FDTD grid, allow back reflected waves to pass through the excitation position, to avoid the interaction between simulated sources and the absorbing boundary conditions (ABCs), and, finally, to decrease the load on the ABCs. A popular method is the use of the total-field/scattered-field (TF/SF) method [5]. By introducing the TF/SF formulation, the simulation domain will be divided into three domains: the total-field domain, the scattered field domain, and the ABCs domain (we use the perfectly matching layer PML ABCs in all our simulations). The SF domain offers information about any scattered field meanwhile decreasing the load on ABCs.

In most of the structures of interest to our work the amount of scattering on the right side of the simulation domain is much less compared to the left side and therefore no scattered field region is added on the right side of the simulation domain. We refer to such formulation the one-sided TF/SF formulation. Implementation as well as illustrative example of the one-sided TF/SF formulation is described in detail in Section 3.

Finally the developed simulation tool was used to analyze a number of structures that are excited by waveguides. The accuracy of the results was compared to the accuracy of the Prometheus program (a beam propagation based solver).

This paper is organized into four sections as follow. Following this Introduction Section, Section 2 introduces the optimized LU decomposition of the Implicit(2,4) FDTD scheme. Section 3 introduces the one-sided TF/SF formulation and some simulation results obtained using this formulation together with the Implicit(2,4) FDTD scheme and the PML-ABCs. Finally, Section 4 presents conclusions about the work we presented.

2. Differential Equations and Difference Notations in 1D

In a 2D setting, assuming that both the fields and the dielectric structure are constant along the $y-$direction, Maxwell equations decouple into two sets (we introduce the normalized fields $\tilde{\mathbf{E}}$ and $\tilde{\mathbf{H}}$ as $\tilde{\mathbf{E}} = \sqrt{\varepsilon_0/\mu_0}\,\mathbf{E}$, $\tilde{\mathbf{H}} = \mathbf{H}$, with the speed of light in free space $c_0 = 1/\sqrt{\varepsilon_0\mu_0}$, and we drop the hat above the normalized fields) One set is constituted by electromagnetic fields with vanishing components $E_x,\ E_z,\ H_y$.

$$\varepsilon_r \partial_t E_y = c_0\left(\partial_z H_x - \partial_x H_z\right), \tag{1}$$

$$\partial_t H_x = c_0 \partial_z E_y, \tag{2}$$

$$\partial_t H_z = -c_0 \partial_x E_y. \tag{3}$$

These fields are called the TE fields. The second set has vanishing $E_y,\ H_x,\ H_z$ components.

$$\partial_t H_y = -c_0\left(\partial_z E_x - \partial_x E_z\right), \tag{4}$$

$$\varepsilon_r \partial_t E_x = -c_0 \partial_z H_y, \tag{5}$$

$$\varepsilon_r \partial_t E_z = c_0 \partial_x H_y. \tag{6}$$

These fields are called TM fields. The two sets are completely decoupled; there is no common field vector component. Therefore TE and TM fields constitute two possible classes of solutions for two-dimensional electromagnetic problems. If the medium is inhomogeneous along the x-direction, then boundary conditions at material interfaces imply that E_y, $\frac{\partial E_y}{\partial x}$, and H_z are continuous for TE fields. For TM fields H_y and E_z are continuous while $\frac{\partial H_y}{\partial x}$ is not.

We introduce and derive some notations for the finite differences that will be used for the FDTD schemes under consideration. For simplicity we consider a one dimensional finite difference notation. We apply and analyze different FDTD schemes in $1\mathbf{D}$ and then extend the implementation of the most appropriate scheme to $2\mathbf{D}$. The TE field equations in $1\mathbf{D}$ are

$$\varepsilon_r \partial_t E_y = c_0 \partial_z H_x, \tag{7}$$

$$\partial_t H_x = c_0 \partial_z E_y. \tag{8}$$

As shown in Figure 1 and as proposed by Yee [1], the discretization points for E_y and H_y are interleaved in space and time. We present notations for approximating the first and second derivatives in space or time at certain position using the neighboring points. We denote by ζ either E_y or H_x. We assume equidistant discretization with the step size Δz in the z-direction and the time step size Δt and define $\zeta_i^n = \zeta(n\Delta t, i\Delta z)$. δ_z and δ_z^2 are the approximations to the first and second derivative with respect to z, respectively.

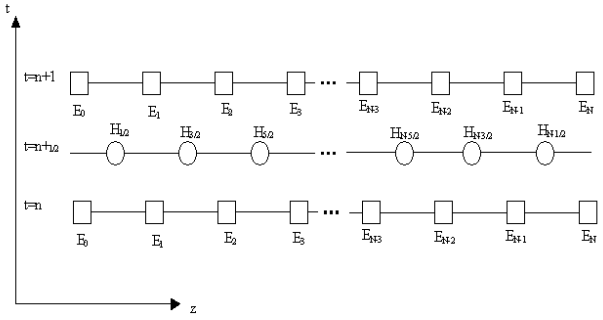

Fig. 1. Position of discretization points in a 1D grid, circles.

We differentiate between two grids. The first grid is the staggered grid in which E_y and H_x are located in space as in Fig. 1, the second grid is the

non-staggered grid in which E_y and Hy are located at the same space and time positions.
For the staggered grid we define the following finite difference expressions

$$\delta_z \zeta_{i+1/2}^n = \frac{\zeta_{i+1}^n - \zeta_i^n}{\Delta z} + O(\Delta z)^2 \quad (9)$$

$$\delta_z \zeta_i^{n+\frac{1}{2}} = \frac{\zeta_{i+1/2}^{n+\frac{1}{2}} - \zeta_{i-1/2}^{n+\frac{1}{2}}}{\Delta z} + O(\Delta z)^2 \quad (10)$$

$$\delta_t \zeta_i^{n+\frac{1}{2}} = \frac{\zeta_i^{n+1} - \zeta_i^n}{\Delta t} + O(\Delta t)^2 \quad (11)$$

$$\delta_t \zeta_{i+\frac{1}{2}}^n = \frac{\zeta_{i+\frac{1}{2}}^{n+\frac{1}{2}} - \zeta_{i+\frac{1}{2}}^{n-\frac{1}{2}}}{\Delta t} + O(\Delta t)^2 . \quad (12)$$

For higher order FDTD schemes we use also the following non-symmetric stencils, for the second order spatial derivatives

$$\delta_z^2 \zeta_{i+1/2}^n = \frac{\zeta_{i-1}^n - 2\zeta_i^n + \zeta_{i+1}^n}{(\Delta z)^2} + O(\Delta z)^2 \quad (13)$$

$$\delta_z^2 \zeta_i^{n+\frac{1}{2}} = \frac{\zeta_{i-3/2}^{n+\frac{1}{2}} - 2\zeta_{i-1/2}^{n+\frac{1}{2}} + \zeta_{i+1/2}^{n+\frac{1}{2}}}{(\Delta z)^2} + O(\Delta z)^2 \quad (14)$$

and for non-staggered grid

$$\delta_z \zeta_i^n = \frac{\zeta_{i+1}^n - \zeta_{i-1}^n}{2\Delta z} + O(\Delta z)^2 \quad (15)$$

$$\delta_t \zeta_i^n = \frac{\zeta_i^{n+1} - \zeta_i^{n-1}}{\Delta t} + O(\Delta t)^2 \quad (16)$$

$$\delta_z^2 \zeta_i^n = \frac{\zeta_{i-1}^n - 2\zeta_i^n + \zeta_{i+1}^n}{(\Delta z)^2} + O(\Delta z)^2 . \quad (17)$$

The minor problem or disadvantage when using staggered grids is the need to perform post-processing calculation/interpolation to evaluate field values at the same spatial and temporal positions. These requirements complicate the simplicity of the FDTD scheme and require additional computation time and programming effort.

2.1 Yee Scheme

Yee formulated the first FDTD scheme [1] on a staggered grid using a second order accurate approximation to the spatial and time derivatives. We will refer to it as Yee(2,2), where (2,2) refers to the order of accuracy in time and space, respectively. For the 1**D** TE fields given by equations (7) and (8), the Yee(2,2) scheme will have the form

$$\varepsilon_r \left| {}_i \delta_t E_y \right|_i^{n+\frac{1}{2}} = c_0 \delta_z H_x \Big|_i^{n+\frac{1}{2}}, \quad (18)$$

$$\delta_t H_x \Big|_{i+\frac{1}{2}}^n = c_0 \delta_z E_y \Big|_{i+\frac{1}{2}}^{n+\frac{1}{2}}. \quad (19)$$

Equations (18) and (19) are rewritten to yield explicit expressions for E_y^{n+1} given $H_x^{n+\frac{1}{2}}$ and E_y^n and for $H_x^{n+\frac{1}{2}}$ given E_y^n and $H_x^{n-\frac{1}{2}}$. Thus, from initial field distribution E_y^0, the algorithm can advance alternatingly E_y and H_x in time. The Yee(2,2) algorithm is a conditionally stable algorithm which means that the time and space steps must satisfy certain criteria. In 1**D** the stability criteria is $\Delta t \le \frac{\Delta z}{c_0}$.

2.2 A Fourth Order Implicit Scheme with Optimized LU Decomposition

In this paper we considered an implicit fourth order scheme in space and second order in time [3]. We refer to it as Implicit(2,4). The derivation of the Implicit(2,4) scheme starts with calculating the truncation error to the fourth order when approximating the first derivatives. This leads to

$$\delta_z \zeta_{i+1/2}^{n+\frac{1}{2}} = (1 + \frac{(\Delta z)^2}{24} \partial_z^2 \Big|_{i+1/2}) \partial_z \zeta_{i+1/2}^{n+\frac{1}{2}} + O(\Delta z)^4 \quad (20)$$

and by introducing a discrete approximation to the operator $\partial_z^2 \Big|_{i+1/2}$ by $\delta^2 \Big|_{i+1/2}$, we obtain

$$\delta_z \zeta_{i+1/2}^{n+\frac{1}{2}} = (1 + \frac{(\Delta z)^2}{24} \delta^2) \frac{\partial \zeta}{\partial z} \Big|_{i+1/2}^{n+\frac{1}{2}} + O(\Delta z)^4 . \quad (21)$$

Demonstrated here for 1D problems, the field values at the grind points are calculated in two steps. In the first step the values of the first order derivatives are calculated directly from the difference equation and in the second step these derivatives are expressed explicitly in terms of the field values of the neighboring grid points. The second step involves the inversion of a matrix, which is tridiagonal except at the first and last rows (this because of the need to use one sided

fourth order accurate implicit approximations to the derivatives at the first and last points at the boundary). In 2D and 3D the spatial derivatives are approximated in the same way and the matrices that relate the fields with their derivatives will be the same.

The inversion of the tridiagonal matrix can be replaced by decomposing the matrix using the LU decomposition. Performing the LU decomposition requires 5N operations and L and U will be bidiagonal matrices, except at a few rows, with one of them containing ones on the diagonal [3]. Therefore it is possible to store the results of the LU decomposition using only 3 vectors each of size N.

We derive a simple and optimized algorithm that can be used to perform the LU decomposition specifically for the discretized matrix from the Implicit(2,4) scheme. The discretized matrix of the system in (21) will have the form, dropping the time dependence notation for the moment

$$\begin{bmatrix} 26 & -5 & 4 & -1 & 0 & . & 0 \\ 1 & 22 & 1 & 0 & 0 & . & 0 \\ 0 & 1 & 22 & 1 & 0 & . & 0 \\ . & . & . & . & . & . & . \\ 0 & . & . & 0 & 1 & 22 & 1 \\ 0 & . & . & -1 & 4 & -5 & 26 \end{bmatrix} \begin{bmatrix} \partial_z\zeta|_{1/2} \\ \partial_z\zeta|_{3/2} \\ \partial_z\zeta|_{5/2} \\ . \\ \partial_z\zeta|_{N-3/2} \\ \partial_z\zeta|_{N-1/2} \end{bmatrix} = \frac{24}{\Delta z} \begin{bmatrix} \zeta_1 - \zeta_0 \\ \zeta_2 - \zeta_1 \\ \zeta_3 - \zeta_2 \\ . \\ \zeta_{N-1} - \zeta_{N-2} \\ \zeta_N - \zeta_{N-1} \end{bmatrix} . \quad (22)$$

Performing one time Gauss elimination to the first and last rows only results in

$$\begin{bmatrix} 0 & 1 & 0 & 0 & 0 & . & 0 \\ 1 & 22 & 1 & 0 & 0 & . & 0 \\ 0 & 1 & 22 & 1 & 0 & . & 0 \\ . & . & . & . & . & . & . \\ 0 & . & . & 0 & 1 & 22 & 1 \\ 0 & . & . & 0 & 0 & 1 & 0 \end{bmatrix} \begin{bmatrix} \partial_z\zeta|_{1/2} \\ \partial_z\zeta|_{3/2} \\ \partial_z\zeta|_{5/2} \\ . \\ \partial_z\zeta|_{N-3/2} \\ \partial_z\zeta|_{N-1/2} \end{bmatrix} = \frac{24}{\Delta z} \begin{bmatrix} b_1 \\ \zeta_2 - \zeta_1 \\ \zeta_3 - \zeta_2 \\ . \\ \zeta_{N-1} - \zeta_{N-2} \\ b_N \end{bmatrix} \quad (23)$$

with

$$b_1 = \frac{1}{(24)^2}(27(\zeta_2 - \zeta_1) - (\zeta_3 - \zeta_0)) \quad (24)$$

and

$$b_N = \frac{1}{(24)^2}(27(\zeta_{N-2} - \zeta_{N-1}) - (\zeta_{N-3} - \zeta_N)) . (25)$$

When simulating TE fields, the process of solving the linear system will be repeated twice for 1**D** problems, four times for 2**D** with PML-ABCs. For a large number of time steps, the computation time of the Implicit(2,4) scheme may limit the use of the scheme for simulating large structures. Hence, any optimization to the LU decomposition process will effectively reduce the total computation time. Rather than performing the LU decomposition on the systems in (22) or (23) as proposed in [3], we eliminate $\partial_z\zeta|_{3/2}$ and $\partial_z\zeta|_{N-3/2}$ from (23) and perform the LU decomposition. The resulting system has the form

$$\begin{bmatrix} 1 & 1 & 0 & 0 & 0 & . & 0 \\ 0 & 22 & 1 & 0 & 0 & . & 0 \\ 0 & 1 & 22 & 1 & 0 & . & 0 \\ 0 & 0 & 1 & 22 & 1 & . & 0 \\ . & . & . & . & . & . & . \\ 0 & . & 1 & 22 & 1 & 0 & 0 \\ 0 & . & 0 & 1 & 22 & 1 & 0 \\ 0 & . & 0 & 0 & 1 & 22 & 0 \\ 0 & . & 0 & 0 & 0 & 1 & 1 \end{bmatrix} \begin{bmatrix} \partial_z\zeta|_{1/2} \\ \partial_z\zeta|_{5/2} \\ \partial_z\zeta|_{7/2} \\ \partial_z\zeta|_{9/2} \\ . \\ \partial_z\zeta|_{N-9/2} \\ \partial_z\zeta|_{N-7/2} \\ \partial_z\zeta|_{N-5/2} \\ \partial_z\zeta|_{N-1/2} \end{bmatrix} = \frac{24}{\Delta z} \begin{bmatrix} b_1 \\ b_2 \\ b_3 \\ \zeta_4 - \zeta_3 \\ . \\ \zeta_{N-4} - \zeta_{N-5} \\ b_{N-2} \\ b_{N-1} \\ b_N \end{bmatrix} \quad (26)$$

with

$$b_2 = (\zeta_2 - \zeta_1) - 22b_1 \quad (27)$$

$$b_3 = (\zeta_3 - \zeta_2) - b_1 \quad (28)$$

$$b_{N-2} = (\zeta_{N-3} - \zeta_{N-2}) - b_N \quad (29)$$

$$b_{N-1} = (\zeta_{N-2} - \zeta_{N-1}) - 22b_N \quad (30)$$

The LU decomposition of the matrix in 20 will result in two matrices L and U of the following form

$$L*U = \begin{bmatrix} 1 & 0 & 0 & 0 & . & 0 & 0 \\ 0 & 1 & 0 & 0 & . & 0 & 0 \\ 0 & a_1 & 1 & 0 & . & 0 & 0 \\ 0 & 0 & a_2 & 1 & . & 0 & 0 \\ . & . & . & . & . & . & . \\ 0 & 0 & 0 & . & a_{p-1} & 1 & 0 \\ 0 & 0 & 0 & . & 0 & a_p & 1 \end{bmatrix} \begin{bmatrix} 1 & 1 & 0 & 0 & . & 0 & 0 \\ 0 & 1/a_1 & 1 & 0 & . & 0 & 0 \\ 0 & 0 & 1/a_2 & 1 & . & 0 & 0 \\ 0 & 0 & 0 & 1/a_3 & . & 0 & 0 \\ . & . & . & . & . & . & . \\ 0 & 0 & 0 & . & . & 1/a_p & . \\ 0 & 0 & 0 & 0 & . & 0 & 1 \end{bmatrix} \quad (31)$$

where p equals to N-2. The values of a_i can be calculated using the simple expression

$$a_1 = \frac{1}{22}, \quad a_i = \frac{1}{22 - a_{i-1}}, \quad i = 2,3,4,...,p. \quad (32)$$

Due to the round off error and the precision accuracy, we found that $a_i \approx a_6$ for $i \succ 6$ with error less than 10^{-15}. This suggests storing only the values $a_i,\ i = 1.2,...,6.$ This not only reduces the number of operations and the storage requirements to perform the LU decomposition but also reduces the number of operations to solve the linear system using the

above LU formulation. The algorithm used to solve the linear system $LUX = b$ will be carried out by solving $LY = b$ with $Y = UX$. For the first system the algorithm will have the form

$$Y_1 = b_1, \quad Y_2 = b_2$$
$$Y_i = b_i - a_{i-2} * Y_{i-1} \qquad i = 3,4,5,....,p+2 \quad (33)$$

and for solving $Y = UX$

$$X_{p+2} = Y_{p+2}, \qquad X_{p+1} = Y_{p+1} * a_p$$
$$X_i = (Y_i - X_{i+1}) * a_{i-1}, \quad i = p-1, p-2, ..., 2$$
$$X_1 = Y_1 - X_2. \quad (34)$$

2.3 Accuracy of Different FDTD Schemes

We confirm the second and fourth order of accuracy with respect to the spatial discretization of the previously presented FDTD schemes in one dimension, similarly the extension in two dimensions. The results shown in Figure 2 are obtained for a sinusoidal wave with wavelength $1.0\mu m$ propagating in free space in the positive $z-$direction over a distance of $10\mu m$, where N is the number of discretization points. For $\varepsilon_r = 1$, angular frequency ω, and wavenumber k, an exact solution of the 1**D** TE field equations can be found.

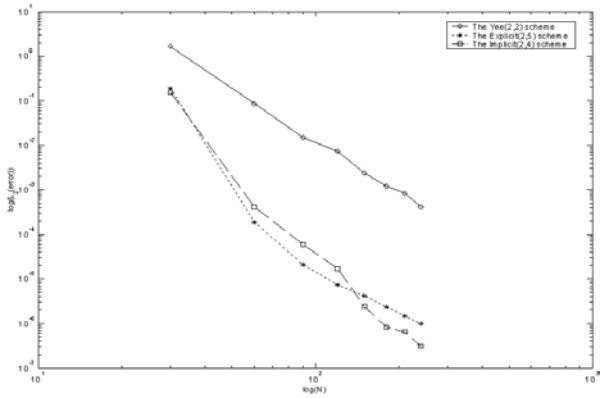

Fig. 2. L_2 norm of the difference between the numerical and exact values for E_y field at the last time step using the Yee(2,2), Explicit(2,4), and Implicit(2,4) scheme at different points per wavelength.

3. One-Sided Total-Field/Scattered-Field Formulation

The total-field/scattered-field (TF/SF) technique [5] is an efficient way to increase the quality of simulations through reducing the load on the ABCs and by offering information about scattered fields. The TF/SF was originally proposed for free space problems and for modeling point sources, which are not of great practical interest in integrated optics problems.

The simulation domain is divided into three domains: the total-field domain, the scattered field domain, and the PML domain, as in Figure 3. The formulation is based on the linearity of the Maxwell equations and on decomposing the electric and magnetic fields as sum of two components, one in the total field region and another in the scattered field region

$$E_t = E_i + E_s, \quad (35)$$
$$H_t = H_i + H_s, \quad (36)$$

where ξ_i is the incident field value, ξ_s is the scattered field value, and ξ_t is the total field value, $\xi = \{E, H\}$.

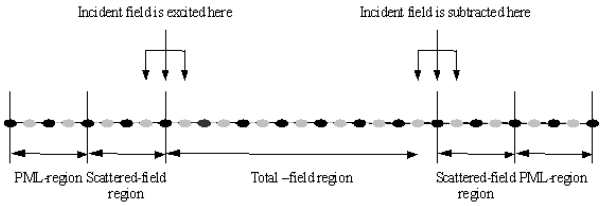

Fig. 3. The FDTD regions for 1D TF/SF grid.

Consider the 1**D** mesh as shown in Fig. 3 where two scattered-field regions are defined on both ends of the simulation domain. We call this formulation two-sided TF/SF formulation. In most of the structures of interest to our work the amount of scattering on the right side of the simulation domain is much less compared to the left side and therefore no scattered field region is added on the right side of the simulation domain. We refer to such formulation the one-sided TF/SF formulation.

The black dots in Fig. 4 are the positions of the electric field E_y, and the gray dots are the positions of the magnetic field H_x. In the total-field region, the FDTD algorithm is applied to the total field, while in the scattered-field region it is applied to scattered field only. On the interface between these two regions the incident field is

taken into account. Details of these formulation in 1**D**, 2**D**, and 3**D** are well documented in [5]. For the 1**D** TE Yee(2,2) scheme, only two FDTD update equations need modification. The first for the E_y field update equation at the TF-SF interface and the second for the H_x field update equation at the first point to the left to the TF-SF interface [5].

The discretization equations of the FDTD scheme with one-sided TF/SF formulation for 2**D** structures are similar to those introduced in [5] with one difference that is simply having no scattered field region at the right side of the simulation domain, see Fig. 4(a). As described in [5] the incident fields at all time steps need to be known for regions around the total-field – scattered-field interfaces. These fields are obtained from a separate simulation and are used as incident fields in the same regions. If the same incident fields are used to excite different structures then these fields can be stored and used in these simulations. Otherwise two simulations are run simultaneously, one for calculating the incident fields and are used as the incident fields in the same regions in the second simulation. Running two simulations approximately doubles both the memory and computational time requirements compared to running a single simulation and using stored values of the incident fields in the incident field regions. For our work the two simulation approach was selected and implemented for arbitrarily choosing the incident structures, the incident propagating mode, the simulation window etc.

Figs. 4(a) and 4(b) show the domains of the two FDTD simulations that run simultaneously. In the first simulation, the waveguide that is used to excite the structure in 4(a) is extended to the right hand side of the FDTD domain, see Fig. 4 (b). The waveguide is excited by incident modal field using the hard source excitation (the modal profile of the propagating mode of interest is obtained from a separate mode solver program, the width and refractive indices of both the exciting waveguide and background are inputs to this mode solver). Hard source excitation has the advantage of coupling the exact power into the FDTD grid compared to other excitations [2], [4].

In the second simulation with the configuration shown in Fig. 4 (a), at each time step fields obtained from the first simulation at the incident field regions are used to introduce the incident field in the same regions. For most of our simulations the size, number of cells, of the scattered-field region was equal to those of the PML region.

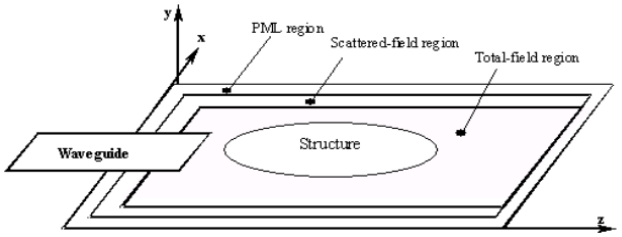

(a)

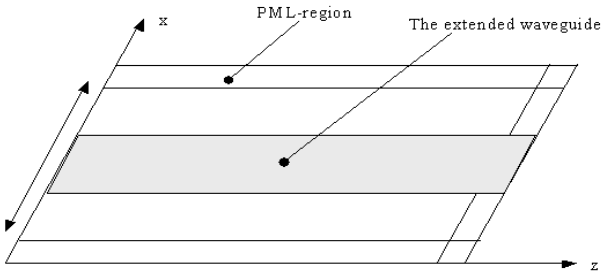

(b)

Fig. 4. (a) 2D one sided-TF/SF problem geometry, (b) 2D-problem domain for simulation of the incident field in the absence of any structures inside the TF region.

The following example demonstrates how the developed FDTD scheme with the one-sided TF/SF formulation works. Fig. 5 (b) shows the intensity plot of the E_y field for TE polarization for the cos-bend waveguide sketched in Fig. 5 (a), with width $0.5\ \mu m$, length $10\ \mu m$, offset $2\ \mu m$, and $d\alpha$ $0.1\ \mu m$. At the plane in and plane out positions the cos-bend is connected to a waveguide with the same width of the cos-bend and a length $2\ \mu m$. The refractive index of the background is 1.0 and a refractive index of 3.0 in the guiding regions. No special treatment was applied to dielectric interfaces and structures with magnetic material were not considered in this work.

The computational window is $5\times15\ \mu m$ in the x- and z-directions, and the wavelength is $1.5\ \mu m$, Δz and Δx were chosen to be $0.05\ \mu m$ and simulation is performed for $300\ fs$ with dt equal to $0.05\ fs$. The values for the PML parameters are 8, 3, 10 for the number of PMLs cells, the polynomial degree of the conductivity profile, and the reflectivity, respectively, in both the z- and x-directions. Fig. 5

(c) shows the intensity of the incident field propagating in the extended waveguide.

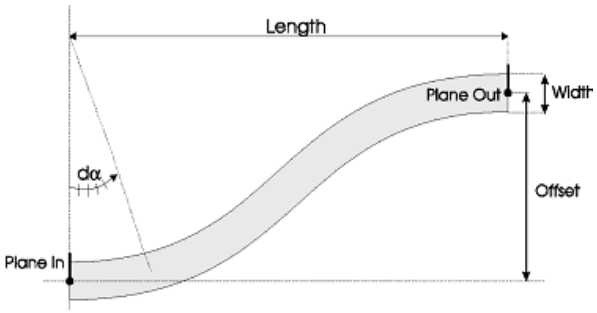

(a)

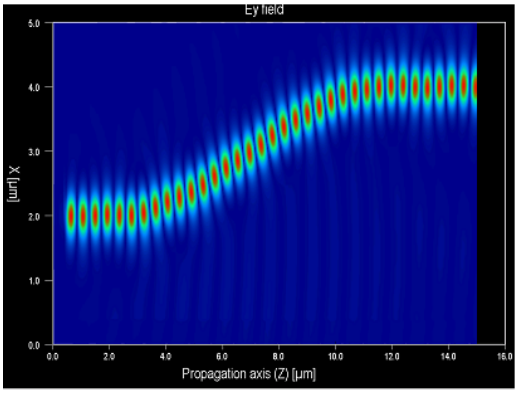

(b)

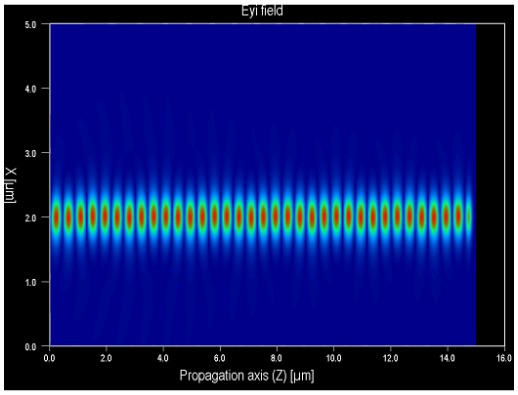

(c)

Fig. 5. (a) cos-bend waveguide, (b) the intensity of the E_y field in the SF region, (c) The intensity plot of TE-E_y field propagating in an extended waveguide used in the TF/SF excitation.

The developed simulation tool was integrated into the Prometheus program, a software package of Kymata Netherlands company (currently C2V) [6]. Prometheus is a design, simulation and mask layout platform for integrated optics devices.

Two examples are presented here to validate the accuracy of the developed simulation tool. In the first example a straight waveguide is excited by the modal filed of the fundamental mode and the overlap coefficient between the input field and the output field at the end of the waveguide is calculated. All the temporal field values of the E_y component for both the input and output field are stored. Then they are Fourier transformed and the overlap is calculated. The overlap coefficient for a waveguide with parameters $1.55\mu m$, $3\mu m$, $1\mu m$, $5\mu m$, $5\mu m$ for the wavelength, the refractive index of the waveguide, the background refractive index, the x-section and z-section of the computational window, respectively, is found to be 0.996. Figure 6 shows the plot of the normalized amplitude of the input and output field of the waveguide.

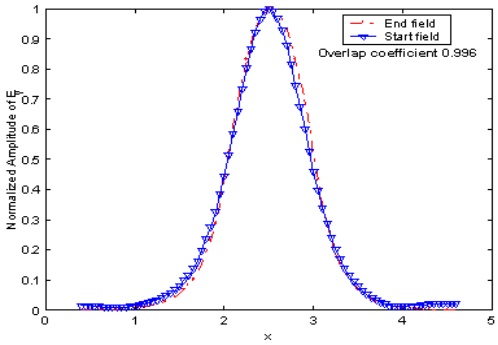

Fig. 6. Start and end field of a waveguide simulation.

The second example that validates the accuracy of the developed simulation tool is a directional coupler was modeled using the Prometheus program and the developed simulation tool. Figure 7 (a) shows the intensity plot of the E_y field for a directional coupler of length 75 μm, this is also the length of the computational window, widths of the waveguides are 1 μm and core separation is 1 μm. Figure 7(b) shows the intensity plot of E_y field calculated using Prometheus program of Kymata software.

The wavelength was 5 μm, smaller wavelengths require long waveguides which means a huge number of grid points, and the width of the computational window in the x-direction was 10 μm. The step size was 0.1 and 0.25 μm in the x- and z-directions, respectively. The coupling length calculated using the Prometheus program 20.6303 μm while the one calculated using the developed simulation tool is 20.62143 μm.

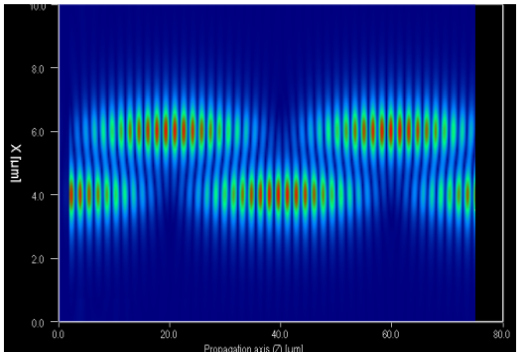

(a)

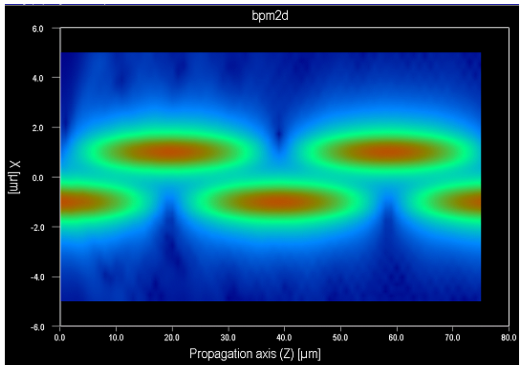

(b)

Fig. 7. The intensity plot of the E_y field component for a directional coupler, (a) calculated using the FDTD method, (b) calculated using the Prometheus software program of Kymata Netherlands.

The results presented in the previous two examples show that the accuracy of the developed simulation tool is in good agreement with the accuracy of the Prometheus program, a widely accepted software package in the integrated optics community.

4. Conclusions

An optimized implicit high-order finite difference time domain (FDTD) solver with one-sided total-field/scattered field formulation for time dependent numerical simulation of integrated optical components is developed and its accuracy was verified versus results calculated by the Prometheus program. A reduced LU decomposition was developed for inverting matrices that arise from the implicit FDTD scheme. Although implicit high -order FDTD schemes are unconditional stable, implementing them seem to be feasible only for 1D or 2D problems due to the increasing computational cost compared to explicit schemes.

5. References

[1] Kane S. Yee, "Numerical solution of initial boundary value problems involving Maxwell's equations in isotropic media", IEEE Trasaction on Antennas and Propagation, vol. Vol. AP-14, No. 3, pp. 302–307, 1966.

[2] H.A. AbdAllah,"General purpose numerical schemes for simulating light propagation in photonic structures", Literature Study Report, part of course work for MSc in Engineering Mathematics, University of Twente, 2001.

[3] A.Yefet and E. Turkel, "Fourth order compact implicit method for the Maxwell equations", Applied Numerical Mathematics, vol. 33, pp. 125–134, 2000.

[4] H. A. AbdAllah, "Simple Dispersion Analysis of 2nd and 4th order FDTD Schemes", The Annual Review of Progress in Applied Computational Electromagnetics Conference, Syracuse NY, 2004

[5] A.Ta‡ove, Computational Electrodynamics: The Finite Difference Time Domain Methods, Artech House, MA, Boston, 1995.

[6] Kymata Prometheus, Kymata Netherlands, Enschede, The Netherlands, 2001. www.kymata.nl (currently, www.c2v.nl)

Acknowledgment

The author would like to acknowledge the valuable discussion and comments from Manfred Hammer, Twente University, Enschede-The Netherlands and Jan Bos, Kymata Netherlands, Enschede-The Netherlands

Hossam A. Abdallah was born in Alexandria, Egypt, in 1973. He received his Bachelor of Science degree in computer science in 1995 from Alexandria University, Alexandria, Egypt. In 2001 he received his MSc degree in Engineering Mathematics from Twente University, Enschede, The Netherlands. Since August 2001, Mr. Abdallah is pursuing his PhD degree in the area of array signal processing and also working as a research assistant at the department of electrical and computer engineering, The George Washington University, Washington DC, USA. His current research activities are computational electromagnetics and array signal processing.

Multiresolution Time Domain Based Different Wavelet Basis Studies of Scattering of Planar Stratified Medium and Rectangular Dielectric Cylinder

Qunsheng Cao and Kumar K. Tamma
AHPCRC,University of Minnesota, Minneapolis, MN 55415

Abstract – In this paper, several wavelet bases, namely, the Daubechies, the biorthogonal Coiflet, the Deslauriers-Dubuc interpolating functions, and the cubic spline Battle-Lemarie, are applied to the multiresolution time domain (MRTD) technique for planar stratified media and electromagnetic scattering. These MRTD schemes are studied via field expansions of the scaling functions in one-dimensional (1D) and two-dimensional (2D) cases. A rigorous treatment method for inhomogeneous media structures is given. We have focused here on the study of reflected and transmission coefficients for an electromagnetic wave propagation on a stratified slab media and the scattering width (SW) of a rectangular dielectric cylinder. The 1D propagation characteristics of single and periodical stratified media and the 2D scattering width of the MRTD schemes are compared with the results of the FDTD method. Finally, we describe the computational accuracy of the relative peaks and shifting position errors, via a comparison of the results of the MRTD scheme based on the different basis with those of the FDTD method.

Key words: Multiresolution Time Domain (MRTD) scheme; orthogonal and the biorthogonal wavelet bases; reflected and transmission coefficients and scattering width.

I. INTRODUCTION

In recent years, the multiresolution time-domain (MRTD) method [1]-[6] has been applied successfully to various electromagnetic field analyses. The fields of the MRTD scheme are first expanded as a summation of scaling functions and wavelet in space and rectangular pulse in time. Although many different orthogonal and bi-orthogonal families of wavelets in theory are available, there are a few fundamental requirements that restrict us to use the wavelet families: (*i*) Smoothness and differentiability, (*ii*) orthogonality, (*iii*) compact support, (*iv*) symmetry or asymmetry, and (*v*) explicit analytic expression [7] in the choice of the scaling functions and wavelet in the Multiresolution Analysis (MRA) used in the MRTD scheme.

In application of the MRTD method, we can frequently choose and use different families of scaling functions and wavelets. The cubic spline Battle-Lemarié (BL) orthogonal wavelet family [8]-[9] is very desirable in the applications of the multiresolution time domain analysis. The Battle-Lemarié family of wavelets has good regularity and symmetry, the basis functions are orthogonal, and although the scaling functions and wavelet of BL don't have compact support, the functions decay exponentially. The Battel-Lemarié wavelet family was first introduced into the time-domain analysis for electromagnetic field applications [1], which is based on Galerkin's procedure of the method of moments (MOM) [10]; and later it progressed towards the introduction of the MRTD scheme in 1996 [1]. Another basis family used in the MRTD scheme is the Daubechies's compact support orthogonal wavelets [3], [7], and the family is with compact support and orthogonality, but they are far from being symmetric. The Daubechies's family is characterized as the one with an external phase and with the shortest support length for the given number of vanishing moments [7]. As a typical biorthogonal wavelet family, namely, the Cohen-Daubechies-Feauveau (CDF) wavelet family [5] used in the MRTD method, the CDF can be thought as a product of the marriage between the spline family and Daubechies' construction. The CDF spline family is therefore indexed by the pair $(n,\hat{n})$ and denoted by CDF$(n,\hat{n})$, n is order of B-spline function and $\hat{n}$ is the vanishing moments of the wavelet. Yet another wavelet basis used in the MRTD scheme, the spline biorthogonal Coiflet wavelets family, a variation of the Daubechies family [6], is with almost symmetric properties, orthonormal and compactly supported on limited intervals. The MRTD schemes also adopt the Deslauies-Dubue

interpolating wavelets family [4], and the Haar wavelet family [6] as field expansion basis. The MRTD schemes based on these different wavelet bases have shown a good potential to approximate the exact solutions. For example, the cubic spline Battle-Lemarie scaling and wavelet basis, which is the first wavelet basis used in the MRTD scheme, can even obtained near Nyquist sampling limit in using the Galerkin's sampling procedure with high computing accuracy [1]. In the MRTD scheme a reduction of grid density is inherent in the computations; however, there is a need to ensure adequate computing accuracy compared with the traditional finite difference time domain (FDTD) method. We note that different wavelet basis used in the MRTD schemes, because of the different wavelet bases; they have different properties of the compact support, and decay exponentially with symmetry. Therefore, there exist varied indexes of summation in the field expansions and for convergence for the different basis, which leads to some differences in computing accuracy for practical structures.

In this paper, we present exact algorithms of the MRTD scheme based on different wavelet basis, and the functions of field expansion are chosen as the scaling functions of the various wavelet bases in one-dimension (1D) and two-dimensions (2D), respectively. We provide the expansion functions of a different wavelet family, and give the exact formulations of the dielectric regions of the MRTD for an inhomogeneous lossless media. Finally, we calculate the wave reflected and transmission coefficients in the 1D, and the scattered width (SW) of a rectangular dielectric cylinder in the 2D case, respectively. We also compare the computing accuracies of the MRTD scheme based on the different wavelet bases with those of the FDTD method, and discuss the implementation aspects and approximations that are employed in providing simplification of the formulations.

II. FORMULATION AND WAVELET BASES CHOSEN

Firstly, we consider a 2D scattering analysis of an inhomogeneous lossless medium with the permittivity ε_r. For the MRTD scheme, we adopt a pure scattered-field formulation employed in the FDTD technique [11], in which the incident field $\vec{E}^{inc}$ is added only to the targets to describe time-domain electromagnetic fields. The Maxwell's equations for 2D TM_Z mode can be written as

$$\frac{\partial H_x^{scat}}{\partial t} = -\frac{1}{\mu_0}\frac{\partial E_z^{scat}}{\partial y} \tag{1}$$

$$\frac{\partial H_y^{scat}}{\partial t} = \frac{1}{\mu_0}\frac{\partial E_z^{scat}}{\partial x} \tag{2}$$

$$\varepsilon_0\varepsilon_r\frac{\partial E_z^{scat}}{\partial t} = -\varepsilon_0(\varepsilon_r - 1)\frac{\partial E_z^{inc}}{\partial t} + \left(\frac{\partial H_y^{scat}}{\partial x} - \frac{\partial H_x^{scat}}{\partial y}\right) \tag{3}$$

where E^{scat} indicates the scattered E-field. The relative permittivity ε_r is given as

$$\varepsilon_r(x,y) = \begin{cases} \varepsilon_r^{\kappa}, & \text{for } x_1^{\kappa} \le x \le x_2^{\kappa}, y_1^{\kappa} \le y \le y_2^{\kappa} \\ 1, & \text{elsewhere} \end{cases}$$
$$(\kappa = 0, 1, 2, \ldots, N) \tag{4}$$

where N is the total number of participating media, x_1^{κ} (y_1^{κ}) and x_2^{κ} (y_2^{κ}) are the x (y)-coordinates of lower and upper limits of the κ-th dielectric medium. Next, the field values are expanded as separable combination for the orthogonal scaling functions $\phi(\xi), (\xi = x, y)$ in space, and the Haar functions (rectangular pulse) $h(t)$ in time, respectively. For example, the scattering fields are expanded as

$$H_x^{scat}(x,y,t) = \sum_{n,i,j=-\infty}^{+\infty} {}_{\phi x}H^n_{i,j+1/2}\tilde{\phi}_i(x)\tilde{\phi}_{j+1/2}(y)\,h_n(t) \tag{5}$$

$$H_y^{scat}(x,y,t) = \sum_{n,i,j=-\infty}^{+\infty} {}_{\phi y}H^n_{i+1/2,j}\tilde{\phi}_{i+1/2}(x)\tilde{\phi}_j(y)\,h_n(t) \tag{6}$$

$$E_z^{scat}(x,y,t) = \sum_{n,i,j=-\infty}^{+\infty} {}_{\phi z}E^n_{i,j}\tilde{\phi}_i(x)\tilde{\phi}_j(y)h_n(t). \tag{7}$$

where $\tilde{\phi}_i(\xi)$ denotes dual scaling shifted by i units. Similarly, the expansion forms of the incident field are similar with that of the scattering field. The functions $h_n(t)$ and $\phi_i(\xi)$ or $\tilde{\phi}_i(\xi)$ are generated from the basic functions by dilation and translation as

$$h_n(t) = h\left(\frac{t}{\Delta t} - n + \frac{1}{2}\right) \tag{8}$$

and

$$\phi_i(\xi)=\phi\left(\frac{\xi}{\Delta\xi}-i\right) \text{ or } \tilde{\phi}_i(\xi)=\tilde{\phi}\left(\frac{\xi}{\Delta\xi}-i\right). \quad (9)$$

If the scaling function $\phi_i(\xi)=\tilde{\phi}_i(\xi)$, then the expansion is called an orthogonal expansion, otherwise it is called a biorthogonal expansion. In this paper, we have considered a variety of different scaling functions $\phi(\xi)$ and its shifted functions $\phi_i(\xi)$ (or shifted dual functions $\tilde{\phi}_i(\xi)$), that is, the cubic spline Battle-Lemarie scaling function, the compact support Daubechies scaling function D_4 $(p=2)$ [12], the compact support spline biorthogonal (Coiflet wavelet) scaling function $(p=2,\ \tilde{p}=2)$ [13], the compact support spline biorthogonal (Coiflet wavelet) scaling function $(p=4,\ \tilde{p}=4)$ [13], and the Deslauriers-Dubuc interpolating functions [14] as a scaling function, respectively. As examples, Figs. 1 give the distributions of the cubic spline Battle-Lemarie scaling function and Daubechies scaling function D_4, and their corresponding shift functions. In particular, the Deslauriers-Dubuc scaling function has its dual scaling function, where the dual function can be chosen as the Dirac delta function: $\tilde{\phi}(\xi)=\delta(\xi)$ [14]-[16], and the interpolating scaling function constructed as the autocorrelation function of the Daubechins' orthogonal scaling function with *N*=2 [14]-[16].

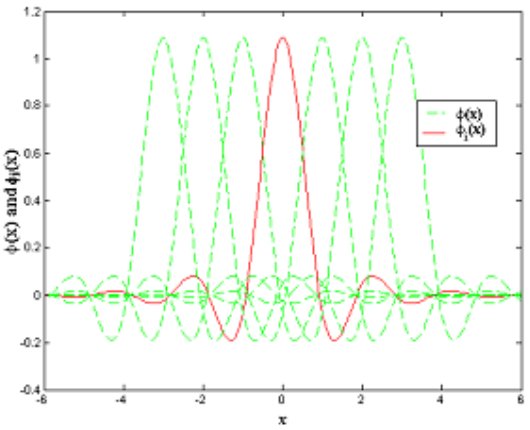

(a)

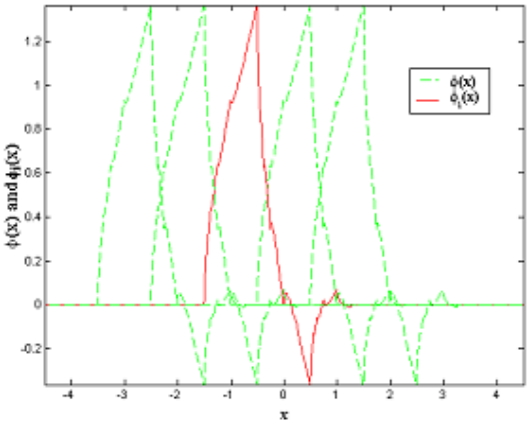

(b)

Fig. 1. The scaling function $\phi(x)$ and its shifted functions $\phi_i(x)$ (or dual shifted functions $\tilde{\phi}_i(x)$). (a) The cubic spline Battle-Lemarie basis, and (b) the Daubechies D_4 basis.

Substitution of the field expansions into the Maxwell equations (1)-(3), and then sampled using the basis function as the test function by the standard a Galerkin's procedure leads to the following two update equations of the *H*-fields:

$$ {}^{scat}_{\phi x}H^{\,n+1/2}_{i,j+1/2} = {}^{scat}_{\phi x}H^{\,n-1/2}_{i,j+1/2} - \frac{1}{\mu_0}\sum_{\nu} a(\nu)\,{}^{scat}_{\phi z}E^{\,n}_{i,j+\nu+1/2}\frac{\Delta t}{\Delta y} \quad (10a)$$

$$ {}^{scat}_{\phi y}H^{\,n+1/2}_{i+1/2,j} = {}^{scat}_{\phi y}H^{\,n-1/2}_{i+1/2,j} - \frac{1}{\mu_0}\sum_{\nu} a(\nu)\,{}^{scat}_{\phi z}E^{\,n}_{i+\nu+1/2,j}\frac{\Delta t}{\Delta x}. \quad (10b)$$

Table I. Connection coefficients $\alpha(\nu)$, $(\alpha(-\nu)=-\alpha(\nu-1))$

ν	Daubechies	Coiflet $(p=2,\tilde{p}=2)$	Coiflet $(p=4,\tilde{p}=4)$
0	1.22953239	1.23464519	1.31103170
1	-0.09358996	-0.09715386	-0.15600966
2	0.01025133	0.01162914	0.04199606
3	0.00003558	-0.00019002	-0.00865439
4			0.00083094

The coefficients $\alpha(\nu)$ connecting the scaling and their derivative functions are obtained by a numerical integral method in the Fourier domain [1] and Table I lists the coefficients $\alpha(\nu)$ of the Daubechies D_4 and biorthogonal Coiflet scaling functions.

The derivation of the update equation for the *E* fields is quite involved, since all orthogonal relations of the bases functions are not valid due to the introduction of the inhomogeneous region. Staring from the time domain equation (3), we derive the following update equation for the *E* field:

$$
\begin{aligned}
{}^{scat}_{\phi z}E^{n+1}_{i,j} = {}^{scat}_{\phi z}E^{n}_{i,j} &+ \frac{1}{\left[1+\sum_{\kappa=1}^{N}\left(\varepsilon_r^{\kappa}-1\right)\alpha_{i,i}^{\kappa}\beta_{j,j}^{\kappa}\right]}\times \\
&\sum_{i'=i-\Lambda}^{i'=i+\Lambda}\sum_{j'=j-\Lambda}^{j'=j+\Lambda}\sum_{\kappa=1}^{N}\left(\varepsilon_r^{\kappa}-1\right)\alpha_{i,i'}^{\kappa}\beta_{j,j'}^{\kappa}\left({}^{inc}_{\phi z}E^{n+1}_{i',j'}-{}^{inc}_{\phi z}E^{n}_{i',j'}\right) \\
&+\frac{1}{\varepsilon_0\left[1+\sum_{\kappa=1}^{N}\left(\varepsilon_r^{\kappa}-1\right)\alpha_{i,i}^{\kappa}\beta_{j,j}^{\kappa}\right]}\times \\
&\sum_{\nu}a(\nu)\left({}^{scat}_{\phi y}H^{n+1/2}_{i+\nu+1/2,j}\frac{\Delta t}{\Delta x}-{}^{scat}_{\phi x}H^{n+1/2}_{i,j+\nu+1/2}\frac{\Delta t}{\Delta y}\right)
\end{aligned}
\tag{11}
$$

and the coefficients $\alpha_{i,i'}^{\kappa}$ and $\beta_{j,j'}^{\kappa}$ are defined as:

$$\alpha_{i,i'}^{\kappa}=\frac{1}{\Delta x}\int_{x_1^{\kappa}}^{x_2^{\kappa}}\phi_{i'}(x)\tilde{\phi}_i(x)dx \tag{12a}$$

$$\beta_{j,j'}^{\kappa}=\frac{1}{\Delta y}\int_{y_1^{\kappa}}^{y_2^{\kappa}}\phi_{j'}(y)\tilde{\phi}_j(y)dy \tag{12b}$$

where $(x_1^{\kappa},x_2^{\kappa})$ and $(y_1^{\kappa},y_2^{\kappa})$ are the lower and upper limits of the κ-th dielectric medium along the *x*- and *y*-directions, respectively. *N* is the number of dielectric media in the computational domain, and Λ is an adjustable constant, which is determined by the size of stencil effect, the computing accuracy requirement and the localization property of the scaling functions. Usually the constant Λ is chosen as 6 to 9 for the cubic spline Battle-Lemarie wavelet basis, and 4 to 6 for the Daubechies D_4 and Biorthogonal Coiflet basis. Equation (11) indicates that for the κ-*th* scattering target, the distribution of *E*-field has relation with that of the fields within an extended region, which is covered by the region: $\left[\left(i_2^k+\Lambda\right)-\left(i_1^k-\Lambda\right),\left(j_2^k+\Lambda\right)-\left(j_1^k-\Lambda\right)\right]$.

In the derivation process we have used the main diagonal approximation in the evaluation, *i.e.*, we replace $\alpha_{i,i'}^{\kappa}\beta_{j,j'}^{\kappa}$ by $\alpha_{i,i'}^{\kappa}\beta_{j,j'}^{\kappa}\delta_{i,i'}\delta_{j,j'}$. This approximation is justified because of the compact support of the bases functions and the fact that the main diagonal coefficients are larger than those of the non-diagonal coefficients [17].

Equation (12) involves the scaling and its dual functions and the products of them. From these multiplicative products of functions $\phi(x)\tilde{\phi}_{i'}(x)$ of the different wavelet bases we can obtain roughly the extended dielectric region for different wavelet bases, that is, we can estimate an adjustable value Λ according to different accuracy requirements.

Now we consider one-dimensional wave propagation *TEM* mode. Considering the constitutive relation for the *E*-field, $D_y=\varepsilon E_y$ we derive the update equation of the *E*-field in the dielectric region, that is,

$${}_{\phi y}D_i^{n+1}={}_{\phi y}D_i^{n}-\sum_{\nu=-\infty}^{+\infty}a(\nu)\,{}_{\phi z}H^{n+1/2}_{i+\nu+1/2}\frac{\Delta t}{\Delta x} \tag{13}$$

$$
\begin{aligned}
\frac{{}_{\phi y}D_i^{n}}{\varepsilon_0} &= \sum_{i'=-\infty}^{+\infty}{}_{\phi y}E_{i'}^{n}\left(\delta_{i,i'}+\sum_{k=0}^{N}\left(\varepsilon_r^{k}-1\right)\alpha_{i'i}^{k}\right) \\
&\approx {}_{\phi y}E_i^n+\sum_{i'=i-\Lambda}^{i+\Lambda}\sum_{k=0}^{N}\left(\varepsilon_r^{k}-1\right)\alpha_{i'i\phi y}^{k}E_{i'}^{n}.
\end{aligned}
\tag{14}
$$

Employing an inverse matrix technique, equation (14) can be re-written as a typical update equation as given by

$${}_{\phi y}E_i^n=\frac{1}{\varepsilon_0}\sum_{k=1}^{N}\sum_{i'=i-\Lambda}^{i'=i+\Lambda}\left(\left[\chi^{\kappa}\right]\right)_{i,j\,\phi y}D_j^n \tag{15}$$

where

$$\left[\chi^{\kappa}\right]=\left[I+\sum_{i'=i-\Lambda}^{i'=i+\Lambda}\left(\varepsilon_r^{k}-1\right)\alpha_{i,i'}^{k}\right]^{-1}. \tag{16}$$

Numerically, for the MRTD solver we can pre-calculate the coefficients $\alpha_{i',i}^{k}$, $\beta_{j',j}^{k}$ and dielectric matrix $[\chi]$, and can pre-store them at the start of

the MRTD code. Due to the requirement of a square matrix, the dimensions of the connected dielectric matrix $[\chi]$ in (16) are $\left(i_2^k - i_2^k + 2\Lambda\right)\times\left(i_2^k - i_2^k + 2\Lambda\right)$ for each dielectric region. As an approximation, we can only consider the main diagonal element in (16) as explained previously; and as a further approximation we can reduce the dielectric region to a real dielectric region, and make the dielectric width equal to the slab width by decreasing $\Lambda \to 0$.

III. NUMERICAL RESULTS

As a first example, we consider a *TEM* plane transient pulse with a maximum frequency $f_{\max} = 10GHz$, generated by an exciting E_y field that is incident on a dielectric slab characterized with a relative permittivity $\varepsilon_r = 4$, and the width is $3\times10^{-2}m$ and $\Delta t = 1.25\times10^{-12}s$. The computational domain and the grid configuration are listed in Table II, in which *NX* is the total computing dimension, i_1, i_2 are the slab positions, and i_{r1}, i_{r2} are the record positions for the reflected and transmission wave, respectively.

Table II. Configuration of dielectric slab

NX (cell)	i_1 (cell)	i_2 (cell)	i_{r1} (cell)	i_{r2} (cell)
300	140	170	120	200
150	70	90	60	100
75	35	45	30	50
60	28	36	24	40

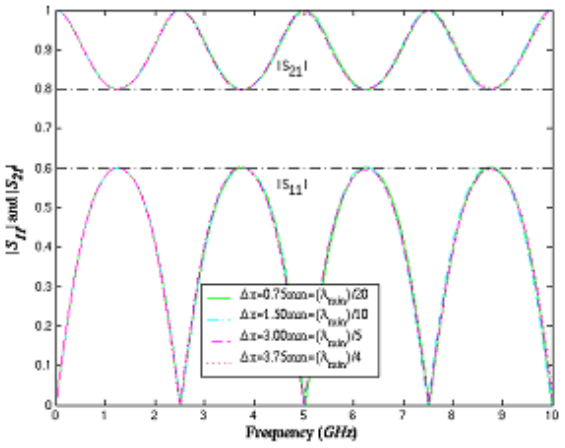

(a)

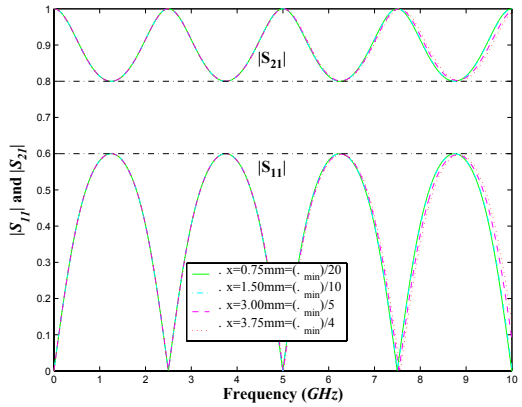

(b)

Fig. 2. Magnitudes of reflection coefficient S_{11} and transmission coefficient S_{21} versus frequency in a single-layer dielectric slab system. (a) the cubic spline Battle-Lemarie basis, and (b) the Daubechies D_4 basis.

Figures 2 show the results of the reflected and transmission coefficients for one dielectric slab for the cubic spline Battle-Lemarie wavelet basis and the Daubechies wavelet basis, respectively. In order to compare the computing accuracy for different wavelet bases, we have to define two relative errors. One is the relative peak error $\Sigma_p = \dfrac{R_{analysis}(n) - R_{MRTD}(n)}{R_{analysis}(n)}$, which is involved with the value change of the reflected coefficient curve at a specified peak position, where $R(n)$ is the corresponding value of the reflected coefficient at the *n*-th peak in the reflected coefficient curves. The other one is the relative shifting error $\Sigma_s = \dfrac{f_0 - f_{MRTD}}{f_0}$, which is involved the frequency position shifting changes along the horizontal axis in the coefficients curves, where f_0 is a corresponding frequency value of the analytical solution along the horizontal axis.

In Table III are given the relative peak errors Σ_p corresponding to the third peak, and the relative shifting error Σ_s corresponds to the frequency value along the horizontal position

$f_0 = 9.98GHz$ for the different MRTD wavelet basis compared with the analytical solution with increasing cell unit Δx . From Figs. 2 and Table III, it is found that the reflected and transmission coefficients of the MRTD scheme based on the cubic spline Battle-Lemarie wavelet are of reasonable accuracy and within the limits of the computational relative peak error and the relative shifting error.

Figures 3(a) and 3(b) show the enlarged local peak portion of the reflected coefficient curve and the enlarged local horizontal portion that correspond to the third peak and the frequency value along the horizontal position with the frequency value of the analytical solution $f_0 = 9.98GHz$ with $\Delta x = \lambda_{\min}/5$, respectively.

Table III. Relative peak error at the third peak and shifting position error of the reflected coefficients at $f = 9.98GHz$

Δx (mm)	Battle-Lemarie (%)		Daubechies (%)		Coifelt $(p=2, \tilde{p}=2)$ (%)		Coifelt $(p=4, \tilde{p}=4)$ (%)	
	Σ_f	Σ_s	Σ_f	Σ_s	Σ_f	Σ_s	Σ_f	Σ_s
0.75	-0.37	-0.29	-0.17	-0.18	0.02	-0.18	0.02	-0.18
1.50	-0.33	-0.12	0.02	-0.29	0.17	-0.29	-0.02	-0.18
3.00	0.32	-0.42	0.48	-1.14	2.75	-1.40	0.70	-0.98
3.75	0.35	-0.72	0.57	-1.70	6.47	-2.18	2.30	-2.25

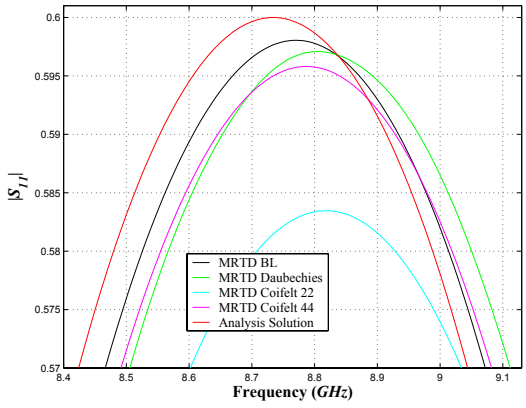

(a)

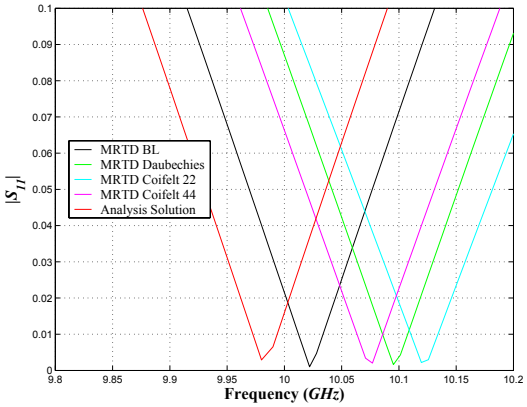

(b)

Fig. 3. Enlarged magnitudes of the reflection coefficients S_{11} versus frequency in a single-layer dielectric slab system. (a) at the third peak position, (b) at the 10GHz frequency position with cell size $\Delta x = \lambda_{\min}/5$.

For the reflected coefficients obtained with only the main diagonal elements in the dielectric matrix, that is, the matrix elements that only correspond to the same units as α_{ii}^k, the Daubechies D_4 scaling basis, the reflected coefficients show a smaller computational relative peak error and smaller relative shifting position error than that of the other bases for the 'coarse' cell size. Therefore, as a simplification of the main diagonal approximation, the Daubechies D_4 scaling basis can be chosen as a basic basis to be used in the MRTD expansion.

Figure 4 give the reflected coefficients of a periodical dielectric stratified 10 layer media using the MRTD scheme based on the Battle-Lemarie scaling functions; the width of the slab is $w_1 = 3 \times 10^{-2} m$, the width between slabs is $w_2 = 3 \times 10^{-2} m$, and the values are compared with the analytic solution. It can be seen that the MRTD scheme exhibits high computing accuracy and larger savings in computing memory, and nearly the same computing time compared with the FDTD method for a complicated periodic structure. The total lengths of the periodic slabs are $NX = 1020$ for the FDTD and $NX = 204$ for

the MRTD. The CPU time is about 92.5 seconds for the FDTD with $\Delta x = \lambda_{\min}/20$, about 107.2 seconds for the MRTD based on Battle-Lemarie scaling functions with $\Delta x = \lambda_{\min}/4$, and about 110 seconds for the MRTD based on the Daubechines D_4 scaling functions with $\Delta x = \lambda_{\min}/4$. A total of 40,000 time steps were used for the same 500 MHz Pentium III (Katmai) computations.

Next, we investigate the scattering width (SW), σ_s, for a square dielectric cylinder with a plane wave incident with a maximum frequency of $f_{\max} = 5GHz$. The dimension of the target is $0.18\times0.18m^2$ with the relative permittivity $\varepsilon_r = 4$, and the discretization employs $\Delta t = 2.5\times10^{-12}s$, and the total number of steps is 4000 for the MRTD scheme and the FDTD method. Ten layers of the APML boundary are used. In Fig. 5 is plotted the SW of the MRTD scheme based on different wavelet bases with that of the FDTD method for the TM_z mode. The results of the MRTD scheme are in good agreement with that of the FDTD for a specified frequency at a specified incident and scattering angle. However, the computational space for the MRTD scheme is $60\Delta x\times60\Delta y$, and is only about 14.1% of that employed in the FDTD, which is given by $160\Delta x\times160\Delta y$.

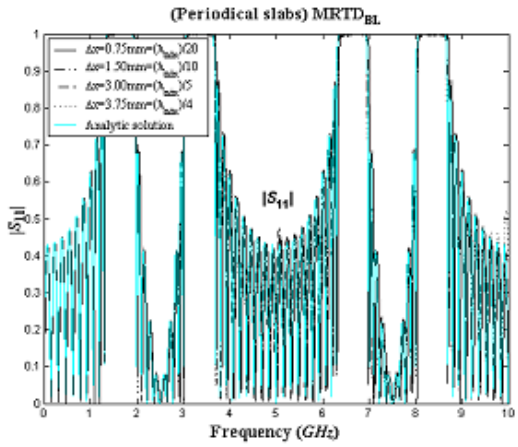

Fig. 4. Magnitudes of the reflection coefficients S_{11} are for a periodical dielectric stratified ten layer media by the cubic spline Battle-Lemarie wavelet basis.

In order to compare the accuracies of scattered width of the MRTD scheme based on different wavelet basis, we again employ the concept of the relative peak error $\Sigma_p = \dfrac{\sigma_{FDTD}(n)-\sigma_{MRTD}(n)}{\sigma_{FDTD}(n)}$, where $\sigma(n)$ is the value of SW at the specified n-th peak in the scatter width curve, and the relative shifting position error $\Sigma_s = \dfrac{f_0 - f_{MRTD}}{f_0}$, where f_0 and f_{MRTD} are corresponding frequency values of the FDTD method and the MRTD scheme in the horizontal axis for the n-th peak in the SW curve, respectively.

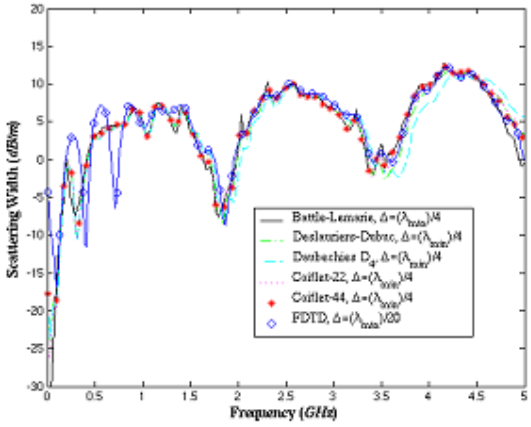

Fig. 5. Magnitudes of the scattering widths as a function of frequency (ϕ_i=30^0, ϕ_s=30^0) for the different wavelet bases and FDTD method are for a TM_z wave incident on a square dielectric cylinder, where ϕ_i and ϕ_s are the incident and scattering angles of the wave, respectively.

Table IV lists the two relative errors, in which the relative peak errors are for the third curve peak and shifting position errors are for the specified frequency value along the horizontal position. For example, for the FDTD method the value of frequency along the horizontal position is about $f_0 = 4.646GHz$.

Table IV. Relative peak and shifting position errors of the scattered width for the third peak curve

Δx (mm)	Battle-Lemarie (%)		Daubechies (%)		Coifelt $(p=2,\tilde{p}=2$ (%)		Coifelt $(p=4,\tilde{p}=4)$ (%)		Deslauriers -Dubuc (%)	
	Σ_f	Σ_s	Σ_f	Σ_s	Σ_f	Σ_s	Σ_f	Σ_s	Σ_f	Σ_s
1.00	-1.88	0.78	13.11	1.92	3.28	1.02	3.69	-3.22	5.98	-0.26.
0.75	-1.00	0.73	10.49	2.90	2.05	1.01	-0.33	-0.30	4.92	-0.74
0.50	-0.57	0.39	9.18	-1.02	0.41	0.17	-1.97	0.56	3.44	-0.04

A careful study of the SW with varied cell sizes of different MRTD wavelet bases and from Table IV, we find that the scattering widths of the cubic spline Battle-Lemarie wavelet basis have reasonable accuracy within the limits of the computational relative error, and higher accuracy than that of other wavelet bases relative to the results of the FDTD method with different cell sizes. Figs. 6(a) and (b) are the enlarged scattered width curves corresponding to different wavelet bases with the cell size $\Delta l = \lambda_{\max}/6$. From Figs. 6(a)-(b) and Table IV, the results of the Daubechies D4 basis show a larger peak and shifting position errors than that of the other wavelet bases.

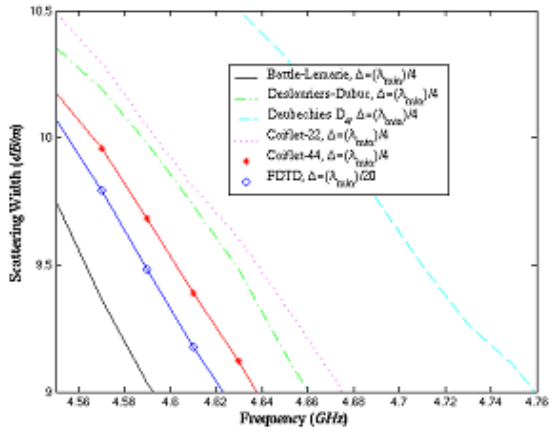

(a)

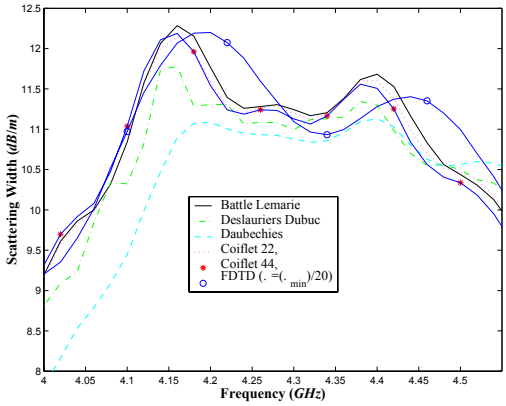

(b)

Fig. 6. Enlarged scattering widths as a function of frequency ($\phi_i = 30^0$, $\phi_s = 30^0$) for different cell sizes are for a TM_z wave incident on a square dielectric cylinder. (a) at the third peak position (b) at the 5.0GHz frequency position with cellsize $\Delta = 0.75\times10^{-2}\, m = \lambda_{\max}/4$.

IV. CONCLUSIONS

In this paper, a multiresolution time domain scheme based on different wavelet bases have been explored, and have been applied to electromagnetic analysis of a 1D wave with reflected and transmission, and a 2D scattering problem in an inhomogeneous dielectric region. The formulations of the update equations of the *E*-field were derived. We have calculated the reflected, transmitting coefficients, and the scattered width in 1D and 2D for the MRTD schemes, respectively, corresponding to different wavelet bases. The computed results have been compared with those derived from the FDTD and analytical solutions. We have also estimated the values of the relative peak errors and the shifting position errors at a specified horizontal frequency for the different MRTD schemes. The different MRTD wavelet schemes show the comparative accuracies of the different wavelet bases at specified frequency and peak positions.

ACKNOWLEDGMENT

The authors are very pleased to acknowledge support by the Army High Performance Computing Research Center (AHPCRC) under the auspices of Department of the Army, Army Research Laboratory (ARL) under contact number DAAD19-01-2-0014. Dr. Raju Namburu is the technical monitor. The content does not necessarily reflect the position or policy of government, and no official endorsement should be inferred. Other related support in form of computer grants from the Minnesota Supercomputer Institute (MSI), Minneapolis, Minnesota is also gratefully acknowledged.

REFERENCES

[1] M. Krumpholz and L.P.B. Katehi, "MRTD: New time domain schemes based on multiresolution analysis," *IEEE Trans. Microwave Theory Tech*., vol. 44, no. 4, pp. 555-571, April 1996.

[2] Q. Cao, Y. Chen and R. Mittra, "Multiple image technique (MIT) and anisotropic perfectly matched layer (APML) in implementation of MRTD scheme for boundary truncations of microwave structures," *IEEE Trans. Microwave Theory Tech.*, vol. 50, no. 6, pp. 1578-1589, June 2002.

[3] Y. W. Cheong, Y. M. Lee, K. H. Ra, J. G. Kang and C. C. Shin, "Wavelet-Galerkin scheme of time-dependent inhomogeneous electromagnetic problem," *IEEE Microwave Guide Lett*., vol. 9, no. 8, p. 297-299, Aug. 1999.

[4] M. Fujii and W.J.R. Hoefer, "A wavelet formulation of the finite-difference method: full-vector analysis of optical waveguide junctions," *IEEE J. Quantum electron.*, vol. 37, no. 8, Aug. 2001.

[5] T. Dogaru and L. Carin, " Multiresolution time-domain algorithm using CDF biorthogonal wavelet," *IEEE Trans. Microwave Theory Tech.*, vol. 49, no. 5, pp. 902-912, May 2001.

[6] M. Fujii and W. J. R. Hoefer, "A three-dimensional Haar-wavelet-based multiresolution analysis similar to the FDTD method Derivation and application," *IEEE Trans. Microwave TheoryTtech*., vol. 46, pp. 2463-2475, Dec. 1998.

[7] I. Daubechies, *Ten Lectures on Wavelets*. Philadelphia, PA: SIAM, 1992.

[8] G. Battle, "A block spin construction of ondeletts. Part I: Lemarié," *Commun. Math. Phys*., vol. 110, pp. 601-615, 1987.

[9] P. G. Lemarié, "Ondelettes à localization exponentielles," *J. Math. Pures et appl*.,

[10] J. J H. Wang, *Generalized Moment Methods in Electromagnetic: Formulation and Computer Solution of Integral Equations*. New York: Wiley Interscience, 1991.

[11] K. S. Kunz and R.J. Luebbers, *The finite difference time domain method for electromagnetics*, CRC Press, Boca Raton, FL, 1993.

[12] I. Daubechies, *Ten Lectures on wavelet* (CBMS-NSF Series in Applied Mathematics). Philadelphia, PA: SIAM, 1992.

[13] S. G. Mallat, *A wavelet tour of signal processing*, Academic Press, 1998.

[14] G. Deslauriers and S. Dubuc, "Symmetric iterative interpolation processes," *Constr. Approx.*, vol. 5, pp. 49-68, 1989.

[15] W. Sweldens and R. Piessens, "Wavelet sampling techniques," in *1993 Proceedings of the Statistical Computing Section, American Statistical Association*, San Francisco, pp. 20-29, August 1993

[16] M. Fujii and W.J.R. Hoefer, "Application of Biorthogonal Interpolating Wavelets to the Galerkin Scheme of Time Dependent Maxwell's Equations," *IEEE Microwave and Wireless Components Letters*, vol.11, no.1, pp.22-24, Jan. 2001.

[17] Q. Cao, Y. Chen and P. K. A. Wai, "MRTD electromagnetic scattering analysis," *Microwave Opt. Technology. Lett.*, vol, 28, no. 3, pp. 189-195, February 2001.

Dr. Qunsheng Cao is Post-doctoral research associate of AHPCRC at the University of Minnesota in Minneapolis. He received the Bachelor of Science degree in Physics from the University of Huai-Nan Mining, PRC, in 1982, and Ph. D degree from The Hong Kong Polytechnic University, Hong Kong, 2001. In 1989 to 1991, he worked as Visiting Scholar in the Department of Physic, Wuhan University in PRC. In 1994, he became an Associate Professor in Wuhan University of Science and Technology, PRC. From 1996-2001, he became a Research Assistant with The Hong Kong Polytechnic University. From 2001-2002, he became a Research Associate in the Department of Electrical Engineering, University of Illinois at Urbana-Champaign. Since 2002 July, he has worked as a Research Associate in AHPCRC, University of Minnesota in Minneapolis. His current research interests are in computational electromagnetics, wavelet application, parallel technique, using the Time-Domain numerical techniques (FDTD, MRTD and TDFEM) to study microwave devices and scattering applications. He has published 30 international publications in refereed journals and conference symposia. He is a co-author of the book, *Multiresolution Time Domain Scheme for Electromagnetic Engineering* (John Wiley & Sons), a contributor of 2 book chapters.

Dr. Kumar K. Tamma is Professor and Technical Director of Mechanical Engineering and the Army High Performance Computing Research Center (AHPCRC) at the University of Minnesota in Minneapolis. His research interests include: Computational Mechanics and Multidisciplinary/Multi-scale Physics research developments encompassing Finite-Element Methodology for Interdisciplinary Problem, Computational Algorithms and Numerical Simulation; Fluid/Thermal/Structure Interactions and Thermal Stresses; Manufacturing: Mechanics of Materials and Process Modeling, Residual Stresses, Solidification, Metal Forming; Structural Dynamics, Contact-Impact and Wave Propagation; Solid Mechanics and Large/Aero Space Structures; Microscale/Macroscale/ Nonoscale Heat Transfer and Computational Heat Transfer in Structures and Materials including Composites and Heterogeneous Materials; Computational Methods and Development of Finite Element Algorithms for Large Scale Applications on High Performance Computing Platforms and Parallel Computations; CAD/FEM Interface, Geometric Modeling and Automated/Adaptive Simulation Based Design Techniques. He has authored/co-authored over 160 research articles in various journals and proceedings, and book chapters, and is on the editorial board for ten journals. Professor Tamma has given numerous invited talks, plenary and keynote lectures at various International /National Conference; conducted numerous Workshops/Trainings/Short Courses, and served as Chair/Co-Chair for several conference presentations. Professor Tamma is a member of ASME, AIAA, the International Association for Computational Mechanics, the International Society for Computational and Engineering Science, and the US Association for Computational Mechanics.

2005 INSTITUTIONAL MEMBERS

AUSTRALIAN DEFENCE LIBRARY
Northcott Drive
Campbell, A.C.T. 2600 AUSTRALIA

BEIJING BOOK COMPANY, INC
701 E Lindon Ave.
Linden, NJ 07036-2495

DARMSTADT U. OF TECHNOLOGY
Schlossgartenstrasse 8
Darmstadt, Hessen
GERMANY D-64289

DARTMOUTH COLL-FELDBERG LIB
6193 Murdough Center
Hanover, NH 03755-3560

DEFENCE RESEARCH ESTAB. LIB.
3701 Carling Avenue
Ottowa, ON, K1A 0Z4 CANADA

DPS/LIBRARY (EABV)
Alion Science & Technology
185 Admiral Cochrane Drive
Annapolis, MD 214017307

DSTO-DSTORL EDINBURGH
Jets AU/33851-99, PO Box 562
Milsons Point, NSW
AUSTRALIA 1565

DTIC-OCP/LIBRARY
8725 John J. Kingman Rd. Ste 0944
Ft. Belvoir, VA 22060-6218

ELSEVIER
Bibliographic Databases
PO Box 2227
Amsterdam, Netherlands 1000 CE

ENGINEERING INFORMATION, INC
PO Box 543
Amsterdam, Netherlands 1000 Am

ETSE TELECOMUNICACION
Biblioteca, Campus Lagoas
Vigo, 36200 SPAIN

FLORIDA INTERNATIONAL UNIV.
ECE Dept./EAS-3983
10555 W. Flagler St
Miami, FL 33174

GEORGIA TECH LIBRARY
225 North Avenue, NW
Atlanta, GA 30332-0001

HRL LABS, RESEARCH LIBRARY
3011 Malibu Canyon
Malibu, CA 90265

IEE INSPEC/Acquisitions Section
Michael Faraday House
6 Hills Way
Stevenage, Herts UK SG1 2AY

IND CANTABRIA
PO Box 830470
Birmingham, AL 35283

INSTITUTE FOR SCIENTIFIC INFO.
Publication Processing Dept.
3501 Market St.
Philadelphia, PA 19104-3302

LIBRARY of CONGRESS
Reg. Of Copyrights
Attn: 40T Deposits
Washington DC, 20559

LINDA HALL LIBRARY
5109 Cherry Street
Kansas City, MO 64110-2498

MISSISSIPPI STATE UNIV LIBRARY
PO Box 9570
Mississippi State, MS 39762

MIT LINCOLN LABORATORY
Periodicals Library
244 Wood Street
Lexington, MA 02420

NA KANSAI KINOKUNNA CO.
Attn: M. MIYOSHI
PO Box 36 (NDLA KANSAI)
Hongo, Tokyo, JAPAN 113-8688

NAVAL POSTGRADUATE SCHOOL
Attn:J. Rozdal/411 Dyer Rd./ Rm 111
Monterey, CA 93943-5101

NAVAL RESEARCH LABORATORY
C. Office, 4555 Overlook Avenue, SW
Washington, DC 20375

OHIO STATE UNIVERSITY
1320 Kinnear Road
Columbus, OH 43212

PAIKNAM ACAD. INFO CTR LIB.
Hanyang U/17 Haengdang-Dong
Seongdong-ki, Seoul, S Korea 133-791

PENN STATE UNIVERSITY
126 Paterno Library
University Park, PA 16802-1808

RENTON TECH LIBRARY/BOEING
PO BOX 3707
SEATTLE, WA 98124-2207

SOUTHWEST RESEARCH INST.
6220 Culebra Road
San Antonio, TX 78238

SWETS INFORMATION SERVICES
160 Ninth Avenue, Suite A
Runnemede, NJ 08078

SYRACUSE UNIVERSITY
EECS, 121 Link Hall
Syracuse, NY 13244

TECHNISCHE UNIV. DELFT
Mekelweg 4, Delft, Holland, 2628 CD
NETHERLANDS

TIB & UNIV. BIB. HANNOVER
DE/5100/G1/0001
Welfengarten 1B
Hannover, GERMANY 30167

TOKYO KOKA UNIVERSITY
1404-1 Katakura-Cho
Hachioji, Tokyo, JAPAN 192-0914

UNIV OF CENTRAL FLORIDA LIB.
4000 Central Florida Boulevard
Orlando, FL 32816-8005

UNIV OF COLORADO LIBRARY
Campus Box 184
Boulder, CO 80309-0184

UNIVERSITY OF MISSISSIPPI
John Davis Williams Library
PO Box 1848
University, MS 38677-1848

UNIV OF MISSOURI-ROLLA LIB.
1870 Miner Circle
Rolla, MO 65409-0001

USAE ENG. RES. & DEV. CENTER
Attn: Library/Journals
72 Lyme Road
Hanover, NH 03755-1290

ACES COPYRIGHT FORM

This form is intended for original, previously unpublished manuscripts submitted to ACES periodicals and conference publications. The signed form, appropriately completed, MUST ACCOMPANY any paper in order to be published by ACES. PLEASE READ REVERSE SIDE OF THIS FORM FOR FURTHER DETAILS.

TITLE OF PAPER:

AUTHORS(S)

PUBLICATION TITLE/DATE:

RETURN FORM TO:

Dr. Atef Z. Elsherbeni
University of Mississippi
Dept. of Electrical Engineering
Anderson Hall Box 13
University, MS 38677 USA

PART A - COPYRIGHT TRANSFER FORM

(NOTE: Company or other forms may not be substituted for this form. U.S. Government employees whose work is not subject to copyright may so certify by signing Part B below. Authors whose work is subject to Crown Copyright may sign Part C overleaf).

The undersigned, desiring to publish the above paper in a publication of ACES, hereby transfer their copyrights in the above paper to The Applied Computational Electromagnetics Society (ACES). The undersigned hereby represents and warrants that the paper is original and that he/she is the author of the paper or otherwise has the power and authority to make and execute this assignment.

Returned Rights: In return for these rights, ACES hereby grants to the above authors, and the employers for whom the work was performed, royalty-free permission to:

1. Retain all proprietary rights other than copyright, such as patent rights.
2. Reuse all or portions of the above paper in other works.
3. Reproduce, or have reproduced, the above paper for the author's personal use or for internal company use provided that (a) the source and ACES copyright are indicated, (b) the copies are not used in a way that implies ACES endorsement of a product or service of an employer, and (c) the copies per se are not offered for sale.
4. Make limited distribution of all or portions of the above paper prior to publication.
5. In the case of work performed under U.S. Government contract, ACES grants the U.S. Government royalty-free permission to reproduce all or portions of the above paper, and to authorize others to do so, for U.S. Government purposes only.

ACES Obligations: In exercising its rights under copyright, ACES will make all reasonable efforts to act in the interests of the authors and employers as well as in its own interest. In particular, ACES REQUIRES that:

1. The consent of the first-named author be sought as a condition in granting re-publication permission to others.
2. The consent of the undersigned employer be obtained as a condition in granting permission to others to reuse all or portions of the paper for promotion or marketing purposes.

In the event the above paper is not accepted and published by ACES or is withdrawn by the author(s) before acceptance by ACES, this agreement becomes null and void.

AUTHORIZED SIGNATURE — TITLE (IF NOT AUTHOR)

EMPLOYER FOR WHOM WORK WAS PERFORMED — DATE FORM SIGNED

Part B - U.S. GOVERNMENT EMPLOYEE CERTIFICATION

(NOTE: if your work was performed under Government contract but you are not a Government employee, sign transfer form above and see item 5 under Returned Rights).

This certifies that all authors of the above paper are employees of the U.S. Government and performed this work as part of their employment and that the paper is therefor not subject to U.S. copyright protection.

AUTHORIZED SIGNATURE — TITLE (IF NOT AUTHOR)

NAME OF GOVERNMENT ORGANIZATION — DATE FORM SIGNED

PART C - CROWN COPYRIGHT

(NOTE: ACES recognizes and will honor Crown Copyright as it does U.S. Copyright. It is understood that, in asserting Crown Copyright, ACES in no way diminishes its rights as publisher. Sign only if *ALL* authors are subject to Crown Copyright).

This certifies that all authors of the above Paper are subject to Crown Copyright. (Appropriate documentation and instructions regarding form of Crown Copyright notice may be attached).

AUTHORIZED SIGNATURE TITLE OF SIGNEE

NAME OF GOVERNMENT BRANCH DATE FORM SIGNED

Information to Authors

ACES POLICY

ACES distributes its technical publications throughout the world, and it may be necessary to translate and abstract its publications, and articles contained therein, for inclusion in various compendiums and similar publications, etc. When an article is submitted for publication by ACES, acceptance of the article implies that ACES has the rights to do all of the things it normally does with such an article.

In connection with its publishing activities, it is the policy of ACES to own the copyrights in its technical publications, and to the contributions contained therein, in order to protect the interests of ACES, its authors and their employers, and at the same time to facilitate the appropriate re-use of this material by others.

The new United States copyright law requires that the transfer of copyrights in each contribution from the author to ACES be confirmed in writing. It is therefore necessary that you execute either Part A-Copyright Transfer Form or Part B-U.S. Government Employee Certification or Part C-Crown Copyright on this sheet and return it to the Managing Editor (or person who supplied this sheet) as promptly as possible.

CLEARANCE OF PAPERS

ACES must of necessity assume that materials presented at its meetings or submitted to its publications is properly available for general dissemination to the audiences these activities are organized to serve. It is the responsibility of the authors, not ACES, to determine whether disclosure of their material requires the prior consent of other parties and if so, to obtain it. Furthermore, ACES must assume that, if an author uses within his/her article previously published and/or copyrighted material that permission has been obtained for such use and that any required credit lines, copyright notices, etc. are duly noted.

AUTHOR/COMPANY RIGHTS

If you are employed and you prepared your paper as a part of your job, the rights to your paper initially rest with your employer. In that case, when you sign the copyright form, we assume you are authorized to do so by your employer and that your employer has consented to all of the terms and conditions of this form. If not, it should be signed by someone so authorized.

NOTE RE RETURNED RIGHTS: Just as ACES now requires a signed copyright transfer form in order to do "business as usual", it is the intent of this form to return rights to the author and employer so that they too may do "business as usual". If further clarification is required, please contact: The Managing Editor, R. W. Adler, Naval Postgraduate School, Code EC/AB, Monterey, CA, 93943, USA (408)656-2352.

Please note that, although authors are permitted to re-use all or portions of their ACES copyrighted material in other works, this does not include granting third party requests for reprinting, republishing, or other types of re-use.

JOINT AUTHORSHIP

For jointly authored papers, only one signature is required, but we assume all authors have been advised and have consented to the terms of this form.

U.S. GOVERNMENT EMPLOYEES

Authors who are U.S. Government employees are not required to sign the Copyright Transfer Form (Part A), but any co-authors outside the Government are.

Part B of the form is to be used instead of Part A only if all authors are U.S. Government employees and prepared the paper as part of their job.

NOTE RE GOVERNMENT CONTRACT WORK: Authors whose work was performed under a U.S. Government contract but who are not Government employees are required so sign Part A-Copyright Transfer Form. However, item 5 of the form returns reproduction rights to the U. S. Government when required, even though ACES copyright policy is in effect with respect to the reuse of material by the general public.

APPLIED COMPUTATIONAL ELECTROMAGNETICS SOCIETY JOURNAL
http://aces.ee.olemiss.edu

INFORMATION FOR AUTHORS

PUBLICATION CRITERIA

Each paper is required to manifest some relation to applied computational electromagnetics. **Papers may address general issues in applied computational electromagnetics, or they may focus on specific applications, techniques, codes, or computational issues.** While the following list is not exhaustive, each paper will generally relate to at least one of these areas:

1. **Code validation.** This is done using internal checks or experimental, analytical or other computational data. Measured data of potential utility to code validation efforts will also be considered for publication.

2. **Code performance analysis.** This usually involves identification of numerical accuracy or other limitations, solution convergence, numerical and physical modeling error, and parameter tradeoffs. However, it is also permissible to address issues such as ease-of-use, set-up time, run time, special outputs, or other special features.

3. **Computational studies of basic physics.** This involves using a code, algorithm, or computational technique to simulate reality in such a way that better, or new physical insight or understanding, is achieved.

4. **New computational techniques**, or new applications for existing computational techniques or codes.

5. **"Tricks of the trade"** in selecting and applying codes and techniques.

6. **New codes, algorithms, code enhancement, and code fixes.** This category is self-explanatory, but includes significant changes to existing codes, such as applicability extensions, algorithm optimization, problem correction, limitation removal, or other performance improvement. **Note: Code (or algorithm) capability descriptions are not acceptable, unless they contain sufficient technical material to justify consideration.**

7. **Code input/output issues.** This normally involves innovations in input (such as input geometry standardization, automatic mesh generation, or computer-aided design) or in output (whether it be tabular, graphical, statistical, Fourier-transformed, or otherwise signal-processed). Material dealing with input/output database management, output interpretation, or other input/output issues will also be considered for publication.

8. **Computer hardware issues.** This is the category for analysis of hardware capabilities and limitations of various types of electromagnetics computational requirements. Vector and parallel computational techniques and implementation are of particular interest.

Applications of interest include, but are not limited to, antennas (and their electromagnetic environments), networks, static fields, radar cross section, shielding, radiation hazards, biological effects, electromagnetic pulse (EMP), electromagnetic interference (EMI), electromagnetic compatibility (EMC), power transmission, charge transport, dielectric, magnetic and nonlinear materials, microwave components, MEMS technology, MMIC technology, remote sensing and geometrical and physical optics, radar and communications systems, fiber optics, plasmas, particle accelerators, generators and motors, electromagnetic wave propagation, non-destructive evaluation, eddy currents, and inverse scattering.

Techniques of interest include frequency-domain and time-domain techniques, integral equation and differential equation techniques, diffraction theories, physical optics, moment methods, finite differences and finite element techniques, modal expansions, perturbation methods, and hybrid methods. This list is not exhaustive.

A unique feature of the Journal is the publication of unsuccessful efforts in applied computational electromagnetics. Publication of such material provides a means to discuss problem areas in electromagnetic modeling. Material representing an unsuccessful application or negative results in computational electromgnetics will be considered for publication only if a reasonable expectation of success (and a reasonable effort) are reflected. Moreover, such material must represent a problem area of potential interest to the ACES membership.

Where possible and appropriate, authors are required to provide statements of quantitative accuracy for measured and/or computed data. This issue is discussed in "Accuracy & Publication: Requiring, quantitative accuracy statements to accompany data," by E. K. Miller, *ACES Newsletter,* Vol. 9, No. 3, pp. 23-29, 1994, ISBN 1056-9170.

EDITORIAL REVIEW

In order to ensure an appropriate level of quality control, papers are peer reviewed. They are reviewed both for technical correctness and for adherence to the listed guidelines regarding information content.

JOURNAL CAMERA-READY SUBMISSION DATES

March issue	deadline 8 January
July issue	deadline 20 May
November issue	deadline 20 September

Uploading an acceptable camera-ready article after the deadlines will result in a delay in publishing this article.

STYLE FOR CAMERA-READY COPY

The ACES Journal is flexible, within reason, in regard to style. However, certain requirements are in effect:

1. The paper title should NOT be placed on a separate page. The title, author(s), abstract, and (space permitting) beginning of the paper itself should all be on the first page. The title, author(s), and author affiliations should be centered (center-justified) on the first page.

2. An abstract is REQUIRED. The abstract should be a brief summary of the work described in the paper. It should state the computer codes, computational techniques, and applications discussed in the paper (as applicable) and should otherwise be usable by technical abstracting and indexing services.

3. Either British English or American English spellings may be used, provided that each word is spelled consistently throughout the paper.

4. Any commonly-accepted format for referencing is permitted, provided that internal consistency of format is maintained. As a guideline for authors who have no other preference, we recommend that references be given by author(s) name and year in the body of the paper (with alphabetical listing of all references at the end of the paper). Titles of Journals, monographs, and similar publications should be in italic font or should be underlined. Titles of papers or articles should be in quotation marks.

5. Internal consistency shall also be maintained for other elements of style, such as equation numbering. As a guideline for authors who have no other preference, we suggest that equation numbers be placed in parentheses at the right column margin.

6. The intent and meaning of all text must be clear. For authors who are NOT masters of the English language, the ACES Editorial Staff will provide assistance with grammar (subject to clarity of intent and meaning).

7. Unused space should be minimized. Sections and subsections should not normally begin on a new page.

PAPER FORMAT

The preferred format for initial submission and camera-ready manuscripts is 12 point Times Roman font, single line spacing and double column format, similar to that used here, with top, bottom, left, and right 1 inch margins. Manuscripts should be prepared on standard 8.5x11 inch paper.

Only camera-ready electronic files are accepted for publication. The term **"camera-ready" means that the material is neat, legible, and reproducible.** Full details can be found on ACES site, Journal section.

ACES reserves the right to edit any uploaded material, however, this is not generally done. It is the author(s) responsibility to provide acceptable camera-ready pdf files. Incompatible or incomplete pdf files will not be processed, and authors will be requested to re-upload a revised acceptable version.

SUBMITTAL PROCEDURE

All submissions should be uploaded to ACES server through ACES web site (http://aces.ee.olemiss.edu) by using the upload button, journal section. Only pdf files are accepted for submission. The file size should not be larger than 5MB, otherwise permission from the Editor-in-Chief should be obtained first. The Editor-in-Chief will acknowledge the electronic submission after the upload process is successfully completed.

COPYRIGHTS AND RELEASES

Each primary author must sign a copyright form and obtain a release from his/her organization vesting the copyright with ACES. Copyright forms are available at ACES, web site (http://aces.ee.olemiss.edu). To shorten the review process time, the executed copyright form should be forwarded to the Editor-in-Chief immediately after the completion of the upload (electronic submission) process. Both the author and his/her organization are allowed to use the copyrighted material freely for their own private purposes.

Permission is granted to quote short passages and reproduce figures and tables from and ACES Journal issue provided the source is cited. Copies of ACES Journal articles may be made in accordance with usage permitted by Sections 107 or 108 of the U.S. Copyright Law. This consent does not extend to other kinds of copying, such as for general distribution, for advertising or promotional purposes, for creating new collective works, or for resale. The reproduction of multiple copies and the use of articles or extracts for commercial purposes require the consent of the author and specific permission from ACES. Institutional members are allowed to copy any ACES Journal issue for their internal distribution only.

PUBLICATION CHARGES

ACES members are allowed 12 printed pages per paper without charge; non-members are allowed 8 printed pages per paper without charge. Mandatory page charges of $75 a page apply to all pages in excess of 12 for members or 8 for non-members. Voluntary page charges are requested for the free (12 or 8) pages, but are NOT mandatory or required for publication. A priority courtesy guideline, which favors members, applies to paper backlogs. Authors are entitled to 15 free reprints of their articles and must request these from the Managing Editor. Additional reprints are available to authors, and reprints available to non-authors, for a nominal fee.

ACES Journal is abstracted in INSPEC, in Engineering Index, and in DTIC.